FMCW Signals for Radar Imaging and Channel Sounding

Xavier Zage Raimundo

School of Engineering and Computing Sciences

Durham University

Durham, United Kingdom

A thesis submitted for the degree of Doctor of Philosophy

2015

Abstract

A linear / stepped frequency modulated continuous wave (FMCW) signal has for a long time been used in radar and channel sounding. A novel FMCW waveform known as “Gated FMCW” signal is proposed in this thesis for the suppression of strong undesired signals in microwave radar applications, such as: through-the-wall, ground penetrating, and medical imaging radar. In these applications the crosstalk signal between antennas and the reflections form the early interface (wall, ground surface, or skin respectively) are much stronger in magnitude compared to the backscattered signal from the target. Consequently, if not suppressed they overshadow the target’s return making detection a difficult task. Moreover, these strong unwanted reflections limit the radar’s dynamic range and might saturate or block the receiver causing the reflection from actual targets (especially targets with low radar cross section) to appear as noise. The effectiveness of the proposed waveform as a suppression technique was investigated in various radar scenarios, through numerical simulations and experiments. Comparisons of the radar images obtained for the radar system operating with the standard linear FMCW signal and with the proposed Gated FMCW waveform are also made.

In addition to the radar work the application of FMCW signals to radio propagation measurements and channel characterisation in the 60 GHz and 2-6 GHz frequency bands in indoor and outdoor environments is described. The data are used to predict the bit error rate performance of the in-house built measurement based channel simulator and the results are compared with the theoretical multipath channel simulator available in Matlab.

List of Symbols

ε_r	Relative permittivity
σ	Radar cross section
Θ	Antenna beamwidth
ΔCR	Cross-range resolution
Δf_D	Doppler resolution
ΔR	Down-range resolution
λ	Wavelength
β	Sweep rate
τ_1, τ_2	Additional receiver's gating sequence off-time delays
ν	Velocity
A_e	Effective aperture of an antenna
$A(x_i,y_j)$	Pixel's coordinate on x and y axis
B	Bandwidth
c	Velocity of the electromagnetic wave in free space
C_{UWB}	UWB channel capacity
D_{SAR}	Length of the (synthetic) array
f_b	Beat-note frequency
f_c	Centre frequency
f_D	Doppler frequency
$f_i(t)$	Instantaneous frequency
f_s	Sampling frequency
G_R	Receiver antenna Gain
G_t	Transmitter antenna Gain

$I(x_i, y_j)$	Pixel's energy / intensity
L	M-sequence length
N	Noise power
P_D	Power density
P_{Dt}	Target's backscattered power density
P_{min}	Minimum detectable power at the radar receiver
P_t	Peak power at the transmitter
Pr	Received power
R	Range
R_{max}	Maximum range
SNR	Signal-to-noise ratio
T	Chirp duration
T_b	Bit duration
T_s	Gating sequence period
X_G	Power loss due to gating sequence

List of Acronyms

2D	Two Dimensional
3D	Three Dimensional
ADC	Analogue to Digital Converter
AMP	Amplifier
AWG	Arbitrary Waveform Generator
BER	Bit Error Rate
BS	Background Subtraction
BPF	Band Pass Filter
BSS	Blind Source Separation
CBE	Complex Based Estimator
CEM	Computational Electromagnetic
CLK	Clock
CST	Computer Simulation Technology
DEM	Differential Equation Method
EM	Electromagnetic
FA	Factor Analysis
FDTD	Finite Difference Time Domain
FEM	Finite Element Method

FFT	Fast Fourier Transform
FIT	Finite Integration Technique
FMCW	Frequency Modulated Continuous Wave
GFMCW	Gated Frequency Modulated Continuous Wave
GPR	Ground Penetrating Radar
ICA	Independent Component Analysis
IEEE	Institute of Electrical and Electronic Engineers
IEM	Integral Equation Method
IFFT	Inverse Fast Fourier Transform
I/O	Input and Output
ISM	Industrial, Scientific and Medical
LNA	Low Noise Amplifier
LO	Local Oscillator
LOS	Line of Sight
LPF	Low Pass Filter
MF	Matched Filter
MIMO	Multiple Input Multiple Output
MIR	Medical Imaging Radar
MISO	Multiple-Input-Single-Output
MoM	Method of Moments
MRS	Mean Received Signal
MRP	Mean Received Power
MWS	Microwave Studio
NLOS	Non-line of Sight
NPL	National Physical Laboratory

OFDM	Orthogonal Frequency Division Multiplexed
PA	Power Amplifier
PBA	Perfect Boundary Approximation
PC	Personal Computer
PCA	Principal Component Analysis
PDP	Power Delay Profile
PEC	Perfect Electrical Conductor
PLL	Phase Locked Loop
PRBS	Pseudo Random Binary Sequence
PSD	Power spectrum density
RCS	Radar Cross Section
RLS	Recursive Least Squares
Rx	Receiver
SIMO	Single-Input-Multiple-Output
SISO	Single-Input-Single-Output
SVD	Singular Value Decomposition
TDR	Time Domain Reflectometry
TLM	Transmission Line Matrix
TTWIR	Through-the-Wall Imaging Radar
Tx	Transmitter
VB	Visual Basic
VNA	Vector Network Analyser
UWB	Ultra Wideband

Declaration

No portion of the work described in this thesis has been submitted in support of an application for another degree or qualification of this or any other university, or institution of learning.

Statement of Copyright

"The copyright of this thesis rests with the author. No quotation from it should be published without the author's prior written consent and information derived from it should be acknowledged."

Acknowledgements

I would like to thank everyone that directly or indirectly helped me or contributed to any part of the work presented in this thesis.

Specially the people below:

- My supervisor (*Professor: Sana Salous*) and co-supervisor (*Dr Wilhelm Klingenberg*) – for their guidance and support throughout the PhD course.
- *Dr Stuart Feenney* – for the invaluable comments and help on hardware related issues.
- Current and previous members of the Centre for Communication Systems (including: *Nasour, Adnan, Francesco, Odiri, Zhe, and Gao*) for their assistance during the measurement campaign and constructive discussions.
- The electronic technicians (including: *Ian Gareth, Ian Hutchinson, Neil Clarey, Colin Dart, and Martin Feeney*) for their help with manufacturing the printed antenna and PCB boards, and wiring the X-Y positioner.
- The mechanical technicians (including: *Colin, Paul, Antony, and Stuart*) for help with the mechanical works related to the project (e.g. X-Y positioner assembly, and discone antenna manufacturing).
- The civil laboratory technicians (*Longley and Richardson*) and the research student *Jonathan Asquith* for providing the soil used in GPR experiments and measuring its permittivity.
- Dr Catherine Mort and Ms. Christine Roughead for reviewing some of the chapters.
- Finally, *my family* and *friends* for their support and encouragement throughout these years.

Dedication

To the loving memory of:

my beloved father "Mr. Raimundo Xavier"

And

To my late uncle "Mr. Francisco Zage"

Table of Content

List of Figures

List of Tables

CHAPTER 1

Introduction and Significance

This chapter gives an overview of the thesis, highlighting the key contributions of the work presented here. A brief summary of the contents of each of the following chapters of this thesis is also given.

1.1 General Overview

The operating principle of a radar system is similar to that of a radio channel sounding system. The differences between both systems are mainly associated with their purpose and objectives [1]. In a *radar system* the propagated electromagnetic waves within an environment are detected and processed in order to locate a specific object (target) and possibly extracting the object related information (e.g. its range, speed, shape, and so on). On the other hand a radio channel sounder detects the electromagnetic waves within an environment (channel) which are processed in order to estimate the parameters that describe the time and/or frequency behaviour of the channel. Understanding of the channel behaviour through channel characterisation is of paramount importance especially for the reliable design and performance evaluation of a wireless communication system. In this thesis primarily, issues related to active microwave radar imaging will be considered.

1.1.1 Radar Imaging

In active microwave radar imaging the scenario under test is illuminated with microwave signals (from the transmitter) and scattered and/or incident signals are collected by the receiver(s) and processed to form an image map of the scenario. Three main microwave radar imaging applications are investigated in the thesis, namely: through-the-wall radar, ground penetrating radar, and medical radar imaging.

Through-the-Wall radar imaging (TTWRI) has gained a great deal of interest lately specially within the radar research community. It aims at detecting and identifying objects and/or life signs within an area which cannot be directly accessed or seen using conventional measures. TTWRI can be used in a range of applications from defence and law enforcement to civilian cases. As examples in defence / law enforcement applications it can be used for detection and surveillance of people behind walls (for cases such as hostages, contraband, or firefighting operations). In civil applications it can be used in rescuing missions for detection of survivors buried under: snow (after an avalanche) or rubble (after an earthquake or landslide) [2, 3]. Results from numerical simulations and experiments of the TTWRI for detection of a human being located behind a wall will be considered in this thesis.

Ground penetrating radar (GPR) techniques aim at detecting objects or interfaces buried below the surface of the earth. A variety of applications have been used / proposed for GPR for instance in defence – for anti-personnel or anti-tank landmine detection; utilities – for locating buried pipes (water or gas) and cables; and in geophysical investigations – mineral formation, glacier mapping, and ground water mapping [4]. In this thesis, consideration is given to the detection of buried metallic objects (e.g. land mines).

Medical radar imaging techniques, based on microwave signals, for breast cancer detection have gained attention over the past decade and are currently being proposed within the research community as an alternative imaging modality for breast cancer detection and diagnoses. Encouraging clinical trial results have been reported in references [5-7]. The technique offers the potential for a low cost screening device, fast screening time, no patient discomfort or health risk. This technique is based on the dielectric contrast between the tissues in the breast which causes an incident electromagnetic signal to be absorbed or scattered differently as it

passes through the breast. The received signal from around the breast is processed to create an energy map of the breast interior. This technique is also referred to in the literature as UWB microwave imaging radar.

A common issue with the aforementioned microwave radar imaging applications is the needed suppression/removal of the unwanted signals (clutter) before the image map of the scenario under test can be created. Unwanted signals such as: antenna crosstalk, wall reflection (in TTWR), ground surface reflection (in GPR), skin reflection (in MIR) can be much stronger than that of the respective target reflection. Therefore if not effectively removed they compromise the efficacy of the overall system. Moreover, strong unwanted signals together with weak target return increase the needed receiver dynamic range, as the receiver must accommodate both signals without being saturated or allowing the stronger clutter overshadowing / masking the weak target return. In this thesis a novel waveform namely: gated frequency modulated continuous waveform is proposed as the early unwanted signals suppression technique and its effectiveness in radar applications (e.g. TTWR, GPR, and MIR) will be investigated through numerical simulation and experiments.

1.1.2 Channel Characterization

It is well known that the fundamental limitations in the performance of a wireless communication system are mostly caused by the characteristics of the channel [8]. Consequently, understanding and characterising the channel behaviour is of great importance, as it aids in the development of more realistic channel models for validation of future wireless systems. Characterising the channel essentially means estimating the relevant parameters that describe the behaviour of the signals that propagate through it, such as the channel impulse response or frequency response. The realistic time-varying impulse or frequency responses of the desired channel are obtained through channel measurements using channel sounders.

In this thesis an in-house built multiband channel sounder has been used in channel measurements for indoor scenarios in the ISM band and for indoor / outdoor scenarios in the millimetre wave band (60 GHz). Statistical parameters which are related to the channel time delay and path-loss have been estimated from the respective measured channel impulse responses. Moreover, multi antenna channel

measurement campaigns have been performed, using the conventional vector network analyser, in a reference environment (i.e. reverberation chamber) for assessment of the diversity gain and channel capacity within the 2-6 GHz frequency band for variable inter-element antenna spacing. Finally, the bit error rate (BER) performances of the in-house built measurement based channel simulator [9], which uses real measurement channel data in the form of a time variant frequency function and that of the theoretical built-in MATLAB SIMULINK multipath fading channel simulator [10], which recreates the channel responses based on user's specified parameters, are compared. Radio channel simulators are used to emulate the effects of the propagation channel under diverse repeatable testing conditions in order to aid in the estimation and assessment of the performance of communication systems. Both simulators were used in conjunction with the IEEE 802.16 physical layer model. The measurement channel data were obtained from the channel sounding in rural/semi-rural environment of Ipswich in both 3.5 GHz and 5.8 GHz frequency bands.

1.2 Thesis Contributions

- A novel methodology for implementation of the FMCW / GFMCW waveforms as the excitation signals in the 3D electromagnetic software (CST Microwave Studio).

- Design and assembly of the radar demonstrator, antennas, and X-Y table positioning system.

- Validation of the effectiveness of GFMCW waveforms as a technique for suppression of crosstalk between antennas and the early clutter return signal from wall, ground surface, and skin in TTWIR, GPR, and MIR radar respectively. The technique was validated through simulations and experiments.

- Measurement and analysis of the MIMO capacity and diversity gain of discone antennas, in a reverberation chamber, for different inter-element antenna spacing.

- Channel measurement and characterisation in the 2.4 GHz and 60 GHz frequency using a frequency agile multiband channel sounder in an indoor or outdoor environment.

- Validation of the bit error rate (BER) performance of the in-house built "playback" channel simulator through comparison with the BER performance of the stochastic multipath channel simulator.

The work related to through-the-wall radar is a continuation from previous work reported in [11-13], to which the author contributed with the followings:

- Implementation in Matlab of the various beamforming algorithms (e.g. DAS, DSI, and DMSI) used to generate the radar images.
- Collaborating/Helping in the setting-up and running the radar experiments (e.g. assembling the radar on the trolley, moving the system or needed instruments, systems troubleshooting in case fault, and acting as the target).
- Performing the measurements and analysis of the antennas performance (e.g. results shown in Figures 20-23 in reference [12].

In this thesis more realistic simulation scenarios (e.g. room with insulated cavity wall; and furnished rooms) are presented. In the simulations the GFMCW is shown to suppress both the direct crosstalk signal and the air-wall reflection which is a more realistic approach. This differs from the earlier approach adopted in [11-13] where the crosstalk was first removed, by subtracting from each antenna recorded waveform the result obtained from the empty scenario simulation, prior to the application of the gating sequence for the removal of the wall reflection. Moreover, further experimental results to detect humans behind a wall are presented.

1.3 Organisation of the Thesis

The original aims of this project included the following:

- Assess the feasibility of using Gated FMCW waveforms as a radar clutter suppression technique and validate its effectiveness, through numerical simulation and experiment, in radar scenarios (such as: through-the-wall, ground penetration, and medical imaging for breast cancer detection).
- Validate the performance of the in-house built "playback" channel simulator.
- Provide an assessment of the radio channel statistics in a number of environments using the in-house developed multiband channel sounder.

As two different areas namely: radar imaging and radio channel (characterisation and modelling) are dealt with in the thesis, and for a coherent interpretation of the discussed concepts, the remaining chapters will cover primarily the radar imaging topic. In particular the proposed clutter suppression technique on radar imaging applications, namely: through-wall, ground penetrating, and breast cancer detection. Issues related to channel are discussed in detail in Appendix C.

Chapter 2: presents the basic operating principles of radar systems together with the definition of the basic radar performance parameters. The different radar modes of operation, possible employed waveforms, and the effect of the dielectric material on the transmitted electromagnetic wave are also discussed. Moreover, the chapter introduces the image algorithm known as the "delay-and-sum imaging algorithm" which has been used to create the image maps of the radar scenarios considered in this thesis.

Chapter 3: includes a review of some of the existing clutter suppression techniques used in radar applications such as: through-the-wall, ground penetrating radar, and medical imaging radar for breast cancer detection. Moreover, at the end of the chapter the novel clutter suppression technique proposed in this thesis is briefly described.

Chapter 4: presents the theoretical discussion in radar waveforms namely: linear frequency modulated continuous waveform (FMCW). The relationship

between system parameters and the methods used to extract the target range and Doppler information is also included. Moreover, the basic architectures of the proposed clutter suppression technique namely "gated frequency modulated continuous waveform (GFMCW)" are later presented as well as a detailed discussion of the range sensitivity of the gating sequences used in the work.

Chapter 5: presents two hardware implementations of the proposed GFMCW radar system adopted in this thesis. The overall synchronization and system performance results are also discussed. Furthermore, the different designed and in-house manufactured antennas as well as the assembled X-Y positioning table together with its control units are also described.

Chapter 6: includes the numerical simulation results for the FMCW and GFMCW radar systems in scenarios, such as: through-the-wall radar imaging, ground penetration radar imaging, and medical imaging radar for breast cancer detection. The benefits of performing numerical simulation as well as the available numerical simulation methods are given.

Chapter 7: presents the experimental results of the proposed suppression technique in applications, such as: through-the-wall radar imaging, ground penetration radar imaging, and medical imaging radar for breast cancer detection.

Chapter 8: conclusions are made and recommendations for future work are given.

Appendix C: includes the results of multiple-input and multiple-output (MIMO) measurement campaign performed within a reference environment, namely "Reverberation Chamber" to assess the MIMO channel capacity and diversity gain for variable inter-element antenna spacing. Moreover the results of the channel measurement campaigns in both indoor and outdoor environments using a newly designed and developed multiband channel sounder are also presented. Finally, bit error rate performance results of the in-house developed measurement based channel simulator and the widely available theoretical Matlab multipath channel simulator are compared.

1.4 References

[1] S. Salous, *Radio Propagation Measurement and Channel Modelling*. Chichester, UK.: John Wiley & Sons, 2013.

[2] D. D. Ferris and N. C. Currie, "Survey of current technologies for through-the-wall surveillance (TWS)," *Proc. SPIE*, vol. 3577, pp. 62-72, 1999.

[3] L. Chen and O. Shan, "Through-wall surveillance using ultra-wideband short pulse radar: numerical simulation," *2nd IEEE Conference on Industrial Electronics and Applications.* pp. 1551-1554, 2007.

[4] D. Daniels, "Applications of impulse radar technology," in *Radar 97 (Conf. Publ. No. 449)*, pp. 667-672, 1997.

[5] T. Henriksson, M. Klemm, D. Gibbins, J. Leendertz, T. Horseman, A. Preece, *et al.*, "Clinical trials of a multistatic UWB radar for breast imaging," *Loughborough Antennas and Propagation Conference (LAPC)*, pp. 1-4, 2011.

[6] E. Porter, A. Santorelli, and M. Popovic, "Time-domain microwave radar applied to breast imaging: measurement reliability in a clinical setting," *Progress In Electromagnetics Research*, vol. 149, pp. 119-132, 2014.

[7] P. Meaney, M. Fanning, D. Li, S. Poplack, and K. Paulsen, "A clinical prototype for active microwave imaging of the breast," *IEEE Transactions on Microwave Theory and Techniques*,vol. 48, pp. 1841-1853, 2000.

[8] L. Dong, G. Xu, and H. Ling, "Prediction of fast fading mobile radio channels in wideband communication systems," *IEEE GLOBECOM '01*, vol.6, pp. 3287-3291, 2001.

[9] K. Khokhar and S. Salous, "Frequency domain simulator for mobile radio channels and for IEEE 802.16-2004 standard using measured channels," *IET Communications*, vol. 2, pp. 869-877, 2008.

[10] C. D. Iskander, "A Matlab-based Object-Oriented Approach to Multipath Fading Channel Simulation," Hi-Tek Multisystems, 2008.

[11] F. Fioranelli, S. Salous, and X. Raimundo, "Frequency-modulated interrupted continuous wave as wall removal technique in through-the-wall imaging," *IEEE Transactions on Geoscience and Remote Sensing*, vol. 52, pp. 6272-6283, 2014.

[12] F. Fioranelli, S. Salous, I. Ndip, and X. Raimundo, "Through the wall detection with gated FMCW signals using optimized patch-like and vivaldi antennas," *IEEE Transactions on Antennas and Propagation,* vol. 63, pp. 1106-1117, 2015.

[13] F. Fioranelli, "Through-the-wall detection using ultra wide band frequency modulated interrupted continuous wave signals," PhD, School of Engineering and Computing Sciences, Durham University, Durham, UK, 2013.

CHAPTER 2

Radar Principles

This chapter presents a basic background of radar systems, their categories and the type of waveforms employed. The image algorithm commonly referred to in the literature as "delay-and-sum" imaging algorithm and often used to create the image map of the scenario under test from the radar received data, is also described in this chapter.

2.1 Basic Radar Equations

2.1.1 Radar Range Equation

The word "RADAR" is an acronym for "radio detection and ranging". Historically, radars were first developed with emphasis on detecting the presence of an approaching target (such as: an hostile aircraft or ship) and providing a measure of the target range [1]. Although detection and ranging are still incorporated in modern radar systems, these systems may also provide a high resolution image of the scene, target tracking, and also extract information from the target signature to aid in the estimation of the type of target, size, and shape.

One of the most basic and well covered equations in radar theory is the range equation. This relates the scatter range to the radar system parameter and the environment. The range equation provides a useful relation not just for determining

the maximum achievable radar range but also as a starting point for understanding the radar operation and the basic system design [2].

In order to derive the range equation let's start by assuming the propagation medium to be lossless and that the ideal radar system has a peak transmitted power P_t in watts (W) to be radiated with a directive antenna of gain G_t. The power density P_D (*ratio of power per unit of area in units of W/m*^{2}) at range R (m) away from the radar and in the direction of maximum radiation can be written as:

$$P_D = \frac{P_t G_t}{4\pi R^2} \tag{2.1}$$

For a target located at range R in the direction of the antenna's maximum gain, the electromagnetic waves with power density given in (2.1) that impinges upon the target is scattered away and towards the radar direction; though some of the wave energy might be absorbed by the target itself. The amount of scattered energy will depend on the physical (shape, size, orientation) and electrical properties of the target. These dependencies are often described with a single target specific quantity called "radar cross section" (RCS). The radar cross section σ, of unit square metres (m^2),is defined as the ratio of the power scattered back towards the radar to the power density incident on the target [3]. The RCS can also be viewed as the target's effective area or as a measure of the target's ability to reflect the signal in the direction of the radar. The target backscattered power density P_{Dt} (W/m^2) at a range R is given as:

$$P_{Dt} = \frac{P_D \sigma}{4\pi R^2} = \frac{P_t G_t \sigma}{[4\pi R^2]^2} \tag{2.2}$$

The total backscattered power received P_r, in units of watts (W), by the radar antenna of an effective aperture A_e in square metres (m^2) is given as:

$$P_r = \frac{P_t G_t \sigma A_e}{(4\pi R^2)^2} \tag{2.3}$$

It is well known from antenna theory that the antenna effective aperture is proportionally related to its gain G_R and the operating wavelength λ (m) [4]. Therefore, the radar received power from (2.3) can be written as:

$$P_r = \frac{P_t G_t G_R \lambda^2 \sigma}{(4\pi)^3 R^4} \tag{2.4}$$

The maximum radar range, in units of metre (m), is the distance at which the receiver detects the minimum backscattered power P_{min} (W), which can be deducted from (2.4) as:

$$R_{max} = \left[\frac{P_t G_t G_R \lambda^2 \sigma}{(4\pi)^3 P_{min}}\right]^{1/4} \tag{2.5}$$

The above equation suggests that in order to double the radar coverage range the transmitted power needs to be increased sixteen times or equivalently both antenna gains must be doubled. In a practical scenario the radar received signal is corrupted by noise therefore the target range is best described as a function of the received signal-to-noise ratio. Therefore for a minimum signal-to-noise ratio SNR_{min} at the receiver and considering the noise power within the operating band to be N, in unit of watts (W), the maximum achievable radar range can be written as:

$$R_{max} = \left[\frac{P_t G_t G_R \lambda^2 \sigma}{(4\pi)^3 N (SNR_{\min})}\right]^{1/4} \tag{2.6}$$

Equation (2.6) still assumes a lossless radar system and propagation medium. In reality, various other factors not explicitly included in the equation may affect the observable maximum radar range. Such factors include the losses and gain occurring throughout the radar system itself, the meteorological condition along the propagation path and so forth. The description of the factors and their effect on equation (2.6) are beyond the topic covered in this thesis. For the avid reader reference [1] provides detailed analysis of the effects these factors have on the achievable radar range.

2.1.2 Down-Range and Cross-Range Resolution

Resolution is a metric that describes the radar ability to distinguish or detect stationary or moving targets in close proximity to each other as different objects. The down-range resolution "ΔR", in unit of metres (m), relates to the ability of the radar to resolve distinct targets positioned within the same angle but at different

ranges. The down-range resolution is proportional to the wave speed v (m/s) in the medium and is inversely proportional to the waveform bandwidth B (Hz), as given in (2.7). Thus, if the radar waveform bandwidth is increased the smaller the down-range resolution it achieves.

$$\Delta R = \frac{v}{2B} \tag{2.7}$$

The cross-range resolution ΔCR, in unit of metres (m), on the other hand refers to the ability of the radar to distinguish targets at the same range but with different angles. For a single antenna with no processing the cross-range is directly proportional to the antenna beamwidth Θ, taken as the two way 3dB beamwidth in radians (rad), and the target range R as in the following equation [5]:

$$\Delta \mathrm{CR} = \theta R \tag{2.8}$$

The cross-range resolution in equation (2.8) degrades for targets at longer range. On the assumption that the range is restricted, the cross-range can be improved by increasing the operating frequency or by using an antenna with a bigger aperture size, as both of these decrease the beamwidth, although the latter seems impractical.

A more practical way of increasing the cross-range resolution is through signal processing with the use of multiple antennas, which could be a physical array of different antenna elements or a synthetic formed array such as those formed through *synthetic aperture radar* (SAR) techniques where measurements are performed at different positions along the scenario under test. The SAR approach has been used throughout the radar experiments reported in this thesis. The cross-range resolution for a synthetic array of length D_{SAR} (m) is given as [2]:

$$\Delta \mathrm{CR} = \frac{\lambda R}{2D_{SAR}} \tag{2.9}$$

Equation (2.9) seems to suggest that the cross-range resolution can be made arbitrarily small by increasing the length of the SAR array. Although theoretically plausible, it should be noted that in practice there are several factors that may limit the actual cross-range resolution as discussed in references [1, 2].

2.1.3 Radar Sensitivity and Dynamic Range

Radar sensitivity for a given bandwidth defines the minimum input RF power that can be detected by the radar. Therefore, it provides a measure of the radar's ability to detect the presence or absence of a target [6]. The dynamic range, normally expressed in dB, is the ratio between the strongest to the weakest signals the radar can handle, simultaneously. This factor is related to the number of bits in the receiver's analogue-to-digital (ADC) converter [7].

2.2 Conventional Radar Systems

A basic radar system comprises three main units: a transmitter, a receiver, and antenna unit. The transmitter generates the electrical waveform that is radiated in the form of an electromagnetic wave by the antenna. The antenna converts the electrical signal, from the transmitter, into electromagnetic wave and the incident reflected wave, from the scatterer, back into an electrical signal for the receiver unit. The receiver processes the signal to evaluate the presence or absence of a target as well as its features [8]. Conventional radar systems can be categorised based on their configuration and the employed waveform.

2.2.1 Radar System Modes of Operations

The radar operational mode can be classified based on the system deployment or on the number of antennas used. Based on the system deployment the radar can be either in a static or dynamic mode of operation. *Static mode* refers to a scenario where both the transmitter and receiver are fixed or stationary; contrary to the *dynamic mode* where the transmitter or receiver or both are in motion. It is worth mentioning that in either the static or dynamic mode of operation the scatterers, target(s) included, may be stationary or in motion [9].

Depending on the number of antennas used, the radar system can be said to operate in monostatic, bistatic, and multistatic. *Monostatic* – a single antenna is used for both transmission and reception, simultaneously. *Bistatic* – use different antennas for transmission and reception. *Multistatic* – uses multiple antennas for transmission or reception or for both (e.g. MIMO radar [10]).

2.2.2 Radar Waveforms

An essential component in the design of a radar system is the choice of the waveform. The radar waveform dictates the system architecture and the parameters that can be estimated. Some factors such as: range / Doppler resolution and measurement accuracy; operational prerequisite (tracking, imaging, covertness, applicable frequency restriction) and hardware cost; operating environment (type of clutter, signal interferences and target); all these influence the selection of a suitable waveform [9, 11]. A variety of waveforms have been in use or proposed in many radar applications, such as the conventional waveforms (e.g. un-modulated CW, pulse, synthetic pulse, and frequency modulated waveform), or more sophisticated waveform (e.g. noise waveforms).

Un-modulated CW Waveform – this is the simplest of the radar waveforms. It is essentially a single tone frequency waveform. With this the radar transmits a continuous stable signal with known frequency f_i. If the illuminated target is in motion then the backscattered received signal will be shifted in frequency, from the transmitted f_i, by an amount proportional to the speed and direction of the target. The frequency shift caused by the target is known as Doppler frequency. Single tone radars are widely used for measurements of a moving target relative velocity. They cannot measure the target range. To overcome the single tone shortcomings on the estimation of range a dual-tone based radar system can be employed. In the dual-tone based radar two single-tones separated in frequency by Δf are transmitted simultaneously or in sequence towards a target. The relative target range can be extracted from the received two-tone phase difference. It is worth mentioning that the maximum unambiguous range that can be measured with the two-tone radar is directly proportional to the wave speed and inversely to $2\Delta f$ [1].

Pulse waveform – a simple pulse waveform is a truncated sinusoid, in which one or more cycles of the sinusoid are transmitted only during the time window equivalent to the pulse width. Standard pulse waveforms come from ideally one of the derivatives of the Gaussian function, e.g. Gaussian waveform, the monocycle, or the doublet. Depending on the desired operating band the Gaussian based pulse can be carrier-free or modulated. Normally, the radar transmits a number of pulses

sequentially, with interval between consecutive pulses T_p being the reciprocal of the pulse repetition frequency. The pulse duration τ_w is inversely proportional to its bandwidth and it is directly related to the radar range resolution. Consequently reducing the pulse width increases the bandwidth and also the system range resolution. In pulse based radar, while the maximum unambiguous range is directly related to the pulse period T_p, the maximum unambiguous Doppler shift that can be measured is inversely related to T_p. Therefore when choosing the pulse period, in practice, a trade-off must be made between the maximum expected target range and the maximum expected Doppler shift [9]. As for small values of T_p high Doppler shift can be estimated but it might lead to ambiguity in range as the reflections from a far-away scatterer may arrive within the time window of a near scatterer. In contrast a large value of T_p covers a large range but may lead to Doppler ambiguity for cases of fast moving scatterers within the scenario. A major disadvantage with pulse waveforms is the hardware, e.g. generating short pulses with a fast rise and fall time is difficult; a high sampling rate ADC is needed to correctly digitize the received pulses; good antenna performance is desirable to avoid pulse dispersion and distortion; higher peak power at the transmitter to achieve a similar average power compared to FMCW or CW waveforms.

Synthetic Pulse waveform – To avoid the hardware limitations of the conventional pulse waveform multiple frequencies are transmitted in sequence to obtain the discrete bandlimited transfer function of the scenario under test. A received pulse is simply synthesised, using basic signal processing techniques, through the inverse Fourier / chirp transform of the product of the idealised transmitted pulse frequency response with the measured transfer function [12, 13]. Measurement of the transfer function of the scenario under test is commonly performed using the commercially available network analyser [14].

FM waveforms – In FM waveforms the waveform frequency is increased or decreased as a function of time over a range of frequencies defined by the bandwidth B within a specified modulation interval T. Within the modulation interval, the frequency can sweep linearly (as in linear FMCW) or in steps sequentially through M intermediate frequencies as in the stepped FMCW. In both cases, the transmission can be continuous (always ON) or gated. The waveform bandwidth is simply the

difference between the minimum and maximum swept frequency and the wider the bandwidth the finer the range resolution. Unlike pulse waveforms in FM waveforms the average power can be equal to the peak power especially for the cases in which the transmitter is always active. Moreover, FM waveforms are generally easier to generate than pulse waveforms. For example FMCW can be generated using a swept / stepped voltage-control oscillator (VCO) or a direct digital frequency synthesiser (DDFS) or even using an arbitrary waveform generator [11]. Contrary to discrete coded waveforms the spectrum of FM waveforms (FMCW) is contained within the swept bandwidth and therefore filtering is not required at the transmitter. But as for discrete coded waveforms the received signal can be compressed through the matched filter or heterodyne detector. Chapter 4 provides a more detailed analysis of FM waveforms particularly linear FMCW and Gated FMCW waveform.

Noise waveform – often referred to as pseudonoise or pseudorandom waveform is characterised by its Gaussian distributed amplitude and uniform power spectral density within the bandwidth. The target range is determined through the correlation of the received target's echo with the delayed copy of the transmitted waveform. The correlation returns a strong peak at a time equivalent to the target back-propagation delay [15]. Some of the inherited advantages of noise waveforms are low probability of detection, anti-jamming capability, and immunity for interference from other sources [11]. Moreover, each noise waveform is uncorrelated with the others, therefore theoretically several noise radars can operate in the same frequency band without affecting each other's performance [16]. The relation between the waveform bandwidth and the achievable range resolution for noise based radar is similar to that in FMCW radar.

Others type of radar waveforms reported in the literature includes *discrete coded waveforms [9, 17]* – in which the carrier waveform is phase modulated by a known code (e.g. Barker, PRBS, or Kasami code) the target profile is determined through a correlation process similar to that in noise waveforms; *Matched illumination waveforms [11, 18]* – which consider the apriori information about the characteristics and property of the target on its design in order to improve the target detection and classification; c*haos modulated waveforms [19];* and *orthogonal frequency division multiplexed (OFDM) waveforms [20]*.

Radar waveforms can be categorised, depending on their fractional bandwidth (FB), into three main groups namely: narrowband, wideband and ultra wideband. The fractional bandwidth of a waveform is defined as the ratio of the waveform's bandwidth to its centre frequency. A waveform is classified as narrowband if the FB is not greater than 1%, wideband if FB is within 1 – 20%, and ultra-wideband for FB greater than 20% [21].

2.2.3 Radar Applications

A radar system is a remote sensing device used in many areas ranging from civilian, law-enforcement, and military applications for purposes of surveillance, detection, tracking, or imaging. A comprehensive list of examples of radar applications are given in references [1, 22, 23] .

In this thesis three radar applications will be considered namely: *through-the-wall radar* – for detection of targets (humans) behind walls or buried under rubble; *medical imaging radar* – for breast cancer detection; and *ground penetrating radar* – detections of buried metallic objects (e.g. land mines). A common problem in these applications is the "*near-far problem*" in which strong early unwanted signals (e.g. direct antenna crosstalk and the wall, soil surface, or skin reflections) overshadow the return signal from the desired target especially for those located far from the radar or with a small RCS. A novel hardware based clutter suppression technique is proposed in the thesis to counteract the near-far effect.

2.3 Propagation Effects

The propagation of electromagnetic waves is influenced by the dielectric and physical properties of the medium or the material with which it interacts. Propagation phenomenon including: variation in the wave velocity, reflection, diffraction, attenuation and phase distortion are some of the impairments suffered by the wave as it interacts or travels through the medium. The theoretical basis of these effects are well covered in the literature, e.g. reference [9] provides a summary background.

A good understanding of the medium or material dielectric properties and heterogeneities are essential in order to accurately model these impairment effects

and moreover find efficient ways to mitigate them [11]. Principally, in the context of radar systems where the main objective is detecting, classifying, and / or tracking target(s), with certain dielectric properties, within an environment, which also may contain other objects, with properties different or similar to that of the target.

The dielectric properties of a material can be described by its parameters: permittivity, conductivity, and permeability which are frequency dependent. While permittivity describes the ability of material to store and release electromagnetic energy, conductivity is related to the loss (dissipation) or attenuation (absorption) the signal suffers as it propagates through the material. The higher the conductivity of the material the higher the loss or the attenuation the wave encounters. The material permittivity slows the speed of the wave that travels through by a factor proportional to the square root of permittivity (dielectric constant). The permeability on the other hand measures the ability of a material to sustain the formation of magnetic field. For the radar scenarios discussed in this thesis the permeability of materials is not considered as the materials (human tissue, soil, and wall) are non-magnetic.

In the radar numerical simulations and experimental work presented in this thesis the dielectric property of the material/medium are assumed to be known or taken from those reported in the literature. Measurements as well as the characterisation of the material dielectric properties are beyond the scope of this thesis. For the interested reader, references [11, 24] describe measurement techniques as well as the dielectric properties within the microwave frequency band for different types of building material applicable to through-the-wall radar imaging. Similarly, references [25, 26] and [27, 28] give the corresponding information for sand / soil for GPR and breast tissues for medical imaging radar for breast cancer detection, respectively.

2.4 Imaging Algorithms

A number of radar imaging algorithms have been reported in the literature that can be applied to the raw / pre-processed received radar data and create an easy to interpret 2-D or 3-D graphical image of the area under test. For the radar work presented in this thesis the well-known "*Delay-and-Sum*" (DAS) beamforming

algorithm has been used to create a planar (2-D) energy map of the scenario under test [29-31].

The main reasons for the choice of this algorithm have been its flexibility and easy computational complexity. This algorithm performs well independent of the antenna array topology (linear or non-linear) and it can also handle data obtained with multistatic, or bistatic / monostatic synthetic aperture radar configuration (SAR). Furthermore, it can easily account for the wave speed in a multi-layered medium, although prior knowledge of the medium dielectric property is needed. In the thesis it is assumed that the medium dielectric properties are known. The DAS algorithm involves the following steps [30]:

- Dividing the area of interest into a spatial grid of small pixels (focal points)
- For each focal point calculate the round trip delay from the transmitter to the focal point and back to the receiver.
- Based on the evaluated time delays, estimate the received amplitude in each transmitter–receiver pair for each pixel.
- The received amplitudes for each focal point are summed and squared, and this energy value is assigned for that pixel.
- The process is repeated for all pixels in the spatial grid.
- An energy map is then created from the pixels stored value.

For a monostatic or bistatic radar in a SAR configuration the energy of the pixel located at position $A(x_i, y_j)$ can be mathematically expressed in dB scaled as,

$$I(x_i, y_j) = 20log\left|\sum_{m=1}^{M} S_m(\tau_{mAm}(r))\right| \tag{2.1}$$

where: "S_m" is the recorded signal at the m^{th} radar position; "$\tau_{mAm}(r)$" is the signal time delay from the transmitter to the pixel "*A*" and back to the receiver.

$$\tau_{mAm}(r) = \frac{T_{mA} + R_{mA}}{\upsilon} \tag{2.2}$$

T_{mA} is the distance between the transmitter to the focal point and R_{mA} the distance from the receiver to the focal point. These distances can be estimated using equations (2.3) and (2.4) respectively:

$$T_{mA} = \sqrt{(x_{Tm} - x_i)^2 + (y_{Tm} - y_i)^2} \tag{2.3}$$

$$R_{mA} = \sqrt{(x_{Rm} - x_i)^2 + (y_{Rm} - y_i)^2} \tag{2.4}$$

For a multistatic array configuration with "*N*" transmitting and "*M*" receiving antennas the energy at the focal point "A" can be re-written as in (2.5).

$$I(x_i, y_j) = 20log\left|\sum_{m=1}^{M}\sum_{n=1}^{N} E_{mn}(\tau_{nAm}(r))\right| \tag{2.5}$$

It is worth mentioning that the effectiveness of the DAS algorithm relies on the accurate estimation of the round trip delay and also on the assumption that if the target is present at a particular focal point, then the signals returned for that point will add coherently while the return from clutter will add incoherently [32].

2.5 Summary

In this chapter background of radar systems, their modes of operation and waveform types was given. The detection of possible target(s) using a simple post-processing imaging algorithm namely "delay-and-sum", which is widely used in many radar applications, have been described. This post-processing algorithm has been used to create radar images presented in this thesis.

2.6 References

[1] M. Skolnik, *Introduction to Radar Systems*, 2nd ed. New York: MxGraw-Hill, 1981.

[2] M. Richards, *Fundamental of Radar Signal Processing*. New York: McGraw-Hill, 2005.

[3] B. Mahafza, *Radar Signal Analysis and Processing Using MatLab*: Chapman and Hall/CRC, 2009

[4] C. Balanis, *Antenna Theory: Analysis and Design*. Wiley-Interscience, 2005.

[5] M. Farwella, J. Rossa, R. Luttrella, D. Cohena, W. China, and T. Dogarub, "Sense through the wall system development and design considerations," *Journal of the Franklin Institute*, vol. 345 pp. 570-591, 2008.

[6] Y. Teng, H. Griffiths, C. Baker, and K. Woodbridge, "Netted radar sensitivity and ambiguity," *IET Radar, Sonar & Navigation*, vol. 1, pp. 479-486, 2007.

[7] S. Hamran, D. Gjessing, J. Hjelmstad, and E. Aarholt, "Ground penetrating synthetic pulse radar: dynamic range and modes of operation," *Journal of Applied Geophysics*, vol. 33, pp. 7-14, 1995.

[8] N. Kinzie, "Ultra-Wideband Pulse Doppler Radar for Short Range Targets," PhD, Department of Electrical, Computer, and Energy Engineering, University of Colorado, 2011.

[9] S. Salous, *Radio Propagation Measurement and Channel Modelling*. Chichester, UK. John Wiley & Sons, 2013.

[10] L. Zhang, B. Lu, Z. Zhou, and X. Sun, "A wall-clutter suppression method based on spatial signature in MIMO through-the-wall radar imaging," *Progress In Electromagnetics Research B*, vol. 55, pp. 277-295, 2013.

[11] M. Amin, *Through-the-Wall Radar Imaging*. United States: CRC Press Taylor & Francis Group, 2010.

[12] I. Craddock, R. Nilavalan, J. Leendertz, A. Preece, and R. Benjamin, "Experimental investigation of real aperture synthetically organised radar for breast cancer detection," *IEEE Antennas and Propagation Society International Symposium*, vol. 1B, pp. 179-182, 2005.

[13] J. Sill and E. Fear, "Tissue sensing adaptive radar for breast cancer detection - experimental investigation of simple tumor models," *IEEE Transactions on Microwave Theory and Techniques*, vol. 53, pp. 3312-3319, 2005.

[14] A. Lazaro, D. Girbau, and R. Villarino, "Simulated and experimental investigation of microwave imaging using UWB," *Progress In Electromagnetics Research*, vol. 94, pp. 263-280, 2009.

[15] T. Thayaparan and C. Wernik, "Noise radar technology basics," Defence R&D Canada - Ottawa Technical Memorandum 2006-266, 2006.

[16] R. Narayanan, "Ultra-wide-band noise radar systems," *SPIE Newroom*, 2012.

[17] C. Cook and M. Bernfeld, *Radar Signals: An Introduction to Theory and Application*: Academic Press, 1967.

[18] F. Ahmad and M. Amin, "Matched-illumination waveform design for a multistatic through-the-wall radar system," *IEEE Journal of Selected Topics in Signal Processing*, vol. 4, pp. 177-186, 2010.

[19] L. Xiaoxiang and L. Henry, "Through the wall imaging using chaotic modulated ultra wideband synthetic aperture radar," *IEEE International Conference on Acoustics, Speech and Signal Processing*, pp. 1257-1260, 2007.

[20] S. Sen and A. Nehorai, "Adaptive OFDM radar for target detection in multipath scenarios," *IEEE Transactions on Signal Processing*, vol. 59, pp. 78-90, 2011.

[21] D. Barras, F. Ellinger, and H. Jackel, "A comparison between ultra-wideband and narrowband transceivers," Proceedings TRLabs/IEEE Wireless, pp.211-214, 2002.

[22] D. Daniels, "Applications of impulse radar technology," in *Radar 97 (Conf. Publ. No. 449)*, pp. 667-672, 1997.

[23] E. Staderini, "UWB radars in medicine," *IEEE Aerospace and Electronic Systems Magazine*, vol. 17, pp. 13-18, 2002.

[24] A. Muqaibel, A. Safaai-Jazi, A. Bayram, A. Attiya, and S. Riad, "Ultrawideband through-the-wall propagation," *IEE Proceedings Microwaves, Antennas and Propagation*,vol. 152, pp. 581-588, 2005.

[25] B. Vishvakarma and C. Rai, "Measurement of complex dielectric constant of sand and dust particles as a function of moisture content," *23rd European Microwave Conference*,pp. 568-570, 1993.

[26] V. Mironov, "Spectral dielectric properties of moist soils in the microwave band," *IEEE Proceedings Geoscience and Remote Sensing Symposium,* vol. 5, pp. 3474-3477, 2004.

[27] C. Gabriel, S Gabriel, and E Corthout, “The dielectric properties of biological tissues: I. Literature survey,” *Physics in Medicine and Biology,* vol. 41, pp. 2231-2249, 1996.

[28] M. Lazebnik, L. McCartney, D. Popovic, C. Watkins, M. Lindstrom, J. Harter, *et al.,* "A large-scale study of the ultrawideband microwave dielectric properties of normal breast tissue obtained from reduction surgeries," *Physics in Medicine and Biology,* vol. 52, pp. 2637-2656, 2007.

[29] X. Li and S. Hagness, "A confocal microwave imaging algorithm for breast cancer detection," in *Microwave and Wireless Components, IEEE Letters,* vol. 11, pp. 130-132, 2001.

[30] L. Chen and O. Shan, "Through-wall surveillance using ultra-wideband short pulse radar: numerical simulation," *2nd IEEE Conference on Industrial Electronics and Applications,* pp. 1551-1554, 2007.

[31] M. Gonzalez-Huici, I. Catapano, and F. Soldovieri, "A comparative study of gpr reconstruction approaches for landmine detection," *IEEE Journal of Selected Topics in Applied Earth Observations and Remote Sensing,* vol. 7, pp. 4869-4878, 2014.

[32] D. Byrne, M. O'Halloran, M. Glavin, and E. Jones, "Data independent radar beamforming algorithms for breast cancer detection," *Progress In Electromagnetics Research,* vol. 107, pp. 331-348, 2010.

CHAPTER 3

Clutter Suppression Techniques – Review

A critical issue in radar imaging systems is the suppression/removal of clutter. Clutter not just obscures and interferes with the target but may also give rise to erroneous detection. In this chapter a review of some of the existing clutter suppression techniques will be given. Moreover, at the end of the chapter a novel clutter technique proposed in this thesis will be briefly described.

In radar systems, the term clutter refers to unwanted return signals which in most cases do not originate from the desired target. These signals may interfere or even overshadow the target signature, consequently making target detection a much more difficult task.

For instance in through-the-wall radar scenario, which aims at detecting and localizing beings (e.g. human) hidden behind a wall or obstacle, the radar's transmitted signal has to propagate through the facing wall and depending on the physical and electric properties of the wall much of it may be reflected back. The part of the signal that passes through-the-wall gets scattered by any physical interface it encounters as it propagates in the environment. Some of these scattered signals may propagate back through the facing wall and are sensed by the radar. So the radar received signal will be the combination of the entire sensed scattered signals. Differentiating the target return from other signals is not a trivial task; for an

improved radar performance suppression / removal of the unwanted signals (clutter) must be performed before target detection takes place.

Some clutter may interfere with the desired target return or even be strong enough in magnitude to overshadow the target's signature. As a consequence the resultant radar image may erroneously indicate no presence of a target, which is referred to as false-negative. Some of these unwanted signals if not effectively removed might appear as a target on the radar image therefore leading to a prediction of presence of a target when in fact there is no actual target in the scenario, this is referred to as false-positive predictions.

Several clutter suppression techniques have been reported in the literature in a number of radar imaging applications, such as the applications considered in this thesis namely: through-the-wall imaging radar, medical imaging radar, and ground penetrating radar.

In this chapter a review of some of the widely used clutter suppression techniques is given. These techniques are divided into two main categories namely: post-processing based techniques and hardware based techniques.

The post-processing based techniques are simply algorithms which are applied to the acquired/received data for clutter suppression purposes. The receivers in this case need to have enough dynamic range and sensitivity to acquire the clutter signals and the desired target return. Otherwise strong clutter may saturate the receiver or worse cause target return particularly from those with low RCS appearing as noise, consequently degrading the overall performance. On the other hand, hardware based techniques perform clutter suppression before signals are digitized. Therefore if the strong clutter is suppressed, weak signals from possible targets can be amplified and better acquired without the risk of saturating the receiver. Apart from antenna polarization techniques hardware based approaches perform some form of range or time gating. This means that they are able to reject signals arriving at a certain time or from a particular range while allowing others to pass through.

The next section reviews post-processing based techniques, and then hardware based approaches. Moreover, an introduction to the proposed hardware based approach is given.

3.1 Post-Processing Based Techniques

3.1.1 Background Subtraction Technique

Background subtraction (BS) is an effective method for the removal of mainly external clutter and has been widely applied in radar simulations and experiments. The basis of the technique is to acquire data from the scenario under test without the presence of the target(s). These data can be viewed as the calibration data of an "empty scenario". The data can then be used to subtract from the actual measured data the undesired reflections seen by each individual antenna. In [1] BS was used for the removal of antenna and the surrounding environment reflections in MIR for breast cancer detection. The calibration data (without the breast phantom present) was obtained by performing initial measurements at the pre-defined antenna position. These data were then subtracted from the actual measurements (with the phantom included). One of the assumptions with the BS technique is that the clutter is static and time-invariant.

Unfortunately, the BS technique is not practical or realistic when it comes to the removal of the unwanted skin, wall, or ground reflection in MIR, TTR and GPR applications respectively. This stems from the fact that the unwanted scatterers, for example: breast skin – is case dependent, with variations on its contour shape, size, and dielectric property. Consequently, it is hard to replicate for a specific scenario in order to extract the needed calibration responses.

The BS technique can in fact be considered as an ideal case, when the calibration responses are acquired from the same scenario under test in the absence of the target. Therefore, it is mostly applied for simplicity purposes as a bench mark, against which other clutter removal techniques can be compared [2, 3]; or when the emphasis is on testing / comparing the image formation algorithms [4-6], or even at the early stages of development of the radar systems [7] [8].

3.1.2 Displacement Based Technique

This technique, also referred to as differential or change detection, exploits the spatial or temporal variation of the target signature in order to suppress unwanted un-displaced clutter. In [9] this technique was used to remove antenna crosstalk and wall reflection in a TTW radar experiment. In the reported experiment, bistatic measurements were performed at predefined positions along a track, forming a linear SAR array. Parallel to the wall a small trihedral corner reflector acted as a stationary target behind the wall. The removal of the unwanted reflections consisted of the subtraction of the consecutive signals along the array, with the assumption that these reflections are similar between successive measurement positions and are thereby removed; whereas for a target, *not equidistant to both positions*, the return appears displaced in the profiles.

This technique is also widely used in TTW radar for the detection of life-sign (heartbeat and breathing) [10] or person movement [11, 12] by exploiting temporal changes in the received signal. This is simply done by subtracting the signals received at different time intervals, which is somewhat different from the above where the subtraction was performed between consecutive measurement positions. In this case for a fixed position the subtraction is performed for signals acquired at different consecutive [11] or non-consecutive [12] time instants. The technique can also be applied after the radar images have been through non-coherent detection, by subtracting images from different instants [13, 14].

Displacement based techniques have also been proposed by a research group at the University of Bristol (U.K) and successfully demonstrated for the removal of skin and clutter reflections in medical imaging radar for breast cancer detection [15, 16]. In their radar configuration a hemispherical shape antenna array surrounds the breast. Two measurement campaigns were performed; the first campaign with the array on its initial or default position and the second campaign after it is rotated (at a chosen angle) around its centre. The removal of unwanted clutter is performed by subtracting from each individual antenna its corresponding displaced or rotated measurement. The assumption made is that the undesired signal such as: antenna crosstalk and reflection from the skin is identical and appear at the same time position in both measurements (normal and displaced) while tumour response appears at different times. So the unwanted reflections can be removed by

subtraction. Although the technique may suppress the strong skin reflection it does so at the expense of adding clutter into the tumour response. Moreover for a tumour located close to or at the array rotation axis, the subtraction may remove its response. This technique may also generate ghost targets in the image as the tumour response from the displaced measurement is also added back [17].

3.1.3 Blind Sources Separation Techniques

Blind sources separation (BSS) techniques also referred to as subspace projection techniques are related to the decomposition / separation of a set of signals called source signals from their mixture without any prior knowledge about the mixing process or the sources [18, 19]. There are many BSS techniques reported in the literature applied to radar imaging applications for the purpose of clutter suppression. Some of these are: singular value decomposition (SVD), factor analysis (FA), principal component analysis (PCA) and independent component analysis (ICA). The theoretical formulations of these techniques are well covered in the literature. References [18-20] provide a detailed discussion and comparison of these techniques in different radar scenarios.

In order to apply any of the aforementioned techniques in TTW, GPR or MIR radar scenarios the received radar signals from the different receiver positions are grouped into a matrix format $M \times N$, also termed B-scan, where M represents the number of receivers and N the length of time samples. An appropriate BSS technique is applied to the matrix in order to decompose it into clutter, target and noise subspaces or matrices. Clutter subspaces, more importantly, need to be disregarded / removed before producing the radar images for successful target detection.

In [21] the SVD technique was applied to through-the-wall radar experiments data to suppress the wall reflections. The experiments were conducted in two different walls, namely: plywood and brick wall, the target was a 30 x 30 cm^2 aluminium sheet in both cases. From the decomposed subspaces in both scenarios the author empirically concluded that the subspace of the stronger eigenvalue, the first subspace, represented the clutter (wall reflections) contribution and therefore needed removal. Only the second subspace was used to create an image of the scenario which successfully showed the target while the other subspaces were disregarded as noise. Similar conclusions regarding the subspaces representing the

clutter and that of the target in a through-the-wall radar scenario were reached in [19, 20] for a monostatic antenna configuration in a SAR case and in [22] for MIMO antenna configuration.

In contrast in [23] it has been shown that clutter (wall reflection) may extend beyond the first subspace. In fact successful wall reflection suppression and consequently target detection were only obtained by removing the four strongest eigenvalues, for the plywood wall scenario, and the seven strongest eigenvalues for the concrete wall scenario. In both scenarios the remaining eigenvalues are made-up of the contributions from the target and the noise.

The SVD technique has also been used in MIR for breast cancer detection, to remove the air-skin and other internal breast tissue reflections [24, 25]. Furthermore this technique was reported in GPR scenarios for the suppression of the strong air-ground reflections [18, 26] which normally overshadow the return signal from the buried target.

Performance comparison amongst the different BSS techniques (SVD, PCA, FA, and ICA) for the purpose of clutter suppression have been performed in TTW [19, 20], and GPR scenarios [18, 27]. The results from the aforementioned references show that ICA outperforms the other techniques in terms of clutter mitigation but it has a higher algorithm complexity. ICA decomposes the data into statically independent components whereas PCA and FA represent it as uncorrelated components [20]. SVD is the simplest and offers the poorest performance among all the BSS techniques.

Although these techniques can offer the advantages of suppressing strong clutter without any priori information about the target or the clutter itself, their drawback is that for some of the clutter with energy comparable to that of the target return will not be suppressed. Therefore the clutter may still appear as a false target in the created image [28]. Moreover, there is no robust methodology for deciding the number of subspaces needed to be removed in order to achieve a higher signal-to-clutter ratio. In most related work, this has been empirically performed through trial and error.

3.1.4 Filtering Techniques

A number of post-processing filter based techniques have been reported in the literature for the suppression of undesired reflections (clutter) in radar applications such as GPR, TTWI and MIR. As mentioned previously undesired reflections such as that of the skin, in breast cancer imaging (MIR), tend to overshadow the return of the target (cancer tumuor). Similarly, the wall return overshadows the target (person) behind it in TTW and air-ground reflections tend to mask those of deep buried targets in GPR. Some of the proposed filter based techniques are:

- ***Averaged Based***

An early example of the averaged based technique for suppression of skin reflections in MIR can be found in [29], where a numerical 2-D FDTD breast model with cancer tumour included was used. In the simulation the breast phantom was surrounded by 17 monopole antennas which were individually excited with a short Gaussian pulse. The backscattered responses in each case were recorded by the same transmitting antenna in a monostatic radar approach. The averaged based technique involved subtracting the average of the received signal for all antennas from each antenna signal.

The main assumption with this technique is that the skin reflection is similar in all antenna positions (channels) and adds coherently. Consequently, when averaged it can be subtracted out from each channel, while the tumour response appears at different times at different antenna positions and it is not filtered out by the averaged signal.

This simple method seems to perform well in simulations and experiments involving a breast phantom with skin of homogeneous dielectric and of constant thickness [1, 30, 31]. In reality, breast skin is a heterogeneous tissue with variations in its dielectric [32, 33] and thickness [34, 35] hence, in practice the skin return signal at different antenna positions will not be so similar. Furthermore, the averaged channels internal breast clutter will be added back to the individual channels, consequently deteriorating the tumour response and causing possible ghost targets appearing in the reconstructed image. For a tumour located equidistantly from all/most antenna positions, a worst case scenario would be that its response will also

appear in the averaged signal. Therefore it will be subtracted out from the individual channels, leading consequently to a false negative.

This technique has been used in [36, 37] for suppression of wall reflections in TTW radar. Furthermore in references [38-40] it was used and compared against other techniques for the removal of air-ground reflection in ground penetration radar.

- ***Wiener Filter***

As an improvement to the averaging subtraction technique in [41] a Wiener filter was introduced as a means of removing the skin reflection in MIR for breast cancer detection. The idea here is to estimate the skin response in individual channels as a filtered combination of all other channels. The estimated channel's skin response is then subtracted from the channel recorded signal. The filter weights are computed to minimise the mean square error over the channel's skin early-time response. The filtering operation adds back residuals from other channels into the channel signal and these needs to be suppressed before imaging. A feedback filter was implemented in [41] to compensate for the unwanted residuals. Although this technique presents an improvement compared to the simple averaging based technique the response of targets (tumours) located on / or close to the antennas rotation axis could still suffer substantially.

- ***Recursive Least Squares Filter***

The recursive least squares (RLS) filter algorithm for the estimation of the skin response was first proposed by Sill et al. in [42]. The RLS is an adaptive algorithm in which the filter weights are computed recursively and updated for every time step. This is contrary to the Wiener filter technique in which the computed filter weights are constant through the selected skin early time window [24].

In [42] the RLS algorithm is applied on individual channels on the early part of the signal, corresponding to the skin response. For the remaining part of the signal, representing the breast interior, the Woody averaging algorithm [43] is applied. Both estimated signals are then concatenated and the total signal is then subtracted from the chosen channel signal. The duration of the skin response as well as the thickness were estimated using the algorithm developed in [44].

3.1.5 Frequency Domain Pole Splitting

This technique was originally proposed by Maskooki et al. [25] for the suppression of skin reflection in MIR for breast cancer detection. One advantage of this technique over the aforementioned filter based techniques is that the clutter (primarily skin) in each channel is suppressed independently from other channels. Therefore, no clutter or residual signals, from other channels, are added to the tumour response of the channel under consideration. The foundation of this technique is the representation of the channel (received radar signal) frequency response as a sum of complex sinusoids, where each complex sinusoid represents an eigenvalue (pole) of a linear system. Each pole on the other hand corresponds to a particular scatter in the environment as viewed by the antenna. Once the poles are estimated, a threshold is applied to remove the poles corresponding to the strongest scatterer (e.g. skin).

As this algorithm is applied to the data in the frequency-domain both early-time and late-time skin responses are suppressed. Simulation results in [24, 25] show that with a good choice of threshold this technique out-performs other methods in terms of tumour to clutter response ratio.

The drawback of the technique is that it relies on the choice of an optimal threshold which is difficult because the tumour return depends on many factors, such as: size, location, and water content. Therefore, choosing a big threshold may not suppress enough the unwanted reflections and also a small threshold can on the other hand cause the removal of the tumour return, which is something to be avoided in the first place.

3.2 Hardware Based Techniques

3.2.1 Time Gating Technique

Time gating techniques essentially mean disabling the receiver system (or part of it) for a certain specified time window(s) in order to avoid unwanted reflection(s) being received. This technique is widely used for the suppression of external clutter caused by distant objects [45, 46]. For a pulse based radar system if the transmitted pulse is short enough, this allows the resolution of the unwanted

early reflections from the wall; skin; or air-ground interface from the wanted reflections of the target, then the unwanted early clutter can be simply gated out. This can be achieved by switching on the receiver slightly after the unwanted time or just before the wanted target reflection. In a pulse based radar, performing time gating in hardware is not a trivial task as it requires: stable synchronisation and timing between the diverse modules (transmitter, receiver and switching mechanism), and a fast switch which depends on the radar application scenario.

Due to the above difficulty, this approach is often performed through post-processing by zeroing the undesired portion of the received signal. This has been suggested for the suppression of the early strong artefacts such as skin reflections in MIR [47], wall reflection in TTWR [48], and ground surface reflection in GPR [49].

It is worth mentioning that some of the materials (i.e. wall or skin) might exhibit a dispersive behaviour therefore distorting and broadening the reflected pulse and this essentially compromises the effectiveness of the technique. If the gating time is misjudged (by increasing it) it may cause the target's response to be also zeroed.

In [50, 51] a hybrid post-process time gating and filtering approach was proposed for suppression of both early and late-time clutter in MIR. Skin location and thickness are first estimated. Based on these estimates gating is applied to remove the external clutter and the early skin artefact. Once time gated the data are then filtered (using the Woody averaging algorithm [43]) to suppress the late time clutter.

3.2.2 Antenna Polarization Technique

It has been long understood from an electromagnetic perspective that the material shape affects the polarization of the waves interacting with it. As an example a wave reflected from a flat surface or diffracted from a straight edge of an object would be in co-polarization with the impinging waveform while its cross-polarised component would be a null [52]. For an object with irregular and/or a curved surface shape the reflected waveform would have a non-zero co-polarised and cross-polarised component.

The polarizations of the reflected wave have been explored as clutter suppression techniques in TTW and MIR radar. Through-the-wall radar numerical

simulations in [5, 52, 53] show that the human body, due to its curved and irregular shape, produces stronger cross polarized radar returns compared to walls or objects of regular, straight edged or right angled shapes. If the comparison is made in terms of the co-polarised components, the wall return was much stronger than that of the target. These results show that by receiving with a cross-polarised antenna one can mitigate the wall return and further may be able to discriminate the human signature from the other objects of a particular shape [52].

By receiving in a cross-polarised mode it was shown through simulation that antenna crosstalk and reflection from planar surfaces (e.g. chest-wall) can be suppressed while enhancing the reflection of axially asymmetric breast tumour reflections [54]. Similar conclusions were reached in [55] through simulation and experiments using a cross-polarised antenna at the receiver to that of the transmitter.

Although, the results in the above references are promising, there are still practical challenges in realising this approach. A cross-polarized component/signal tends to be very weak, therefore if a receiving system is not sensitive enough it may just be perceived as noise. Designing pure cross polarised antennas operating in a wide bandwidth is still a challenge. Moreover, although a planar surface reflection can be suppressed, a breast surface outline is not planar. Consequently breast skin reflections may still be considerably stronger than that of the tumour, especially for tumours located deep in the breast.

3.2.3 Hardware Based Filtering Techniques

Strong reflections, e.g.: antenna crosstalk, wall, skin, or air-ground backscatter, affect the radar's performance. These reflections tend to be much greater in magnitude in comparison to that of the desired target, therefore setting the upper limit of the radar dynamic range. This effectively limits the ability of the system in detecting weak signals such as the return of a low RCS target [56]. These strong undesired reflections not only may overshadow the target's signature but may also lead to the weak target signal to be buried in the system's noise floor. This makes the target detection more difficult even after application of the post-processing clutter suppression techniques. By eliminating these unwanted reflections in hardware (prior to the signal being recorded) the receiver can be more sensitive to the time delays related to possible target positions.

In [56, 57] a hardware filtering based technique was implemented for the suppression of wall reflection and antenna crosstalk in TTWR scenario using a FMCW based radar system. The operation of a FMCW based radar system is widely covered in the literature and is also described in detail in Chapter 4 Section 4.1. For the sake of understanding the implementation of the aforementioned suppression techniques a brief note on FMCW radar is given here.

In FMCW radar a chirp (as it is known) or appropriately a sinusoidal signal with linear time varying frequency is transmitted. The received delayed copy of the signal is correlated with a copy of the transmitted signal resulting in a frequency tone signal mostly referred to as a beat-note. The frequency of the tone is related to the target distance.

In through-the-wall radar scenarios the front wall interface is closer to the radar compared to any possible scatterer (targets) within the room. Therefore, the received tone related to the wall would have the lowest frequency. The antenna crosstalk would also produce a lower frequency tone as the distance between the antennas (for bistatic or multistatic mode) is still shorter than that to the target within the room. Consequently, the basic idea of this suppression technique is to filter out these undesired beat-note signals by using a suitable band pass filter. The performance of this technique is of course affected by the choice of the filter employed, as this needs to provide a steep transition from stop to pass band and constant pass band to suppress wall and crosstalk reflections while allowing the possible target signature to pass through unaffected.

It is worth mentioning that the received beat-note frequency is not only dependent on the distance between the scatterer and the radar, but also on other system parameters such as bandwidth and the duration of the chirp. For flexibility purposes a tuneable oscillator was used to shift the bandwidth of the transmitted chirp which resulted in a shift of the received beat-note frequencies. In this mode the receiver had a fixed bandwidth high-Q band pass filter and the tuneable oscillator could then be adjusted to bring the beat-note frequencies related to crosstalk and wall into the filter's stop band while maintaining those of possible targets into the filter's pass band.

3.3 Proposed Clutter Suppression Technique

This thesis presents "*Gated Frequency Modulated Continuous Waveform (GFMCW)*" as the proposed technique for the suppression of crosstalk and the strong early reflection that originates from the wall in TTWR, or breast skin interface in MIR for cancer detection, or soil surface in GPR application. It is well known that these reflections are much stronger in magnitude than that of a desired target, therefore making target detection difficult.

GFMCW signals have been used in applications such as ionospheric channel sounding and sea-surface remote sensing, to counter the drawbacks of a normal FMCW system. In FMCW systems both the receiver and transmitter are active simultaneously. Consequently, for a high transmitted power the receiver is generally blocked / saturated as a result of antenna crosstalk in a bistatic or multistatic system or poor isolation of the circulator device in a monostatic system. To counter this effect it is necessary to provide the receiver with listening intervals, during which no transmission occurs. This is achieved by switching the FMCW waveforms at the transmitter and receiver in an on-off pattern so to ensure the transmission and reception are not simultaneous.

GFMCW signals can be simply viewed as a FMCW signal that has been switched "on" and "off". It can be modelled as a product of a FMCW signal with "on" and "off" patterns (usually referred to as a gating sequence). The applied complementary gating sequences cause the radar system to exhibit range dependent sensitivity. Consequently, gating sequences can be suitably designed so the receiver only listens to reflections from the range related possible target while suppressing those from range(s) (time delays) related to unwanted scatterers.

In order to test the proposed technique on the aforementioned radar application scenarios numerical simulations as well as experimental measurement campaigns have been performed.

For the experimental work related to the proposed technique two hardware radar demonstrators have been built. The first radar system is based around two arbitrary waveform generators (AWG), one for the transmitter and the other for the receiver part, to generate simultaneously the transmitter and the receiver GFMCW / or normal FMCW waveforms. So no waveform switching through the hardware is

performed in this set-up as the AWGs can be loaded with the already gated FMCW waveforms. The FMCW waveforms are multiplied with the complementary gating sequence in software prior to being loaded into the respective AWG modules. To further provide flexibility and agility custom made software was created, through a combination of Matlab and C++, to provide control of the AWGs and give the ability to change all the parameters of the desired waveform. This demonstrator can generate a waveform with a maximum frequency range of 3.5 GHz. Therefore it was used in experiments involving: through-the-wall radar scenarios – for suppression of crosstalk and the strong wall reflections; and ground penetrating radar scenarios – for suppression of crosstalk and soil surface reflections.

The second radar system is based on a vector network analyser (VNA). The employed VNA is able to generate the FMCW waveform with maximum frequency of 8.5 GHz. In order to create GFMCW waveform fast pin diode switches were connected separately into the transmitter and receiver, switching the transmitted and received waveform on-off with complementary sequences. The switches were driven by the AWGs which in this case were pre-loaded with the respective gating sequence. This hardware demonstrator has been used in medical imaging radar scenarios for the suppression of crosstalk and the supposed breast skin reflection. The reason this demonstrator was used in this scenario was mostly due to the large achievable bandwidth with the VNA. Consequently, this enabled a much lower range resolution which is desirable in MIR scenarios.

3.4 Summary

Clutter or unwanted signals negatively affect the performance of a radar system, as they tend to mask and overshadow the desirable target signature. If not suppressed effectively the detection and identification of the desirable target becomes more difficult.

In this chapter a review of some clutter suppression techniques was outlined, with focus on those applied to TTWR, MIR, and GPR scenarios for the suppression of wall, breast skin, and ground surface reflection respectively. These techniques were divided into two main groups: post-processing based and hardware based. Post-processing based techniques are simply algorithms that can be applied to the collected radar data in order to remove the clutter. The radar system in these cases needs to be sensitive enough to record not just the target return but also those of the strong unwanted reflections e.g. antenna crosstalk. It is well known that the unwanted reflections can be in some cases strong enough that may cause the desired target reflection to appear as noise in the receiver or even creating a false-positive which increases the difficulty in detecting the target.

Hardware based approaches on the other hand suppress the unwanted clutter return in the hardware before the signal is acquired or digitised. Therefore, offering the advantage of avoiding the receiver being saturated by strong unwanted scatterer's return and crosstalk, thus improving the system's sensitivity towards weak returns such as those of targets at far distances or of low radar cross section.

The proposed clutter suppression technique in this thesis has also been briefly introduced at the end of this chapter. The proposed technique termed GFMCW can also be classed as hardware based approach as it provides the suppression before the signals at the receiver are digitised. GFMCW can also be paired with other post-processing techniques to further enhance the overall system performance in terms of clutter mitigation.

3.5 References

[1] S. Salvador, and G. Vecchi, “Experimental tests of microwave breast cancer detection on phantoms,” *IEEE Transactions on Antennas and Propagation,* vol. 57, no. 6, pp. 1705-1712, 2009.

[2] A. Lazaro, D. Girbau, and R. Villarino, “Simulated and experimental investigation of microwave imaging using UWB” *Progress In Electromagnetics Research,* vol. 94, pp. 263-280, 2009.

[3] M. Elahi, A. Shahzad, M. Glavin, E. Jones, and M. O'Halloran, “Hybrid artifact removal for confocal microwave breast imaging,” *IEEE Antennas and Wireless Propagation Letters,* vol. 13, pp. 149-152, 2014.

[4] B. Boudamouz, P. Millot, and C. Pichot, “Through the wall radar imaging with mimo beamforming processing - simulation and experimental results,” *American Journal of Remote Sensing,* vol. 1, no. 1, pp. 7-12, 2013.

[5] T. Dogaru, C. Le, and L. Nguyen, “Synthetic aperture radar images of a simple room based on computer models,” *ARL Technical Report, Adelphi, MD, ARL-TR-5193*, 2010.

[6] M. O'Halloran, M. Glavin, and E. Jones, “ Performance and robustness of a multistatic beamforming algorithm for breast cancer detection,” *Progress In Electromagnetics Research,* vol. 105, pp. 403-424, 2010.

[7] X. He, J. Li, and C. Wu, "A novel UWB imaging system setup for computer-aided breast cancery diagnosis," *IEEE International Conference on Ultra-wideband,* pp. 260-264, 2014.

[8] C. Dionisio, S. Tavares, M. Perotoni, and S. Kofuji, “Experiments on through-wall imaging using ultra wideband radar,” *Microwave and Optical Technology Letters,* vol. 54, no. 2, pp. 339-344, 2012.

[9] M. Dehmollaian, M. Thiel, and K. Sarabandi, “Through-the-wall imaging using differential SAR,” *IEEE Transactions on Geoscience and Remote Sensing,*vol. 47, no. 5, pp. 1289-1296, 2009.

[10] B. Yilmaz, S. Demirci, E. Yigit, and C. Ozdemir, “An Experimental study of through-the-wall radar for lifesign detection,” *PIERS Proceedings, Stockholm*, pp. 1602-1604, 2013.

[11] B. Lu, Q. Song, Z. Zhou, and H. Wang, "A SFCW radar for through wall imaging and motion detection." *European Radar Conference*, pp. 325-328, 2011.

[12] F. Ahmad, and M. Amin, "Through-the-wall human motion indication using sparsity-driven change detection," *IEEE Transactions on Geoscience and Remote Sensing*, vol. 51, no. 2, pp. 881-890, 2013.

[13] B. Lu, Q. Song, Z. Zhou, and X. Zhang, "Detection of human beings in motion behind the wall using SAR interferogram," *IEEE Geoscience and Remote Sensing Letters*, vol. 9, no. 5, pp. 968-971, 2012.

[14] A. Martone, K. Ranney, and C. Le, "Noncoherent approach for through-the-wall moving target indication," *IEEE Transactions on Aerospace and Electronic Systems*,vol. 50, no. 1, pp. 193-206, 2014.

[15] T. Henriksson, M. Klemm, D. Gibbins, J. Leendertz, T. Horseman, A. Preece, *et al.*, "Clinical trials of a multistatic UWB radar for breast imaging," in *Loughborough Antennas and Propagation Conference (LAPC)*, pp. 1-4, 2011.

[16] M. Klemm, I. Craddock, J. Leendertz, A. Preece, and R. Benjamin, "Experimental and clinical results of breast cancer detection using UWB microwave radar," *IEEE Antennas and Propagation Society International Symposium*, pp. 1-4, 2008.

[17] J. Deprez, M. Klemm, P. Smith, and I. Craddock, "Twin target correction for ultra-wideband radar imaging of breast tumours," *IEEE International Symposuim on Nano to Macro*, pp. 213-216, 2010.

[18] F. Abujarad, "Ground Penetrating radar signal processing for landmine detection," PhD, Institute of Electronics Signal Processing and Communications Engineering, University of Magdeburg, Germany, 2007.

[19] P. Verma, A. Gaikwad, D. Singh, and M. Nigam, "Analysis of clutter reduction techniques for through wall imaging in UWB range," *Progress in Electromagnetics Research B*, vol. 17, pp. 29-48, 2009.

[20] A. Gaikwad, D. Singh, and M. Nigam, "Application of clutter reduction techniques for detection of metallic and low dielectric target behind the brick wall by stepped frequency continuous wave radar in ultra-wideband range," *IET Radar, Sonar & Navigation*, vol. 5, no. 4, pp. 416-425, 2011.

[21] R. Chandra, A. Gaikwad, D. Singh, and M. Nigam, “An approach to remove the clutter and detect the target for ultra-wideband through-wall imaging,” *Journal of Geophysics and Engineering*, vol. 5, pp. 412-419, 2008.

[22] H. Zhou, Z. Shu, and S. Tan, “Joint wall reflection suppression and parameters estimation for MIMO TWR imaging,” *Journal of Information and Computational Science* vol. 10, no. 17, pp. 5671-5679, 2013.

[23] L. Zhang, B. Lu, Z. Zhou, and X. Sun, "The clutter suppression based on statistical techniques in TWI application," *IEEE International Conference on Ultra-wideband*, pp. 130-135, 2013.

[24] M. Elahi, M. Glavin, E. Jones, and M. O'Halloran, “Artifact removal algorithms for microwave imaging of the breast,” *Progress In Electromagnetics Research*, vol. 141, pp. 185-200, 2013.

[25] A. Maskooki, E. Gunawan, C. Soh, and K. Low, “Frequency domain skin artifact removal method for ultra-wideband breast cancer detection,” *Progress In Electromagnetics Research*, vol. 98, pp. 299-314, 2009.

[26] A. Yoldemir, R. Gürcan, G. Kaplan, and M. Sezgin, “Comparative analysis of clutter suppression techniques for landmine detection using ground-penetrating radar ” *Proc. of SPIE* vol. 8017, 2011.

[27] B. Karlsen, J. Larsen, H. Sorensen, and K. Jakobsen, "Comparison of PCA and ICA based clutter reduction in GPR systems for anti-personal landmine detection," *IEEE Workshop on Statistical Signal Processing*, pp. 146-149, 2001.

[28] L. Zhang, B. Lu, Z. Zhou, and X. Sun, “A wall-clutter suppression method based on spatial signature in MIMO through-the-wall radar imaging,” *Progress In Electromagnetics Research B*, vol. 55, no. 277-295, 2013.

[29] X. Li, and S. Hagness, “A confocal microwave imaging algorithm for breast cancer detection,” *IEEE Microwave and Wireless Components Letters*, vol. 11, no. 3, pp. 130-132, Mar, 2001.

[30] H. Lim, N. Nhung, E. Li, and N. Thang, “Confocal microwave imaging for breast cancer detection: delay-multiply-and-sum image reconstruction algorithm,” *IEEE Transactions on Biomedical Engineering*,vol. 55, no. 6, pp. 1697-1704, 2008.

[31] E. Fear, X. Li, S. Hagness, and M. Stuchly, “Confocal microwave imaging for breast cancer detection: Localization of tumors in three dimensions,”

IEEE Transactions on Biomedical Engineering, vol. 49, no. 8, pp. 812-822, Aug, 2002.

[32] C. Gabriel, S. Gabriel, and E. Corthout, "The dielectric properties of biological tissues: I. Literature survey," *Physics in Medicine and Biology*, vol. 41, pp. 2231-2249, 1996.

[33] S. Gabriel, R. Lau, and C. Gabriel, "The dielectric properties of biological tissues: II. Measurements in the frequency range 10 Hz to 20 GHz," *Physics in Medicine and Biology*, vol. 41, no. 11, pp. 2251-2269, 1996

[34] H. Ulger, N. Erdogan, S. Kumanlioglu, and E. Unur, "Effect of age, breast size, menopausal and hormonal status on mammographic skin thickness," *Skin Research Technology*, vol. 9, pp. 284-289, 2003.

[35] S. Willson, E. Adam, and A. Tucker, "Patterns of breast skin thickness In normal mammograms," *Clinical Radiology*, vol. 33, pp. 691-693, 1982.

[36] Y. Sun, and M. Amin, "Spatial filtering for wall-clutter mitigation in through-the-wall radar imaging," *IEEE Transactions on Geoscience and Remote Sensing*, vol. 47, no. 9, pp. 3192-3208, 2009.

[37] R. Solimene, and A. Cuccaro, "Front wall clutter rejection methods in TWI," *IEEE Transactions on Geoscience and Remote Sensing Letters*, vol. 11, no. 6, pp. 1158-1162, 2014.

[38] R. Solimene, A. Cuccaro, A. Dell'Aversano, I. Catapano, and F. Soldovieri, "Background removal methods in GPR prospecting," *IEEE European Radar Conference*, pp. 85-88, 2013.

[39] A. Mayordomo, and A. Yarovoy, "Optimal background subtraction in GPR for humanitarian demining," *IEEE European Radar Conference*, pp. 48-51, 2008.

[40] I. Nicolaescu, P. van Genderen, K. Van Dongen, J. van Heijenoort, and P. Hakkaart, "Stepped frequency continuous wave radar-data preprocessing," *IEEE Workshop on Advance Ground Penetrating Radar*, pp. 177-182, 2003.

[41] E. Bond, X. Li, S. Hagness, and B. Van Veen, "Microwave imaging via space-time beamforming for early detection of breast cancer," *IEEE Transactions on Antennas and Propagation*,vol. 51, no. 8, pp. 1690-1705, 2003.

[42] J. Sill, and E. Fear, “Tissue sensing adaptive radar for breast cancer detection - experimental investigation of simple tumor models,” *IEEE Transactions on Microwave Theory and Techniques,*vol. 53, pp. 3312-3319, 2005.

[43] C. Woody, “Characterization of an adaptive filter for the analysis of variable latency neuroelectric signals,” *Medical and Biological Engineering,* vol. 5, no. 6, pp. 539-554, 1967.

[44] T. Williams, E. Fear, and D. Westwick, "Tissue sensing adaptive radar for breast cancer detection: investigations of reflections from the skin." *IEEE International Syposium on Antennas and Propagation,* vol. 3, pp. 2436-2439, 2004.

[45] M. Zhao, J. Shea, S. Hagness, and D. Van Der Weide, “Calibrated free-space microwave measurements with an ultrawideband reflectometer-antenna system,” *IEEE Transactions on Microwave and Wireless Components Letters*, vol. 16, no. 12, pp. 675-677, 2006.

[46] X. Li, S. Davis, S. Hagness, D. Van der Weide, and B. Van Veen, “Microwave imaging via space-time beamforming: experimental investigation of tumor detection in multilayer breast phantoms,” *IEEE Transactions on Microwave Theory and Techniques,* vol. 52, no. 8, pp. 1856-1865, 2004.

[47] R. Nilavalan, A. Gbedemah, I. Craddock, X. Li, and S. Hagness, “Numerical investigation of breast tumour detection using multi-static radar,” *Electronics Letters*, vol. 39, no. 25, pp. 1787-1789, 2003.

[48] W. Yazhou, and A. Fathy, “Advanced system level simulation platform for three-dimensional UWB through-wall imaging sar using time-domain approach,” *IEEE Transactions on Geoscience and Remote Sensing,* vol. 50, no. 5, pp. 1986-2000, 2012.

[49] R. Solimene, A. D'Alterio, and F. Soldovieri, "Half-space estimation by time gating based strategy." *13th IEEE Conference on Ground Penetrating Radar* pp. 1-5, 2010.

[50] E. Fear, J. Sill, and M. Stuchly, “Experimental feasibility study of confocal microwave imaging for breast tumor detection,” *IEEE Transactions on Microwave Theory and Techniques*, vol. 51, no. 3, pp. 887-892, 2003.

[51] E. Fear, and J. Sill, "Preliminary investigations of tissue sensing adaptive radar for breast tumor detection." *25th International IEEE Conference on Engineering in Medicine and Biology Society*, vol. 4, pp. 3787-3790, 2003.

[52] T. Dogaru, and C. Le, "Simulated radar range profiles of a simple room as computed by FDTD and Xpatch", *ARL Technical Report, Adelphi, MD, ARL-TR-4420*, 2008.

[53] T. Dogaru, and C. Le, "SAR Images of rooms and buildings based on FDTD Computer models," *IEEE Transactions on Geoscience and Remote Sensing,* vol. 47, no. 5, pp. 1388-1401, 2009.

[54] S. Hagness, A. Taflove, and J. Bridges, "Three-dimensional FDTD analysis of a pulsed microwave confocal system for breast cancer detection: design of an antenna-array element," *IEEE Transactions on Antennas and Propagation,* vol. 47, no. 5, pp. 783-791, 1999.

[55] X. Yun, R. Johnston, and E. Fear, "Radar-based microwave imaging for breast cancer detection: tumor sensing with cross-polarized reflections." *IEEE International Syposium on Antennas and Propagation,* vol. 3, pp. 2432-2435, 2004.

[56] G. Charvat, L. Kempel, E. Rothwell, C. Coleman, and E. Mokole, "A Through-dielectric radar imaging system," *IEEE Transactions on Antennas and Propagation,* vol. 58, no. 8, pp. 2594-2603, 2010.

[57] N. Maaref, and P. Millot, "Array-based ultrawideband through-wall radar: prediction and assessment of real radar abilities," *International Journal of Antennas and Propagation,* vol. 2013, pp. 1-9, 2013.

CHAPTER 4

Gated FMCW Signal Principle

This chapter presents the theoretical concept of linear frequency modulated continuous waveform used in radar and channel sounding systems. The relationship between system parameters and the processing method used to extract the target range and Doppler information is also investigated. The basic architectures of the gated frequency modulated continuous waveform system are later presented as well as a detailed discussion on the range sensitivity of gating sequences employed in this thesis.

4.1 FMCW Signal

The principles and theory behind FMCW signals for radar and channel sounding applications are well covered in many radar textbooks [1-3]. Included in this chapter is a brief analysis of a linear FMCW signal. In a linear FMCW system the transmitted signal's frequency is linearly swept upward or downward over a frequency range *B* during a sweep period *T*.

The phase of a linear FMCW signal can be mathematically expressed as:

$$\emptyset(t) = \pi\beta t^2 + 2\pi f_c t \qquad -T/2 \le t \le T/2 \tag{4.1}$$

where: $\beta = B/T$ is the sweep rate; and f_c is the waveform centre frequency.

Hence, the waveform instantaneous frequency $f_i(t)$ can be calculated as:

$$f_i(t) = \frac{1}{2\pi}\left\{\frac{d}{dt}\emptyset(t)\right\} = \beta t + f_c \qquad -T/2 \le t \le T/2 \tag{4.2}$$

The linear FMCW signal is also commonly referred to as a "chirp waveform" in similarity to the sound of an audio waveform with a linearly changing frequency. In (4.2) when β is positive the signal frequency ramps upward, and if β is negative it ramps downward [1]. Figure 4.1 shows the time-frequency relation of a linear FMCW signal for a positive and negative β respectively.

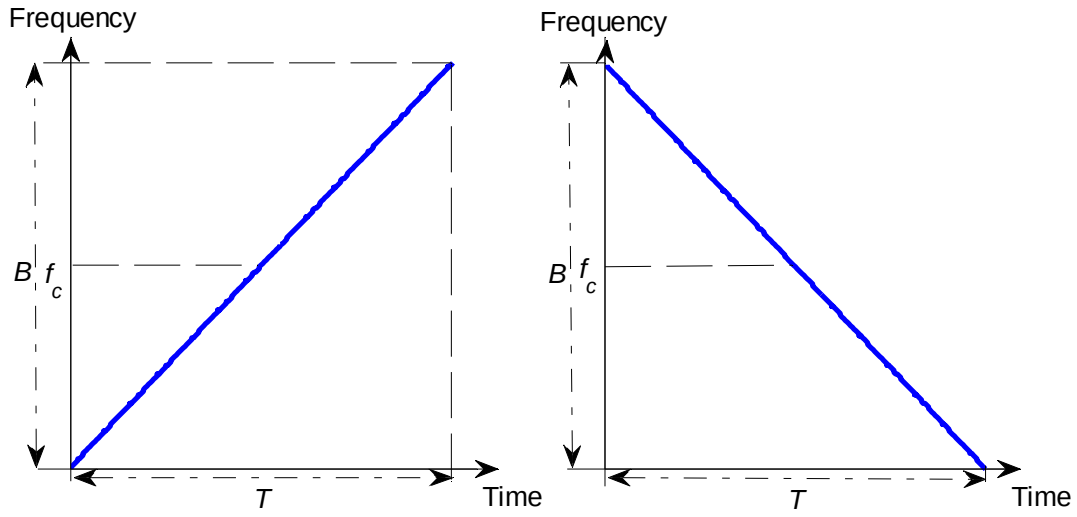

Figure 4.1: Time – Frequency relation of a linear FMCW waveform, (left) sweeping upward, and (right) sweeping downward.

Mathematically a real linear FMCW signal with constant amplitude can be expressed as:

$$x(t) = A_T \cos\{\emptyset_T(t)\} = A_T \cos(\pi\beta t^2 + 2\pi f_c t) \quad -T/2 \le t \le T/2 \tag{4.3}$$

where: A_T is the amplitude and $\phi_T(t)$ the phase of the transmitted linear FMCW signal. The corresponding waveform of (4.3) is shown in Figure 4.2 for a positive and negative β respectively. The spectrum of $x(t)$ can be obtained from the Fourier transform of (4.3). The analytical expression of the spectrum of a linear FMCW signal has been derived in [4-7]. For large time-bandwidth product ($BT >> 10$) the magnitude of the spectrum can be considered to be a constant across the signal bandwidth, and it is approximated by the following equation [4]:

$$X(f) = F\{x(t)\} \approx \sqrt{\frac{1}{4\beta}} \exp\left[-j\left(\frac{\pi(f-f_c)^2}{\beta} + \frac{\pi}{4}\right)\right] \tag{4.4}$$

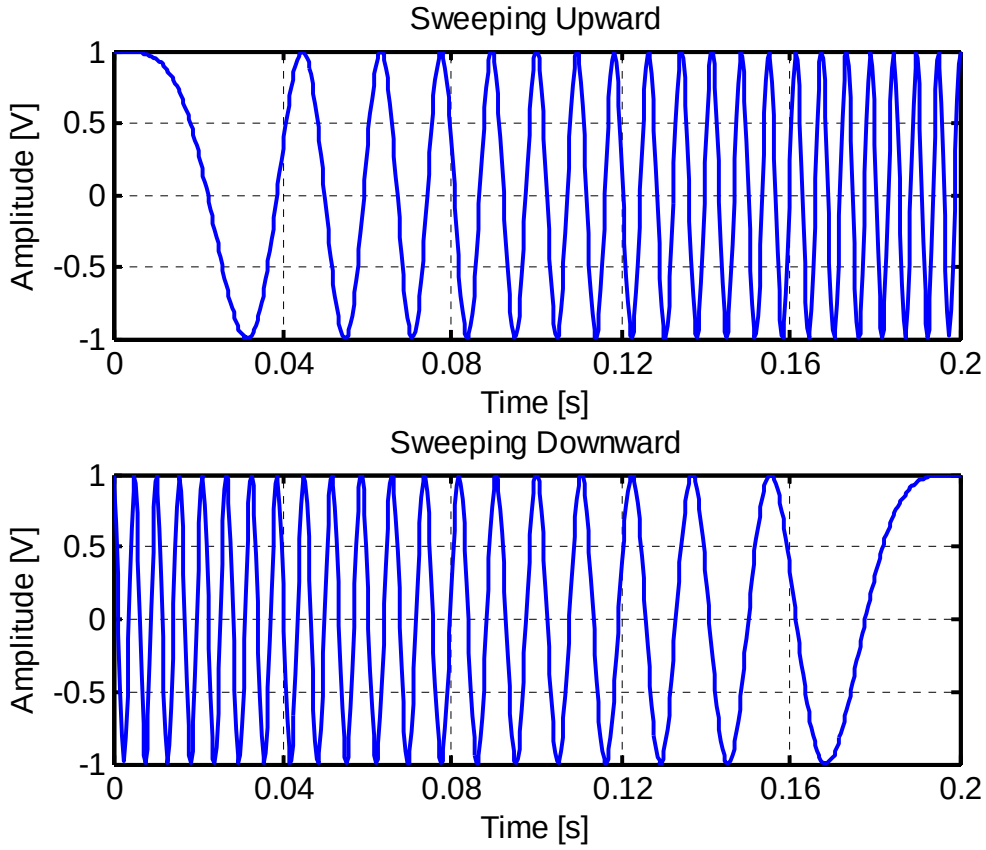

Figure 4.2: Linear FMCW signal in time domain.

It should be noted that the time-bandwidth product of linear FMCW signal has an effect on the signal spectrum shape or on the spectral energy confined within the bandwidth. Figure 4.3 shows the spectrum of a waveform with the bandwidth of 400 Hz and a centre frequency of 200 Hz for different *BT* products. As can be seen from the figure as *BT* increases the spectrum takes a more defined shape similar to a rectangular shape. In practice *BT* is usually much greater than 100, therefore more than 98% of the signal energy is contained within the bandwidth [2].

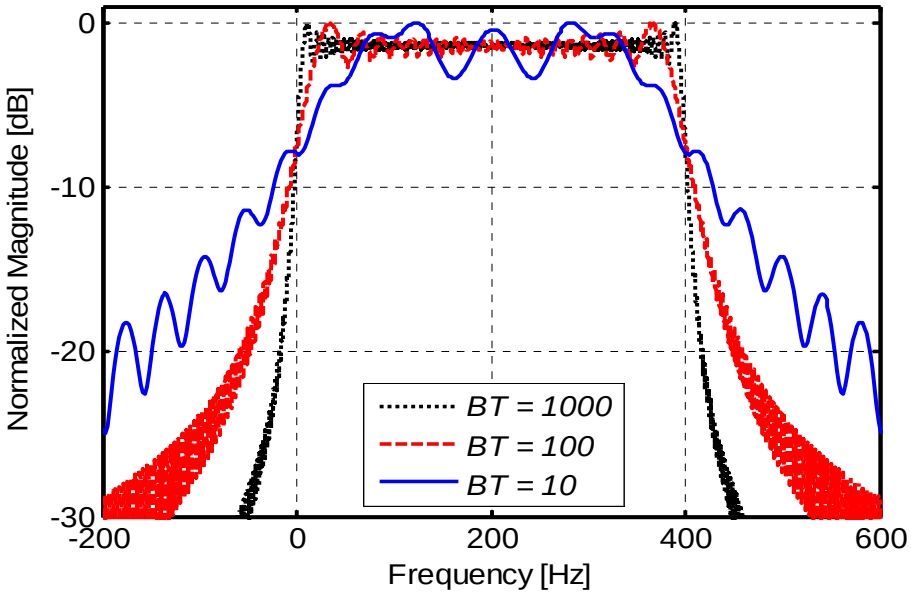

Figure 4.3: Linear FMCW signal spectrum for different time-bandwidth product.

4.1.1 Retrieving Range and Doppler Information

The range and the Doppler information of a chirp based system can be extracted from the output signal of a matched filter or a heterodyne detector employed at the receiver. The matched filter (MF) detector uses a filter with an impulse response equal to the conjugate and time reversed version of the transmitted signal, delayed accordingly to ensure casualty [5]. The MF detector outputs a signal that is compressed in time with a bandwidth similar to the chirp bandwidth. Consequently, for wideband chirp the digitization of the MF output signal would require a much higher bandwidth analogue to digital converter (ADC) to satisfy the Nyquist sampling criterion. The need for a high bandwidth ADC makes the matched filter detector less favourable in practise compared to the other approach. A detailed analysis of the matched filter detector can be found in the following references [1, 5, 8].

In this thesis the heterodyne detector has been used to retrieve the target or channel information. In a heterodyne detector the incoming signal is mixed with a copy of the transmitted chirp, resulting in a signal that contains both the addition and subtraction of their frequency components. By means of a low pass filter the frequency components of the addition are filtered out leaving those of the subtraction. This signal is often referred to as beat-note. The beat-note is then

digitised and processed to retrieve the wanted information. Figure 4.4 provides an illustration of the block diagram of a heterodyne receiver.

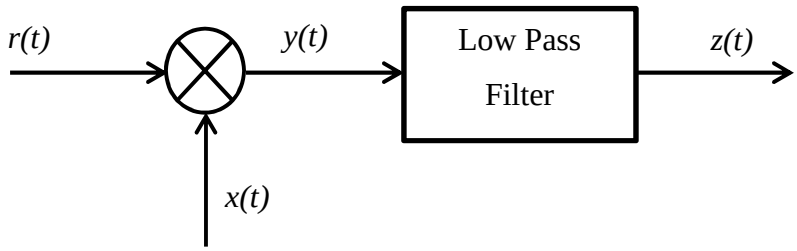

Figure 4.4: Heterodyne receiver block diagram

For simplicity of the mathematical analysis a stationary environment is assumed with zero Doppler, and the received signal is a weighted delayed version of the input. The received signal *r(t)* for a multipath environment or for a radar scenario with multiple targets can be mathematically represented as given in (4.5) as the sum of weighted and delayed versions of the transmitted signal.

$$r(t) = \sum_{i=1}^{K} A_{R,i} \cos\left(\emptyset_T(t-\tau_i)\right)$$

$$= \sum_{i=1}^{K} A_{R,i} \cos(\pi\beta(t-\tau_i)^2 + 2\pi f_c(t-\tau_i)) \tag{4.5}$$

where: $A_{R,i}$ and τ_i are the amplitude and time delay of the i^{th} received multipath or target reflected signal, and K is the number of multipath components or targets. At the heterodyne detector the received signal is mixed with a copy of the transmitted signal *x(t)*. Consequently, the output of the mixer *y(t)* can be written as:

$$y(t) = r(t) \times x(t)$$

$$= \sum_{i=1}^{K} A_{R,i} A_T \cos\left(\emptyset_T(t-\tau_i)\right)\cos(\emptyset_T(t)) \tag{4.6}$$

For the multiplication of cosines the following trigonometric identity can be applied:

$$cos(\varphi)\cos(\theta) = \frac{1}{2}\cos(\varphi - \theta) + \frac{1}{2}\cos(\varphi + \theta) \tag{4.7}$$

Applying (4.7) into (4.6) , and assuming $A_{R,i}\, A_T/2 = A_i$ results:

$$\begin{aligned} y(t) = &\sum_{i=1}^{K} A_i\{\cos(\emptyset_T(t-\tau_i) - \emptyset_T(t))\} \\ &+ \sum_{i=1}^{K} A_i\{\cos(\emptyset_T(t-\tau_i) + \emptyset_T(t))\} \end{aligned} \tag{4.8}$$

Without further mathematical manipulation (4.8) can be written as:

$$\begin{aligned} y(t) = &\sum_{i=1}^{K} A_i \cos\left\{2\pi\left(\beta t\tau_i + f_c\tau_i - \frac{1}{2}\beta{\tau_i}^2\right)\right\} \\ &+ \sum_{i=1}^{K} A_i\, cos\left\{2\pi\left(\beta t^2 + 2f_c t - \beta t\tau_i - f_c\tau_i - \frac{1}{2}\beta t\tau_2\right)\right\} \end{aligned} \tag{4.9}$$

The signal *y(t)* is low pass filtered which removes the second term of (4.9) as its frequency is centred at twice the carrier f_c. Therefore, the beat-note signal *z(t)* at the output of the filter can be written as:

$$z(t) = \sum_{i=1}^{K} A_i \cos\left\{2\pi\left(\beta t\tau_i + f_c\tau_i - \frac{1}{2}\beta{\tau_i}^2\right)\right\} \tag{4.10}$$

By assuming the transmitted signal to be periodic, as often used in practice, with period "*T*" then for each i^{th} signal in (4.10) two different beat-note frequencies will be produced as illustrated in Figure 4.5. By omitting the time limits these frequencies can be written as [9]:

$$f_{a,i}(t) = \frac{1}{2\pi}\left\{\frac{d}{dt}[\emptyset_T(t-\tau_i) - \emptyset_T(t)]\right\} \tag{4.11}$$

$$f_{b,i}(t) = \frac{1}{2\pi}\left\{\frac{d}{dt}[\emptyset_T(t-\tau_i) - \emptyset_T(t+T)]\right\} \tag{4.12}$$

Figure 4.5 shows that the beat-note frequency at the receiver output is proportional to the target's time delay "τ", or equivalently its range. This is only true for beat-note frequency "f_a" during the time window W_1 = T-τ; for frequency "f_b" in time window W2 = τ the assumption of proportionality does not hold. Therefore, "f_b" provides range ambiguity or false information about the target delay. In order to eliminate "f_b" from the receiver output, one can increase the signal bandwidth, resulting in "β" becoming steeper and "f_b" larger, therefore falling outside the low pass filter band. Another alternative is to make the chirp duration (T) smaller than the chirp repetition rate. This creates a silent interval at the receiver, at the end of the chirp duration.

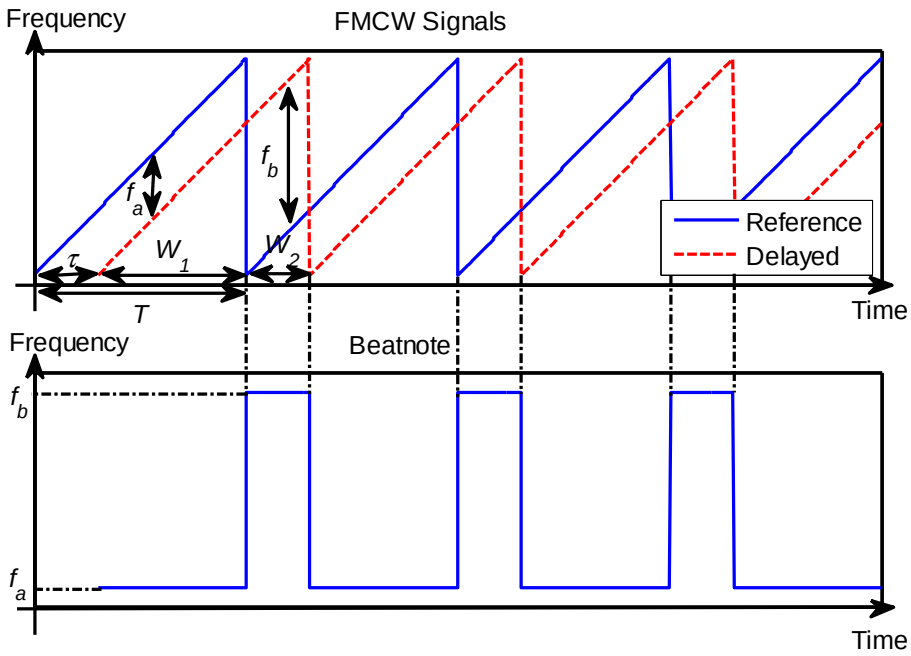

Figure 4.5: Instantaneous frequency of the transmitted and delayed received signal, and frequency of the beat-note at the heterodyne receiver output.

Following from (4.11) the beat-note frequency ($f_{a,i}$) corresponding to the i^{th} static target can be expressed as a function of its range R_i as:

$$f_{a,i}(t) = \beta\tau_i = \frac{\beta R_i}{c} \tag{4.13}$$

where: "R_i" is the target range, given as: $R_i = \tau_i/c$; and "c" is the EM wave propagation speed in the medium, which for free space it is equal to c = $3x10^8$ m/s.

The maximum range R_{max} that can be detected with a heterodyne receiver depends on the maximum beat-note frequency allowed through the low pass filter. Assuming an ideal low pass filter with a cut-off frequency f_{max} the maximum range can be expressed as:

$$R_{max} = c\tau_{max} = \frac{cf_{max}}{\beta} \tag{4.14}$$

On the assumption that the target or the receiver is moving with a constant speed "v" then the time delay associated with the target will change as a function of time due to changes in range as in (4.15). The time varying delay associated with the target can be expressed as in (4.16).

$$R(t) = R_o + vt \tag{4.15}$$

$$\tau(t) = \frac{R(t)}{c} = \frac{R_o + vt}{c} = \tau_o + \frac{vt}{c} \tag{4.16}$$

where: R_o is the initial target range; $R(t)$ target range as a function of time; τ_o is the initial time delay; and $\tau(t)$ is the target delay as a function of time. By assuming a single path the phase term in (4.11) can be written as:

$$\begin{aligned} \emptyset_a(t) &= \emptyset_T(t - \tau(t)) - \emptyset_T(t) \\ &= 2\pi(\beta t + f_c)\tau(t) - \pi\beta\tau(t)^2 \end{aligned} \tag{4.17}$$

By substituting τ(t) from (4.16) into (4.17) and as the target or receiver speed is much smaller than that of light ($v << c$), some terms can be ignored and the phase reduces to:

$$\emptyset_a(t) = 2\pi f_c \tau_o + \left(2\pi f_c \frac{v}{c} + 2\pi\beta\tau_o\right)t - \pi\beta{\tau_o}^2 \tag{4.18}$$

The beat-note frequency in this case can be defined as:

$$f_a = \frac{1}{2\pi}\left\{\frac{d}{dt}[\emptyset_a(t)]\right\} = \beta\tau_o + f_c\frac{v}{c} \tag{4.19}$$

The equation above shows that the beat-note frequency for a mobile target or receiver is dependent on the target range or time delay (τ_o) and on the Doppler shift caused by motion. Most often in linear FMCW systems a number of chirps (sweeps) are transmitted / received periodically as depicted in Figure 4.5. By analysing the changes in target range over N consecutive sweeps, the target time delay at the nth sweep would have been increased by *nT*, as expressed in (4.20).

$$\tau_n = \frac{R_n(t)}{c} = \tau_o + \frac{v(nT+t)}{c} \tag{4.20}$$

Consequently, the beat-note frequency at the nth sweep can be found by substituting "τ_o + *(v/c)nT*" expression into "τ_o" in equation (4.19). This frequency is defined as [2, 9]:

$$f_{a,n} = \beta\tau_o + f_c\frac{v}{c} + Bn\frac{v}{c} \tag{4.21}$$

Equation (4.21) shows that only the term (*Bnv/c*) differs from (4.19). This term indicates the movement of the target from sweep to sweep. Since the target speed v is assumed to be much smaller than the speed of light c, it can be assumed that the measured beat-note frequency on a sweep basis to be mainly proportional to the target's range. For large values of a number of sweeps and high bandwidths the extra term in equation (4.21) cannot be neglected [2].

By assuming the target to be moving with a maximum speed "v_{max}" the maximum expected Doppler shift f_{Dmax} can be related to the target speed by the following equation.

$$f_{Dmax} = f_c\frac{v_{max}}{c} \tag{4.22}$$

In order to avoid range Doppler ambiguity the maximum Doppler shift the system is expected to measure needs to be smaller than the chirp repetition rate as given in (4.23). This equation shows that in order to detect a fast moving target a short sweep duration is needed.

$$f_{Dmax} \leq \frac{1}{2T} \leftrightarrow T \leq \frac{1}{2f_{Dmax}} \tag{4.23}$$

The mathematical analyses so far showed that in a heterodyne receiver the information related to target speed (Doppler), range (time delay) and relative amplitude can be estimated through the spectrum of the beat-note signal. While the target information can be retrieved by observing the detector's output on a spectrum analyser; it is most common to employ an analogue to digital converter (ADC) to digitise the beat-note and spectrum analysis is performed through the use of the Fast Fourier Transform algorithm (FFT).

In order to avoid ambiguity and therefore satisfy the Nyquist criterion, the sampling frequency (f_s) of the ADC needs to be higher than twice the maximum expected beat-note frequency as given in (4.24). There are two main digital processing techniques used to extract the target information from the detector output [9], namely: single FFT technique and double FFT technique. In this work a double FFT technique has been used.

$$f_s \geq 2f_{max} \equiv f_s \geq \frac{2\beta R_{max}}{c} \tag{4.24}$$

- ***Double FFT Processing Technique***

The double FFT technique has been widely used in channel sounding and radar as a processing technique to extract the time delay (range) and Doppler shift (due to motion) of the radar targets or multipath components in the channel. The earlier mathematical analysis showed that the path delay and Doppler information is contained in the spectrum of the beat-note signal. With the double FFT technique the first fast Fourier transform is carried out on each "n^{th}" sweep (of duration T) to obtain the time delay spread (range) and multipath amplitude information. The second FFT is carried over *N* sweeps at each "m^{th}" time delay bin to obtain the Doppler information [2].

Assuming a multipath environment the equation of the beat-note signal for a single sweep "*n*" is of that in (4.10), with the sweep time interval redefined so that the origin falls in the middle of the interval (*–T/2 ≤ t ≤ T/2*), the first Fourier transform in the double FFT technique is given as [10]:

$$h_n(f) = \int_{-T/2}^{T/2} \sum_{i=1}^{K} A_{n,i} cos\left(\emptyset_{n,i}(t)\right) e^{-j2\pi f t}\, dt \quad -\frac{nT}{2} \le t \le \frac{nT}{2} \tag{4.25}$$

Without further mathematical manipulation the transform results in:

$$h_n(f) = \sum_{i=1}^{K} \frac{A_{n,i}T}{2}\left[\frac{\sin(2\pi(f - f_{n,i})T/2)}{[2\pi(f - f_{n,i})T/2]}\right] e^{-j\emptyset_{o,i} + j2\pi f_{c,i}\frac{v_i}{c}nT}$$

$$+ \sum_{i=1}^{K} \frac{A_{n,i}T}{2}\left[\frac{\sin(2\pi(f + f_{n,i})T/2)}{[2\pi(f + f_{n,i})T/2]}\right] e^{j\emptyset_{o,i} - j2\pi f_{c,i}\frac{v_i}{c}nT} \tag{4.26}$$

Equation (4.26) suggests that the spectrum of the beat-note signal is made of sin(x)/x or sinc(x) functions centred at their corresponding beat frequency "f_i". Although, the transform has been applied on a continuous signal, in practice it is applied on the measured discrete samples obtained by an ADC through the FFT algorithm. By assuming "*M*" to be the number of discrete samples used by the FFT per sweep, the output of the FFT will be "*M*" discrete frequency points in the range of "$–f_s/2 \le f \le f_s/2$", where f_s is the sampling frequency. Due to the symmetry in the spectrum only the positive frequencies ($0 \le f \le f_s/2$) are retained as given in (4.27).

$$h_n(f) = \sum_{i=1}^{K} \frac{A_{n,i}T}{2}\left[\frac{\sin(2\pi(f - f_{n,i})T/2)}{[2\pi(f - f_{n,i})T/2]}\right] e^{-j\emptyset_{o,i} + j2\pi f_{c,i}\frac{v_i}{c}nT} \quad 0 \le f \le \frac{f_s}{2} \tag{4.27}$$

Therefore for *M* time samples per sweep only *M/2* beat frequency points are used for further processing, and these can be converted into time delay or range using (4.13). The required number of samples "*M*" per sweep is given as [9, 10]:

$$M \ge f_s T \equiv M \ge 2B\frac{R_{max}}{c} \tag{4.28}$$

For Doppler shift and time variability analyses a number of sweeps is required. Thus, the complex M/2 FFT points of each successive sweep are stored in a row of a matrix. So for N sweeps the matrix will be of N x M/2 size as in (4.29), where the n^{th} row holds the response at time "nT" and the m^{th} column represents the time-delay bin or range bin, whose elements are samples of the "m^{th}" beat-note frequency or delay "τ" component that are stored every T second.

$$h(t,\tau) = \begin{pmatrix} h_{11} & h_{12} & \cdots & h_{1m} & \cdots & h_{1M/2} \\ h_{21} & h_{22} & \cdots & h_{2m} & \cdots & h_{2M/2} \\ \vdots & \vdots & \ddots & \vdots & \cdots & \vdots \\ h_{n1} & h_{n2} & \cdots & h_{nm} & \cdots & h_{nM/2} \\ \vdots & \vdots & \ddots & \vdots & \cdots & \vdots \\ h_{N1} & h_{N2} & \cdots & h_{Nm} & \cdots & h_{NM/2} \end{pmatrix} \tag{4.29}$$

The 2D matrix "$h(t,\tau)$" is often referred to as *time-variant response* due to the fact that for successive sweeps the amplitude and phase of the elements in the column may change due to the relative motion of the target or multipath. The target's motion is the bases of the relative shift in the beat-note frequency (as seen in 4.30); this frequency shift causes both amplitude and phase variation of column samples. The amplitude tends to vary slowly from sweep to sweep, as demonstrated in [9]. The main variations within the column samples, due to target's motion, are in fact the result of the phase factor [2, 9]. Therefore, the samples of the "m^{th}" column can be represented as:

$$h_{nm} = Ke^{j2\pi f_c \frac{v}{c} nT} = Ke^{j2\pi f_c \frac{v}{c} T_n} \tag{4.31}$$

where: K represents the amplitude variation, and "$t_n = nT$" represents the discrete time from sweep to sweep. The Fourier transform of the m^{th} column, (4.31), over t_n from 0 to NT gives [10]:

$$S_m = KNT \frac{\sin\left(2\pi\left(f - \frac{v}{c} f_c\right)\frac{NT}{2}\right)}{2\pi\left(f - \frac{v}{c} f_c\right)\frac{NT}{2}} \quad -\frac{1}{2T} \le f \le \frac{1}{2T} \tag{4.32}$$

The above analysis shows that the relative motion of a mobile target causes a frequency displacement of the sin(x)/x function. This effect is termed as Doppler shift "$f_D = f_c v/c$". For N consecutive sweeps the output of this FFT would consist of

N discrete number of frequency points in the interval $\pm 1/(2T)$. Consequently, the Doppler frequency resolution would be the inverse of NT. If the FFT is performed on all columns of the $h(t,\tau)$ matrix, the resultant 2D matrix shown in (4.33) is called the *Delay-Doppler spread function, "S(τ,ν)*".

$$S(\tau,\nu)=\begin{pmatrix} S_{11} & S_{12} & \cdots & S_{1m} & \cdots & S_{1M/2} \\ S_{21} & S_{22} & \cdots & S_{2m} & \cdots & S_{2M/2} \\ \vdots & \vdots & \ddots & \vdots & \cdots & \vdots \\ S_{n1} & S_{n2} & \cdots & S_{nm} & \cdots & S_{nM/2} \\ \vdots & \vdots & \ddots & \vdots & \cdots & \vdots \\ S_{N1} & S_{N2} & \cdots & S_{Nm} & \cdots & S_{NM/2} \end{pmatrix} \tag{4.33}$$

The table below provides a summary of the parameters of the linear FMCW signal applied to a heterodyne detector and the related processing parameters in a radar system.

Table 4.1: Linear FMCW signal and processing parameters

Number of sweeps	N
Minimum number of samples per sweep	$M = f_s T$
Maximum expected beat-note frequency	$f_{max} = \beta R_{max}/c$
Sampling frequency	$f_s \geq 2f_{max}$
Range / delay window	$0 \leq \tau \leq fs/(2\beta)$
Range resolution	$\Delta R = c/(2B)$
Sweep duration and unambiguous Doppler	$T \leq 1/(2f_{Dmax})$
Unambiguous Doppler window	$-1/(2T) \leq f_D \leq 1/(2T)$
Doppler resolution	$\Delta f_D = 1/(NT)$

4.1.2 Side Lobe Reduction Through Windowing

As shown in equations (4.27) and (4.32) the amplitude of the impulse response and the Doppler spectrum are both sin(x)/x pulses. One disadvantage of the sin(x)/x pulse is that apart from the main lobe it also contains unwanted high level of side lobes, which can be as high as -13.4 dB below the main lobe. In a multi scatterers scenario these unwanted lobes present a challenge as they may be mistaken as targets or even overlap and overshadow the other scatterers or targets. Therefore, there is a need to suppress them before further processing.

The sin(x)/x function is a direct result of the finite duration or truncation of the signal before the Fourier transform [5, 11]. If the signal is assumed to be infinite then the truncation in this case can be explained as a product of the signal with a weight function which is "1" within the finite interval and "0" elsewhere. This weight function is termed as a rectangular window and its spectrum corresponds to sin(x)/x. By having a weight function that places smaller weights (values) at and close to the discontinuity, lower side lobes can be achieved and this is more desirable than the rectangular window. It is worth mentioning that although lower side lobes can be achieved by different windowing functions this is offset by the widening of the main lobe, therefore a trade-off must be sought [5].

In this work three window functions have been used, namely: Rectangular, Hamming, and Kaiser window. By assuming the signal to be of length L the window function "*w(n)*" can be written as:

- ***Rectangular Window***

$$w(n) = 1\,; \quad 0 \le n \le L-1 \tag{4.34}$$

- ***Hamming Window***

$$w(n) = 0.54 - 0.46\cos\left(\frac{2\pi n}{L-1}\right); \quad 0 \le n \le L-1 \tag{4.35}$$

- ***Kaiser Window***

$$w(n) = \frac{I_o\left[\propto \sqrt{1-(2n/L)^2}\right]}{I_o(\propto)}\,; \quad 0 \le n \le L-1 \tag{4.36}$$

where: I_o is the zero-order modified Bessel function of the first kind; and α is the Kaiser window parameter.

Figures 4.6 and 4.7 show the weight of the chosen windows and their corresponding normalised power spectra. As expected the rectangular window offers a narrower main lobe width but stronger side lobes compared to the other chosen windows. Table 4.2 gives a summary of the width of the main lobes and the respective side lobes. An extended analysis on window functions and their performances in terms of side lobe levels reduction and main beam width are given in references [5, 11, 12] .

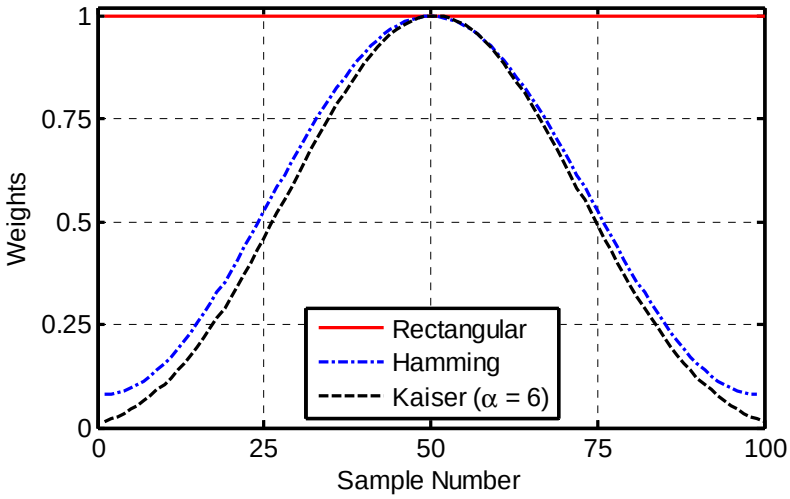

Figure 4.6: Window functions weights

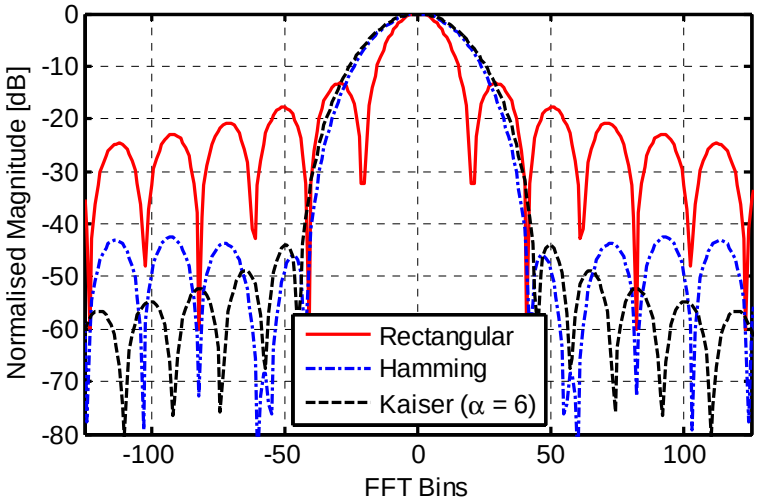

Figure 4.7: Window functions normalised spectrum

Table 4.2: Used window function properties

Window Function	**Main lobe width (rectangular window as reference) at 6dB point**	**Peak side lobe**
Rectangular	1	-13.4
Hamming	1.58	-42.5
Kaiser ($\alpha = 6$)	1.7	-43.9

4.2 Gated Frequency Modulated Continuous Waveform

The use of Gated Frequency Modulated Continuous Waveform (GFMCW) in radar systems dates back to the early 1970's for applications such as vertical sounding of the ionosphere and sea-surface remote sensing [13, 14], for which a single antenna operating simultaneously at the transmitter and receiver was desirable. The increased interest in GFMCW stems from the fact that it is able to overcome one of the major limitations of the normal FMCW approach regarding the isolation of both the transmitter and the receiver.

In FMCW based systems both the transmitter and receiver are active simultaneously during the chirp duration *T*. Consequently, the direct crosstalk signal between antennas (in bistatic radar) or the leakage signal due to poor circulator isolation (in monostatic radar) may considerably damage the receiver's sensitivity [15], therefore making it harder to detect weaker return signals especially from targets far from the radar.

To counteract this problem without causing significant effect on the FMCW radar performance it is necessary to separate the transmission from reception period. This can be achieved by employing gating sequences to switch the transmitted and received signals and to allow the radar to operate in transmit and receive mode [16]. As a result, no signal reception occurs during the transmission and vice versa. The use of switching sequences in conjunction with FMCW radar have been termed in

the literature as: Gated frequency modulated continuous waveform [17] or frequency modulated interrupted continuous waveform [18].

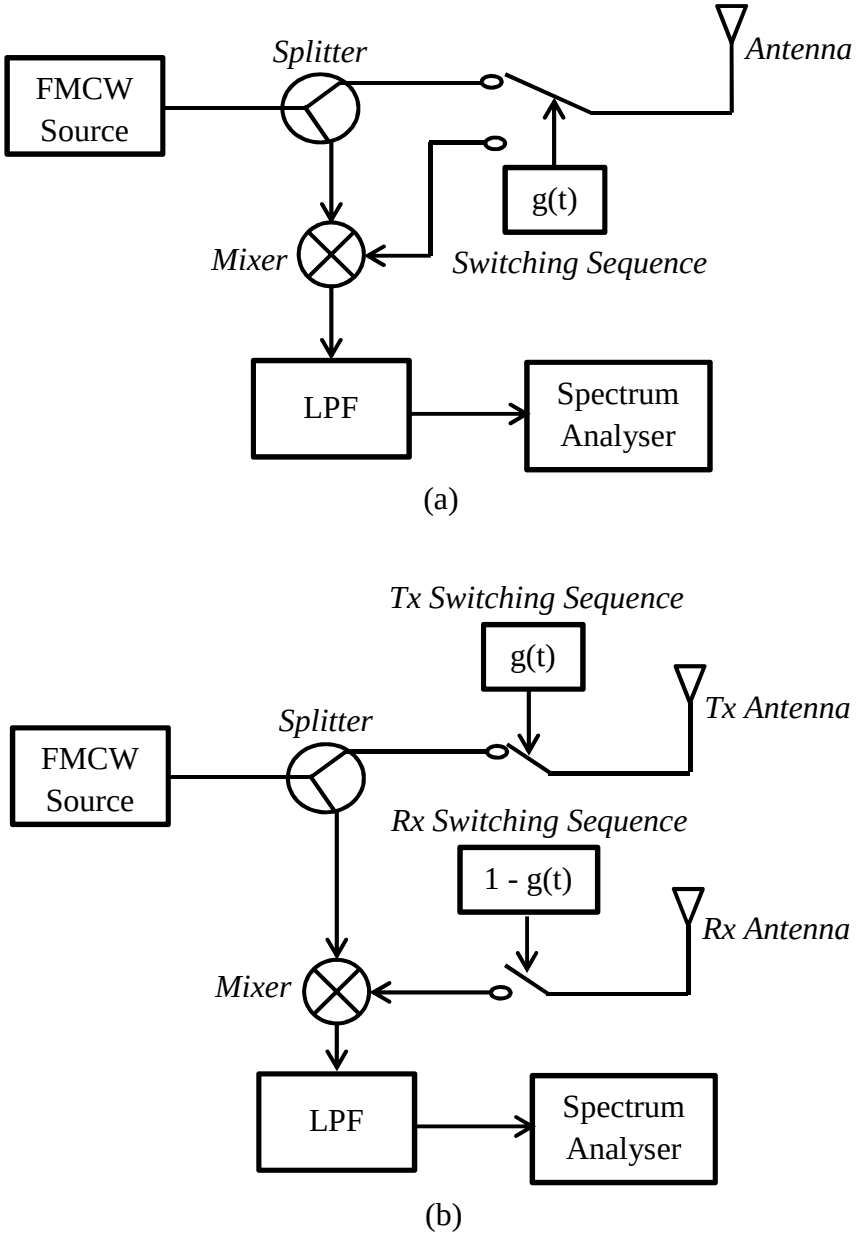

Figure 4.8: Basic block diagram of GFMCW radar, (a) Monostatic configuration; (b) Bistatic configuration

Figure 4.8 presents the basic block diagram of a monostatic and bistatic heterodyne based GFMCW radar. Although by employing gating sequences a good isolation between the transmitter and receiver can be achieved. It also introduces some drawbacks, such as: range ambiguity, blind range, reduction of the mean received power, and spectrum spread. These effects can be compensated by choosing

a suitable gating sequence and window function as in previous studies [14, 16, 18, 19].

One of the aspects of the GFMCW, which is of interest in this work, is the fact that the mean received signal from a scatterer at any range is also dependent on the cross correlation function of the employed gating sequence [2]. Hence, these sequences could be designed to provide range sensitivity, so that nearby strong clutter, i.e. wall reflection in TTWIR, air-ground surface reflection in GPR, and skin reflection in MIR, can be suppressed while improving the receiver sensitivity to detect distant weak targets. The next sections will provide analyses of the mathematical model of the GFMCW radar as well as a discussion of the effects on the radar performance.

4.2.1 Mathematical Model of GFMCW

As illustrated in Figure 4.8 GFMCW signal is generated by switching "on" and "off" the transmitted and received signals, of a normal FMCW source, in a complementary pattern to ensure isolation between the transmitter and receiver. These gating sequences of period 'T_s' can be modelled through binary functions with '1' or '0' representing transmit and receiving states respectively. Furthermore instead of switches, multipliers can be used. Therefore, it can be said that the GFMCW is the product of a normal transmitted and received FMCW signal with complementary gating sequences employed at the transmitter and receiver.

Equation (4.37) gives the transmitted signal and (4.38) shows the received signal at the mixer's input assuming a single path/scatterer in the environment.

$$x(t) = A_T \cos\{\emptyset_T(t)\} g(t) \qquad -\frac{1}{T} \le t \le \frac{1}{T} \tag{4.37}$$

$$r(t) = A_R x(t-\tau)[1-g(t)]$$

$$= A_T A_R \cos\{\emptyset_T(t-\tau)\} g(t-\tau)\,[1-g(t)] \quad -\frac{1}{T} \le t \le \frac{1}{T} \tag{4.38}$$

By using a heterodyne detector the received signal in (4.38) is mixed with a copy of the un-gated transmitted signal and the output is low pass filtered which results in the beat-note signal, given in (4.39). This signal is an interrupted waveform

whose frequency is related to the path delay "τ", as in (4.13) for the linear FMCW case, but with the power proportional to the time-delay sensitivity of the gating sequence, as analysed in the next subsection.

$$z(t) = g(t-\tau)[1-g(t)]A\cos\left\{2\pi\left(\beta t\tau + f_c\tau - \frac{1}{2}\beta\tau^2\right)\right\}$$

$$-\frac{1}{T} \le t \le \frac{1}{T} \tag{4.39}$$

4.2.2 Gating Sequence Effect on Mean Received Power

In GFMCW systems the mean received signal (MRS) for a target at a particular range is proportional to the amount of signal that passes through the gating sequence over the period "*Ts*". This dependency could be expressed as the cross-correlation function between the delayed gating sequence, due to target range, and the sequence at the receiver [2, 14], as shown in equation (4.40).

$$MRS(\tau) = \frac{1}{T_s}\int_{T_s} g(t-\tau)[1-g(t)]\,dt \tag{4.40}$$

In [16] the gating sequence range sensitivity was also proposed in terms of its "mean received power" MRP, which is the square of MRS, as expressed in (4.41). By selecting the gating sequence parameters, i.e. sequence period, the number of bits (*N*), and the bit duration it is possible to design a MRP that suppresses the undesired return signal(s) from a certain range while allowing a return signal from another range to pass through with minimum or no attenuation. This basic principle related to GFMCW is what will be explored to suppress the unwanted early time delay reflections in GPR, TTWIR, and MIR while providing minimum possible attenuation at time delays related to the targets in the area under test.

$$MRP(\tau) = (MRS(\tau))^2 = \left(\frac{1}{T_s}\int_{T_s} g(t-\tau)[1-g(t)]\,dt\right)^2 \tag{4.41}$$

Since GFMCW is gated "on" and "off" the maximum received power is significantly reduced, compared to a normal FMCW signal. This is due to the fact

that the reception is only possible during silent transmitter intervals. This power loss factor (X_G) can be expressed in decibel (dB) scale as,

$$X_G = -20\log\left(\frac{t_r}{T_s}\right) \tag{4.42}$$

where: t_r is the total time duration the receiver is in the "on state" during a sequence duration T_s. In [14] it has been shown that the square wave gating sequence with 50% duty cycle provides the maximum power efficiency. In other words the minimum power reduction factor is 6 dB.

4.2.3 Effect of the Gating Sequence Periodicity

- ***Blind range***

As discussed earlier the duration of the gating sequence "T_s" is usually much smaller than the chirp duration "T". Consequently, the gating sequence is made repetitive in order to provide the required transmitter/receiver isolation throughout the chirp duration. Assuming a finite gating sequence $g(t)$ has a period "T_s", then $g(t) = g(t \pm lT_s)$, where $l = 1, 2, 3, 4, \ldots$. For a target with back-propagation time delay $\tau = lT_s$ the MRP from (4.41) becomes [14, 16]:

$$MRP(lT_s) = \left(\frac{1}{T_s}\int_{T_s} g(t - lT_s)[1 - g(t)]\,dt\right)^2$$

$$= \left(\frac{1}{T_s}\int_{T_s} g(t)[1 - g(t)]\,dt\right)^2 = \left(\frac{1}{T_s}\int_{T_s} [g(t) - g(t)]\,dt\right)^2 = 0 \tag{4.43}$$

It can be stated from (4.43) that the return signal from such a target will be totally blocked by the receiver gating sequence. Hence, those ranges associated with a zero MRP are referred to as "blind ranges" as targets in these ranges are not detected. In order to avoid the blind ranges falling on the area of interest, the duration of the gating sequence should be made greater than the maximum expected delay, as given in (4.44).

$$T_s = NT_b > \tau_{max} \tag{4.44}$$

In this thesis the suppression of unwanted early reflections in GPR, TTWIR, and MIR will be achieved by designing the gating sequence so that the blind ranges fall on the range associated with the unwanted reflection.

- ***Range Ambiguity***

Unlike the FMCW system, the beat-note signal for a single point target in GFMCW is a gated sinusoid as shown in (4.39). Due to the periodicity of the gating sequence replicas of the spectrum of the equivalent ungated beat-note signal will appear at frequencies given by [20],

$$f = f_b \pm \frac{n}{T_s} \tag{4.45}$$

where: f_b is the frequency of the beat-note, T_s is the gating sequence period, and n is an integer. Since there is a direct proportionality between the target range and the beat frequency "f_b" then from (4.45) it can be said that for a target located at an arbitrary range (R_x) it will also produce responses at other ranges (R) as shown in (4.46). This effect is known as range ambiguity due to the periodicity of the gating sequence.

$$R = R_x \pm n\left(\frac{c}{2\beta T_s}\right) \tag{4.46}$$

The range ambiguity can be circumvented by ensuring the first spectrum replica caused by the gating sequence is outside the frequency range of interest. This is performed by choosing a sequence repetition rate "f_G", the inverse of *Ts*, to be greater than twice of the maximum expected beat frequency (f_{max}). Equation (4.47) expresses the parameter of the gating sequence (bit duration "T_b" and number of bit "N") that can be chosen as a function of the chirp parameters (bandwidth "B" and sweep duration "T") and of the maximum achievable range "R_{max}" to avoid aliasing or in this case range ambiguity [15, 21].

$$f_G > 2f_{max} \tag{4.47}$$

$$\frac{1}{T_s} = \frac{1}{NT_b} > 2\left(\frac{2\beta R_{max}}{c}\right) \quad result\ on: T_b < \frac{cT}{4BNR_{max}}$$

In practice given a chirp duration and bandwidth a trade-off must be sought between the desired maximum range and the bit duration in order to satisfy both (4.44) and (4.47).

4.2.5 MRP Profile of Known Gating Sequences

A number of gating sequences have been reported in the literature, these include: square wave sequence with 50% duty cycle [13, 14], m-sequences [14], 16 bit Barry sequence [16], and the 20 bit sequence and 23% duty cycle square wave proposed by Salous and Nattour [22]. The criteria for selecting the gating sequence to be used depends on the sequence MRP profile, the range of interest, and the chirp parameters bandwidth and chirp duration. In this subsection, examples of the MPR profile of the gating sequences used in this thesis are analysed.

- ***Square Wave Gating Sequence***

A square wave sequence with 50% duty cycle is the simplest form of gating sequence since the transmission and reception are complementary and of the same duration. Its length is of two bits long, g(t) = [1 0]. Figure 4.9 shows two periods of the sequence waveform (*g(t)*) and its complement (*1-g(t)*).

As expected the sequence MRS is of triangular shape with maximum and minimum (blind range) at every odd and even multiple of the bit duration respectively. One of the drawbacks of this sequence is the occurrence of a blind range at every "*Ts*". To avoid the blind range falling within the range of interest, the sequence bit duration is chosen to correspond to the maximum target time delay [15].

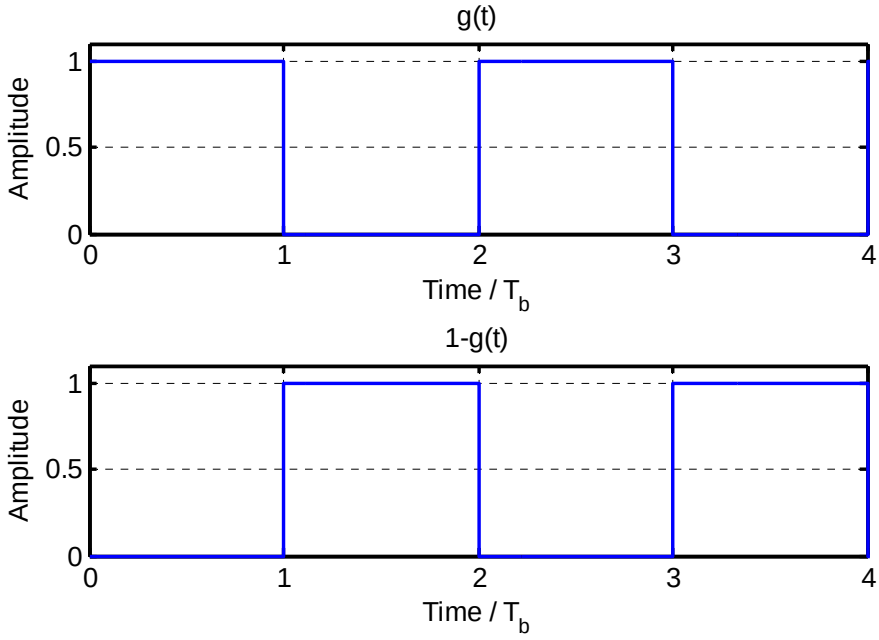

Figure 4.9: Pattern of a square wave gating sequence

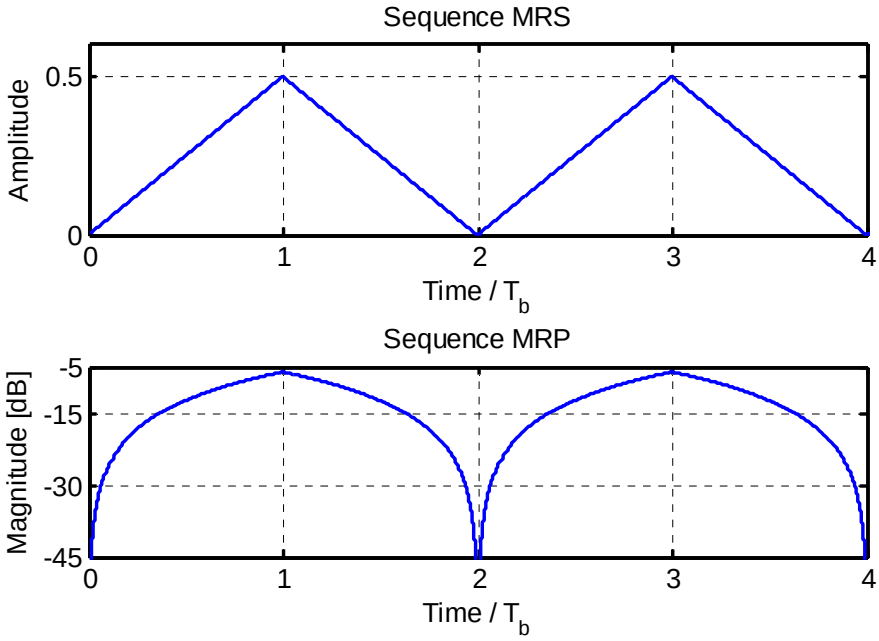

Figure 4.10: MRS and MRP profile of square wave gating sequence

From the MRP profile (in Figure 4.10) it can be concluded that a minimum attenuation of 6 dB will be suffered by a target with time-delay equivalent to "T_b", and more for a target located in the profile's ramp. For short range radar with an unknown target position, this can present a problem as the response of a target too close may be strongly suppressed by the MRP ramp for being close to the blind range.

If the suspected target position is known then the square wave gating may be suitable as it can be designed to have a maximum at that area of interest while suppressing neighbouring clutter or targets.

- ***Maximum length binary gating sequence***

Maximum length binary gating sequence (m-sequence) also known as pseudo random binary sequence, had been proposed to overcome the blind range limitation of the square wave gating sequence. The length (L) of an m-sequence in bits, can be defined as:

$$L = 2^k - 1\,; \quad k \geq 2\,; k\ is\ integer \tag{4.48}$$

The blind range of an m-sequence happens at multiples of the sequence period $T_s = LT_b$. From equation (4.48) the shortest possible length is 3-bit long (k = 2), g(t) =[1 1 0], and it is followed by (k = 3) 7-bit, g(t) = [1 0 0 1 1 1 0], and so on.

Figures 4.11 and 4.13 show the bit pattern of the gating sequence and its complement for 3-bit and 7-bit m-sequences respectively. Looking at the MRS and MRP profiles of both sequences, in Figures 4.12 and 4.14, it can be seen that apart from the first and last bit, where the ramp exists, the profile is completely flat. This means that the target(s) with time delay or range that fall on that portion of the profile will suffer no additional attenuation.

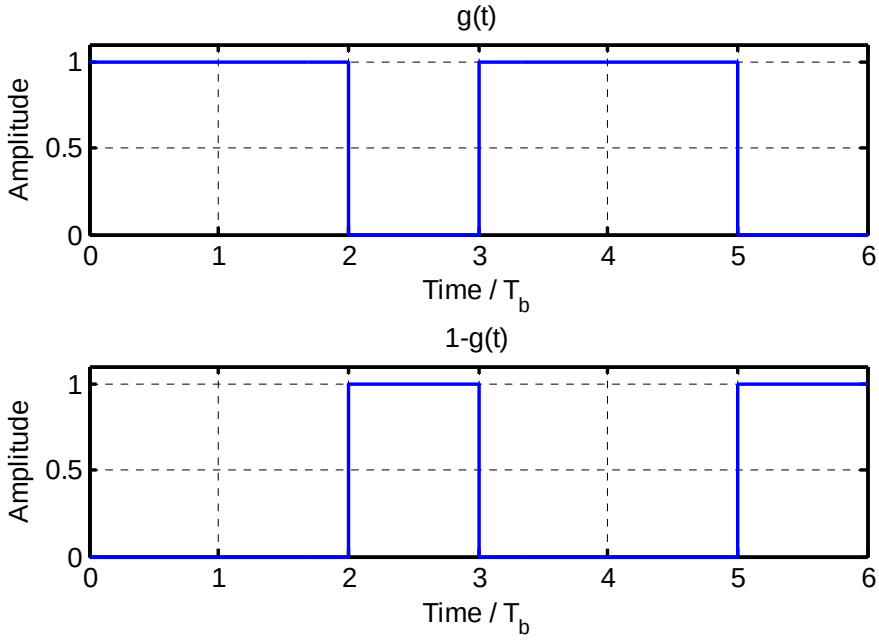

Figure 4.11: Pattern of 3-bit m-sequence

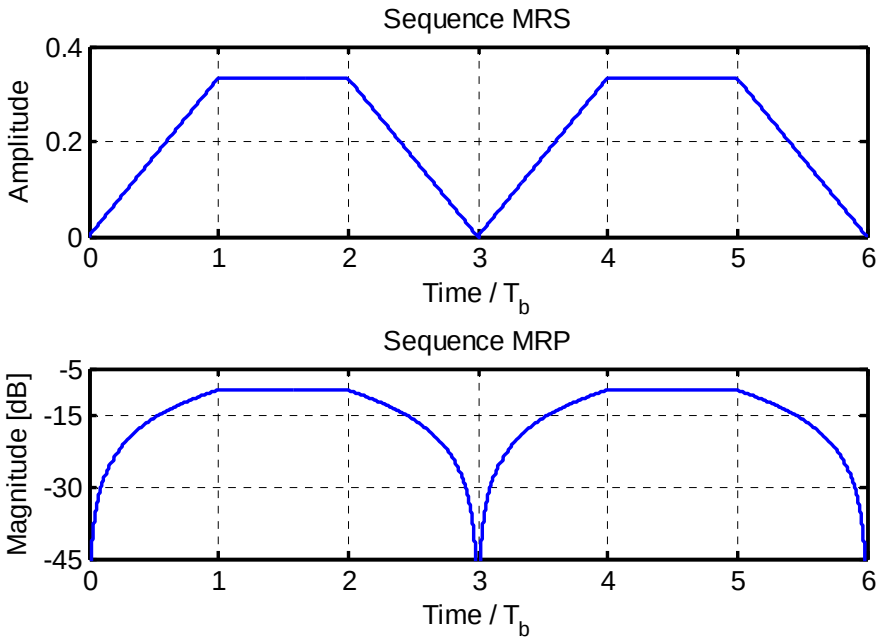

Figure 4.12: MRS and MRP profile of 3-bit m-sequence

For a larger range of interest the m-sequence length or bit duration can be increased so that the blind range falls outside that range. Note that due to the 'on' and 'off' of the transmitted and received signals a power loss of 9.5 dB and 7.35 dB are expected for the 3-bit and 7-bit m-sequences respectively as given in (4.42). This loss of power can be compensated, if necessary, by increasing the transmitted power accordingly.

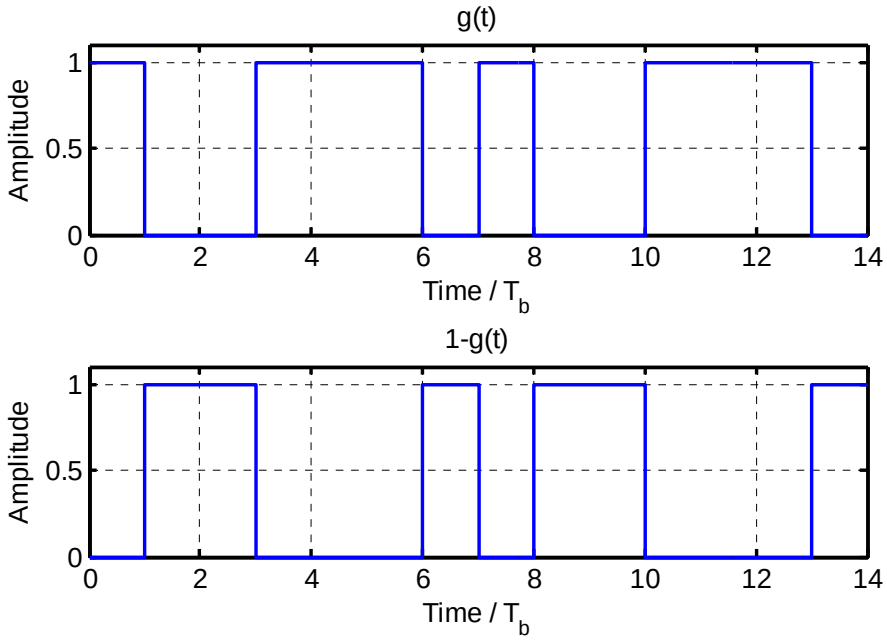

Figure 4.13: Pattern of 7-bit m-sequence

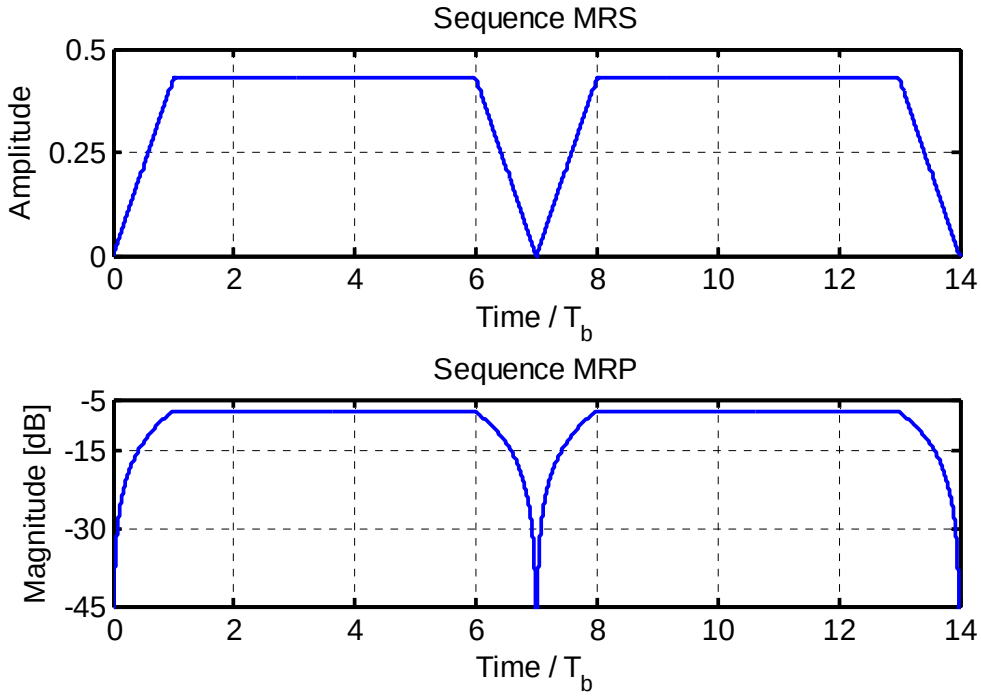

Figure 4.14: MRS and MRP profile of 7-bit m-sequence

4.2.6 Blind Range Extension

In the previous subsection it was shown that the square wave gating sequence can enhance the detection of return signals with a time delay equivalent to the sequence bit duration while suppressing other signals with different time delay (signals on the profile ramp). The m-sequence on the other hand may cover a wider range with a constant attenuation while suppressing return signals with time delays less than a bit duration (on the first ramp).

In practice, due to the finite bandwidth, the return signal from a scatterer point is not an impulse but a sinc function, (see (4.27)), which may further be broadened or extended in time if the scatterer is dispersive. Moreover, the antenna crosstalk response may appear at a different time delay from that of the unwanted early clutter reflection depending on the spacing between antennas and the early clutter, such as: wall (in TTWR), ground surface (in GPR), or skin (in MIR).

This presents a problem as the blind range (notch) on the MRP profile of the complementary gating sequence (see Figures 4.10, 4.12, and 4.14) may not provide enough attenuation to fully suppress those strong reflections as some of which may

extend onto a later part of the ramp. Furthermore, the MRP attenuation ramp is of one bit duration which may cause problems, as targets near the early clutter (i.e. wall, skin, or ground surface) may also fall onto the ramp and be attenuated. Therefore a compromise must be sought since the bit duration needs to be large enough to suppress the undesired reflections in the early part of the MRP ramp (where the attenuation is strongest), while a steeper ramp (short bit duration) is preferable to avoid attenuating reflections from targets close to the radar.

One possible solution results in extending the blind range while making the ramp steeper. This is achieved by introducing additional "*off-time*" into the receiver or transmitter gating sequence making them non-complementary. Meaning that the receiver sequence is switched onto "*off-state*" slightly before the transmitter is switched onto the "*on-state*", or the receiver sequence is switched onto "*on-state*" slightly after the transmitter is switched onto the "*off-state*". This is contrary to what has been seen in the previous section where the sequence was complementary.

Assuming that the times 'τ_1' and 'τ_2' are the additional "*off-time*" durations employed in the receiver sequence, Figures 4.15 and 4.17 show how the pattern of a square wave and 3-bit m-sequence would be for different off-time values, respectively. Due to these additional receiver *off-times* the power loss factor (X_G) would increase as the receiver would be on for a shorter time.

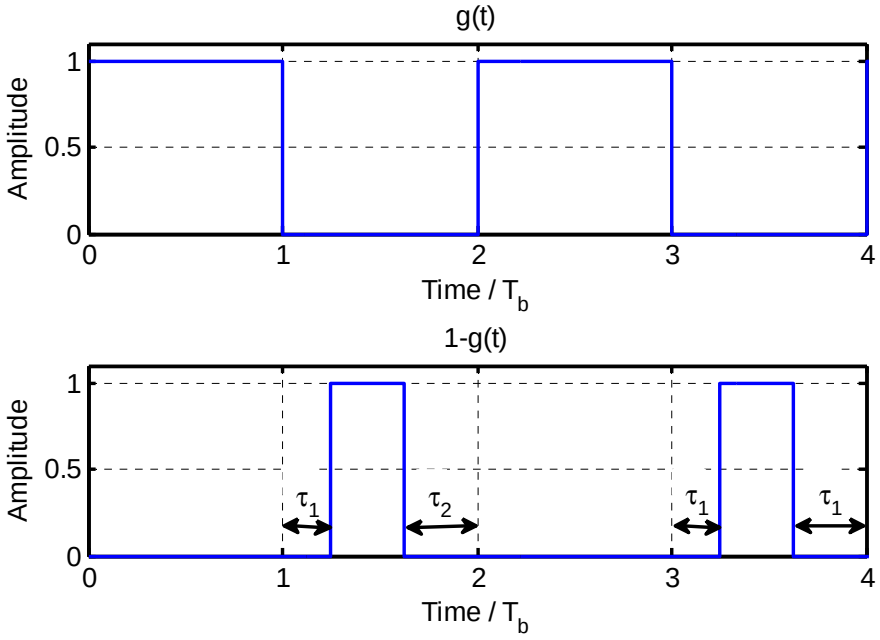

Figure 4.15: Pattern of the modified square wave gating sequences with τ_1 = 25% and τ_2 = 38% of the bit duration (T_b)

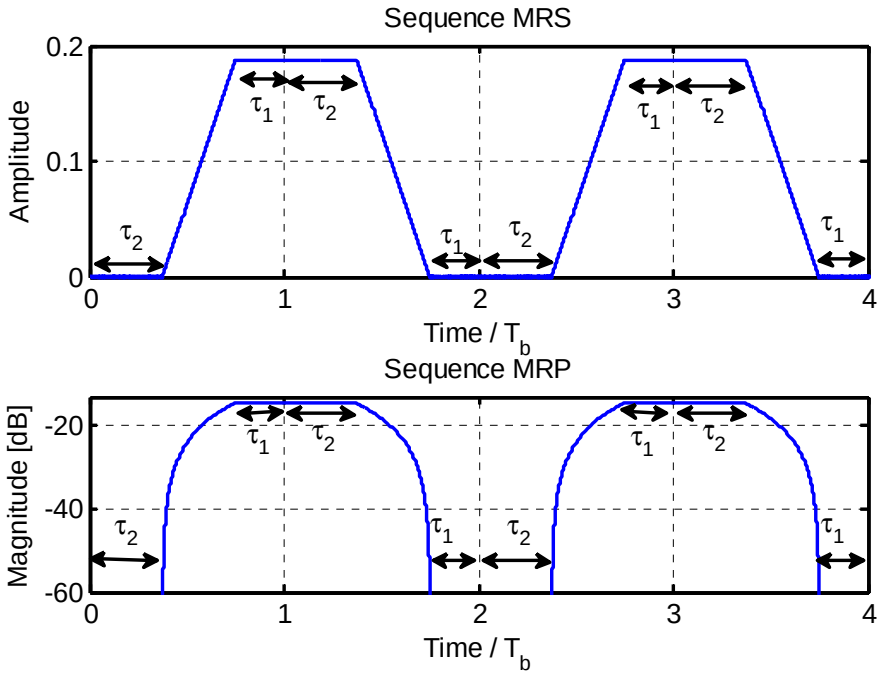

Figure 4.16: MRS and MRP profile of the modified square wave gating sequence with τ_1 = 25% and τ_2 = 38% of the bit duration (T_b)

Figure 4.16 shows the MRP profile of the square wave gating sequence for off-time delay values of τ_1 = 25% and τ_2 = 38% of T_b. As expected the profile's blind range is extended (*on the second and consecutive notch*) to cover a range delay

equivalent to $\tau_1 + \tau_2$. Moreover the pass band has also increased consequently causing the MRP slope to be much steeper compared to the case where no off-time delay is added (see Figure 4.10). Figures 4.17 and 4.18 show the profile and MRS as well as MRP of a 3-bit m-sequence with added off-time delays of $\tau_1 = \tau_2 = 33.3\%$ of the T_b.

With added off-time delay(s) the receiver is in the "on-state" for a much shorter time consequently the power loss factor 'X_G' would be higher compared to a normal complementary sequence. In the presented sequence, the minimum power loss factor of the modified square wave sequence is 14.5 dB and for the modified 3-bit m-sequence is 19.08 dB.

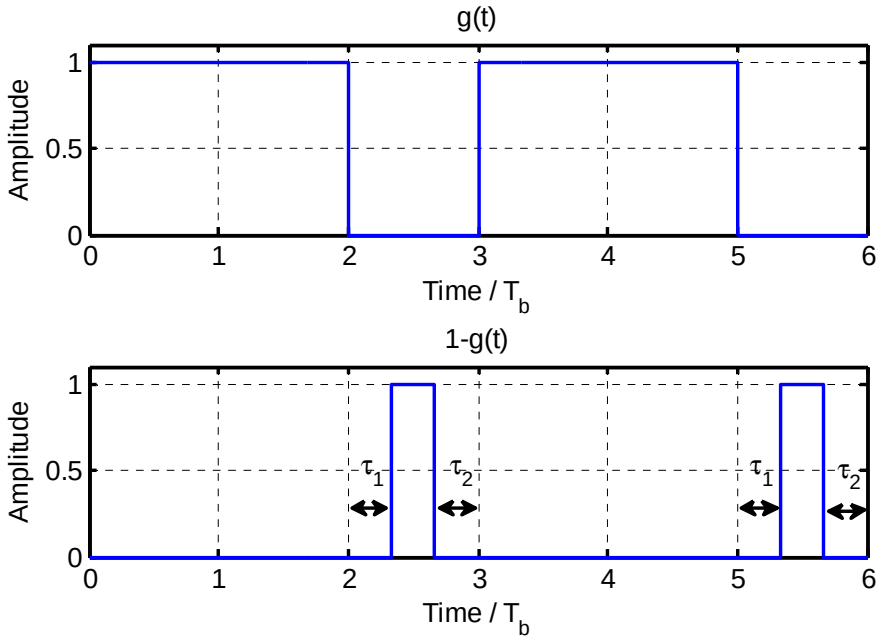

Figure 4.17: Pattern of the modified 3-bits m-sequence with $\tau_1 = 33.3\%$ and $\tau_2 = 33.3\%$ of the bit duration (T_b)

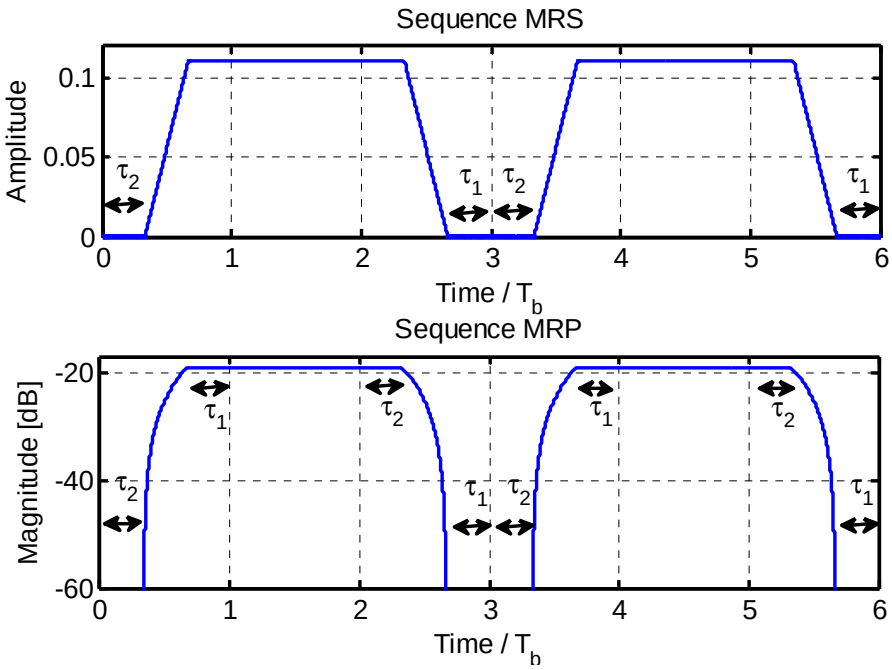

Figure 4.18: MRS and MRP profile of the 3-bits m- sequence with τ_1 = 33.3% and τ_2 = 33.3% of the bit duration (T_b)

Table 4.3 provides a summary of the relationship between the parameters in a GFMCW system.

Table 4.3: Summary of GFMCW parameters

Maximum target delay 'τ_{max}' to avoid blind ranges for a sequence of period 'T_s'	$T_s = N.T_b > \tau_{max}$
Sequence Period to avoid aliasing	$Ts < c / (4\beta R_{max})$
Power Loss factor due to Gating	$X_G = -20log(t_r / T_s)$
M-sequence length in bits	$L=2^k-1;\ k=2, 3, 4, ...$

4.3 Summary

The chapter provided an overview of the linear FMCW signal as applied to channel sounding and radar systems. A mathematical description of this signal with a heterodyne detector was given. The double FFT processing technique as a method to extract the range delay and Doppler information from the received signal was examined.

The GFMCW signal has been introduced as a technique to suppress the unwanted clutter signals in radar systems. Gating sequences used in the simulation and measurements to be presented in the next chapters have been modelled. Analyses of the effects such as range sensitivity, power reduction, aliasing and range gating due to the gating sequence have also been outlined.

4.4 References

[1] M. Richards, *Fundamentals of Radar Signal Processing*. New York: McGraw-Hill, 2005.

[2] S. Salous, *Radio Propagation Measurement and Channel Modelling*. Chichester, UK.: John Wiley & Sons, 2013.

[3] M. Skolnik, *Introduction to Radar Systems*, 2nd ed. New York: MxGraw-Hill, 1981.

[4] S. Salous, "Dispersion of chirp pulses by the ionosphere," *Journal of Atmospheric and Terrestrial Physics*, vol. 56, pp. 979-994, 1994.

[5] B. Mahafza, *Radar Signal Analysis and Processing Using MatLab*: Chapman and Hall/CRC, 2009

[6] M. Turley, "FMCW radar waveforms in the HF band," *ITU-R JRC 1A-1C-8B Meeting*, 2006.

[7] M. Turley, "Bandwidth formula for Linear FMCW radar waveforms," in *International Radar Conference - Surveillance for a Safer World*,pp. 1-6, 2009.

[8] C. Cook and M. Bernfeld, *Radar signals: An Introduction to Theory and Application*: Academic Press, 1967.

[9] D. Barrick, "FM/CW radar signals and digital processing," *U.S. Department of Commerce, NOAA TECHNICAL REPORT ERL 283-WPL 26*, 1973.

[10] H. Gokalp, "Characterisation of UMTS FDD Channels," PhD, Department of Electrical and Electronics, UMIST, Manchester, UK, 2001.

[11] A. Oppenheim, R. Schafer, and J. Buck, *Discrete-time Signal Processing*, 2nd ed.,Prentice-Hall, 1999.

[12] F. Harris, "On the use of windows for harmonic analysis with the discrete Fourier transform," *Proceedings of the IEEE*, vol. 66, pp. 51-83, 1978.

[13] G. Barry, "A low-power vertical-incidence ionosonde," *IEEE Transactions on Geoscience Electronics*,vol. 9, pp. 86-89, 1971.

[14] A. Poole, "On the use of pseudorandom codes for chirp radar," *IEEE Transactions on Antennas and Propagation*, vol. 27, pp. 480-485, 1979.

[15] J. McGregor, E. Poulter, and M. Smith, "Switching system for single antenna operation of an S-band FMCW radar," *IEE Proceedings Radar, Sonar and Navigation,* vol. 141, pp. 241-248, 1994.

[16] M. Ghannad, "Beamwidth Reduction for HF radars," PhD, Department of Electronic and Electrical Engineering, University Birmingham, Birmingham, UK, 1984.

[17] M. Oyan, S. Hamran, L. Hanssen, T. Berger, and D. Plettemeier, "Ultrawideband Gated Step Frequency Ground-Penetrating Radar," *IEEE Transactions on Geoscience and Remote Sensing,* vol. 50, pp. 212-220, 2012.

[18] R. Khan and D. Mitchell, "Waveform analysis for high-frequency FMICW radar," *IEE Proceedings on Radar and Signal Processing,* vol. 138, pp. 411-419, 1991.

[19] S. Solous, "Weighted sequences for HF FMCW sounding," *7th International Conference on HF Radio Systems and Techniques,* pp. 423-427, 1997.

[20] H. Chan, "Evaluation of the FMICW Waveform in HF surface Wave Radar Applications," *Defence Research Estabilishment Ottawa, Report No. 1219,* 1994.

[21] J. Gonzalez-Partida, M. Burgos-Garcia, B. P. Dorta-Naranjo, and F. Perez-Martinez, "Stagger procedure to extend the frequency modulated interrupted continuous wave technique to high resolution radars," *IET Radar, Sonar & Navigation,* vol. 1, pp. 281-288, 2007.

[22] S. Salous and O. Nattour, "Switching Sequences for monostatic pulse compression ionospheric sounders," in *Proceedings of the 4th Bangor Communication Symposium*, Bangor, pp. 346-349, 1992.

CHAPTER 5

Hardware Implementation

This chapter describes the hardware implementation of the proposed GFMCW radar system. The system synchronization and performance is also discussed. Furthermore, the designed and in-house manufactured antennas for the works presented in this thesis as well as the assembled X-Y positioning table together with its controls mechanism will also be examined.

Two radar systems have been built to validate the proposed hardware based technique (GFMCW) through experiments in various set-up scenarios, such as: through-the-wall life detection, buried metallic landmine detection and breast cancer detection.

The first radar system is based around two arbitrary waveform generators (AWG) acting as the transmitter and receiver reference signal source. The AWG can generate a waveform with frequency up to 4 GHz and maximum duration of 0.9 ms. This system has been used mostly in experiments related to through-the-wall detection and ground penetrating radar.

The second radar system is based around a vector network analyser (VNA) acting as both transmitter and receiver. The VNA can be configured to operate with frequency ranges up to 8.5 GHz. Due to its higher achievable bandwidth this system has been used in experiments related to breast cancer detection.

The next sections provide more details of the radar systems block diagram, system's performance and component description.

5.1 GFMCW Radar System Based on AWG

At the heart of the radar system shown in Figure 5.1 are two arbitrary waveform generators (AWG-1 and AWG-2) capable of generating predefined and user defined waveforms with frequencies up to 4 GHz and of maximum duration of 0.9 ms (this is limited by the generator internal memory). The wanted linear FMCW or GFMCW waveform is designed and generated in Matlab software prior to being transferred into the AWG memory. The AWGs are locked to an external 4 GHz clock and they output the waveform samples from their memory at a rate of 8 GSample/s (i.e. 125 ps sample interval). A replica of the 4 GHz clock is also generated at the AWG outputs by default.

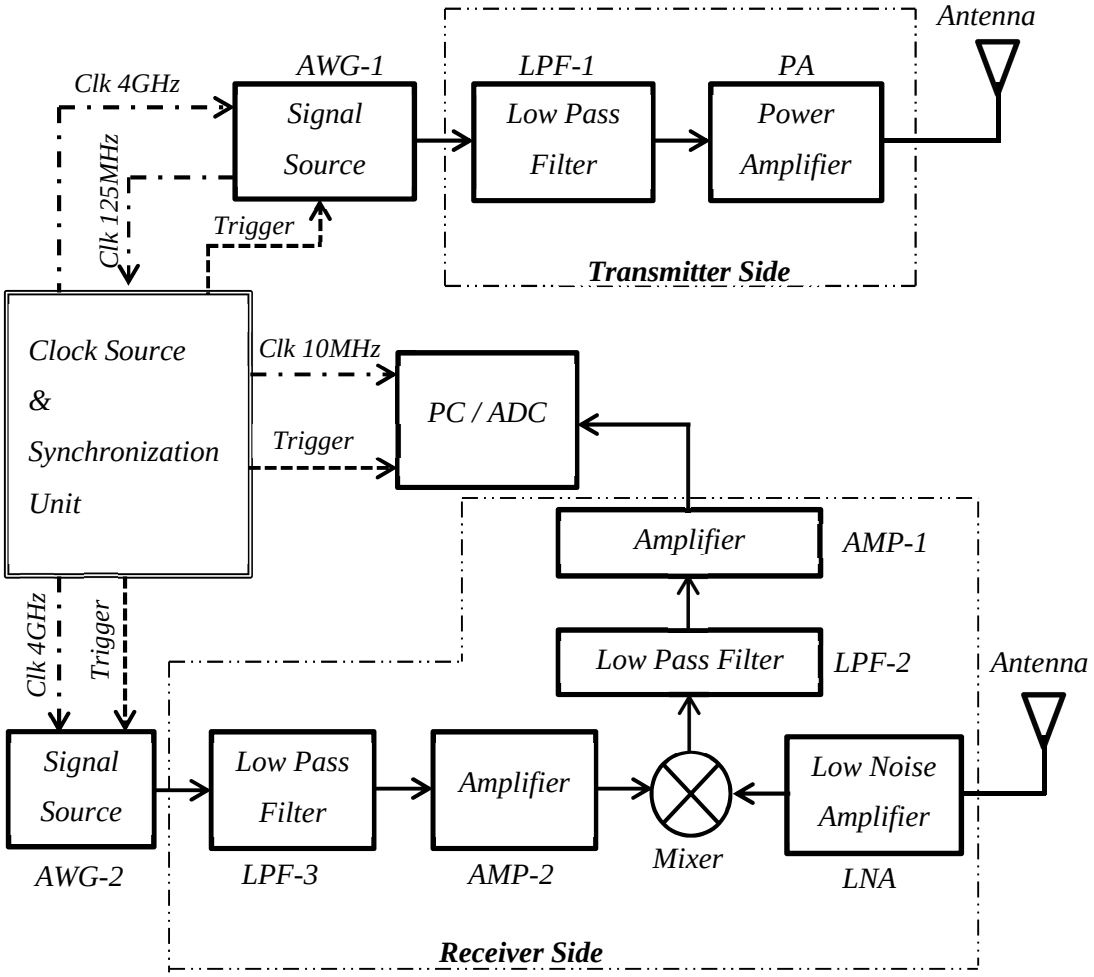

Figure 5.1: Block diagram of FMCW and GFMCW radar system based on AWG.

The system illustrated in Figure 5.1 operates as follows: at the transmitter the chirp signal generated by AWG-1 is first low pass filtered, to suppress the 4 GHz clock component, and then amplified, to boost the signal power before being transmitted through the antenna.

The receiver side operates as a heterodyne detector (see Section: 4.1.1) where the reference chirp signal, generated by AWG-2, is low pass filtered, to suppress the clock component, and amplified (by AMP-2) to the necessary level to drive the mixer's local oscillator (LO) port. This signal is multiplied with the amplified received signal. The resultant mixed signal is passed through a low pass filter, to remove the high frequency components, producing the beat-note signal. The beat-note is then amplified (by AMP-1), digitised by the ADC, and stored onto the PC for further off-line processing. As discussed in Chapter 4 the beat-note signal carries information related to target position and Doppler.

The beat-note signal is digitized using a 14 bit resolution ADC with a sampling rate of 20 MSample/s. The ADC 20 MHz internal clock is locked to a stable 10 MHz signal generated by the clock source and synchronization unit. The digitized data are stored on Dell T7500 workstation, which houses the ADC in one of its PCI express slots. For the purposes of synchronization and stability the AWG-1, AWG-2, and the ADC are connected to the same clock source and are all triggered simultaneously.

Figure 5.2: Metallic rack housing both the transmitter and receiver components.

The components making the transmitter and receiver side of the block diagram are all housed within a single metal enclosure (rack), for easy portability, as displayed in Figure 5.2. Table 5.1 details the operating parameters of the components and devices of the assembled radar system based on the AWG.

Table 5.1: Components specification for the radar system based on AWG

Device	***Manufacture / Model***	***Frequency [GHz]***	***Power***	***Other***
AWG-1,2	Euvis / AWG 801	DC-4	-4-0 dBm	-
AMP-1	Mini – Circuit / ZHL – 6A	$2.5x10^{-6}$-0.5	Max = 22 dBm Gain ≈ 23 dB	-
AMP-2	Mini – Circuit / ZKL – 2R7	0.01-2.7	Max = 13 dBm Gain ≈ 22 dB	-
LPF-1,3	-	DC-3.5	-	-
LPF-2	-	DC-0.01	-	-
LNA	Mini – Circuit / ZX60 – 3011	0.4-3	Max = 21 dBm Gain ≈ 13 dB	-
Mixer	Mini – Circuit / ZEM – 4300	0.3-4.3 (RF and Lo) DC-1 (IF)	LO = 13 dBm	-
PA	Mini – Circuit / ZHL – 4240	0.7-4.2	max = 28 dBm Gain ≈ 40 dB	-
ADC	Signatec PX14400A	0.02-0.40	-	14 bit

Figure 5.3 shows the back and front view of the AWGs used in the experiments with one of its differential output ports terminated with 50 ohm load.

Figure 5.3: Back and front view of the Euvis AWG.

Tests have been carried out to identify the sensitivity of the proposed radar system. Sensitivity is a measure of the ability of the system to detect weak signals. For this test the transmitter and the receiver were connected directly, in back-to-back configuration, through a cable and a set of attenuators. Measurements were performed for various attenuator values, starting with a value of 50 dB and going-up in steps of 10 dB until the received signal was at the noise level. The signal used in the test was a linear FMCW waveform with duration of 400 µs and a bandwidth of 1.4 GHz. Figure 5.4 shows the received signal power delay profile normalised with the maximum of the 50 dB attenuation profile. It can be seen from the figure that with 100 dB attenuation the path or target peak (at around 25.4 ns) is still distinguishable with a SNR around 10 dB. For an attenuation of 110 dB the target peak is at the noise level. Therefore, it can be said that the sensitivity of this system is 100 dB with a SNR of 10 dB.

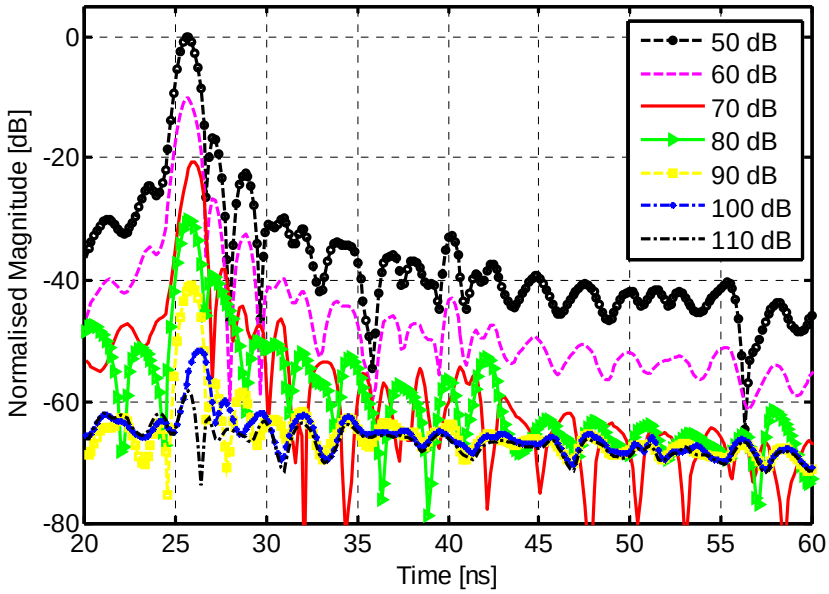

Figure 5.4: Radar system sensitivity test.

A dual tone test was also performed, to validate the proposed technique, by splitting the transmitted signal, using a power splitter, in two ways through different cable lengths and combining the signals at the receiver, by using a power splitter. In one of the cables an extra 12 dB attenuator was used.

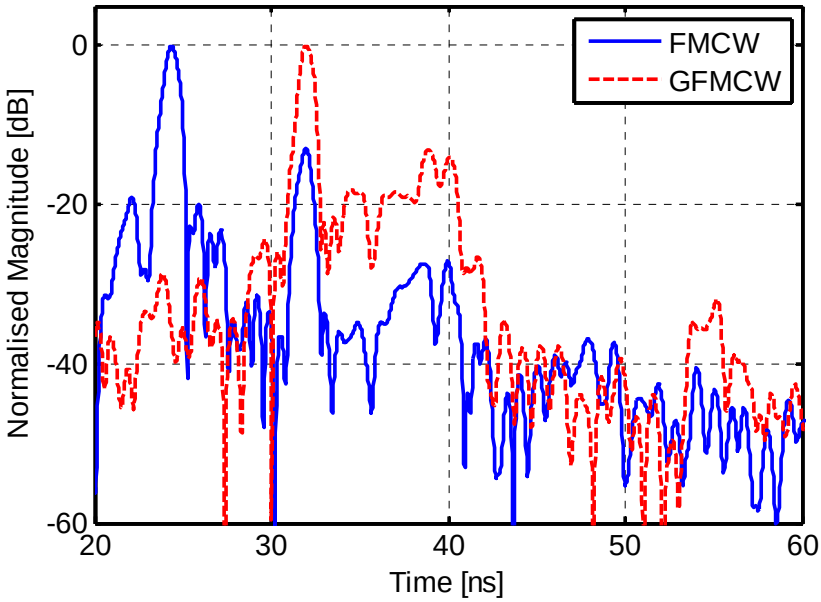

Figure 5.5: FMCW and GFMCW dual tone test.

Figure 5.5 shows the results of a dual tone test with the first and second component positioned at time delays of 24.5 ns and 31.8 ns respectively. For a normal FMCW signal the first component is 13 dB above the second one. This is due

to cable losses and the extra attenuators employed in the second component's cable. As discussed previously GFMCW signals can suppress the return signal of certain time delays while allowing other signals to pass through without attenuation. In this case a square wave gating sequence of parameters T_b = 11.5 ns and delay τ_1 and τ_2 equal to 4 ns was used to suppress the first component response. As shown in the same figure the dashed line for the GFMCW signal the first component has been suppressed to a level of 30 dB below the second component peak.

In order to generate the GFMCW from both AWGs, the transmitted and receiver reference GFMCW waveforms are first generated in Matlab by multiplying respectively into a normal FMCW waveform the gating sequences g(t), for the transmitter, and the complementary sequence (1 – g(t)), for the receiver. These waveforms are then loaded into the respective units and are generated once the devices are triggered. A similar process applies for a normal FMCW signal.

5.2 GFMCW Radar System Based on VNA

At the centre of this radar system is a vector network analyser (VNA) which acts as an FMCW transmitter and receiver. Network analysers have long been used as part of a radar system in applications such as: through-wall life detection [1, 2], ground penetration [3, 4], and medical imaging [5-7].

The signal generated by a network analyser is generally a linear or stepped FMCW signal. The GFMCW signal is created by switching (*on* and *off*) with a complementary function the analyser's transmitted signal and received signal.

Figure 5.6 illustrates the block diagram of the proposed bistatic GFMCW radar system based on the VNA. In the system the VNA generates an FMCW signal on *port-1*, before it is transmitted through the antenna. This signal is gated or switched '*on*' and '*off*' by *switch-A*. The received signal is also switched, by *switch-B*, with a sequence complementary to the one used in the transmitter, before it is fed to the receiver port. A basic background on the internal structures and operation of the network analyser can be found in references [8, 9].

User defined gating sequences are designed in Matlab software and loaded / transferred onto the memory of the AWGs. The output voltage levels of the Euvis AWGs, which range from -0.6 V to 0 V, are insufficient to directly drive the

employed fast switches, these require a minimum of -3.6 V and a maximum of 0.6 V to switch the state '*on*' and '*off*'. Therefore 10 Gb/s modulator drivers, referred to as switch drivers, have been used to act as voltage level converters for the Euvis. The switch driver operates with an output voltage high of 0 V and an output voltage low of -3.6 V. The driver's output offset voltage control ranges from -10 V to 5.5 V was set to 0 V by adjusting the potentiometer on the switch driver external circuit.

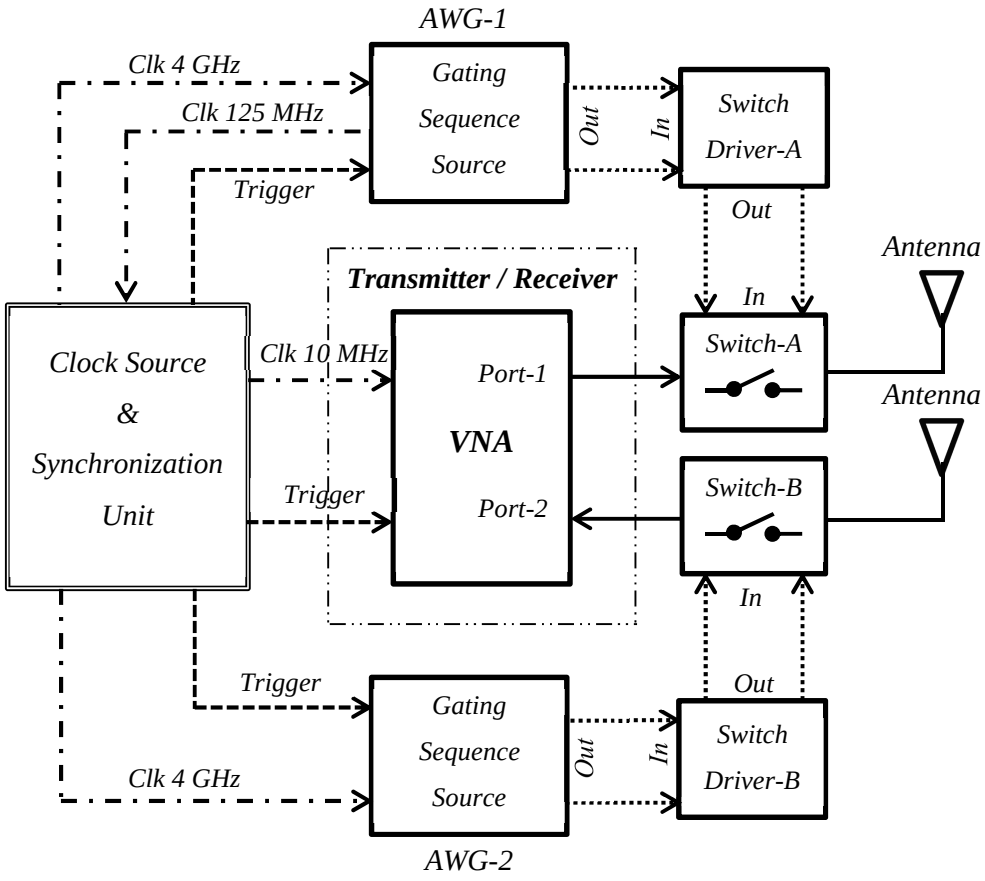

Figure 5.6: Block diagram of the Bistatic GFMCW radar system based on VNA.

The AWGs have differential outputs and these are connected to the switch driver differential input. The driver differential outputs are connected to the switch differential input as shown in Figure 5.7. The switches operate as single pole double throw (SPDT). Thus the unused output on each switch is terminated with a 50 ohm load.

The AWGs are the same Euvis generators used in the first set up and have a sample interval of 125 ps. Therefore the designed gating sequence can have a minimum rise and fall time of 125 ps. The fast switches have a rise and fall time of 100 ps and 90 ps respectively, and are able to operate on signals with frequencies up-

to 50 GHz. Table 5.2 provides a brief summary of the specification and manufacture of the devices used in this radar set-up.

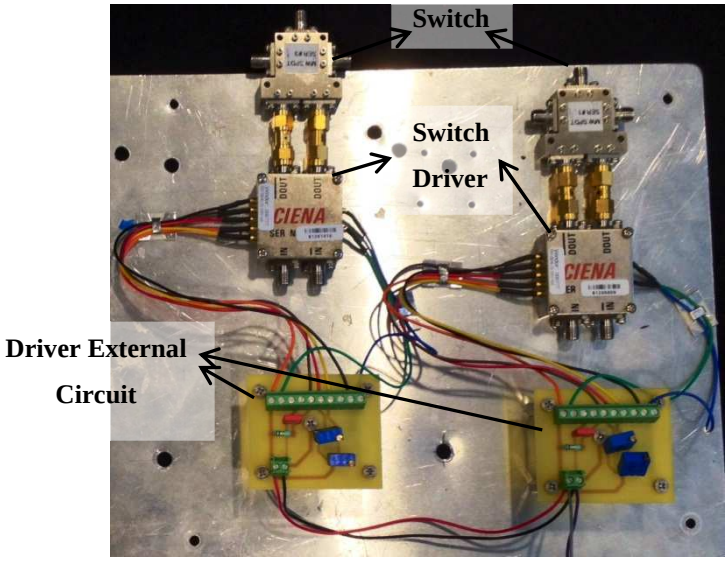

Figure 5.7: Connections between switch drivers and the fast switches.

Table 5.2: Device manufacture and specification

Device	***Manufacture / Model***	***Frequency [GHz]***	***Rise time [ps]***	***Fall time [ps]***
AWG–1,2	Euvis / AWG 801	DC – 4	125	125
Switch Driver	Fujitsu / FMM3109PG	-	40	40
Switches	Avago / AMMC-2008	DC – 50	100	90
VNA	Agilent / E5071A	0.3 – 8.5	-	-

The radar system has been synchronised by having the devices sharing the trigger from the same source and using specified clock signals which are locked onto a single clock source. The clock signals as well as the trigger signal are discussed in the next section.

A test has been performed to validate the radar system in using FMCW and GFMCW signal. The VNA was set to operate on a frequency range of 2-8.5 GHz with an output power of 0 dBm. A 30x30 metal plate was set 39 cm in front of both antennas (Tx and Rx antenna).

Figure 5.8 presents the normalised profiles of tests with the antenna crosstalk appearing at a time delay of 39.20 ns and the metal plate response at 41.38 ns. As expected with an FMCW signal the crosstalk appears stronger than the target response (i.e. metal plate). With the GFMCW signal the gating sequence has been designed to attenuate the crosstalk response while enhancing that of the target. The gating sequence used in this case was a square wave sequence with parameters Tb = 750 ps and $\tau_1 = \tau_2 = 0$ s. It can be seen that with GFMCW the target response is 11 dB above the crosstalk.

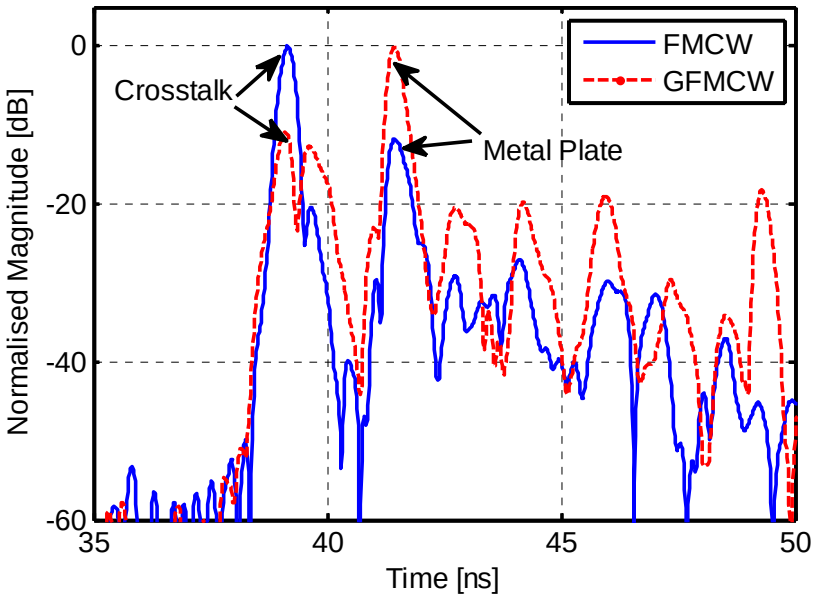

Figure 5.8: FMCW and GFMCW radar profiles.

5.3 Clock Source and Synchronization Unit

Synchronisation in a radar system is vital in order to correctly estimate the target position and / or the velocity due to its movement. Lack of stable synchronisation may also create unwanted artefacts that may not be related to the actual target, consequently giving rise to false-positive.

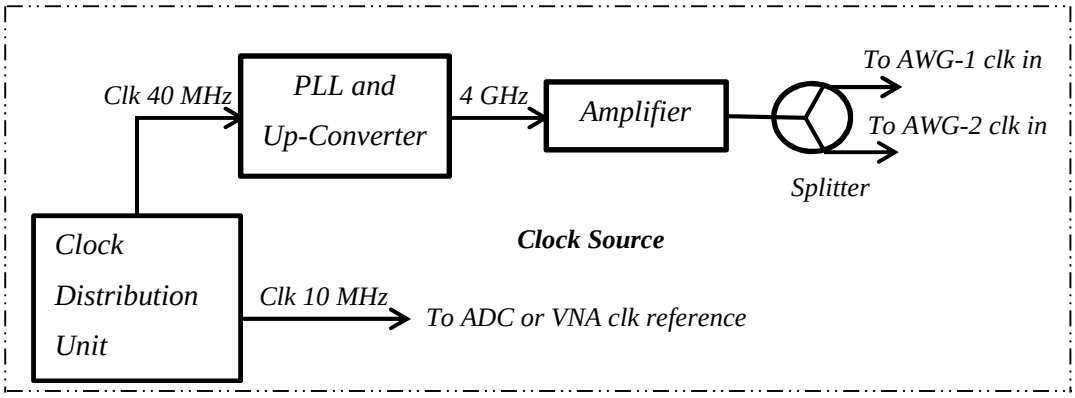

(a)

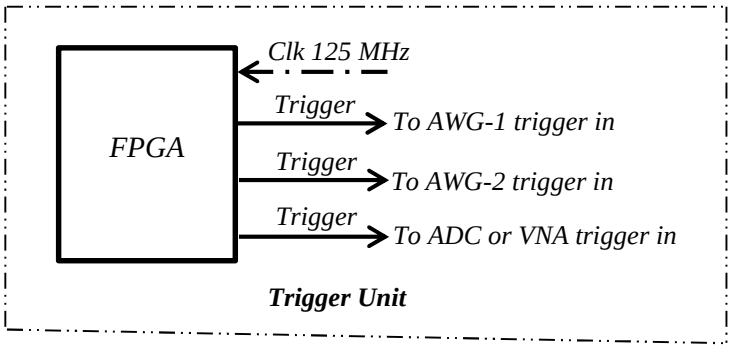

(b)

Figure 5.9: Block diagram of the system synchronisation. (a) Clock source; (b) Trigger Unit.

Since for the bistatic radar systems presented in the previous subsection, the transmitter and receiver are collocated, for overall system stability the clock signals can be locked to a single source. In addition the trigger signals can be generated from the same module.

The crucial device in the synchronisation of the radar systems is the clock distribution unit shown in Figure 5.9 (a). At the core of the unit is a stable, ultra-low noise 10 MHz signal reference, generated by the PRS10 Rubidium frequency standard module from the manufacturer Stanford Research Systems. In the clock distribution unit the 10 MHz signal generated by the PRS10 is divided, amplified and multiplied to generate pairs of output waveforms at the following frequencies: 10 MHz sine wave, 10 MHz square wave, 20 MHz sine wave, 40 MHz sine wave and 80 MHz sine wave. Figure 5.10 shows a picture of the clock distribution unit with frequency legend on the outputs. The unit has been designed and assembled in-house at Durham University.

Figure 5.10: Clock distribution unit.

From Figure 5.9 (a) a 40 MHz output sine wave signal is fed into the input of the PLL and up-converter unit, shown in Figure 5.11, which generates a locked 4 GHz sine wave at its output. This signal is amplified accordingly, using a mini-circuit ZX60-591 6M-S component, split into two, using a power splitter, and each output is used as a clock input signal for each AWG module, respectively. The internal clock rate of the AWG module is twice that of the input signal clock; therefore the samples stored in the module memory are outputted at a rate of 8 GS/s.

A 10 MHz sine wave output of the clock distribution unit is used as clock reference for the ADC or the VNA.

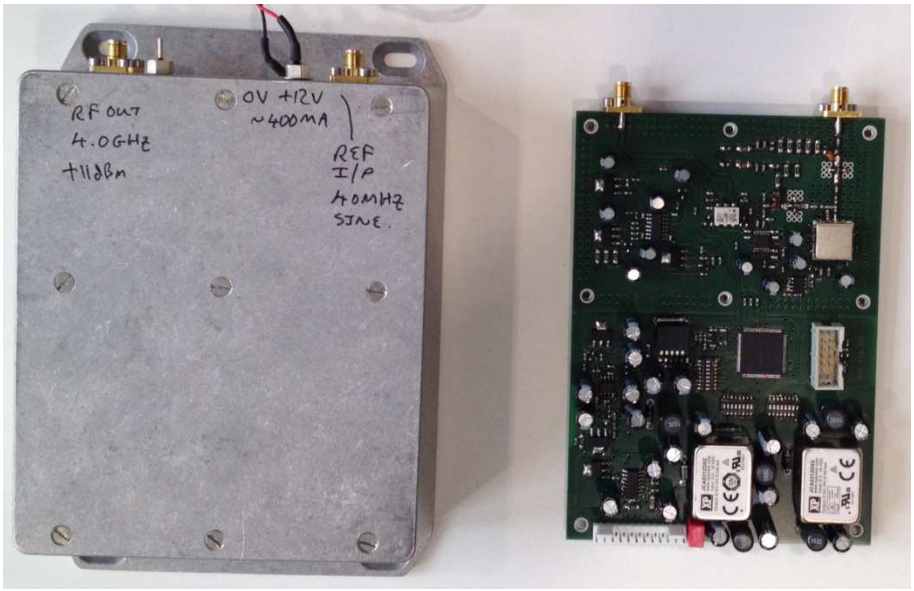

Figure 5.11: PLL and up-converter unit (left) inn its metallic enclosure, (right) the unit circuit board.

By default the AWG modules output on its *SYNCO* port a reference sine wave of 125 MHz, which constitute a division of its internal 8 GHz clock by a factor of 32. This signal is locked onto the external 4 GHz clock reference signal. For the purpose of stability one of the AWG modules SYNCO signals is used as a clock signal input to the trigger unit, shown in Figures 5.9 (a) and (b).

At the heart of the trigger unit is a programmable FPGA component (Altera Cyclone II), which divides the input clock signal accordingly to generate the same trigger signal on its output ports. The signal generated by the trigger unit outputs are a square wave of TTL level (3.5 V), moreover the devices (AWGs, VNA or ADC) have been set to be edge triggered. Figure 5.12 shows the hardware circuitry of the trigger unit.

The user defined division factor for the FPGA input clock signal is set depending on the duration of FMCW / GFMCW signal. The factor is pre-set so that the period of the trigger signal is longer than the duration of the AWGs or VNA generated waveform.

For measurements involving the radar system based on AWG, the trigger period was set to 500 µs equivalent to the inverse of the division of the 125 MHz input clock signal by a factor of 62500. The generated AWG waveform in this case was set to 400 µs duration.

For the radar system based on VNA the FPGA is programmed to use a clock division factor of 156.25×10^6. This gives a trigger signal of 1.25 s period. To avoid trigger ambiguity the VNA is set to generate a sweep of 600 ms duration almost half of the trigger period. Moreover, the AWGs in this configuration are loaded with a gating sequence of 100 µs duration and set to repeat 10000 times in a loop, for each trigger signal, resulting in 1s overall sequence duration, which is enough to cover the 600 ms duration of the chirp.

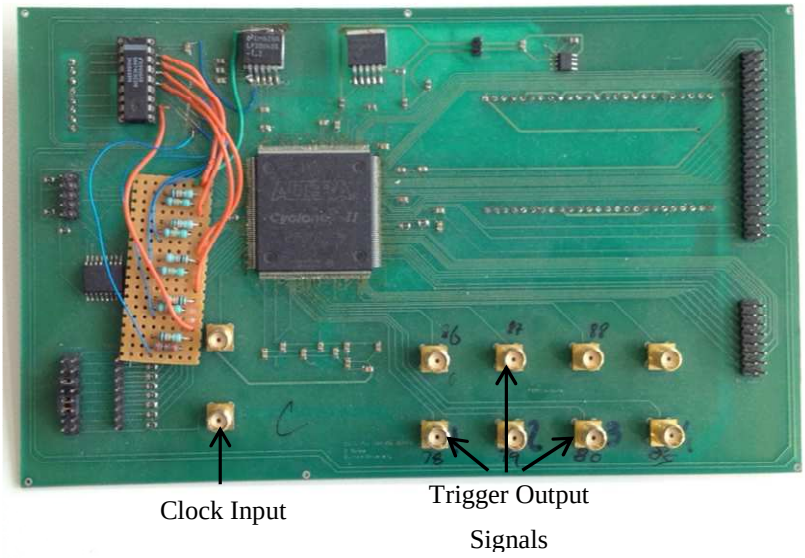

Figure 5.12: FPGA based Trigger unit.

5.4 X-Y Positioner System

An X-Y positioner system has been designed and assembled to move the antenna(s) and the radar system into predefined positions along two axes. The positioner covers an area of 40 cm x 40 cm. The positioner system is controlled by motor's motion control software, namely Mach3 by Artisoft, which process the user defined G-Code and M-code.

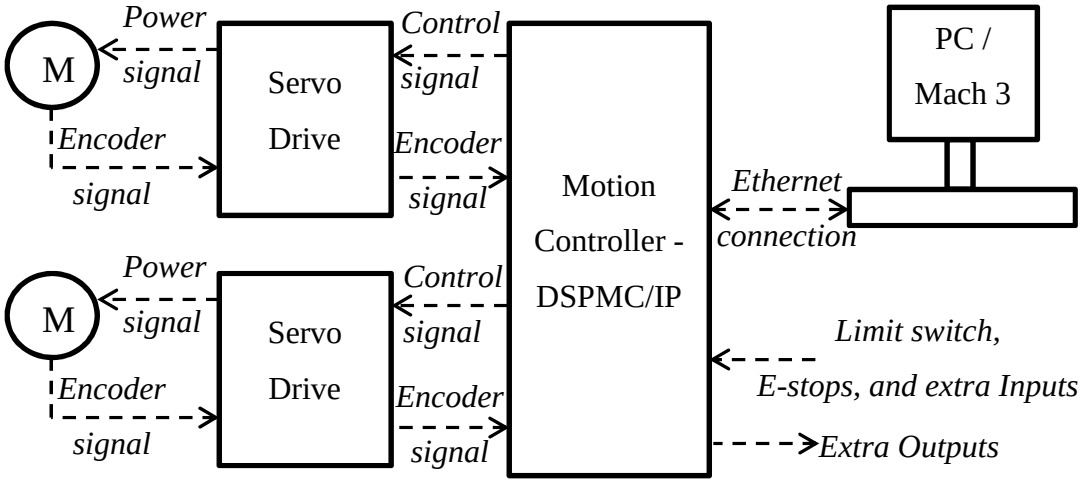

Figure 5.13: Block diagram of X-Y positioning system.

Figure 5.13 shows the block diagram of the X-Y positioner system with the devices interconnections. At its heart is the software Mach3 installed on a PC which controls the overall system, and issues user defined commands, e.g. to move or stop the motors, changes speed, activates output(s) and interacts or responds to external input and so forth. The PC is connected through the Ethernet with a motion controller device "DSPMC / IP", manufactured by Vital Systems, this acts as an interface or translator, converting the digital signal instructions from MACH3 into analogue or the digital signal for the external devices and peripherals connected to it, and likewise converting input signals (from the devices and peripheral) into instructions for the PC.

The DSPMC/IP is connected with the other devices and peripheral through opto-isolated 7535 breakout board for digital signals and 7721 breakout board for the analogue signal. The servo drive provides control over the motor and converts the DC speed control voltage (ranging from ± 10 V) from DSPMC into the required signal power level necessary to drive the motor at an equivalent speed. The servo drive and the servo motor are both manufactured by "Omron" and their model is R88D-UA12V and R88M-UA40030VA respectively.

Both servo motors are able to output feedback signals in the form of "incremental encoder signal". This signal carries information related to the motor's shaft rotation. This is further processed by the Mach-3 software to extract information such as speed, travelled distance and current position.

The used axes are of length 40 cm; in order to avoid the axis being overrun by the limit switches employed at each end of the axis. Consequently, if a switch is

activated Mach-3 was configured to stop the motor motion immediately. For safety purposes extra E-stop (emergency stop) buttons were also employed, when activated the servos (drive and motor) are powered off immediately.

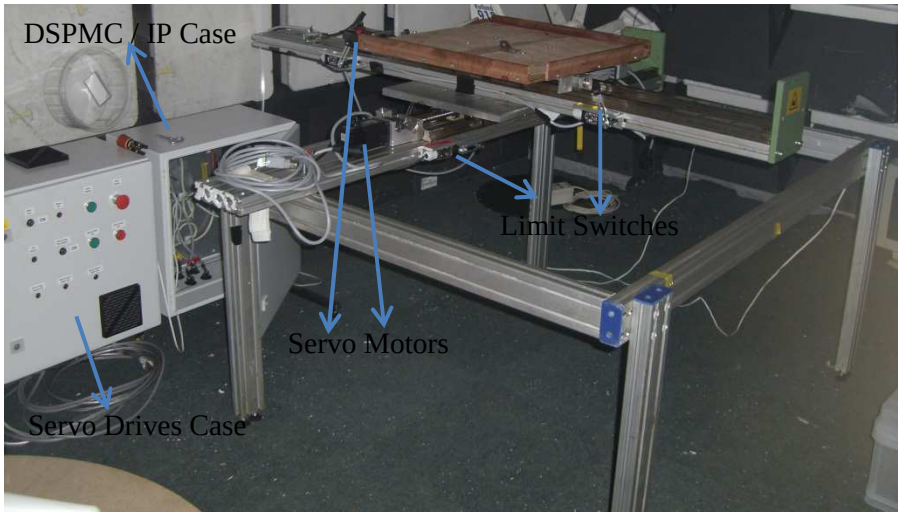

Figure 5.14: X-Y positioning system.

Figure 5.14 shows the assembled X-Y positioning system and the metallic cases housing the high power servo drives and the DSPMC/IP device together with the breakout boards. Figure 5.15 shows the devices inside the metallic cases and how they are interconnected.

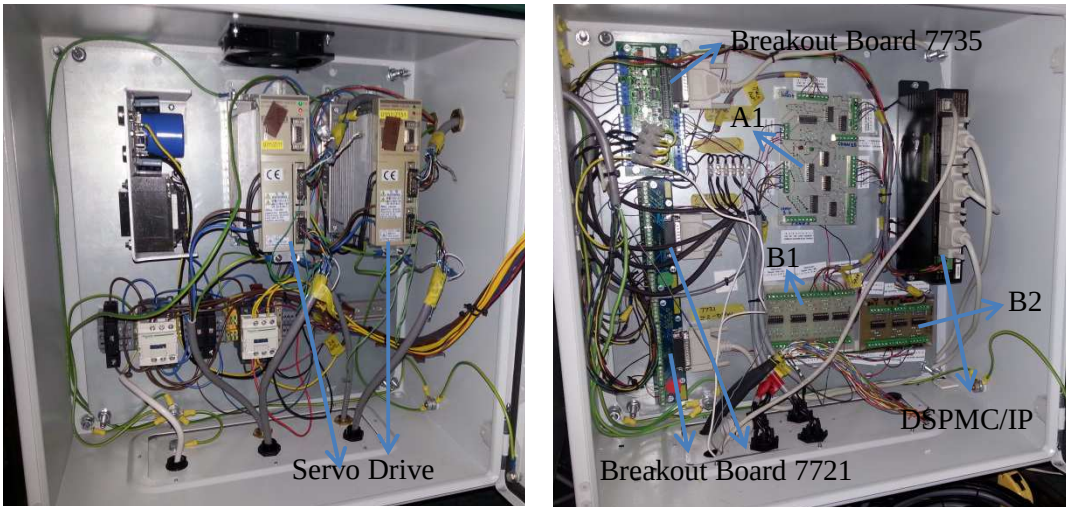

Figure 5.15: Connections inside the (left) Servo drive case, (Right) DSPMC/IP case.

In order to automate and synchronise the radar system together with the X-Y positioner movement, a program was written in visual basic (VB) software to provide control and communication of both the Mach3 (controlling the X-Y) and the

radar system. For GFMCW radar system based on the VNA the VB program operated the following way:

1) VB program sends a command to Mach3 to move the antennas into a predefined position.
2) Once the positioner completes the movement Mach3 reports back to VB program.
3) VB sends a command to the VNA to start the measurement.
4) Once the measurement is completed data are transferred and saved on the PC.
5) Repeat steps (1) – (4) until the measurement have been completed on all the predefined positions.

The communication between the Mach3 and VB is performed through the I/O ports of the VNA and of the DSPMC/IP 7735 breakout board. On Mach3 apart from the G-Code, which contains the coordinate and the move command, an M-code or micro have been written to check predefined DSPMC/IP inputs (for the VB program response), and to generate a signal from a predefined output (which indicates, to VB program, that it is the last position). The predefined inputs of DSPMC/IP are connected to the VNA outputs and vice versa.

The I/O of the 7735 breakout board operates with 0 V and 24 V representing logic-low and logic-high, whereas the VNA operates with a TTL based I/O. As a straight connection is not advisable due to a difference in voltage logic levels between the two devices a voltage level converter circuit (*marked as "A1" on Figure 5.15*) was designed, using a combination of the Darlington transistor ICs (ULN2803A) and Logic gate ICs (74LS04N), to convert the 24 V output of the breakout board into 5 V (for the VNA input) and the 3.5 V output of the VNA into 24 V (for the breakout board).

Although the system was working in this configuration it had been found that the ground potential voltage of the VNA differed from that of the 7735 breakout board. This was performed by measuring the difference voltage between both grounds. In order to protect from the ground potential imbalance both devices have been isolated by using a phototransistor opto-coupler IC (ACP847) which can be seen on the circuit boards marked as *"B1"* and *"B2"* in Figure 5.15.

For the GFMCW radar system based on AWG the automation process described above does not apply as the VNA is not used in this set-up. Consequently, for simplicity, a push button switch has been added to the X-Y positioner and the Mach3 M-code micro code modified to expect a single input. Therefore, once the X-Y has completed its movement into a predefined location, the micro code runs checking the push button logic state; meanwhile the user can perform the measurement. Once completed, the user can activate the push button sending a signal onto Mach3 to move to the next predefined position. This procedure is repeated until the measurements are performed in all the predefined positions.

5.5 UWB Antennas

In a wireless system antennas play a crucial role. At the transmitter it converts the electrical signal into electromagnetic waves, whereas at the receiver it converts the energy from the electromagnetic waves back to an electrical signal. Antennas can also be viewed as a filter allowing signals within their operating band to radiate or receive while rejecting signals outside its band.

An antenna is termed “UWB antenna” if the percentage ratio between its bandwidth and the centre frequency, known as fractional bandwidth, is no less than 20% or it has an absolute bandwidth no less than 500 MHz, regardless of the fractional bandwidth. A vast number of UWB antennas can be found in the literature. For the interested reader, references [10-12] provide an overview of these types of antennas.

Some of the classical UWB antennas have been designed and manufactured for the radar and channel propagation experiments detailed in this thesis. These include discone and tapered slot antennas (TSA). These were designed and simulated using the commercially available electromagnetic solver “CST Microwave Studio” and were manufactured using the facilities available at Durham University.

5.5.1 TSA Antenna

Tapered slot antennas also commonly known as Vivaldi antennas have been around since the late 70's and are widely used in radar applications due to their wide operational bandwidth, directional pattern and compact size [13].

The TSA antennas presented in this section follow from the guidelines shown in reference [14]. Following from the TSA geometry shown in Figure 5.16 two TSA (TSA-A and TSA-B) of different dimensions, substrate thickness and material have been both simulated and manufactured. The exponential tapering profile of the antennas is defined by the function in equation (5.1), where R is the taper ratio.

$$y(x) = Se^{Rx} + V \tag{5.1}$$

The first antenna (TSA-A) of dimension 77 mm x 84 mm have been designed on a Roger RT6010LM substrate of permittivity 10.2 and thickness of 1.27 mm. The exponential tapering parameters were optimised to values S = 0.062 mm, V = 0.14, and R = 0.4 mm^{-1}. The TSA-B with size of 36 mm x 42 mm was designed on a Taconic Cer-10 substrate with a permittivity of 10 and thickness of 0.64 mm. In addition the parameters of the exponential tapering function for this antenna were: S = 0.14 mm, V = 0.0012 mm and R = 0.165 mm^{-1}.

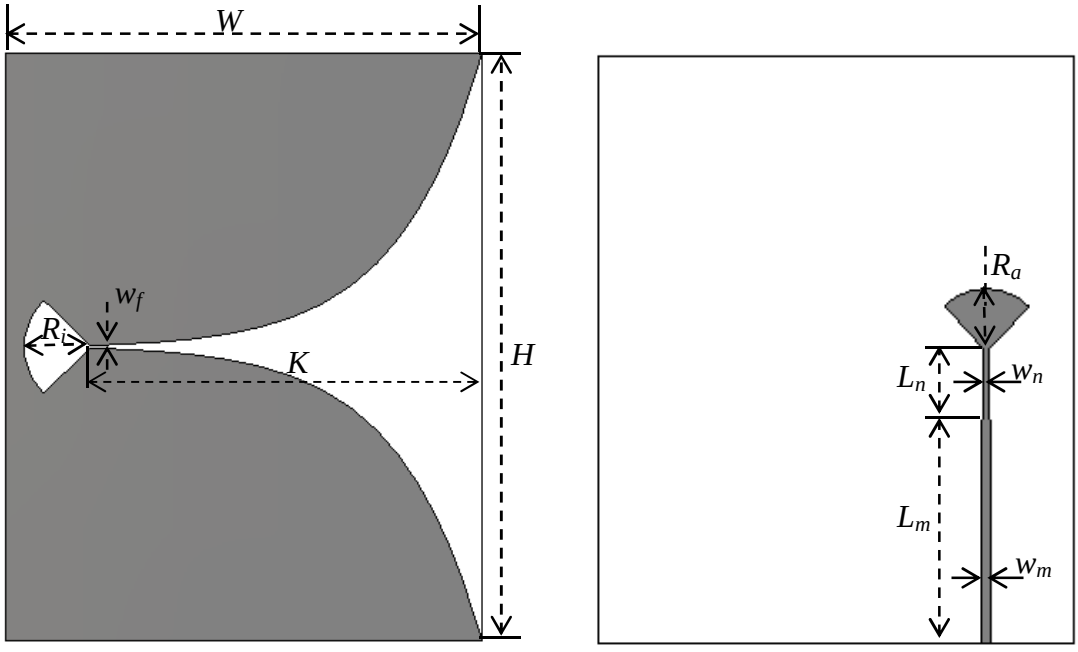

Figure 5.16: The geometry of the proposed exponential TSA.

Table 5.3 gives the final dimensions of both antennas in mm scale. Figure 5.17 shows the antennas return loss, with the TSA-A and TSA-B achieving a bandwidth of 3.1 GHz and 6.6 GHz, respectively, assuming -10 dB return loss as a reference. Figure 5.18 shows top and back view of the in-house manufactured TSA-A and TSA-B antennas.

Table 5.3: Proposed TSA antennas parameters

	W	H	w_f	R_i	K	L_m	L_n	w_n	w_m	R_a
TSA-A	77	84	0.40	8.40	65	28	14.2	0.91	28	8.25
TSA-B	36	42	0.30	4.60	30	16	5.15	0.40	16	4.10

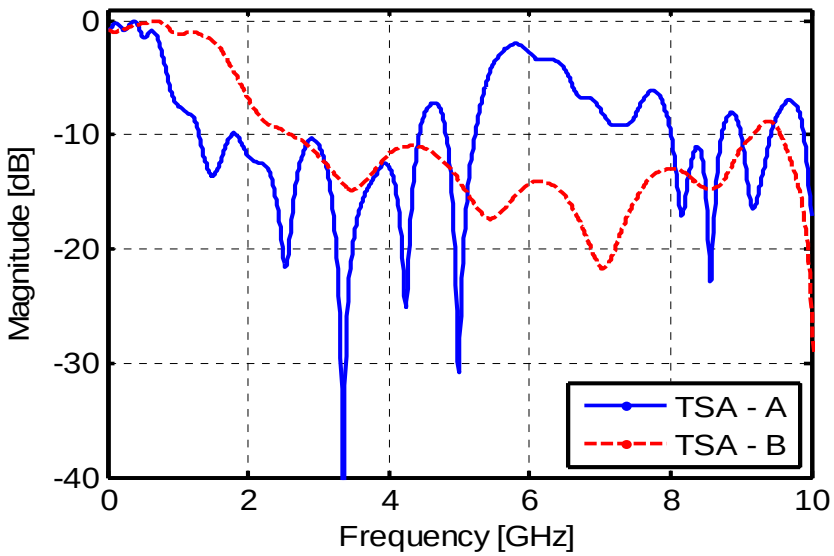

Figure 5.17: Return loss of the proposed TSA antennas.

(a) (b)

Figure 5.18: The front and back view of the fabricated antennas, (a) TSA-A; (b) TSA-B.

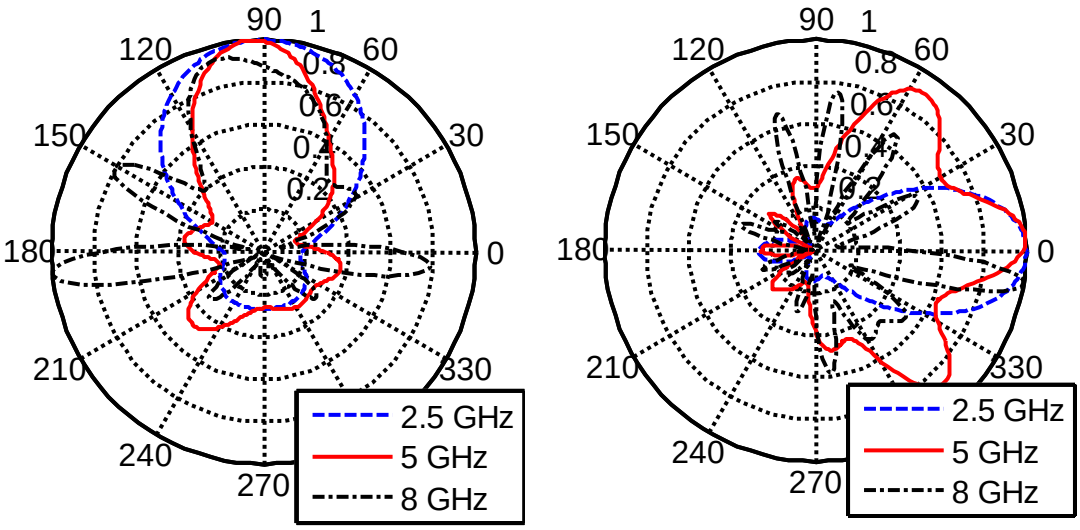

(a) H-plane (b) E-plane

Figure 5.19: Normalized simulated radiation pattern of TSA-A antenna.

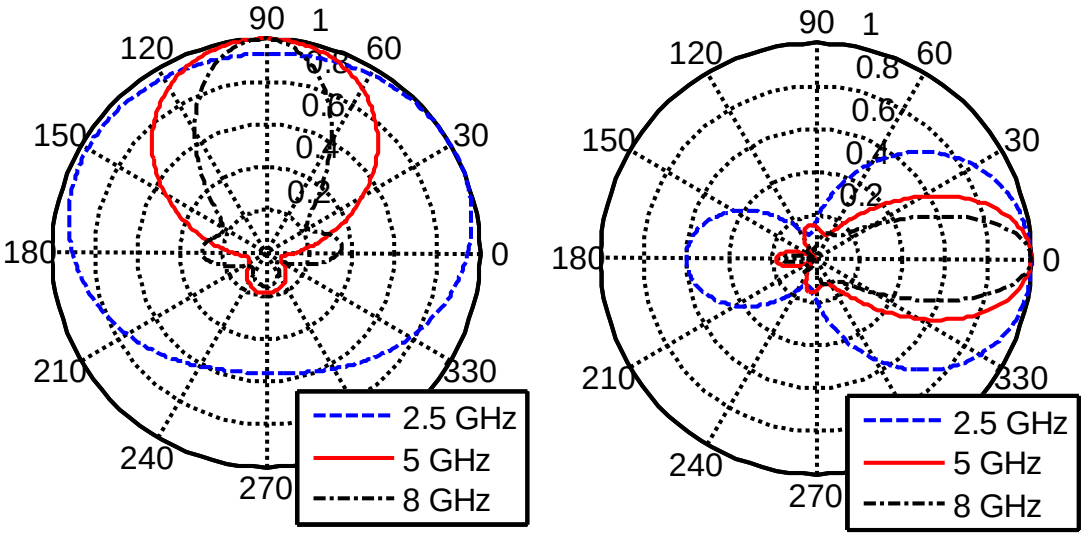

(a) H-plane (b) E-plane

Figure 5.20: Normalized simulated radiation pattern of TSA-B antenna.

Figures 5.19 and 5.20 show the simulated normalised radiation pattern of TSA-A and TSA-B antennas at 2.5 GHz, 5 GHz and 8 GHz. The radiation pattern of the TSA-B is lesser directive at the lower part of the UWB frequency (2.5 GHz) compared to the TSA-A antenna. As the frequency increases, the TSA-B antenna shows considerable improvement in the radiation pattern and becomes more directive than the TSA-B. For the TSA-B the pattern deteriorates with many more extra lobes appearing as the frequency increases.

5.6 Summary

This chapter provided a description of the two radar systems used in the measurement campaign. Both systems namely “radar system based on AWG” and “radar system based on VNA” can be operated with either FMCW or GFMCW signals. For stability purposes the clock and trigger signals of the radar system are locked onto a single clock source generated by a stable and ultra-low noise rubidium clock source.

An X-Y positioning system has been built to move the antennas / system into predefined position around the area of interest. A visual basic program as well as motion control program was written to make the movement and measurement process automatic. Consequently, once the X-Y system has moved into a new position, the measurement is performed without the user’s intervention.

Classical UWB antenna namely Vivaldi antennas have been designed and manufactured for the radar work presented in this thesis.

5.7 References

[1] F. Ahmad and M. Amin, "Through-the-wall radar imaging experiments," *IEEE Workshop on Signal Processing Applications for Public Security and Forensics*, pp. 1-5, 2007.

[2] F. Soldovieri, F. Ahmad, and R. Solimene, "Validation of microwave tomographic inverse scattering approach via through-the-wall experiments in semicontrolled conditions," *IEEE Geoscience and Remote Sensing Letters*, vol. 8, pp. 123-127, 2011.

[3] A. Amiri, K. Tong, and K. Chetty, "Feasibility study of multi-frequency ground penetrating radar for rotary UAV platforms," *IET International Conference on Radar Systems*, pp. 1-6, 2012.

[4] T. Counts, A. Gurbuz, W. Scott, J. McClellan, and K. Kangwook, "Multistatic Ground-penetrating radar experiments," *IEEE Transactions on Geoscience and Remote Sensing*, vol. 45, pp. 2544-2553, 2007.

[5] E. Fear, P. Meaney, and M. Stuchly, "Microwaves for breast cancer detection?," *IEEE Potentials*, vol. 22, pp. 12-18, 2003.

[6] M. Klemm, I. Craddock, J. Leendertz, A. Preece, and R. Benjamin, "Experimental and clinical results of breast cancer detection using UWB microwave radar," *IEEE Antennas and Propagation Society International Symposium*, pp. 1-4, 2008.

[7] X. Li and S. Hagness, "A confocal microwave imaging algorithm for breast cancer detection," *IEEE Microwave and Wireless Components Letters*, vol. 11, pp. 130-132, 2001.

[8] National Instruments. (16 July 2014). *Introduction to Network Analyzer Measurements Fundamentals and Background*. Available: http://download. ni.com/evaluat ion/rf/Introduction_to_Network_Analyzer_Measurements.pdf

[9] D. Ballo, "Network analyzer basics," in *Back to Basics Seminar*, H.P. Company, 1997.

[10] L. Jianxin, C. Chiau, C. Xiaodong, and C. Parini, "Study of a printed circular disc monopole antenna for UWB systems," *IEEE Transactions on Antennas and Propagation*,vol. 53, pp. 3500-3504, 2005.

[11] H. Schantz, "A brief history of UWB antennas," *IEEE Aerospace and Electronic Systems Magazine,*vol. 19, pp. 22-26, 2004.

[12] W. Wiesbeck, G. Adamiuk, and C. Sturm, "Basic properties and design principles of UWB antennas," *Proceedings of the IEEE,* vol. 97, pp. 372-385, 2009.

[13] P. Fei, Y. Jiao, Y. Ding, and F. Zhang, "A compact coplanar waveguide fed wide tapered slot ultra-wideband antenna," *Progress In Electromagnetics Research Letters,* vol. 25, pp. 77-85, 2011.

[14] Y. Wang, A. Bakar, and M. Bialkowski, "Reduced-size UWB uniplanar tapered slot antennas without and with corrugations," *Microwave and Optical Technology Letters,* vol. 53, pp. 830-836, 2011.

CHAPTER 6

Numerical Radar Simulation

This chapter presents the numerical simulation results of FMCW and GFMCW radar systems in applications such as: through-the-wall radar imaging, ground penetration radar imaging, and medical imaging. The benefits of performing numerical simulations as well as the available numeral techniques are given.

Numerical simulation aims at replicating the operation of a system in the real world, through a conceptual model. It may allow a more detailed analysis of the performance and limitations of a complex system prior to its implementation. This is particularly advantageous for radar systems as successful target detection depends in general on a number of parameters, such as: transmitted power, waveform shape, duration and bandwidth, number of antenna, the type and their orientation, target radar cross section (RCS), and the involved scenario parameters like the number of clutter, their shape and electrical properties. With numerical simulations one or more of these parameters can be easily varied or changed allowing one to establish their impact on the system and moreover, gain more knowledge on the system capabilities as well as needed improvements.

Simulations save time and money, as the system performance can be analysed in detail prior to being built or tested. However, it requires certain understanding of what is intended to be simulated in order to create a realistic simulation scenario.

Numerical radar simulations are mostly performed through the use of computational electromagnetic (CEM) techniques. These techniques predict the behaviour of the electromagnetic wave as it propagates through or interacts with the modelled environment and physical objects within the problem domain. The numerical solutions to Maxwell's equations provide a starting point to the operation of these techniques. Various CEM techniques have been developed and reported in the literature. A comparative overview of the existing techniques can be found in [1-4], and more extensive analyses are dealt with in the following textbooks [5, 6].

Depending on the formulation of Maxwell's equations the CEM techniques can be divided into two main methods, these are: the integral equation method (IEM) and differential equation method (DEM). The former method formulates the electromagnetic problem using the integral-form of Maxwell's equations. This method includes techniques such as: Finite Integral Technique (FIT) and Methods of Moments (MoM). The latter method uses the differential or the curls form of Maxwell's equations and includes techniques such as: Finite Element Methods (FEM), Finite Difference Time Domain (FDTD) and Transmission Line Matrix (TLM).

Both the IEM and DEM method can be applied to problems in the time domain or in the frequency domain, although some of the above mentioned techniques operate only in a particular domain. CEM techniques require the discretization of Maxwell's equations quantities such as time, frequency and space. In this thesis, numerical simulations were performed using the commercially available software "CST Microwave Studio".

6.1 Chirp Based Radar Simulation in CST (MWS)

CST Microwave Studio (MWS) is a specialised 3D electromagnetic tool for the design, analysis and optimisation of components and systems operating in a wide range of frequencies. CST offers an accurate and efficient "full-wave" solution to Maxwell's equations without any simplifying assumptions or approximations. Consequently, the software is able to accurately model the electromagnetic propagation phenomena including near and far field effects, scattering, diffraction and absorption. The CST MWS is based on the FIT technique with a perfect boundary approximation (PBA) for spatial discretization, giving it the ability to solve a range of electromagnetic problems in time or frequency [7]. For flexibility the software offers a variety of field solvers, to suit specific applications. These solvers include the general transient solver, frequency domain solver, and integral and asymptotic solver.

Transient Solver: allows real time domain simulation of the system's transient behaviour in a wide frequency range in a single run. This solver is a popular choice in a number of EM problems including devices that are electrically large dimensions, non-resonant and with open boundaries, as well as applications such as time domain reflectometry (TDR). Being a time domain based solver the simulation's frequency response of an arbitrarily fine frequency resolution can be obtained through the Fast Fourier Transform (FFT) without an extra computational cost. Therefore, it enables the capturing of the resonances inside the simulation spectrum [4, 7]. The modulated Gaussian waveform, which is dependent on the user's specified frequency range, is the default excitation signal. The solver also allows arbitrary user defined signals to be fed into the simulator.

Frequency Solver: operates in the frequency domain and is well suited to analyse electrically small or mid-sized problems as well as narrowband resonant structures. Unlike the transient solver, which delivers a broadband response in a single run, for the frequency solver a number of simulations have to be performed (one for each frequency point) to cover the broadband frequency range.

Integral and Asymptotic Solver: both solvers are mostly used in the analyses of the radar cross section (RCS) of electrically large structures, such as: aeroplanes and ships.

The work reported in this chapter uses the Transient Solver in CST MWS as it allows imported and user defined excitation waveforms (such as FMCW signals). Moreover it is also the preferable choice of solver for simulations involving non-resonant and electrically large structures such as the radar scenarios (TTWIR, GPR, and MIR) under consideration in this thesis.

The transient solver in CST MWS has as default excitation "the Gaussian modulated pulse" whose shape depends on the user specified operating frequency. For an arbitrary user defined waveform such as the FMCW waveforms, the user has a choice of either importing from an external file the waveform in the form of an ASCII table file or writing the desired waveform equation(s) in the available built-in VBA micro.

Although the mathematical equation that describes the FMCW and GFMCW waveforms is straight forward (see: Chapter 4) in order to perform a successful simulation with this type of waveform a series of issues have to be addressed. Generally, for a successful simulation the used excitation waveform in CST transient solver has to have a smooth transition (e.g. Gaussian excitation). For a waveform with sharp transition, the simulation normally becomes unstable. This causes large ripples to appear in the resultant time domain signals. These ripples are a result of the effects of the waveform's sharp transition in the FIT technique employed by the solver and it has nothing to do with the response of the device or scenario under investigation. To bypass this software limitation, in the context of FMCW and GFMCW waveforms, the chirp signal is windowed before the simulation and the gating sequence is applied through post-processing. These two steps are discussed in the rest of this subsection. Numerical electromagnetic simulation of a radar system based FMCW or GFMCW signals is novel and has not yet been reported in the literature by other research groups.

6.1.1 Chirp Windowing Before Simulation

The ripples due to the sharp transition on the excitation waveform may compromise the effectiveness and performance of the device or scenario under test. The user defined chirp or linear FMCW waveform can be considered as a truncated cosine function whose frequency varies as function of time. The truncation of the FMCW signal creates sharp transitions on its amplitude, from '0.0' to '1.0' and from '1.0' to '0.0', at the beginning and at the end of the sweep (*see: Figure 4.2 in Chapter 4*). This transition causes the aforementioned instability in the CST solver.

A solution to this problem is to apply a windowing function to the FMCW signal in order to attenuate or smooth the discontinuity at both the beginning and at the end of the sweep. Consequently, the user excitation in CST is written as the product of the FMCW waveform with the windowing function. After simulation the received or recorded FMCW signals are correlated, through post-processing in Matlab software, with a copy of the windowed transmitted chirp to produce the range delay profile. In the radar simulations reported in this thesis the Hamming window was used to smooth the chirp transitions.

6.1.2 GFMCW Signal Through Post-Processing

Gated frequency modulated continuous waveform is the result of the product between a chirp waveform and a gating sequence. The gating sequence assumes values of '0' and '1' representing the transmitter or receiver states. For the time interval in which the sequence is "1" the transmitter or receiver is said to be active and for the sequence value of "0" the transmitter or receiver is not active. Sharp transitions between states of the GFMCW causes the same problems highlighted in the previous subsection, i.e. simulation instability and unwanted ripples. Consequently, the user defined GFMCW signals cannot be directly simulated in CST.

To get around this problem, the scenario under test is simulated using a normal FMCW waveform. Once the simulation is completed the recorded or received waveforms are loaded, together with the user defined FMCW excitation, into Matlab for further processing. Using a written Matlab code the GFMCW radar simulation is realised by multiplying the receiver gating sequence ($1 - g(t)$) with the

loaded CST recorded waveforms and multiplying the transmitter gating sequence *g(t)* with the loaded CST user defined excitation. The resultant transmitter and receiver GFMCW waveforms are correlated for extraction of the beat-note or range profile signal.

Realising GFMCW radar simulation through post-processing provides flexibility and time saving advantages. As an example: for a set of data recorded in the simulation of FMCW radar scenarios, different gating sequences can be applied in the post-processing to the same data set without the need to re-run the simulation.

6.1.3 CST Excitation Source

In the radar simulations presented in this chapter a "*plane wave*" has been chosen as the transmitter's excitation source. CST E-field probes placed at user specified positions within the scenario under test were used as receivers to record the incident and scattered electromagnetic field. A plane wave in CST is a planar excitation source of an electromagnetic wave with constant phase wave front parallel to the source and of constant amplitude. The wave direction of propagation is normal to the plane.

Although antennas could have been used in place of a plane wave, their physical shape, size and the number required to cover the radar scenario to be considered would have increased the computational burden of the simulation resulting in longer simulation time or even quite possibly instability due to the limitation of the computer memory and processing power. Despite the fact that a plane wave is an ideal electromagnetic field source, it is mostly considered as a realistic approximation to the field emanating from an antenna located at a far distance [8], commonly referred to as "*the far field*".

The CST E-field probes, used as receiving antennas, are able to measure individually the total electric field at their predefined position. This field is the superposition of the incident field (E_{INC}), direct signal impinging on the probe from the plane wave, the scattered field (E_{REF}), the signal reflected by the surrounding objects (clutter) and the target. Equation 6.1 gives the formulation of the recorded / measured electric field signal by a probe.

$$E_{Total}(t) = E_{INC}(t) + E_{REF}(t) \quad (6.1)$$

The probes recorded signal, as well as the excitation signal, were loaded into Matlab for post-processing, in order to extract the range profile of each probe. Further processing using an image algorithm was applied to the extracted range profiles in order to create meaningful image maps of the simulated radar scenario under consideration.

6.2 Simulation Results

The effectiveness of the GFMCW technique compared to the normal FMCW signal approach is shown in the form of radar energy map of the numerical simulations of realistic radar scenarios, such as: through-the-wall radar, ground penetrating radar, medical imaging radar. Issues regarding the selection of the appropriate gating sequence and its defined parameters for a particular scenario under consideration are also described. The radar image / energy map results presented in this section were obtained through the post-processing of the range profiles using the previously described "*Delay-and-Sum*" image algorithm (see: Chapter 2).

6.2.1 Through-the-Wall Imaging Radar Simulation

The scenarios simulated in this section are three dimensions with the walls, target made of different material and electrical properties. In the scenarios the target is in the form of human phantom placed inside the room. For simulation speed the phantom is modelled as a uniform material of electrical properties (permittivity of 36) similar to that of the reported human's skin [9-11].

The pre-windowed normal FMCW excitation signal is in the frequency range of 0.7-2.5 GHz. The transmitter (Tx) is modelled as a plane wave and it is placed 60 cm from the wall, whereas the receiver (Rx) is a linear array of 19 E-field probes with 10 cm spacing between inter-element and positioned 45 cm from the wall.

The work presented in this section differs from the early work reported in references [12, 13] and in the thesis [14], by:

- Crosstalk suppression: In the simulation presented here it is shown that the GFMCW signal can be designed to suppress both the wall reflections and the direct crosstalk or incident signal between the Tx and the Rx. This is relevant as antenna crosstalk signals can be much stronger than the target response therefore overshadowing it in the radar image. In the early work the incident signal $E_{INC}(t)$ in Equation (6.1), which represents the antennas crosstalk, was removed from the total received field ($E_{Total}(t)$) through subtraction of two different simulations, one with the wanted scenario (i.e. room with target(s) and clutter) present and the other an empty scenario. Although, the subtraction removes the antenna crosstalk it is impractical, as it would require having antenna calibration waveforms for a combination of gating sequence parameters.

- Realistic Scenario: A more realistic through-the-wall scenarios are presented here. For example: glass window, wood door and furniture are added into the room to provide a cluttered scenario (similar to an office or home environment); moreover an insulated wall similar to what can be found in most houses or buildings in the UK are simulated.

Scenario – A: Normal Room

Figure 6.1 shows the top and perspective view of the normal room scenario. The room dimension are 325 x 325 x 200 cm^3 with a 20 cm thick solid wall made of uniform brick material with permittivity of 3.8 similar to the values reported in [15, 16]. The floor and ceiling are made of the same material (i.e. concrete) with permittivity of 4.8 and the door and window are made of wood and Pyrex glass with permittivity of 2.25 and 4.8, respectively. The target, a human phantom, is placed 130 cm from the front wall.

The excitation signal (normal FMCW signal) used in this simulation has a 2.5 µs duration. For simplicity the maximum distance to be covered is assumed to be 4 m. In order to satisfy the anti- aliasing condition set by equation (4.46), the chosen gating sequence duration (for GFMCW cases) should not be greater than 13.02 ns. In other words for "*N*" bit sequence the maximum bit duration (T_b) that can be used without causing aliasing is 13.02/N ns.

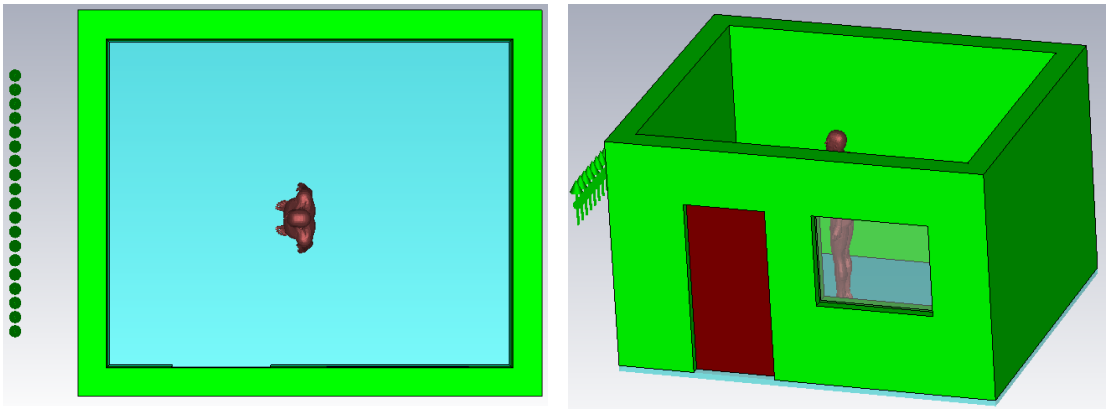

(a) (b)

Figure 6.1: Scenario – A: Normal room, (a) top view; (b) perspective view

Figure 6.2 shows the normalised range delay profiles (seen by the centre receiver probe) for a normal FMCW signal (*No Gating*) and for different GFMCW cases with sequences such as: square wave sequence (*SQ wave*) and 3-bit m-sequence (*3-Bit Mseq and 3-Bit Mseq+*) respectively. The profiles are normalised with respect to the peak / maximum of FMCW profile. It can be seen from the figure that for the normal FMCW case, the reflections from the walls (front and back) as well as the direct crosstalk are much stronger than the desired target reflections which is -30.2 dB below the peak of the unwanted crosstalk reflection.

By carefully designing the parameters (bit duration and off-time delays) of the gating sequence the unwanted reflection can be suppressed while enhancing that of the target. Parameters of the used gating sequence in this scenario are given in Table 6.1. As expected, due to the on and off of the gating sequence apart from the suppression, further power loss occurs which depends on the sequence duration and the receiver off-time. This loss can be seen in Figure 6.2 where the target peak level is at -30.2 dB for the normal FMCW case compared to -43.1 dB, -40.9 dB, and -48.2 dB for the GFMCW cases with gating sequence SQ wave, 3-Bit Mseq, and 3-Bit Mseq+ respectively.

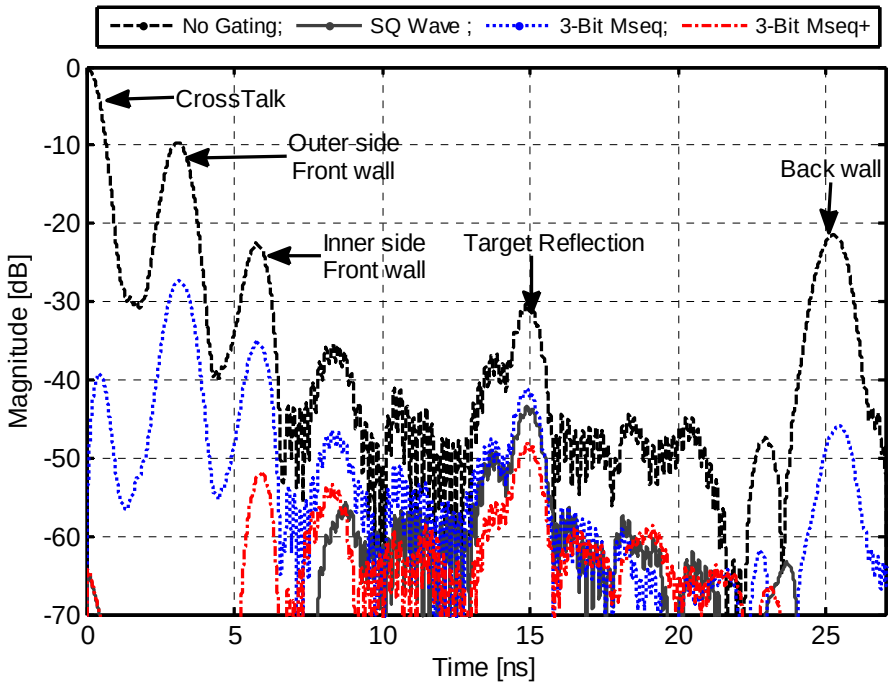

Figure 6.2: Normalised range profiles seen by the centre probe for FMCW and GFMCW cases

Table 6.1: Gating Sequence parameters and its power loss values

Gating Sequence	**T_b**	**τ_1**	**τ_2**	**Power Loss X_G**
SQ Wave	12 ns	0 ns	6.5 ns	12.8 dB
3-Bit Mseq	8 ns	0 ns	0 ns	9.5 dB
3-Bit Mseq+	8 ns	0 ns	5 ns	18.0 dB

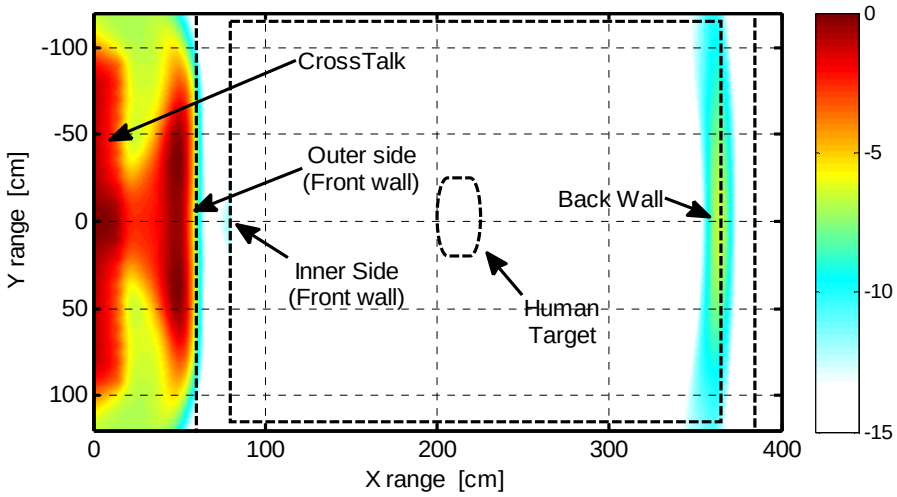

Figure 6.3: Scenario-A radar image for FMCW (*No Gating*) case

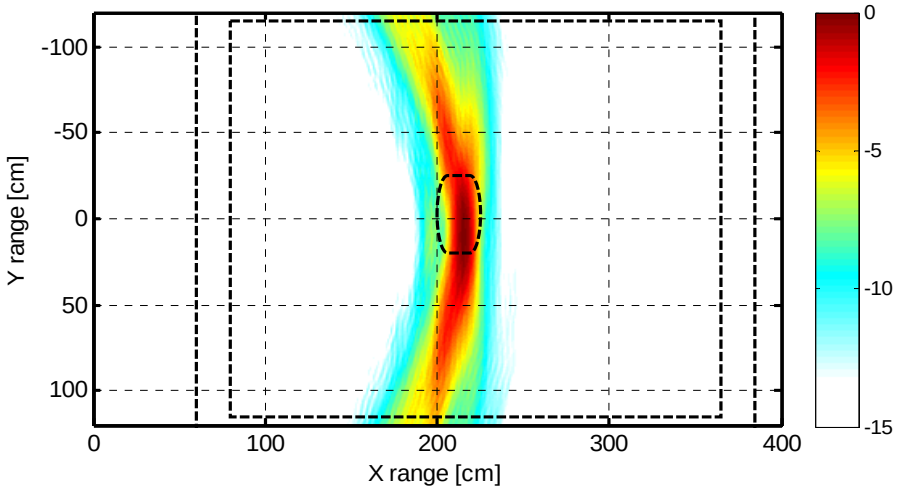

(a)

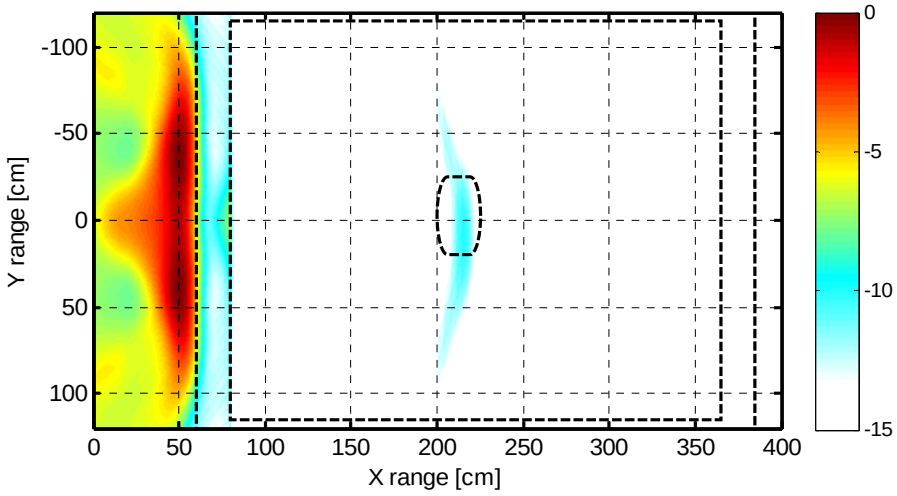

(b)

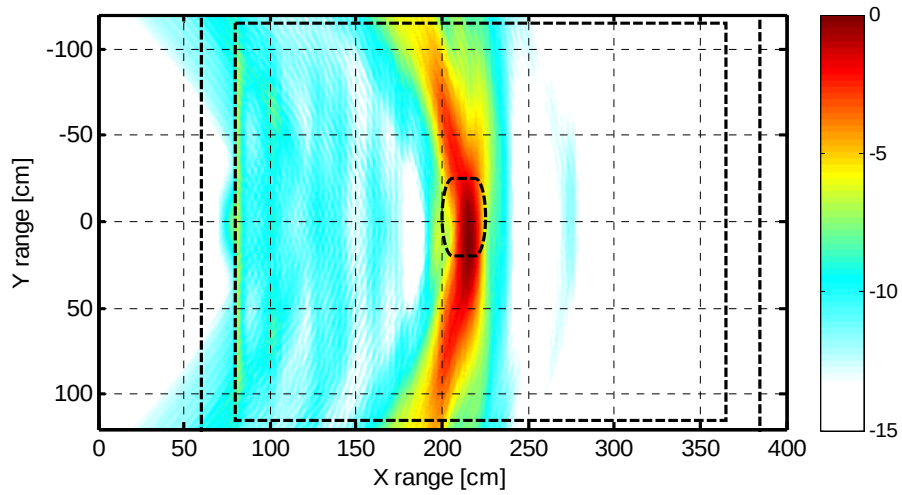

(c)

Figure 6.4: Scenario – A radar image for GFMCW cases, (a) SQ wave; (b) 3-Bit Mseq; and (c) 3-Bit Mseq+

Figures 6.3 and 6.4 (a)-(c) show the obtained normalised radar images for the normal FMCW and Gated FMCW cases respectively. It can be seem from the FMCW case the crosstalk and front wall reflections are the strongest in the image, with the target reflections being totally obscured by the unwanted early reflections. Although the back wall is much farther from the probe compared to the target its reflections can also be seen in the image. As observed in the "*No Gating*" profile in Figure 6.2 the round-trip time from the probe to the target appears at approximately 15 ns and the unwanted wall reflections appear before the 6.5 ns and at roughly 25 ns (for the back wall). The parameters of the gating sequence were chosen such that the sequence MRP blind range coincided with the unwanted reflections, while providing a flat area of the MRP to cover the expected target delay so that target reflections are not attenuated.

In Figure 6.4 (a, c) the target is clearly detected while the crosstalk and (front and back) wall reflections seem to have been suppressed. In Figure 6.4 (b) the front wall reflections are still stronger compared to the target, although the crosstalk and back wall have been suppressed. The reason for this is that the crosstalk and the back wall reflections fall into the deep or blind range of the MRP of the 3-Bit Mseq sequence but the front wall reflection on the other hand falls onto the MRP slope which in this case is not attenuating enough to enhance the target. By extending the blind range (by using the sequence delays) as is the case for the 3-Bit Mseq+

sequence the front wall reflections are further suppressed making the target more distinguishable, as shown in Figure 6.4 (c).

Scenario – B: Room with Furniture

Figure 6.5 shows the top and perspective view of the scenario in question. The room dimension is 375 cm x 280 cm x 200cm and is made of brick of 15 cm thickness. The material property of the human phantom, brick, glass window and the wooden door are the same as the previous scenario. The human phantom in the upright position is placed at approximately 160 cm from the wall. Additionally, the wooden furniture (table, chairs and book shelf) are placed in the room together with a metallic plate to provide a more realistic environment. The FMCW excitation signal in this case is of 4 µs duration.

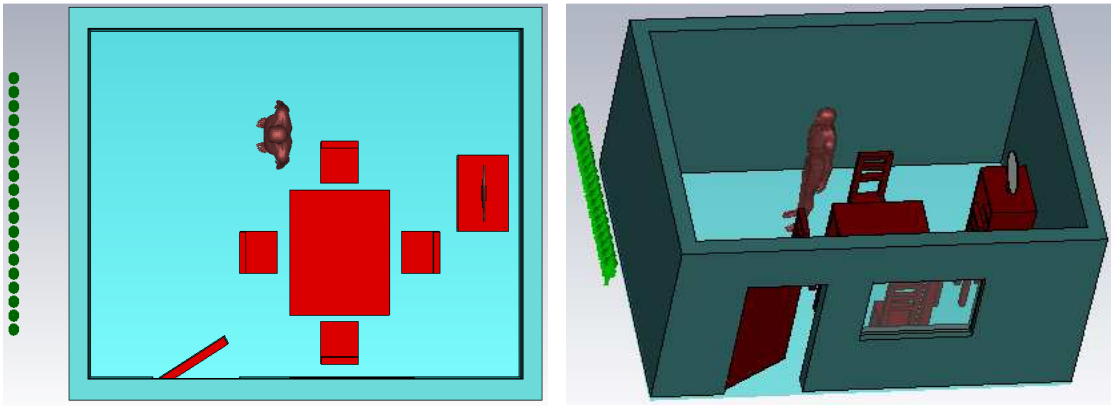

(a) (b)

Figure 6.5: Scenario – B: Room with furniture, (a) top view; (b) perspective view

It can be observed from the radar profile of the 12th probe (see Figure 6.6) that for the FMCW case the target reflection that appears at 15 ns time delay is weaker compared to the unwanted early and late reflections. As expected the radar image for the FMCW case shows a stronger energy level at the position of the crosstalk and wall, the target and metallic plate responses are both obscured by those unwanted reflections, as shown in Figure 6.7.

In order to suppress the wall and crosstalk reflections, a 3-bit m-sequence (*3-Bit Mseq*) with bit duration T_b = 9.25 ns and delays τ_1 = 0 ns, and τ_2 = 6 ns was used to suppress the first 6 ns of the range profile which falls on the first null of the MRP and also the back wall is removed as it falls on the MRP second null. Radar images

of the GFMCW signal with the "*3-Bit Mseq*" sequence (*displayed in Figure 6.8*) shows indeed that the crosstalk and wall reflection energy have been suppressed.

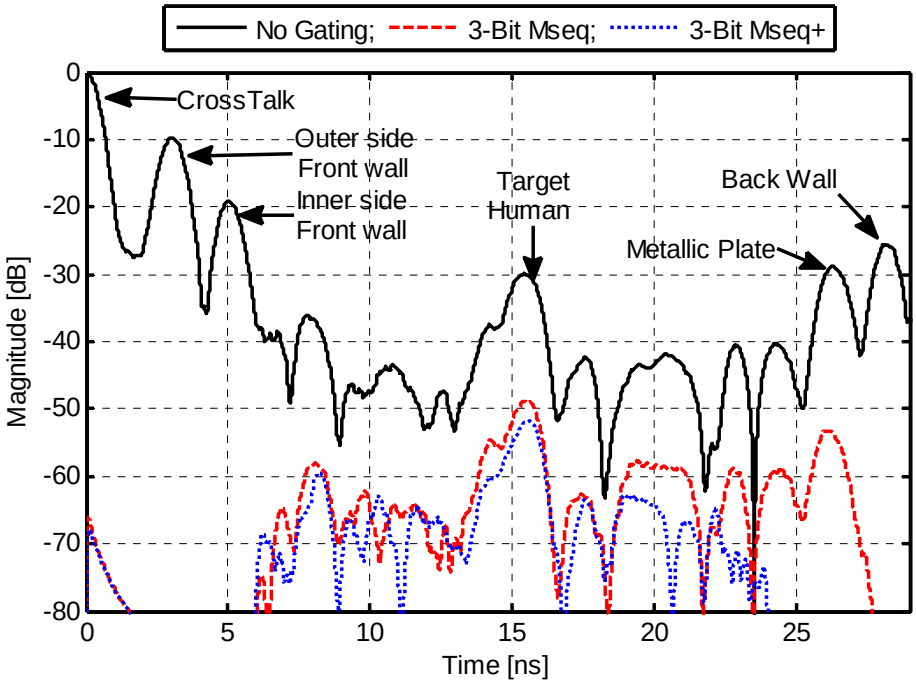

Figure 6.6: Normalised range profiles seen by the 12th probe for FMCW and GFMCW cases

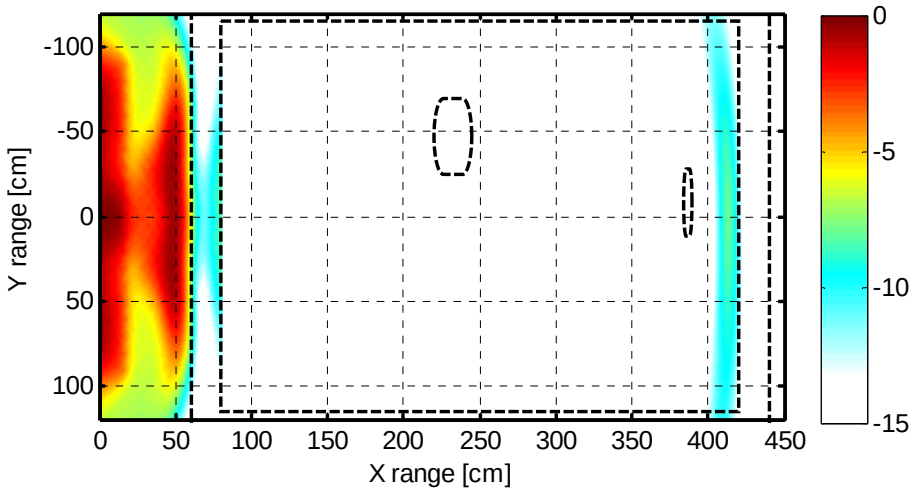

Figure 6.7: Scenario – B radar image for the FMCW (*No Gating*) case

An interesting fact of this image is that it also shows the detection of the metallic plate. Consequently, in a cluttered environment mostly the presence of strong energy maps inside the area of interest may not necessarily mean a presence of a human as the reflected energy of a metallic object or a strong reflector may be significant in the image. In [12, 13] it was showed that apart from the energy map,

Doppler processing can be used to extract features such as human movement or breathing [14]. This enables to differentiate humans from other static strong reflector objects (such as the metallic plate) in this case inside the room.

By decreasing the bit duration of the 3-bit m-sequence (T_b = 8 ns) while maintaining the delay values unchanged the metal plate's return energy is suppressed by the second null of the sequence MRP, as observed in the profile (*3-Bit Mseq+*) in Figure 6.6 and in the radar image displayed in Figure 6.8 (b).

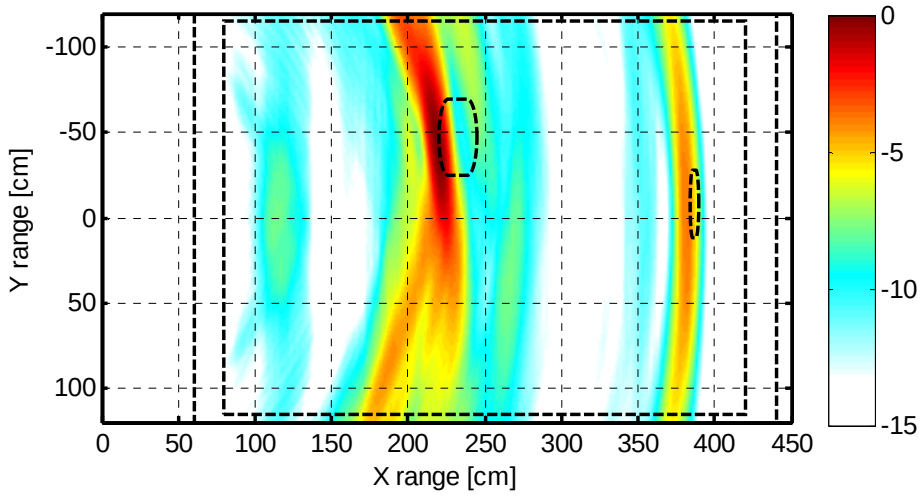

(a)

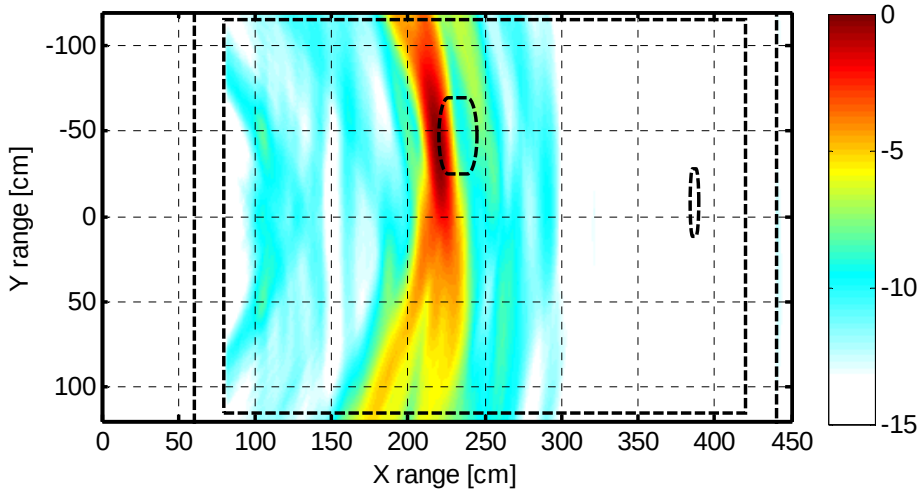

(b)

Figure 6.8: Scenario – B: Radar image for the GFMCW cases, (a) 3-Bit Mseq; (b) 3-Bit Mseq+

Scenario – C: Room with Cavity Wall Insulation

In most residential homes in the UK the external walls are mostly built out of two masonry walls with a gap or cavity [17]. For heating purposes the cavity between the walls are often filled with insulating material.

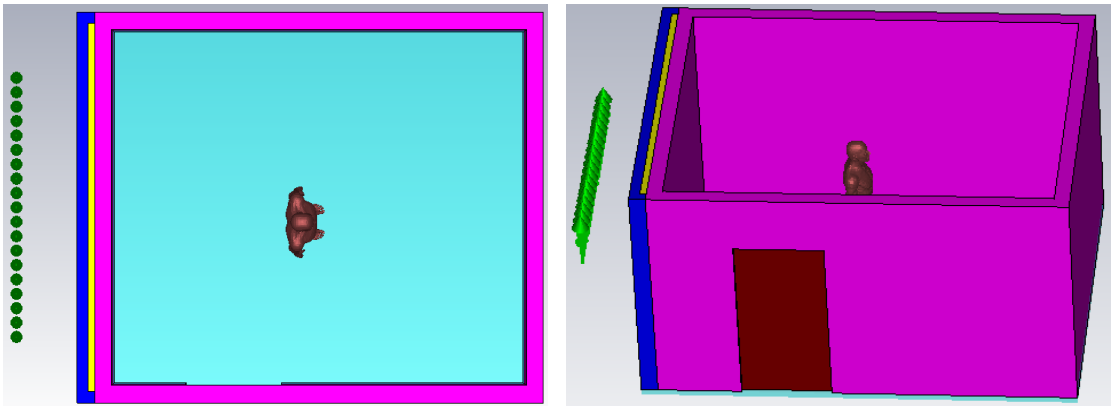

(a) (b)

Figure 6.9: Scenario – C: room with insulated cavity wall, (a) top view; (b) perspective view

Figure 6.9 shows the top and perspective view of the scenario in question. The room's dimensions are 338 cm x 270 cm x 200 cm with the external wall (in blue) made of 8 cm thick brick of permittivity value of 6, whereas the 5 cm cavity (in yellow) is filled with polystyrene insulating material with permittivity value of 2.6, and the internal wall (in purple) is made of 12 cm concrete block of permittivity 5.5. The wooden door, the floor and the human phantom permittivity values are the same as those used in scenario – A. The FMCW excitation signal is of 4 µs duration.

Figure 6.10 shows the normalised radar profiles seen by the centre probe. As expected the crosstalk and wall reflections are stronger than that of the target. Figure 6.11 shows the radar image for the case of the FMCW signal where no gating sequence is used. It can be seen that the target energy is overshadowed by the crosstalk and the (front and back) walls reflections.

GFMCW have been used in this scenario to suppress the unwanted crosstalk and wall reflections, Figures 6.12 (a)-(b) shows the radar image for sequences: SQ wave gating sequence, with parameter T_b = 14 ns, τ_1 = 2 ns, and τ_2 = 7 ns, and 3-bit m-sequence, with parameter T_b = 9 ns, τ_1 = 2 ns, and τ_2 = 7.5 ns, respectively. It can be seen from these figures that the target is clearly visible.

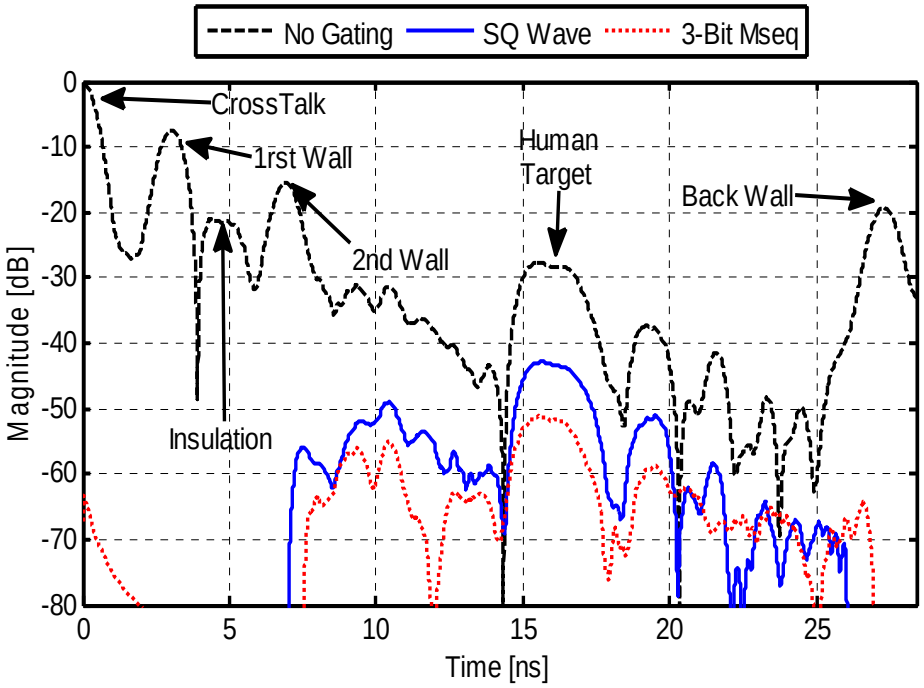

Figure 6.10: Normalised range profile seen by the centre probe for the FMCW and GFMCW cases

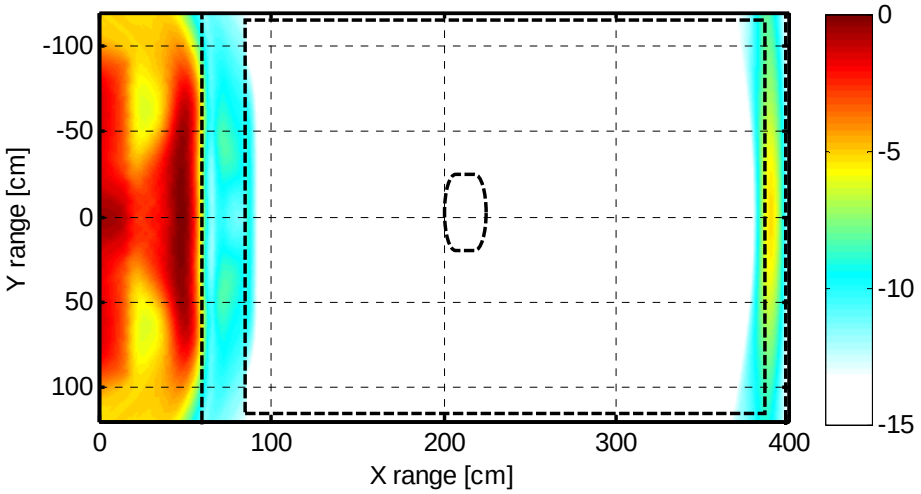

Figure 6.11: Scenario – C radar image for the FMCW (No gating) case

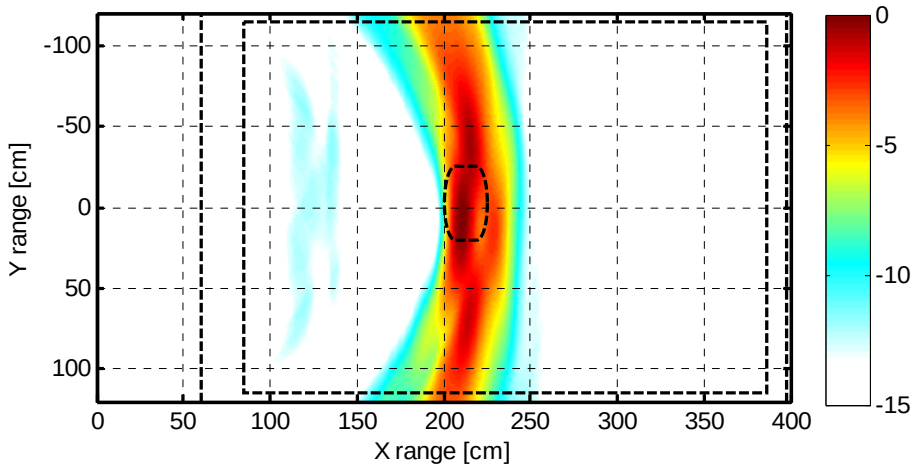

(a)

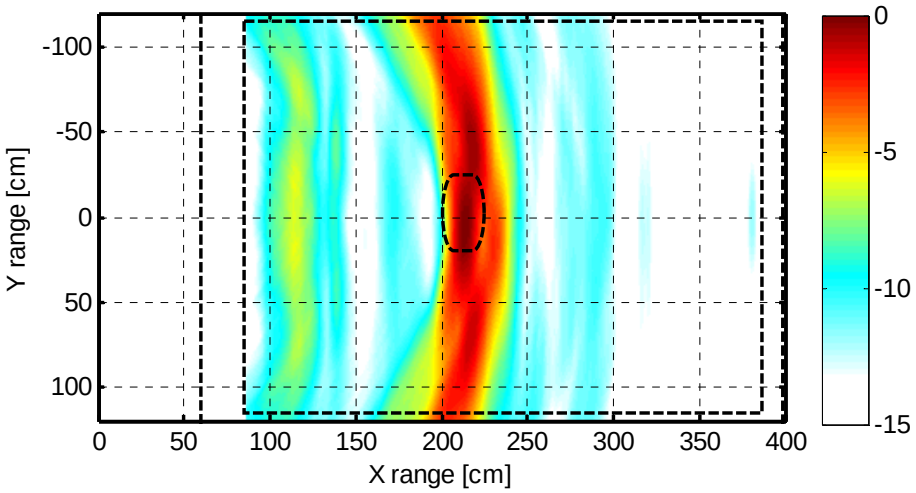

(b)

Figure 6.12: Scenario – C radar image for the GFMCW cases, (a) SQ wave, (b) 3-Bit Mseq

6.2.2 Ground Penetrating Radar Simulation

In this section the use of GFMCW signal to suppress antenna crosstalk and early air-ground reflections will be analysed. The FMCW excitation signal used in the simulations presented in this section has a frequency range of 0.5-3.0 GHz. For simplicity only metallic target(s), modelled as PEC cylinder, are considered in the simulations to mimic landmines or metallic pipes. As in the previous section the transmitter is modelled as a plane wave while the receiver is a linear array of 21 E-field probes with 5 cm inter-element spacing.

Scenario – D: GPR on Uniform Soil

Figure 6.13 shows the view of the GPR simulation scenario with three metallic targets buried at a depth of 12 cm, 25 cm, and 40 cm respectively. The soil is made of smooth surfaces with homogenous material of permittivity value of 7. The receiver array was placed 35 cm above the ground surface and the transmitter excitation signal (FMCW) was of 2 µs duration.

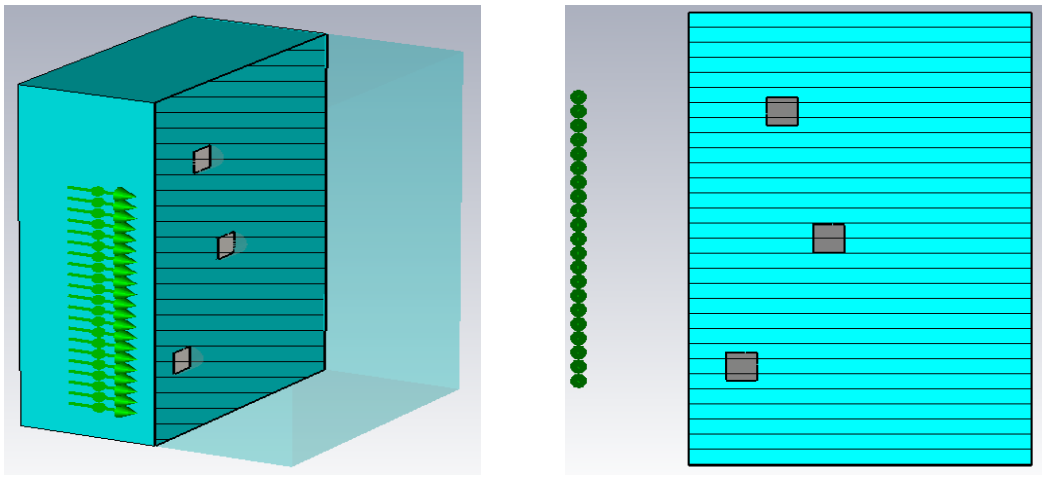

(a) (b)

Figure 6.13: Scenario – D uniform soil with 3 targets, (a) perspective view; (b) cut through the z-plane

Figure 6.14 shows that the crosstalk and air-ground interface reflections overshadows or masks the reflected energy from the target when an FMCW signal is used. By gating those undesirable early reflections, using the GFMCW, the target

detection can be enhanced as shown in Figure 6.15, for the case of 3-bit m-sequence with parameters T_b = 4.2 ns, τ_1 = 0 ns, and τ_2 = 3.2 ns.

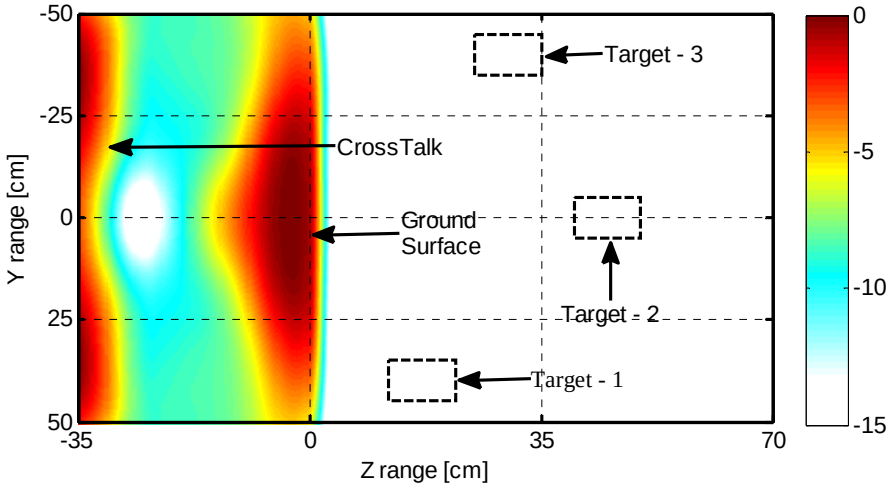

Figure 6.14: Scenario – D radar image for FMCW (*No Gating*) case

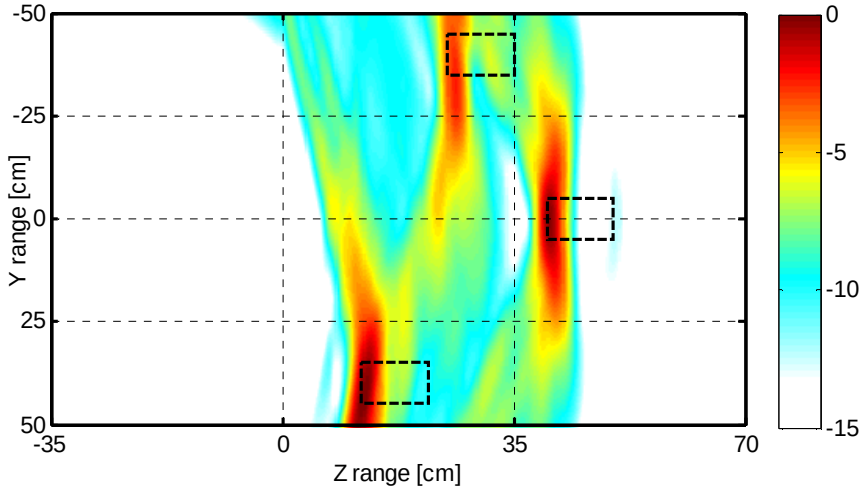

Figure 6.15: Scenario – D radar image for GFMCW case

Scenario – E: GPR in Multilayer Ground

Figure 6.16 shows the view of the simulated multilayer ground scenario. The ground is made of 8 cm thick concrete pavement, of 5.5 permittivity (as given by CST for the year old concrete), followed by a layer of dry soil of 2.53 permittivity. Two targets at a depth of 25 cm and 40 cm respectively have been included in the model. The receiver probes were placed 22 cm above the pavement and the transmitter plane wave was excited with the pre-windowed FMCW signal of 0.5 µs duration.

As expected for the FMCW case the crosstalk and pavement reflection overshadows the target return, as shown in the energy in Figure 6.17. By gating the FMCW signal, with a square wave sequence with parameters T_b = 4.5 ns, τ_1 = 0 ns, and τ_2 = 3.2 ns, the early unwanted return is suppressed while enhancing the return signal from the deep targets as seen in Figure 6.18.

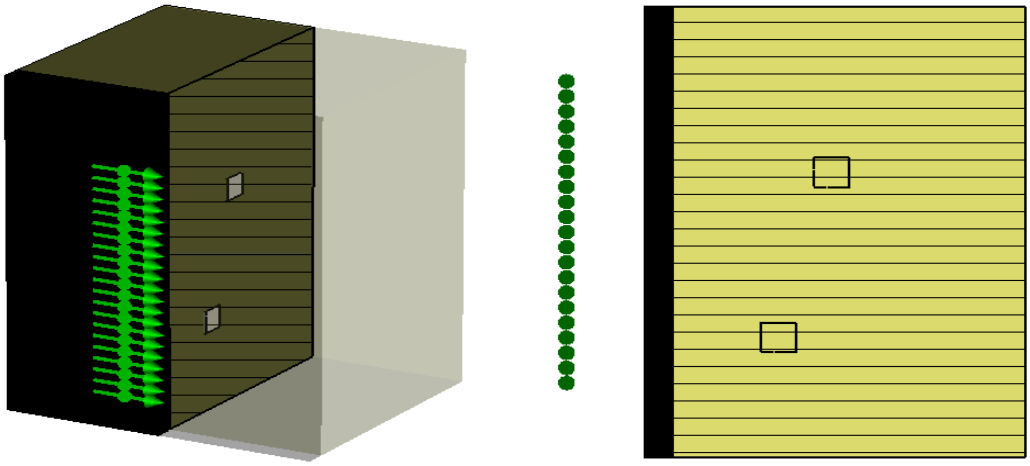

(a) (b)

Figure 6.16: Scenario – E Multilayer ground with 2 targets, (a) perspective view; (b) cut through the z-plane

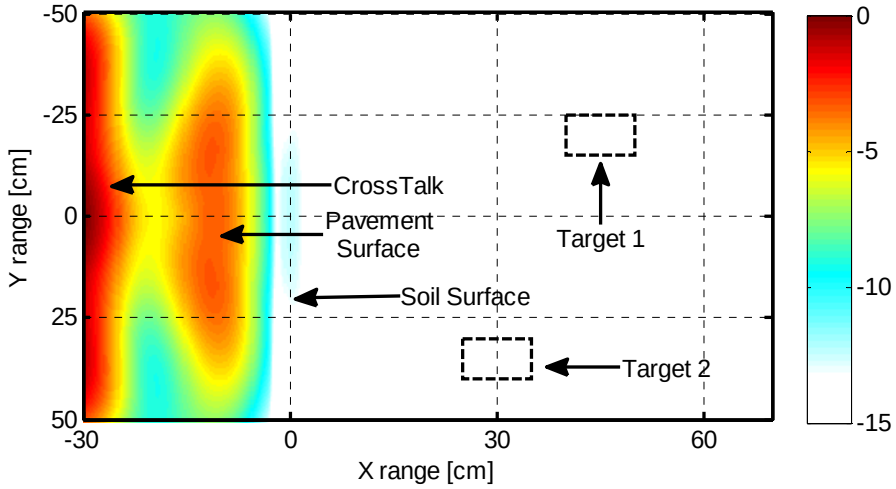

Figure 6.17: Scenario – E radar image for FMCW (*No Gating*) case

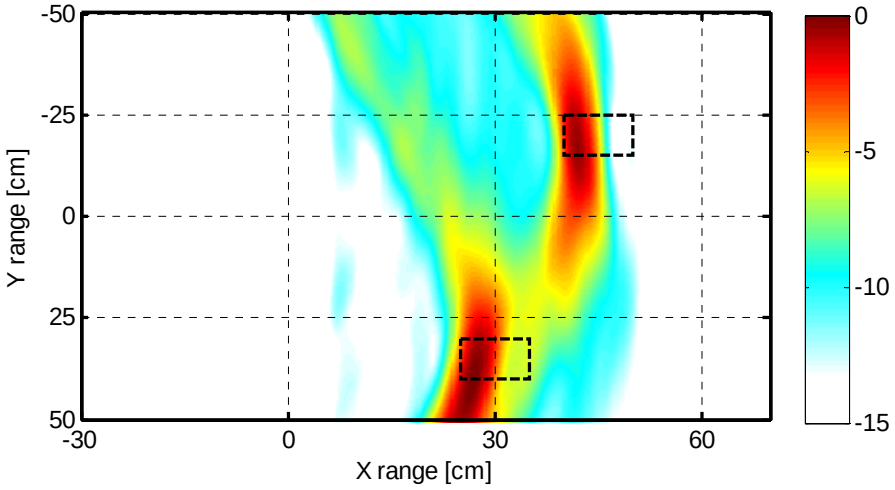

Figure 6.18: Scenario – E radar image for GFMCW case

Scenario – F: GPR on Inhomogeneous Ground

Figure 6.19 shows the perspective and z-plane cut view of the scenario set up. The ground is made of dry soil with permittivity value of 2.53. Materials of irregular shapes and of different permittivity were added into the soil to create inhomogeneity.

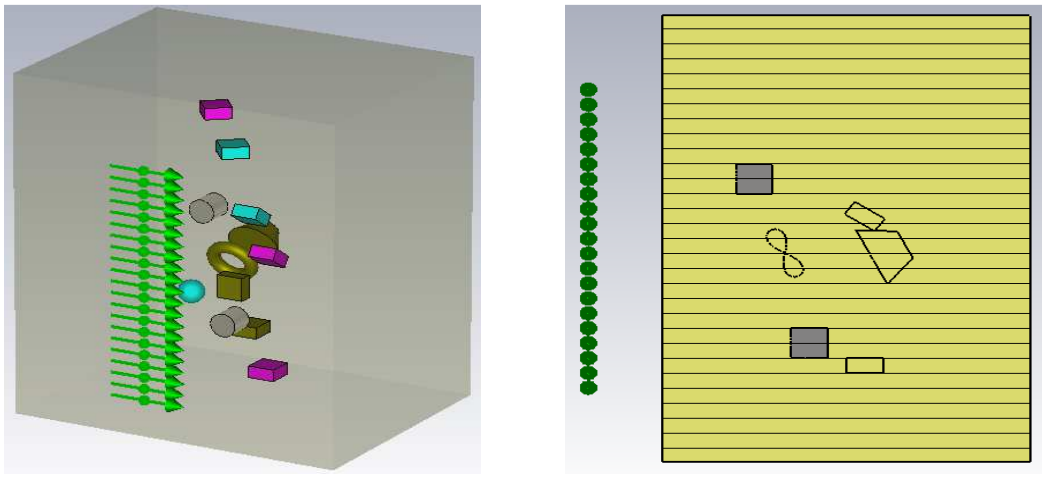

(a) (b)

Figure 6.19: Scenario – F Inhomogeneous ground with 2 targets, (a) perspective view; (b) cut through the z-plane

The dielectric parameters of these materials, based on their colour in Figure 6.21 (a), are: 4.55 (light blue), 8 (purple), and 17.5 (gold). The metallic targets placed 20 cm and 35 cm deep respectively, represented with silver colour, are

modelled as PEC. The receiver probes are placed 20 cm from the surface and the duration of the excitation signal was set to 0.5 µs.

Figure 6.20 shows the obtained radar image for the FMCW case, where it can be seen that the crosstalk and surface ground reflections are stronger than that of the target. Target – 1 is still visible in this case while Target – 2 is clearly overshadowed (cannot be detected). By using GFMCW both targets can be detected in Figure 6.21 while the unwanted reflections are suppressed. The parameter of the gating sequence used in the GFMCW simulation is 3-bit m-sequence with T_b = 3 ns, τ_1 = 0 ns, and τ_2 = 2 ns.

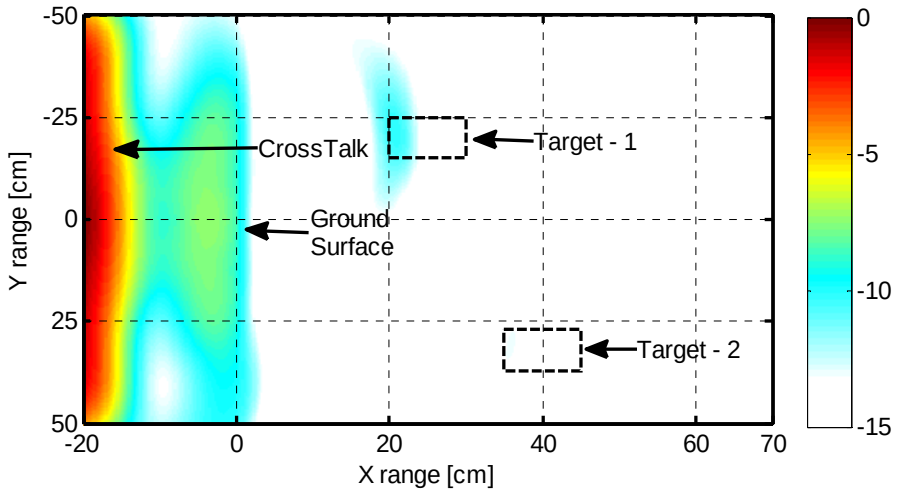

Figure 6.20: Scenario – F radar image for FMCW (*No Gating*) case

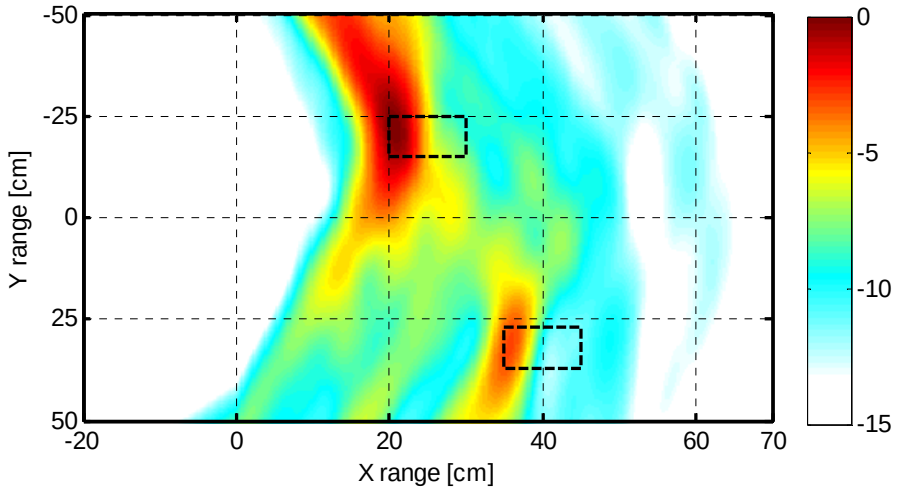

Figure 6.21: Scenario – F radar image for GFMCW case

6.2.3 Medical Imaging Radar Simulation

Medical imaging radar systems have gained a great deal of interest within the research community especially in issues of detection of breast cancer [18-20], brain haemorrhage [21, 22], and water accumulation in human body (i.e. urine in the bladder or water in the lungs) [23, 24]. In this section the results of the application of GFMWC signal for the suppression of crosstalk and early skin reflection in breast cancer detection scenario will be presented. The author believes that this suppression technique can be applied to the other MIR scenarios.

The adopted 3-D breast model assumes a planar configuration, representing a patient in supine position with the antennas scanning over the top of the flattened breast. Similar models have been used in references [20, 25-27]. For simulation simplicity the breast phantom is immersed in a medium with the same electrical properties as that of the normal tissue (fat) with permittivity of 9. The transmitter as before is modelled as plane wave while the receiver is modelled as a linear array of 21 E-field probes with an inter-element gap of 5 mm and spaced 10 mm from the 3 mm thick skin. In the simulations the pre-windowed FMCW excitation signal has a duration of 2.0 μs with a frequency range 0.5-5.0 GHz.

Scenario – G: Homogeneous Breast Model

Figure 6.22 shows the two layers of fat and skin of the modelled homogenous breast with cancer tumour included. The target / tumour was placed 75 mm from the skin and it was modelled as a cube of water of dimension 10 mm x 15 mm x 20 mm and relative permittivity value of 78. While the 3 mm thick skin was given a value of 36, similar values of thickness and permittivity for the skin were found in references [9, 11, 28, 29].

Figure 6.23 shows an energy map for the case of FMCW waveform. As expected, the crosstalk and skin reflections dominate and overshadow that of the tumour. The skin reflections are not differentiated from the crosstalk in the image because of the closer proximity of the probes from the skin (10 mm). This distance is much smaller than the range resolution. By using a gating sequence for the GFMCW case the unwanted reflections can be suppressed which enables the detection of deep tumour, as shown in Figure 6.24 for the gating 3-bit m-sequence with T_b = 1.5 ns, τ_1 = 0 ns, and τ_2 = 1 ns.

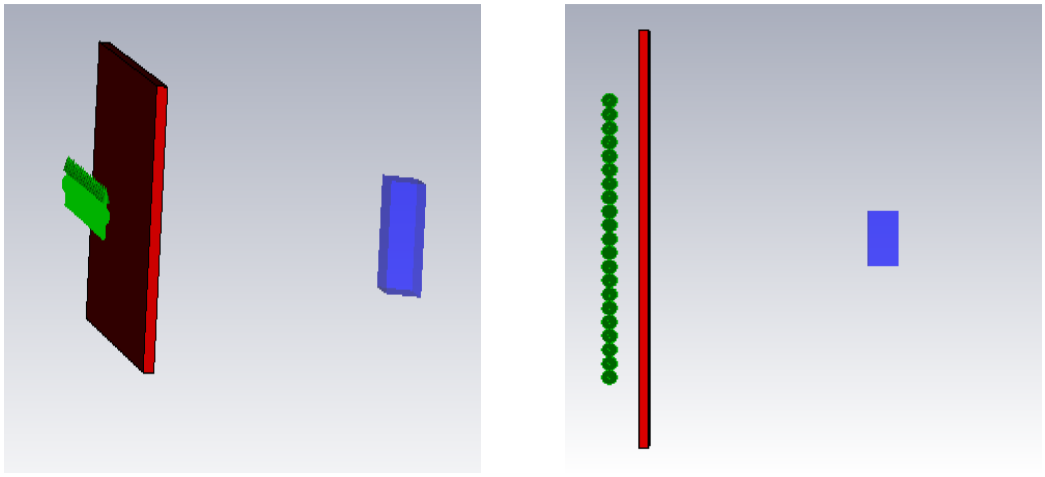

(a) (b)

Figure 6.22: Scenario – G Homogeneous breast, (a) perspective view; (b) top view

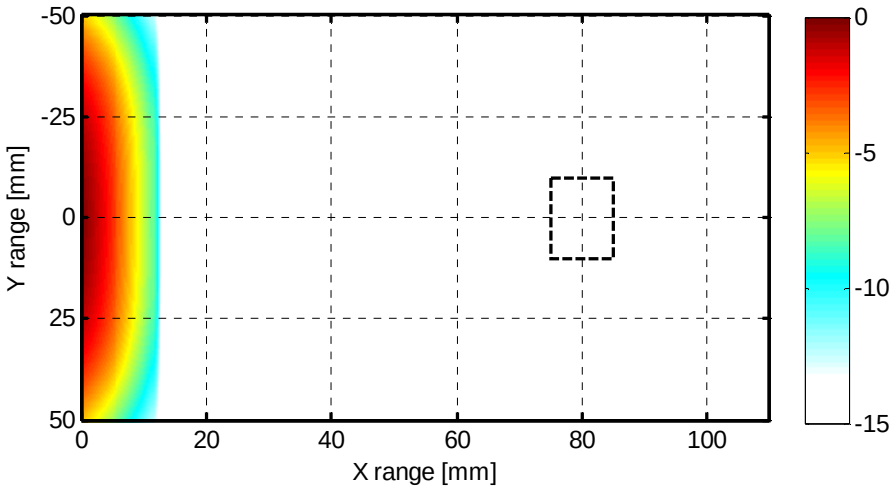

Figure 6.23: Scenario – G radar image for FMCW (*No Gating*) case

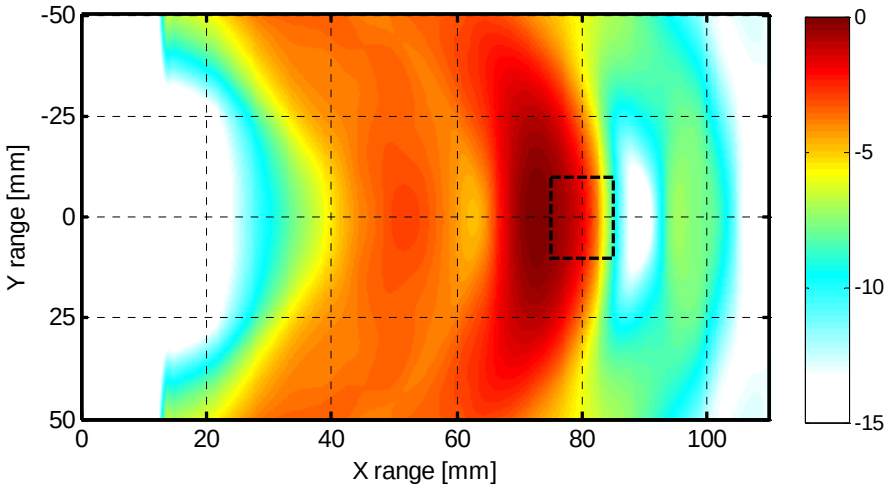

Figure 6.24: Scenario – G radar image for GFMCW case

Scenario – H: Heterogeneous Breast Model

Breast heterogeneity was created by adding tissues of different shape and dielectric into the homogeneous model. The skin is 3 mm thick but with permittivity of 31, whereas the tumour position, size and permittivity are the same as in the previous scenario. The permittivity of the added clutter / tissues, based on the colour in Figure 6.25, is 31 (yellow), 20 (magenta), 12 (blue), and 2.8 (green). The normal tissue or fat and surrounding material have a permittivity equal to 9.

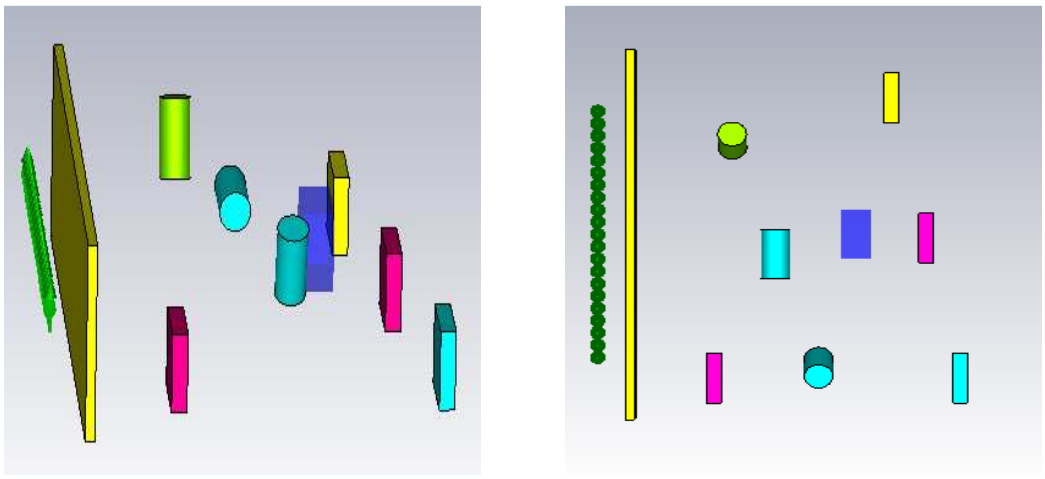

(a) (b)

Figure 6.25: Scenario – H Heterogeneous breast, (a) perspective view; (b) top view

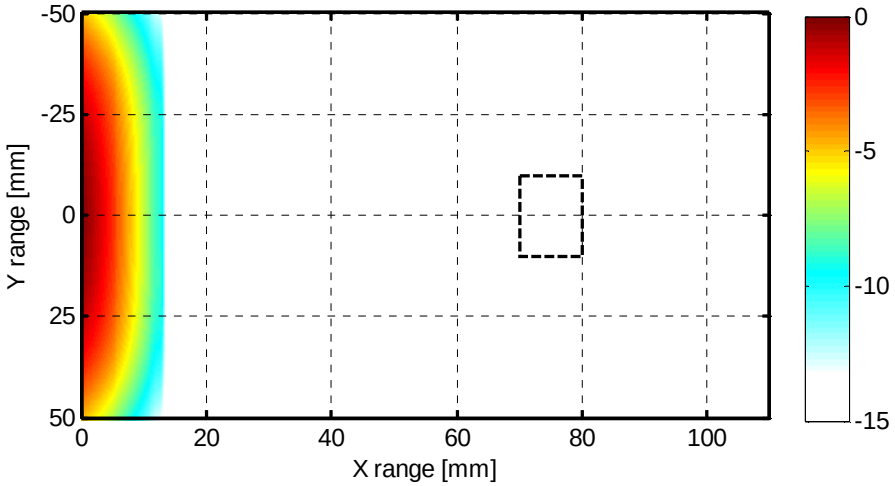

Figure 6.26: Scenario – H radar image for FMCW (*No Gating*) case

Figure 6.26 shows the radar image for the case of FMCW signal. As can be seen the crosstalk and skin reflections obscure the reflections from the tissues inside the breast including the tumour. By applying the GFMCW signal the early

reflections (crosstalk and skin) were removed (as displayed in Figure 6.27) using a 7-bit m-sequence with parameters T_b = 1.5 ns, τ_1 = 0 ns, and τ_2 = 0.9 ns. Although the target is visible in the figure, clutter reflections can also be seen. This in practical terms may lead to false-positive diagnosis as the information of the tumour position is unknown beforehand. In order to further minimise / remove the clutter within the area of interest further post-processing steps can be applied.

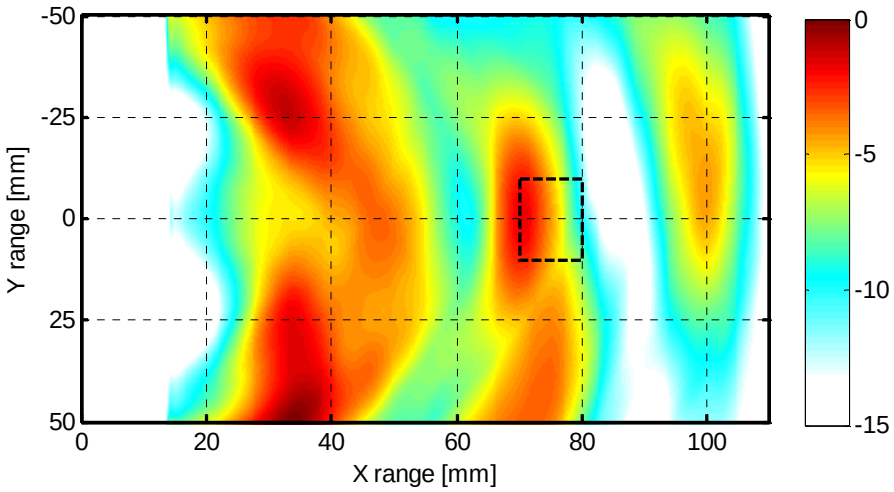

Figure 6.27: Scenario – H radar image for GFMCW case

6.3 Summary

In this chapter numerical radar simulations were presented using the commercial electromagnetic solver, "CST Microwave Studio" for both FMCW and GFMCW waveforms. The radar systems have been tested on realistic models of room environments for through-the-wall radar, soil for ground penetration radar, and breast for medical imaging radar.

The CST simulation results have been processed using the Delay-and-Sum algorithm to create an energy map of the scenario under test. It has been shown that for the FMCW cases the unwanted early reflections such as: wall, ground surface, and skin combined with that of the antenna crosstalk largely overshadows the wanted target return signal. By selecting a suitable gating sequence (GFMCW cases) the target return can be enhanced while suppressing the unwanted early clutter return signal.

CST discretizes the scenario under test into small cells "known as mesh cell". Table 6.2 gives a summary of the radar simulations, the excitation duration, the number of mesh cells, and overall time taken by CST to complete the simulation.

Table 6.2: Summary of the Radar Simulations

Scenario	**Radar System**	**FMCW Duration [µs]**	**Mesh Cell [Millions]**	**Simulation Time [hours]**
Scenario – A	TTWIR	2.5	175	140
Scenario – B	TTWIR	3	390	562
Scenario – C	TTWIR	3	383	398
Scenario – D	GPR	2	40	58
Scenario – E	GPR	0.5	16	4.5
Scenario – F	GPR	0.5	28	22
Scenario – G	MIR	2	2	6
Scenario – H	MIR	2	2.4	10

6.4 References

[1] M. Celuch-Marcysiak and W. Gwarek, "Comparative study of the time-domain methods for the computer aided analysis of microwave circuits," *International Conference on Computation in Electromagnetics,* pp. 30-34, 1991.

[2] E. Miller, "A selective survey of computational electromagnetics," *IEEE Transactions on Antennas and Propagation,* vol. 36, pp. 1281-1305, 1988.

[3] A. Vasylchenko, Y. Schols, W. De Raedt, and G. Vandenbosch, "Quality Assessment of Computational Techniques and Software Tools for Planar-Antenna Analysis," *IEEE Antennas and Propagation Magazine,* vol. 51, pp. 23-38, 2009.

[4] T. Weiland, M. Timm, and I. Munteanu, "A practical guide to 3-D simulation," *IEEE Microwave Magazine,* vol. 9, pp. 62-75, 2008.

[5] F. Gustrau, *EM Modeling of Antennas and RF Components for Wireless Communication Systems*: Springer-Verlag, 2009.

[6] A. Taflove and S. Hagness, *Computational Electrodynamics: The Finite-Difference Time-Domain Method, Third Edition*: Artech House, 2005.

[7] "CST STUDIO SUITE 2006 - Advance topic", ed. Darmstadt, Germany: CST Computer Simulation Technology, 2005.

[8] J. Bennett and E. Schoessow, "Antenna near-field/far-field transformation using a plane-wave-synthesis technique," *Proceedings of the Institution of Electrical Engineers,*vol. 125, pp. 179-184, 1978.

[9] S. Gabriel, R. Lau, and C. Gabriel, "The dielectric properties of biological tissues: II. Measurements in the frequency range 10 Hz to 20 GHz," *Physics in Medicine and Biology,* vol. 41, pp. 2251-2269, 1996

[10] T. Dogaru, L. Nguyen, and C. Le, "Computer Models of the Human Body Signature for Sensing Through the Wall Radar Applications," *Army Research Laboratory, Adelphi, MD 20783-1197,* 2007.

[11] S. Gabriel, R. Lau, and C. Gabriel, "The dielectric properties of biological tissues: III. Parametric models for the dielectric spectrum of tissues," *Physics in Medicine and Biology,* vol. 41, pp. 2271-2293,1996.

[12] F. Fioranelli, S. Salous, and X. Raimundo, "Frequency-modulated interrupted continuous wave as wall removal technique in through-the-wall imaging," *IEEE Transactions on Geoscience and Remote Sensing,* vol. 52, pp. 6272-6283, 2014.

[13] F. Fioranelli, S. Salous, I. Ndip, and X. Raimundo, "Through the wall detection with gated FMCW signals using optimized patch-like and vivaldi antennas," *IEEE Transactions on Antennas and Propagation,* vol. 63, pp. 1106-1117, 2015.

[14] F. Fioranelli, "Through-the-wall detection using ultra wide band frequency modulated interrupted continuous wave signals," PhD, School of Engineering and Computing Sciences, Durham University, Durham, UK, 2013.

[15] T. Dogaru and C. Le, "SAR Images of Rooms and Buildings Based on FDTD Computer Models," *IEEE Transactions on Geoscience and Remote Sensing,* vol. 47, pp. 1388-1401, 2009.

[16] C. Yang, C. Ko. and B. Wu, "A free space approach for extracting the equivalent dielectric constants of the walls in buildings," *International Symposium Antennas and Propagation,* vol. 2, pp. 1036-1039, 1996.

[17] (13 October 2014). *Insulation*. Available: http://www.planningportal.gov.uk /perm- ission/commonprojects/insulation#CavityWall

[18] S. Aguilar, M. Al-Joumayly, M. Burfeindt, N. Behdad, and S. Hagness, "Multiband miniaturized patch antennas for a compact, shielded microwave breast imaging array," *IEEE Transactions on Antennas and Propagation,* vol. 62, pp. 1221-1231, 2014.

[19] E. Zastrow, S. Davis, and S. Hagness, "Safety assessment of breast cancer detection via ultrawideband microwave radar operating in pulsed-radiation mode," *Microwave and Optical Technology Letters,* vol. 49, pp. 221-225, 2007.

[20] E. Fear, X. Li, S. Hagness, and M. Stuchly, "Confocal microwave Imaging for breast cancer detection: Localization of tumors in three dimensions," *IEEE Transactions on Biomedical Engineering,* vol. 49, pp. 812-822, 2002.

[21] M. Jalilvand, E. Pancera, X. Li, T. Zwick, and W. Wiesbeck, "Hemorrhagic stroke detection via adaptive UWB medical imaging radar," *European Radar Conference*, pp. 317-320, 2011.

[22] D. Ireland, K. Bialkowski, and A. Abbosh, "Microwave imaging for brain stroke detection using Born iterative method," *IET Microwaves, Antennas & Propagation*, vol. 7, pp. 909-915, 2013.

[23] L. Xuyang, M. Jalilvand, L. Zwirello, and T. Zwick, "Array configurations of a UWB near field imaging system for the detection of water accumulation in human body," *European Radar Conference*, pp. 170-173, 2011.

[24] L. Xuyang, M. Jalilvand, L. Zwirello, and T. Zwick, "Synthetic aperture-based UWB imaging system for detection of urine accumulation in human bladder," *IEEE International Conference on Ultra-Wideband*, pp. 351-354, 2011.

[25] H. Lim, N. Nhung, E. Li, and N. Thang, "Confocal microwave imaging for breast cancer detection: delay-multiply-and-sum image reconstruction algorithm," *IEEE Transactions on Biomedical Engineering*,vol. 55, pp. 1697-1704, 2008.

[26] A. Shaheen and K. Quboa, "Pole splitting algorithm for UWB breast cancer imaging," *16th IEEE Mediterranean Electrotechnical Conference*, pp. 417-420, 2012.

[27] A. Abdolali, M. Bazrafshan, and M. Salary, "Effect of tissue compression in ultra wide band (UWB) radar detection of breast cancer," *Biomedical Imaging and Intervention Journal*, vol. 9, 2013.

[28] S. Willson, E. Adam, and A. Tucker, “Patterns of breast skin thickness In normal mammograms,” *Clinical Radiology*, vol. 33, pp. 691-693, 1982.

[29] H. Ulger, N. Erdogan, S. Kumanlioglu, and E. Unur, “Effect of age, breast size, menopausal and hormonal status on mammographic skin thickness,” *Skin Research Technology, vol. 9*, pp. 284-289, 2003.

CHAPTER 7

Radio Imaging Experimental Results

This chapter presents the experimental results of the GFMCW technique in applications such as: through-the-wall radar imaging, ground penetration radar imaging, and medical imaging. The effectiveness of the technique will be given through a comparison of the radar images obtained from normal FMCW and GFMCW waveforms in various realistic scenarios.

The radar experiments presented in this chapter used the AWG and the VNA based radars described in Chapter 5. These were used to demonstrate the effectiveness of the GFMCW waveform in suppressing the undesirable crosstalk and unwanted reflections in TTWRI, GPR and MIR scenarios.

Both radar systems operate in a bistatic configuration (i.e. separated transmitter and receiver antennas) with measurements performed using the "synthetic aperture radar" approach in which, the measurements are taken in pre-defined positions forming a linear or circular array. Radar images are created combining the measurements radar profiles from the pre-defined position using the known "Delay-and-Sum" imaging algorithm. The effectiveness of the GFMCW technique in suppressing strong clutter signals will be given through a comparison of the radar images using the FMCW signal and using the proposed method.

Measurement Methodology

The following methodology is applied before performing GFMCW measurements:

1) *Identify the time delay related to the undesired components*: FMCW signal is initially applied onto the scenario under test in order to identify the time delay and peak power related to the undesired reflections, such as; antennas crosstalk and wall, ground surface, or skin reflection. These reflections are identified by inspecting the radar profiles.
2) *Selecting a suitable gating sequence and its parameters:* Once the undesired reflection(s) absolute time delay(s) "t_r" has been identified from the FMCW profiles, a gating sequence of length "N" bits can be selected to suppress the undesired reflections. The undesired reflection is suppressed by setting the sequence MRS notch to fall onto the time "t_r" related to the undesired reflection. The notches on the gating sequence MRS are periodic of duration "NT_b", therefore for "t_r" to fall onto the "k^{th}" notch of the MRS the bit duration T_b should be selected as in (7.1). If a wider blind range or a steeper slope on the MRS is needed, then sequence delays "τ_1" and "τ_2" can be used.

$$T_b = \frac{t_r}{kN} \tag{7.1}$$

4) *Loading into Euvis and Measurement:* Once the parameters of the gating sequence or GFMCW signal have been defined it is then loaded into the Euvis modules through Matlab. On the completion of the measurement the resultant radar range profile can be used in further processing to create an image of the scenario under test.

The scenario depicted in Figure 7.1 where the metallic target is placed 1.2 m away from the tip of the antennas illustrates the procedure. The Euvis based radar system operates with a bandwidth of 1.5 GHz and chirp duration of 400 µs. From the normalised radar profiles in Figure 7.2 it can be seen that for the FMCW case the undesired signal "antennas crosstalk" is at 25.07 ns, whereas the target response appears at approximately 33.5 ns at -11.5 dB.

Figure 7.1: Metallic target in an open environment

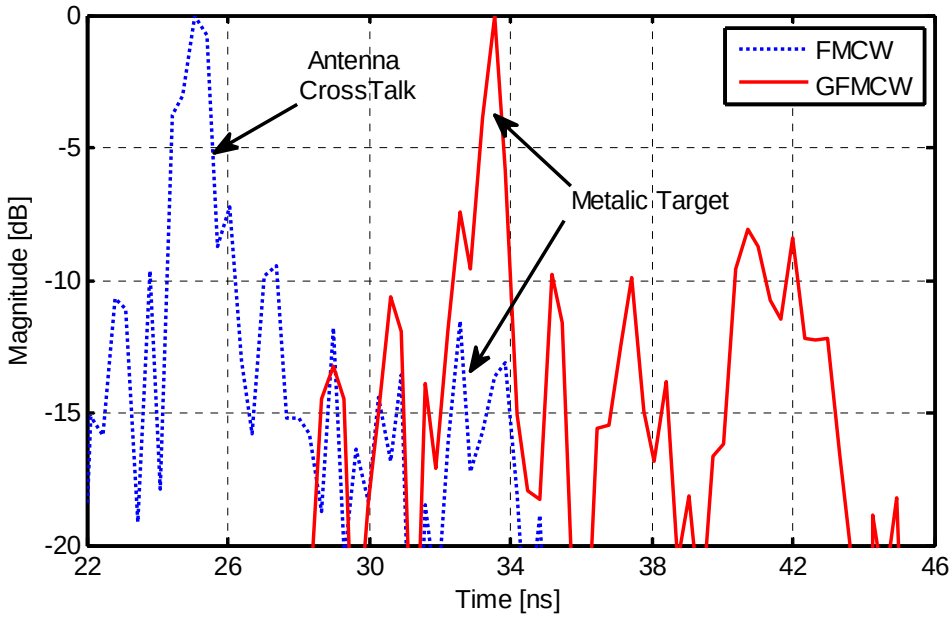

Figure 7.2: Normalised radar profiles for FMCW and GFMCW case

A 3-bit Msequence was used to remove the crosstalk signal while enhancing the target return. The sequence bit duration as given by (7.1) was chosen to provide a range suppression on the second ($k = 2$) notch of the MRP. Therefore the bit duration was set to T_b = 8.375 ns and the delays τ_1 and τ_1 set to 3.5 ns and 3 ns respectively. Figure 7.3 shows two periods of the used gating sequence profile, and Figure 7.4 shows that the 2nd notch of the sequence MRP falls at around 25 ns. The target response at 33.5 ns falls onto the MRP flat part, and therefore suffers no suppression. The normalized radar profile for the GFMCW case is given in Figure 7.2.

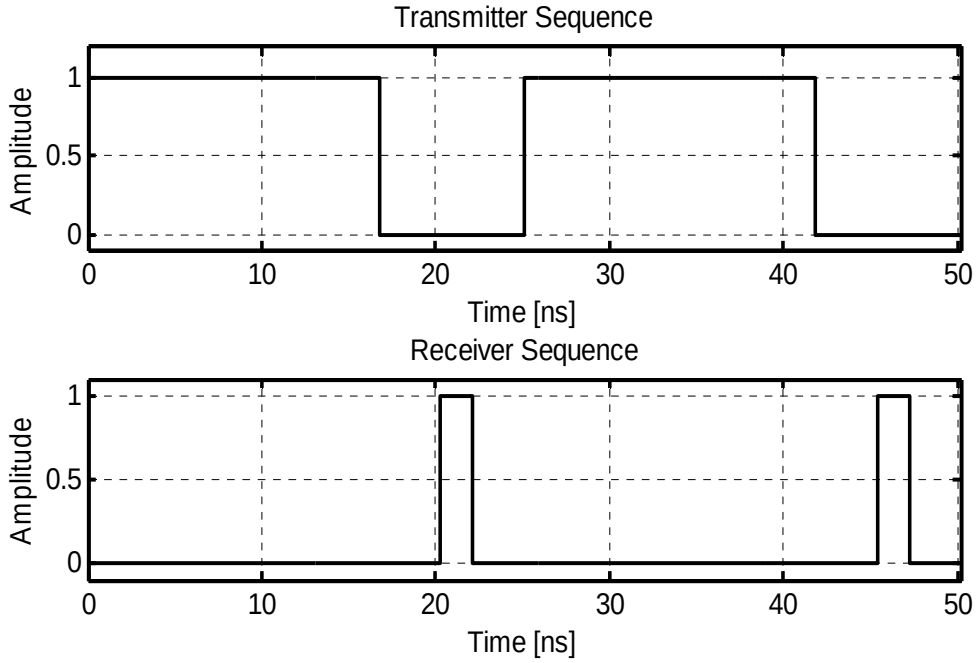

Figure 7.3: Profile of the used 3-bit m-sequence on transmitter and receiver

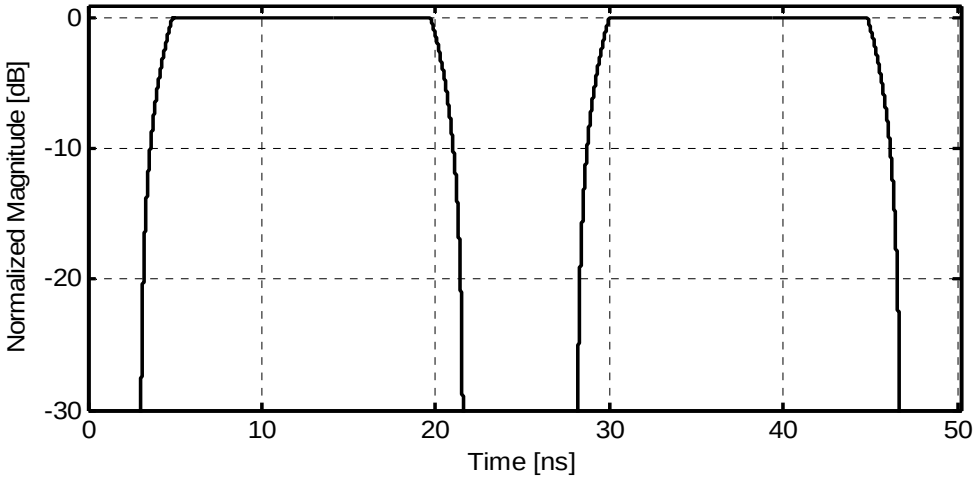

Figure 7.4: MRP of the used 3-bit m-sequence

This example illustrates the measurement methodology applied onto the radar experimental scenarios described in the next sections.

7.1 Through-the-Wall Imaging Radar

This section presents the results of the through-the-wall radar experiments. The focus was on detection of metallic and non-metallic stationary targets within an office like environment of walls made of plywood or concrete blocks. The measurements were performed using the radar system based on AWG. The AWGs were configured to produce FMCW or GFMCW waveforms with a frequency range of 0.7-2.5 GHz and sweep duration of 400 µs, the system ADC was set with a sampling frequency of 20 MHz. Two Vivaldi antennas, operating with a return loss less than -10 dB across the specified band [1], have been used as transmitting and receiving antennas respectively and were separated by 20 cm and moved in a linear trajectory into 6 specified positions of 10 cm interspace. The antennas were placed at the top of the trolley at 110 cm above the ground.

7.1.1 Target Behind Plywood Wall

The walls of the office environment in this scenario are made of plywood panels with air gap or cavity between the inner and outer side of the wall. The overall measured wall thickness is 8 cm and the assumed value for its permittivity is 1.7. As an air gap exists between the plywood panel the wall permittivity was assumed as the mean between the values of air (1) and plywood (2.49) [2, 3].

Figure 7.5: Radar system mounted on a corridor overlooking the Plywood wall

It is worth mentioning that the errors in the estimation of the material (wall) permittivity and thickness may lead to a displacement or blurring of the target energy in the created radar image. However the assumed values permit the target positioning error in the radar image to be within the system settings down-range resolution, which in this case is roughly 8.3 cm (1.8 GHz bandwidth). Figure 7.5 shows the radar system in a corridor with the antennas (placed 2 cm from the plywood wall) orientated towards the scenario under test. The room serves as a meeting place and contains furniture such as tables, chairs and computers.

Scenario – A: Target a Metallic Plate Placed Inside a Bag

Figure 7.6 shows the inside of the room with a 35 cm x 25 cm metal plate placed inside an office bag. The bag was placed on top of a 1.0 m long plastic cylinder, which was 1.0 m away from the wall.

(a) (b)

Figure 7.6: Plywood wall, (a) inside the room; (b) Metallic target

Figure 7.7 shows the normalised profiles seen by the antennas, at the 2nd position, for the FMCW cases with and without (Empty) target and GFMCW with the target. From the FMCW profile it can be seen that the crosstalk and wall reflection peaks at 22.14 ns and 24 ns respectively overshadow that of the metallic target which is roughly at 30 ns. By applying the GFMCW with the chosen 3-bit m-sequence with parameters T_b = 7.5 ns and delays τ_1 = 2 ns, and τ_2 = 2 ns, these unwanted reflections are suppressed.

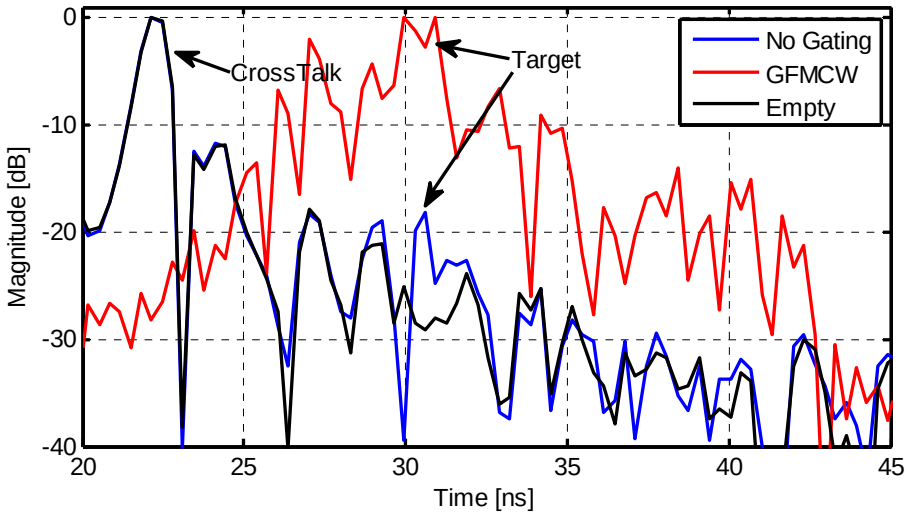

Figure 7.7: Scenario – A: radar profiles for FMCW and GFMW Cases

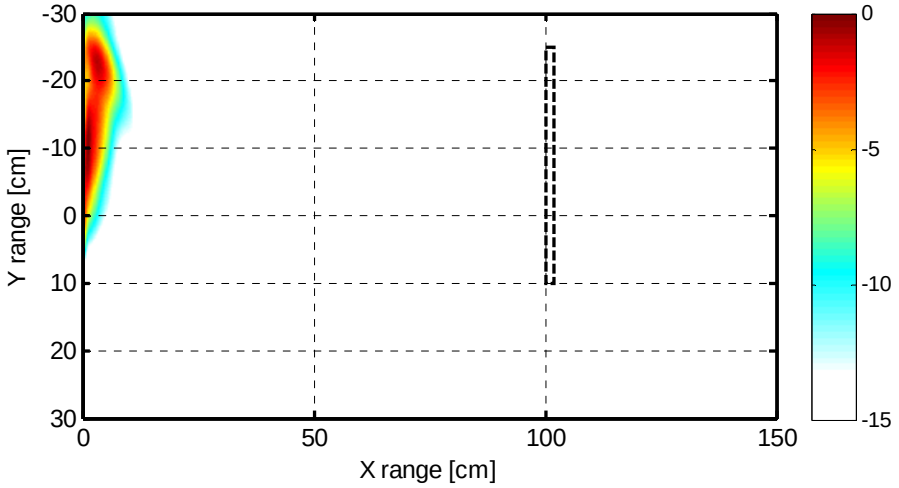

Figure 7.8: Scenario – A: radar image for the FMCW (No Gating) case

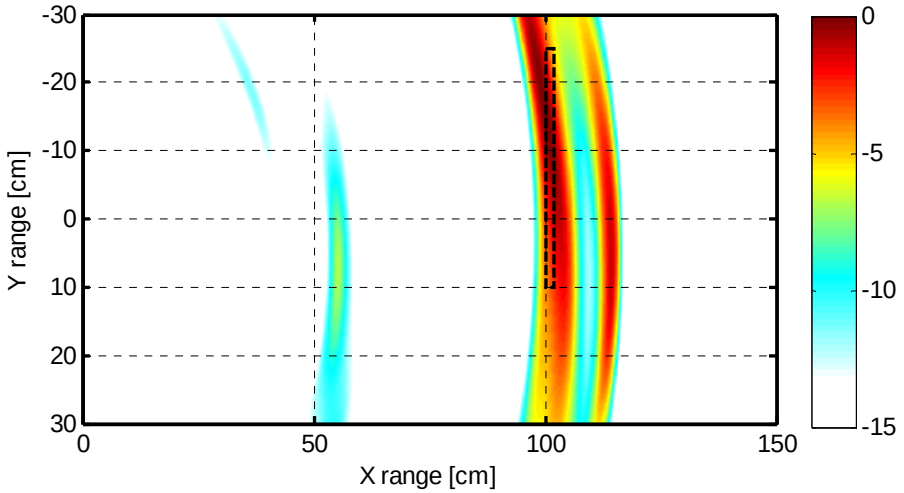

Figure 7.9: Scenario – A: radar image for GFMCW case

Figures 7.8 and 7.9 show the obtained radar images for the FMCW and GFMCW case. It can be seen from the figures that with the GFMCW case early wall reflections have been suppressed and the target is more distinguishable.

Scenario – B: Target Human Being

In the scenario shown in Figure 7.10 the target is a human being standing with his back facing the wall. The target is positioned 60 cm from the wall. Figure 7.11 shows the radar profiles seen by the antenna at the 2nd position of the array. As expected, early reflections are stronger than the target signal; consequently it is overshadowed in the radar image in Figure 7.12. By using GFMCW waveforms similar to the previous scenario the unwanted early reflections were removed and the target can be detected in Figure 7.13.

Figure 7.10: View of the room with a Human as target

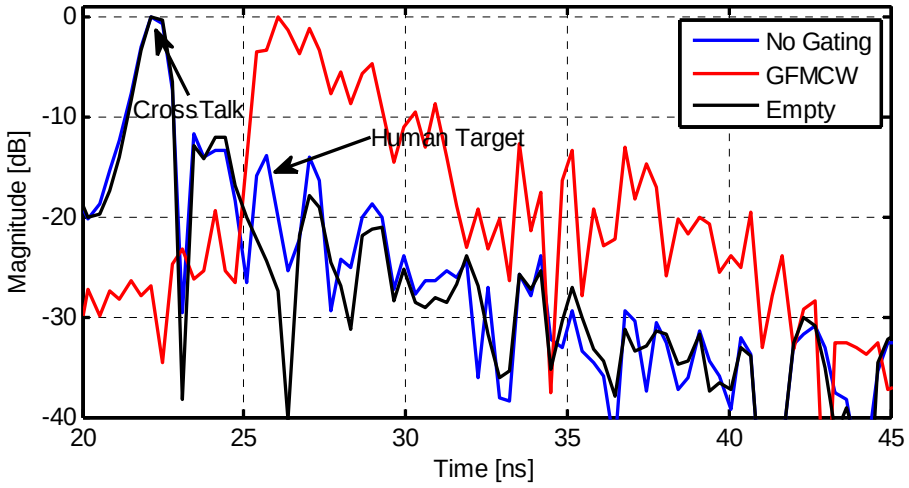

Figure 7.11: Scenario – B: radar profiles for FMCW and GFMW Cases

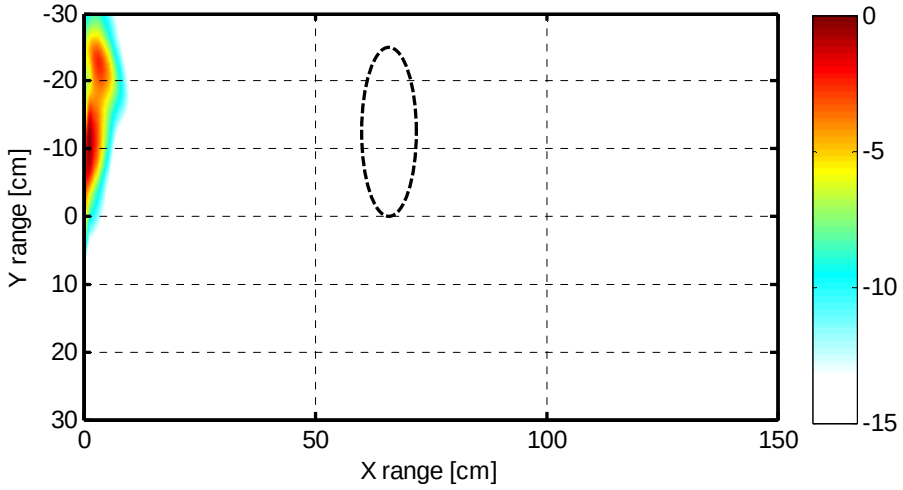

Figure 7.12: Scenario - B radar image for FMCW (No Gating) case

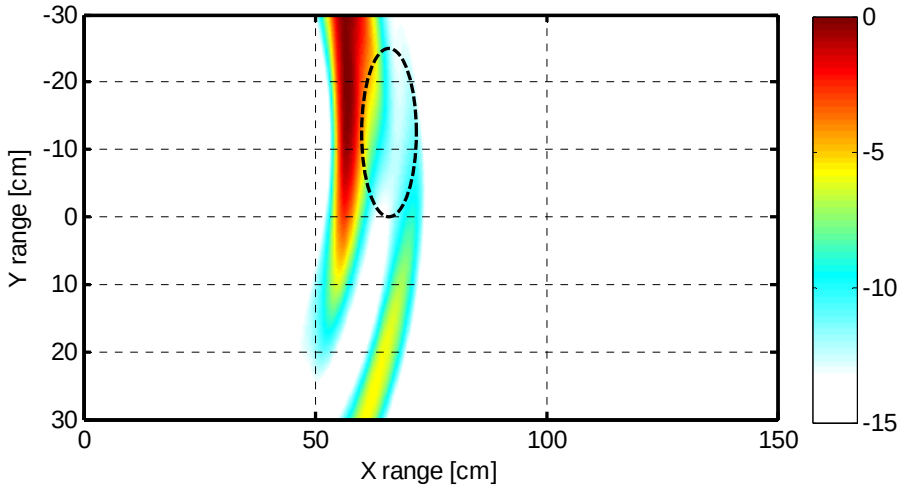

Figure 7.13: Scenario - B radar image for GFMCW case

7.1.2 Target Behind Concrete Wall

Scenario – C: Target a Bucket Filled with Water

In this scenario the target a "*plastic bucket filled with water*" was placed behind a concrete wall of an office environment as depicted in Figure 7.14. The target was positioned 90 cm and 150 cm from the wall. The wall thickness and permittivity were assumed to be 20 cm and 4.6 respectively. In this scenario the antennas were touching the wall.

Figure 7.15 shows the radar image when a FMCW signal was used. The unwanted early peaks, namely crosstalk and wall refelection, are located around 19-

21 ns in the radar range profiles, therefore by using the GFMCW waveform with the 3-bit m-sequence with parameters T_b = 7 ns and delays τ_1 = 2.5 ns and τ_2 = 3.5 ns, as well as the square wave sequence with parameters T_b = 10.5 ns and delays τ_1 = 3 ns and τ_2 =2.5 ns, the unwanted reflections are suppressed. Figures 7.16-7.18 display the radar image of the scenario under consideration when a GFMCW signal with the above mentioned gating sequences is used. Note that for the GFMCW waveform the target is clearly detectable and as expected the unwanted early reflections are suppressed.

Figure 7.14: View of the scenario a water filled bucket behind a concrete wall

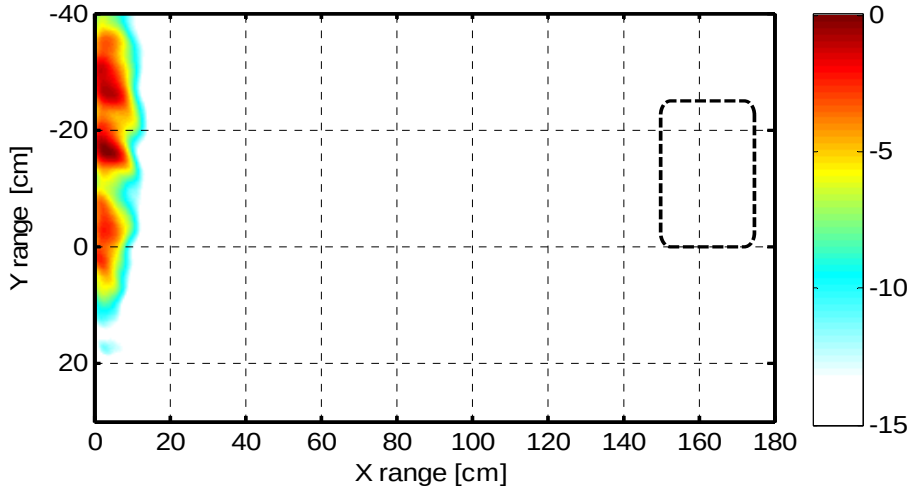

Figure 7.15: Scenario – C radar image for FMCW (*No Gating*) case

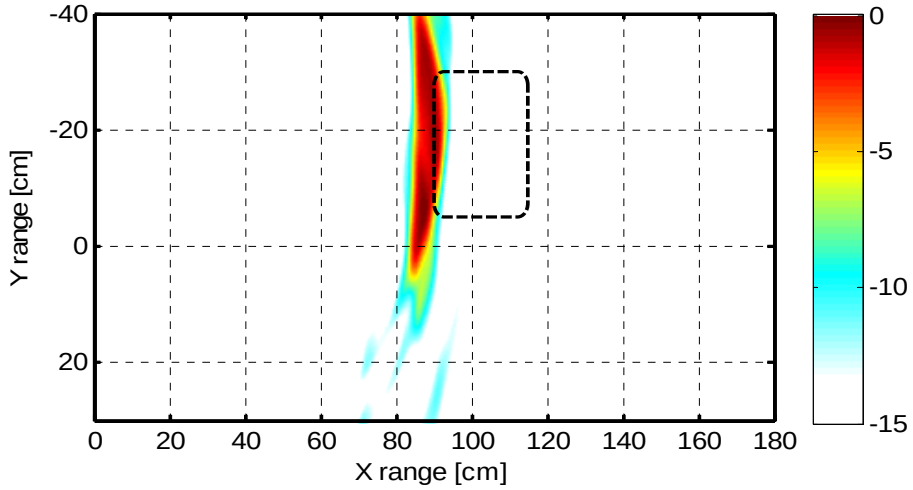

Figure 7.16: Scenario – C radar image GFMCW case with 3-bit m-sequence and the Target 90 cm from the front wall

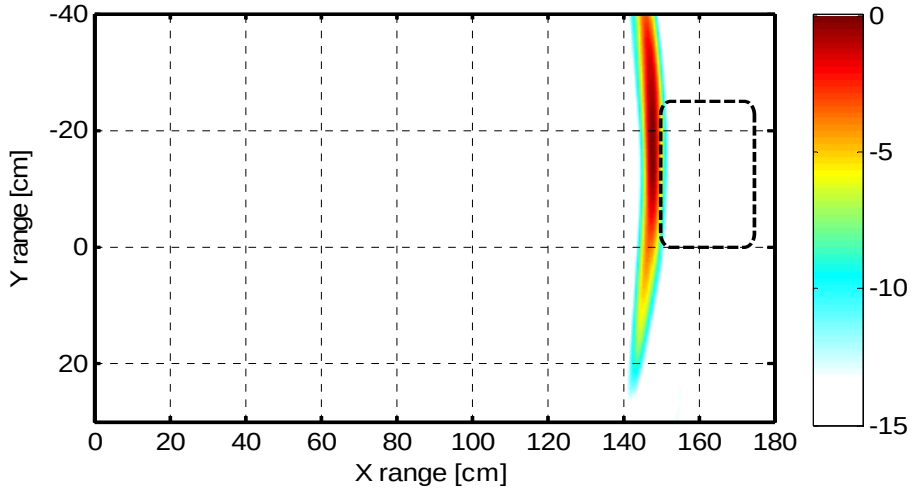

Figure 7.17: Scenario – C radar image GFMCW case with 3-bit m-sequence and the Target 150 cm from the front wall

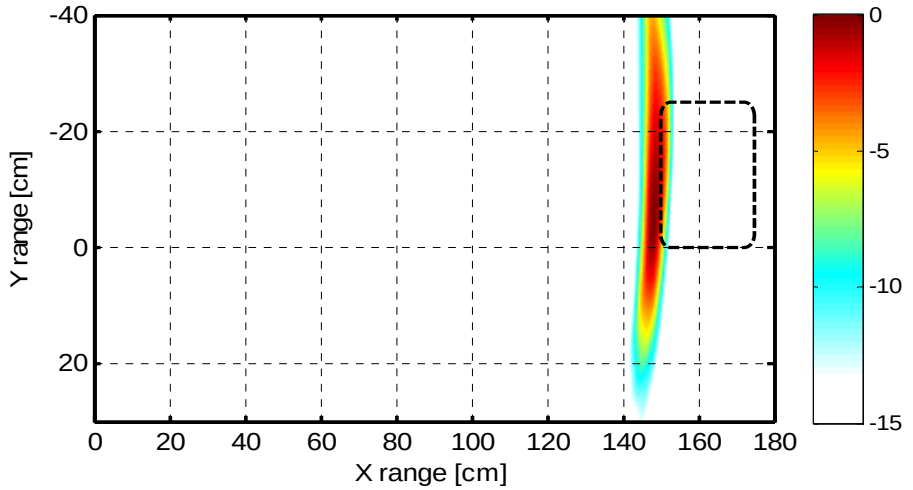

Figure 7.18: Scenario – C radar image GFMCW case with SQ wave sequence

7.2 Ground Penetrating Radar

This section presents the preliminary results of the ground penetrating radar experiments performed in the anechoic chamber at Durham University. The focus was on detection of a metallic target buried in the sand using the GFMCW suppression technique. Experiments were performed using a 42 cm x 50 cm x 48 cm plastic box filled with builder sand, with a measured gravimetric water content of 7.5%, with the target buried at different depths. The gravimetric water content was measured as the ratio of the mass of the water to that of the dry soil.

Two antipodal slot antennas (*presented in Chapter 5 as TSA-A*) separated by 5.5 cm were used at the transmitter and receiver respectively, and were moved using the X-Y positioner along a linear synthetic array of 27 positions with inter position spacing of 1 cm. The radar system based on the AWG was used throughout the measurement campaign. The system was configured to operate with a frequency range of 1.4-3.5 GHz, a sweep repetition rate of 0.4 ns, and with 20 MHz sampling frequency. Figure 7.19 shows part of the experimental set-up used in this section,

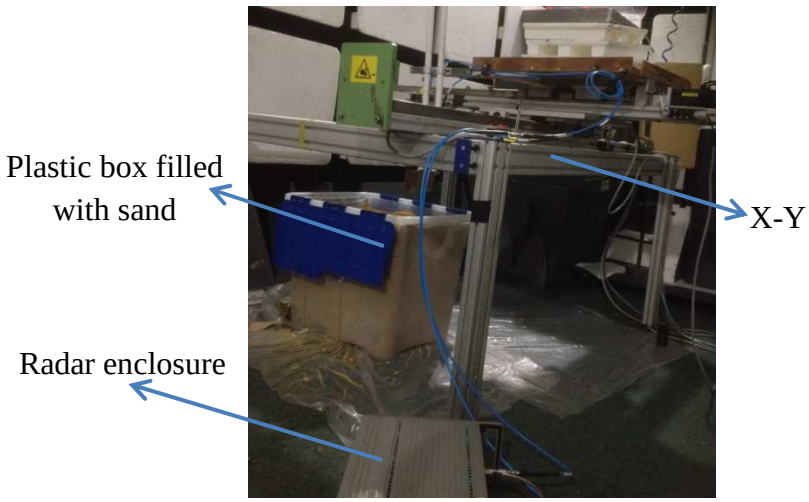

Figure 7.19: Ground penetrating radar experimental set-up

Scenario – D: Target Metallic Plate

Figure 7.20 shows the view of the target, which is a 20 cm x 15 cm metallic plate. The target was buried 30 cm deep and the distance from the antennas tip to the soil surface was set to 10 cm. As expected in the radar profile shown in Figure 7.21

early reflections, such as antenna crosstalk and ground surface, are much stronger than the target reflection, which is approximately -19 dB below the main peak.

Figure 7.20: View of the metallic plate target on this scenario

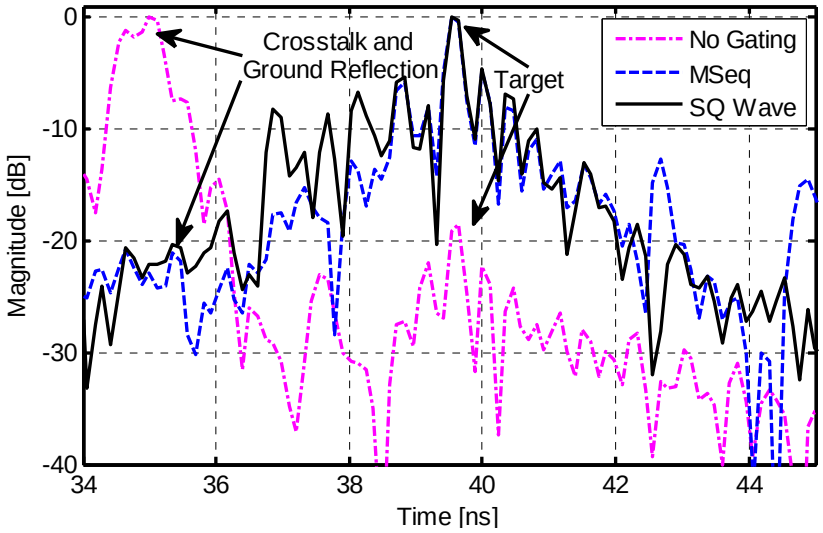

Figure 7.21: Scenario – D radar profiles for FMCW (*No Gating*) and GFMCW cases

Figure 7.22 shows the radar image for the case of FMCW signal. On which it can be seen that the target is overshadowed by those unwanted early responses. By using the GFMCW with 3-bit m-sequence (MSeq) of parameters T_b = 5.875 ns and delays τ_1 = 2 ns and τ_2 = 2 ns; and a square wave (SQ Wave) sequence of parameters T_b = 4.375 ns and delays τ_1 = 1.5 ns and τ_2 = 1.5 ns the unwanted reflections were suppressed as can be seen in their respective profiles in Figure 7.21 and in the corresponding computed radar images in Figures 7.23 and 7.24.

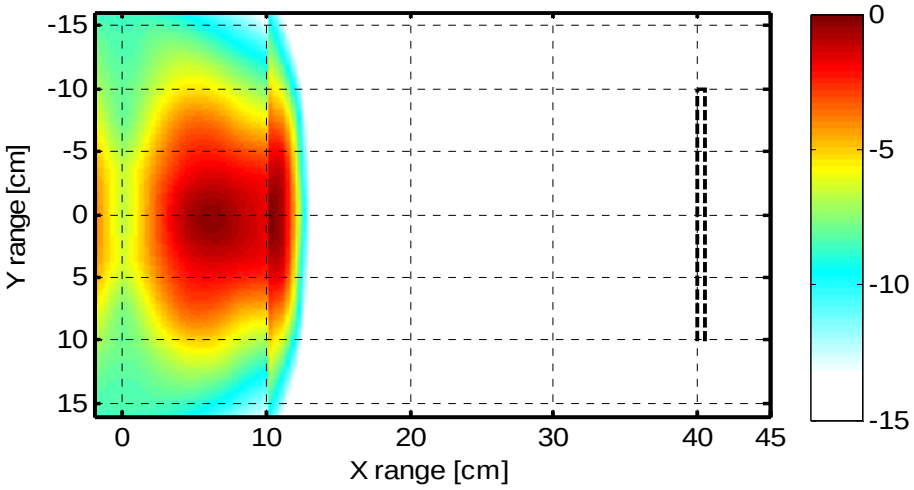

Figure 7.22: Scenario – D radar image for FMCW (*No Gating*) case

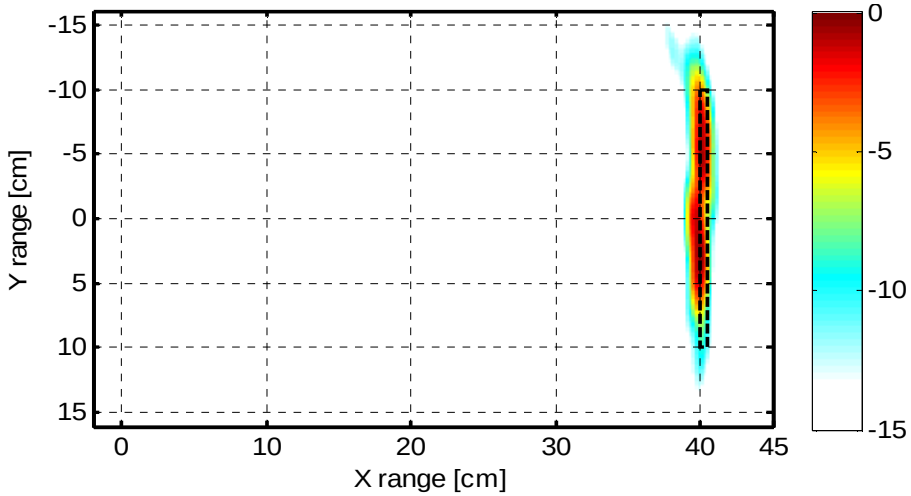

Figure 7.23: Scenario – D radar image for GFMCW (*Mseq*) case

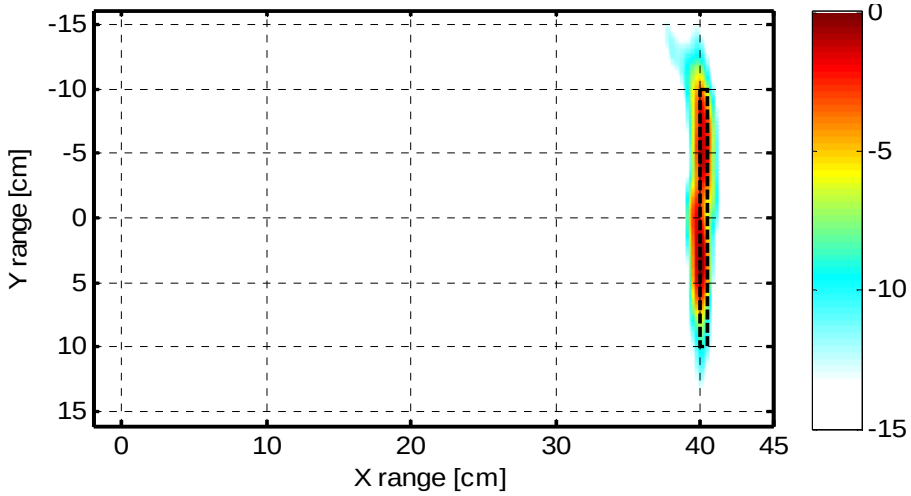

Figure 7.24: Scenario – D radar image for GFMCW (*SQ Wave*) case

Scenario – E: Target a Metallic Disk

In this scenario, the target was a 13 cm diameter plastic disk wrapped in aluminium kitchen foil, as shown in Figure 7.25. The target was buried 13 cm deep and the antenna to ground surface spacing was similar to the previous scenario of 10 cm.

Figure 7.25: View of the metallic disk target on this scenario

The measurement with FMCW signal shows that the peak(s) of unwanted early reflections is at roughly 34 ns, whereas the target reflection is at 36.5 ns and is -16 dB below the strongest peak in the profile, as seen in Figure 7.26.

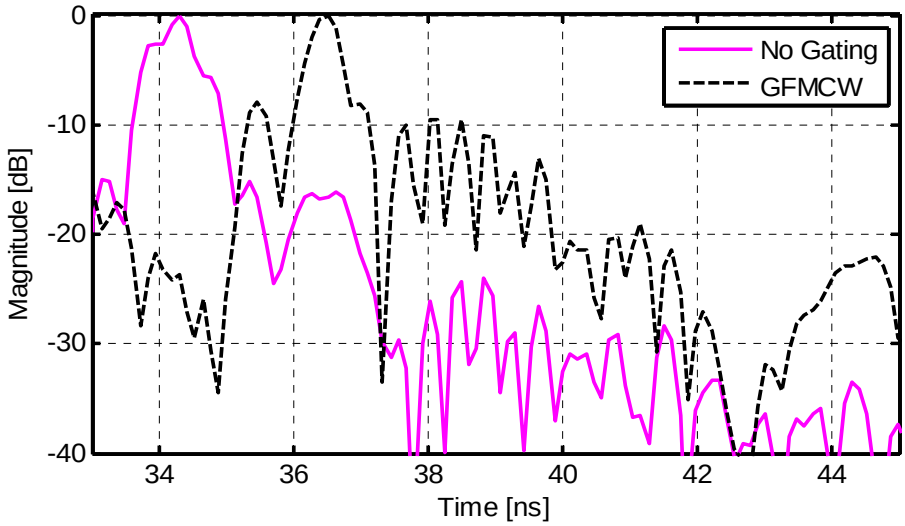

Figure 7.26: Scenario – E radar profiles for FMCW (*No Gating*) and GFMCW case

A 3-bit m-sequence with parameters T_b = 4.375 ns and delays τ_1 = 1.5 ns and τ_2 = 1.5 ns have been chosen to provide the suppression. Figures 7.27 and 7.28 show the radar image when FMCW and the proposed GFMCW signal is used. For the FMCW signal the target is overshadowed by the early crosstalk and air-ground reflection. By using the GFMCW signal these unwanted reflections are suppressed and the target is clearly visible in the image.

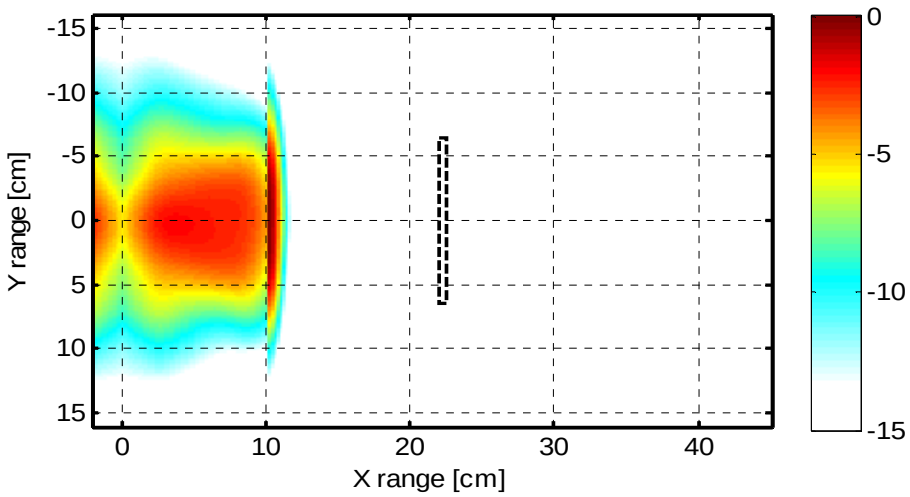

Figure 7.27: Scenario – E radar image for FMCW (*No Gating*) case

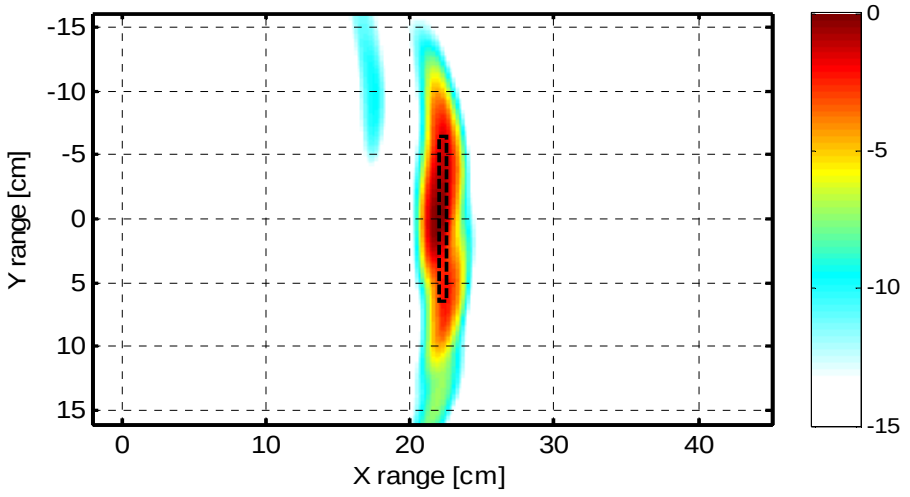

Figure 7.28: Scenario – E radar image for GFMCW case

7.3 Medical Imaging Radar

Research in microwave radar imaging techniques for breast cancer detection has been going on for well over a decade, with recently reported clinical trials in [4-6] showing good potential for the technique as breast cancer screening modality. Although, the technique offers the potential for a low cost screening tool, a number of challenges still remain. One of which is the suppression or elimination of clutter reflections due to crosstalk, skin, chest wall, equipment around the screening area and other internal breast tissues (i.e.: glandular) all of which tend to overshadow the tumour response.

In this section, a preliminary experimental result on the use of GFMCW signals for the suppression of early unwanted reflections (crosstalk and skin) in microwave medical imaging radar systems for breast cancer detection will be presented.

The experimental set-up presented in this section is made up of: the radar system, breast phantom, and for a particular antenna configuration the X-Y positioner. The radar systems based on VNA have been the preferable choice in these experiments due to its wide bandwidth compared to the other radar system with a frequency range limited to 4 GHz. The wider bandwidth enables the resolution of closer targets. The system was operated in a bistatic mode with both the transmitter and receiver antennas sequentially moved into pre-defined positions, either physically or through the X-Y positioner, to form a synthetic array. Two different synthetic antenna array configurations namely planar and circular arrays have been used throughout the experiment. The first had been initially developed by Hagness et al. in [7] and the latter by Paulsen et al. in [8]. The definition of the antenna configuration is based on the relative orientation of the patient in relation to the location of the array [9].

For a planar array configuration the patient can be orientated in supine position (face upward) while the array scans across the naturally flattened breast. On the other hand for a circular configuration the patient is orientated or lying on the table in prone position (chest down and back up) with the breast comfortably extended through an opening on the examination table while the circular antenna array is placed around the breast. The radar system used in this work operates in a

bistatic mode and the antenna array (in planar or circular configuration) is created by moving both antennas into predefined measurement positions around the breast phantom creating in this away a synthetic array through post-processing, similar to the measurement procedure reported in [10-14].

The breast phantom is mostly built, to mimic real breast electrical properties, by using a liquid mixture or solid materials with dielectric properties comparable to or of a ratio similar to that of the real breast tissues. Immersion medium mostly referred to coupling medium can also be used to reduce the dielectric mismatch between the phantom and the external environment [12]. Normally, the coupling medium of similar electrical properties of the normal tissue (fat) is chosen [5].

The experiments presented in the next sections, the antennas and the phantom were separated by air. A simplistic homogenous breast phantom made of sunflower oil (ε_r = 2.6), representing the fat tissue, metallic object or water (ε_r = 75), representing the tumour tissues, and Vaseline body lotion (ε_r = 40), representing the skin tissue, was used in the experiments related to the planar antenna configuration. For the case of circular antenna configuration the skin was represented by the plastic cylinder surface whereas the breast fat and tumour tissue were made of oil and water respectively. Breast cancer detection experiments involving homogenous breast phantom made out of similar material have also been reported in references [10, 12, 13, 15-17].

7.3.1 Measurements with Planar Antenna Configuration

Figure 7.29 shows a view of the breast phantom for the planar antenna configuration. A 2 mm non-uniform layer of body lotion contained in a 1 mm thick plastic container represents the breast skin, a plastic box filled with sunflower oil represents the breast fat layer, whereas the tumour is represented with either a water filled cylinder or a plastic bar wrapped in metallic kitchen foil.

Figure 7.29: View of the Breast phantom for the planar antenna configuration

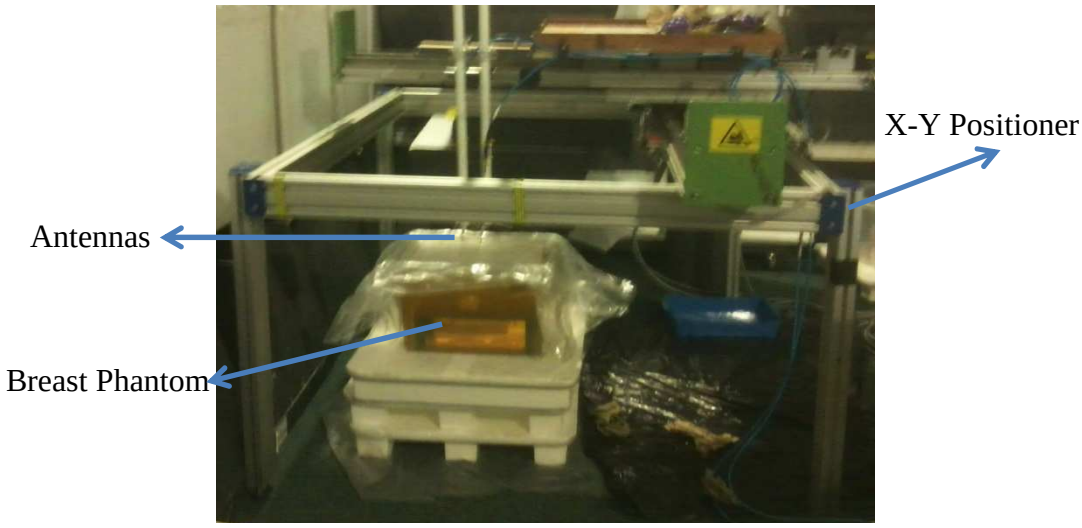

Figure 7.30: View of the breast phantom under the antenna positioning table

The breast phantom was placed under the X-Y antenna positioner (as shown in Figure 7.30) with the taper slot antennas (TSA - B) fixed 50 mm above the skin material. The network analyser was set–up to negative edge trigger and operates with a frequency range of 2-8.5 GHz, an output power of 0 dBm, and a sweep duration of 502 ms. Both Euvis modules, used to generate the gating sequence, were also set to operate as negative edge triggered and the trigger signal generator (FPGA board) was programmed to generate a trigger signal with a period of 1.2 s.

The antennas were moved into predefined positions along the Y axis and measurements were performed at each location with a total of 40 predefined positions spaced 5 mm apart.

Scenario – F: Target a Plastic Wrapped in Aluminium Kitchen Foil

In this scenario the target representing the tumour is a 50 x 100 mm^2 plastic bar wrapped in kitchen foil, as shown in Figure 7.31. The target was placed 90 mm deep, from the skin.

Figure 7.31: View of the used metallic target

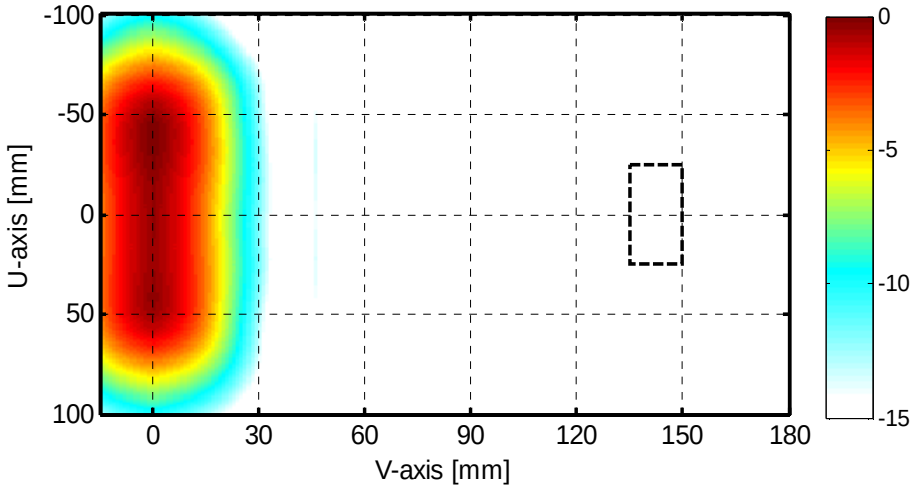

Figure 7.32: Scenario – F radar image for FMCW (*No Gating*) case

Figure 7.32 shows the radar image with FMCW signal. From the figure it can be seen that the target is completely overshadowed by those unwanted early responses (i.e. antennas crosstalk at the origin on the V-axis). By using GFMCW with sequences: square wave (SQ wave) sequence of parameters T_b = 1.75 ns and delays τ_1 = 0 s and τ_2 = 0.75 ns or the 3-bit m-sequence (Mseq) of parameters T_b = 2.50 ns and delays τ_1 = 0.5 ns and τ_2 = 0 s these unwanted reflections are suppressed as depicted in Figures 7.33 (a)-(b) respectively. With a square wave sequence some residual from the crosstalk remains visible in the image whereas with the 3-bit m-sequence the crosstalk has been fully suppressed at the given threshold.

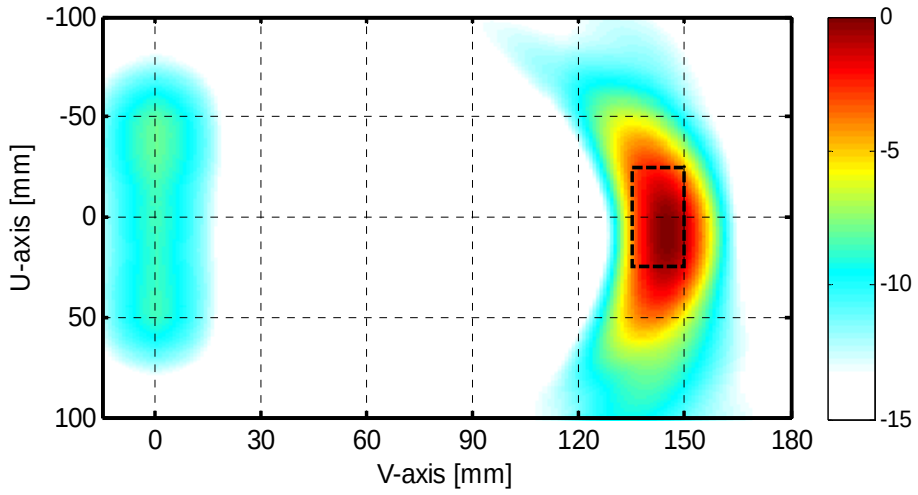

(a)

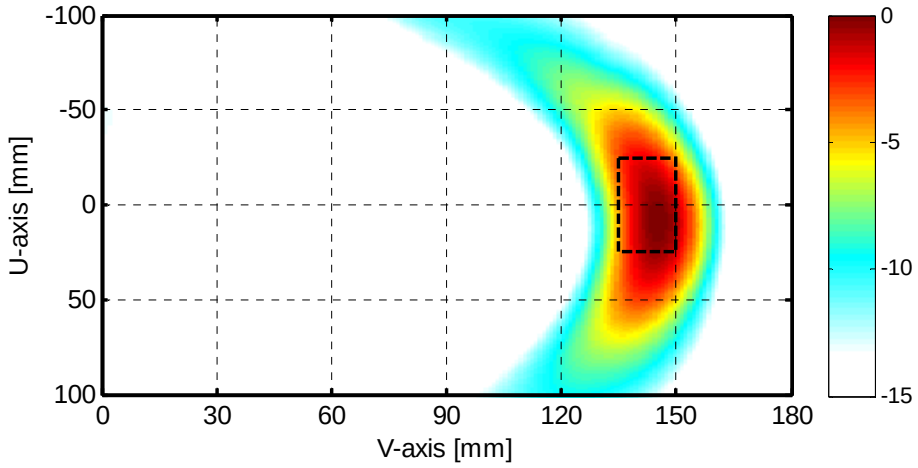

(b)

Figure 7.33 Scenario – F radar image for GFMCW case, (a) SQ wave, (b) Mseq

Scenario – G: Target Water Filled Plastic Cylinder

The target representing the tumour is a 30 mm thin plastic cylinder filled with water was placed inside the breast phantom at a depth of 80 mm from the skin (*as depicted in Figure 7.29*). Figure 7.34 shows the radar image for the case of FMCW and GFMCW signals. As expected the antenna crosstalk dominates and overshadows the tumour response in the FMCW case. By using a GFMCW signal with the 3-bit m-sequence (*with* T_b *= 2.50 ns and delays* τ_1 *= 0.5 ns and* τ_2 *= 0 s*) this early reflection is attenuated (as shown in Figure 7.34 (b)) and the target energy can be clearly identified.

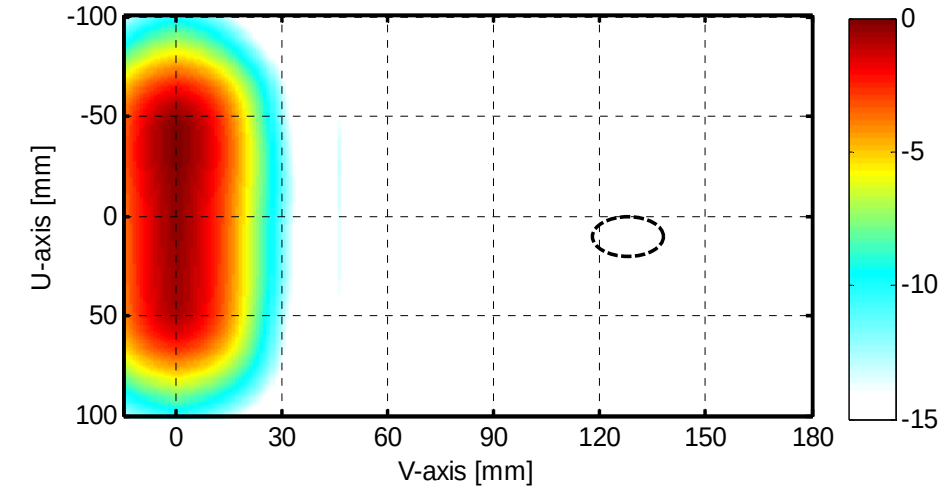

(a)

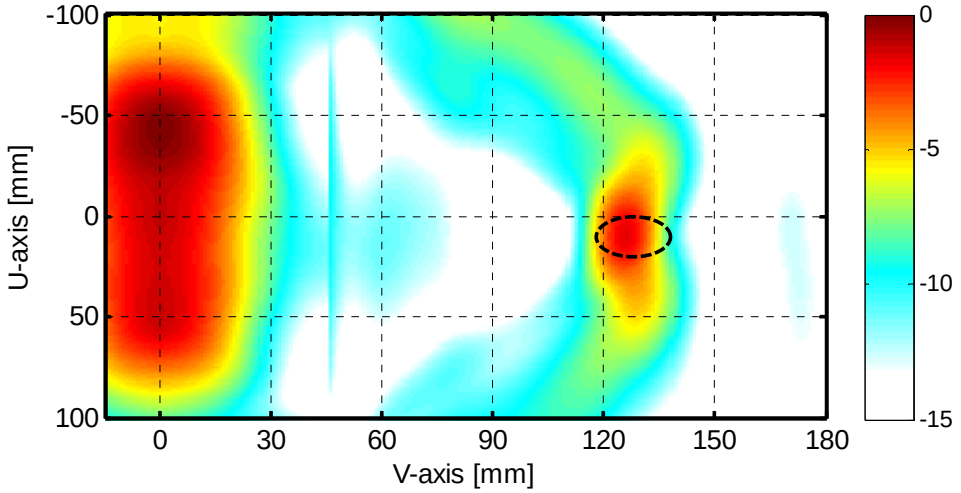

(b)

Figure 7.34: Scenario – G radar image for (a) FMCW, (b) GFMCW case

7.3.2 Measurements with Circular Antenna Configuration

Figure 7.35 shows the used measurement set-up for the circular antenna configuration. The radar system is based on the VNA operating in the frequency range 2-8.5 GHz with an output power of 0 dBm. In this set-up, similar to the previous one, two of the VNA ports (A and B) are connected individually to the input port of a two-way switch, respectively. Two switches were used one for each VNA port. One of the outputs of each switch was connected to the respective antenna (TSA-B) and the other was terminated with 50 ohm load. The switches were driven, through the switch driver, by two Euvis modules which generated the

user-defined gating sequences. The clock distribution unit was responsible for synchronizing the devices.

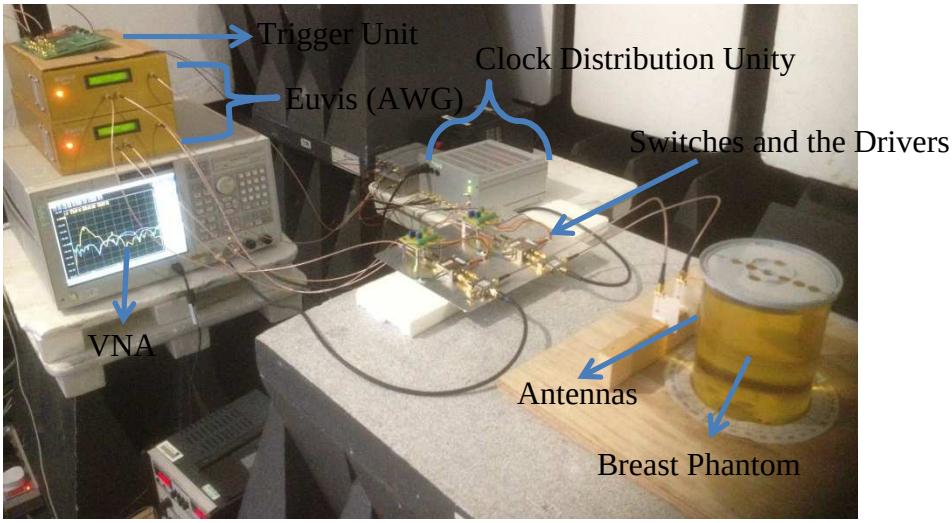

Figure 7.35: Experimental set-up for circular antenna configuration

Figure 7.36: Target container

The used homogeneous breast phantom was made of 130 mm diameter plastic cylinder filled with sunflower oil representing the normal breast tissue. The tumour was represented by water contained in a 10 mm diameter plastic tube, shown in Figure 7.36. In this configuration the skin was represented by the thin layer of the plastic cylinder. The antennas were spaced 40 mm apart from each other and were roughly 15 mm from the phantom surface. Measurements were performed in 36 positions around the phantom. After each measurement the phantom was manually rotated in 10° steps.

Scenario – H: Target Water Filled Plastic Tube – I

In this scenario the target (water filled plastic tube) was placed on the first quadrant of the cylindrical phantom. As expected the antenna crosstalk energy dominate the radar image and overshadows the target return signal, as shown in Figure 7.37. By using the GFMCW signal with gating sequence such as: SQ wave

(*with* T_b *= 875 ps and delays* τ_1 *and* $\tau 2$ *both set to 0 s*) or 3-bit m-sequence (*with* T_b *= 1.625 ns and delays* $\tau_1 = 0$ *s and* $\tau_2 = 125$ *ps*) the antenna crosstalk signal was attenuated as can be seen in Figures 7.38 (a)-(b).

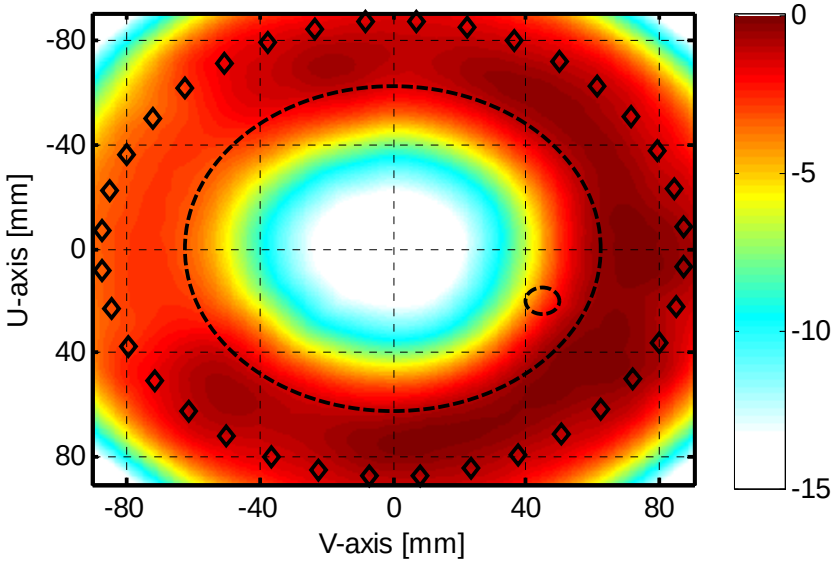

Figure 7.37: Scenario – H radar image for FMCW (*No Gating*) case

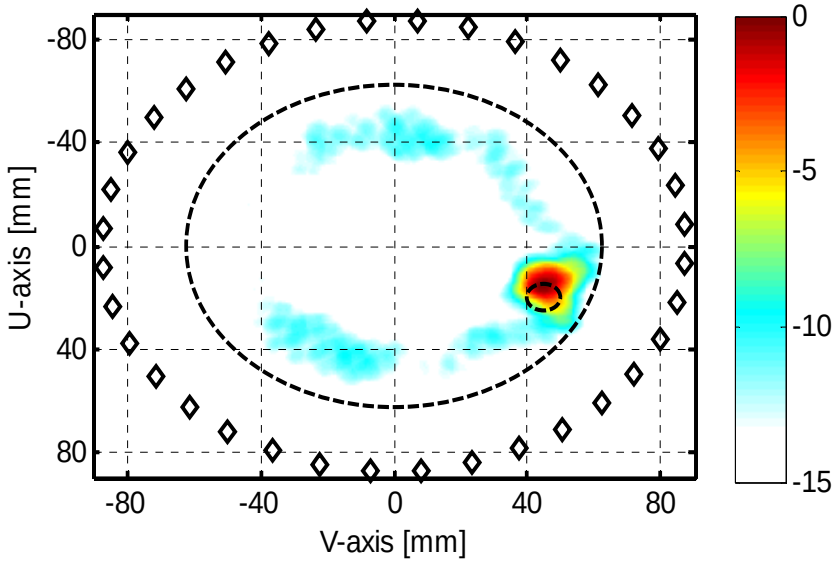

(a)

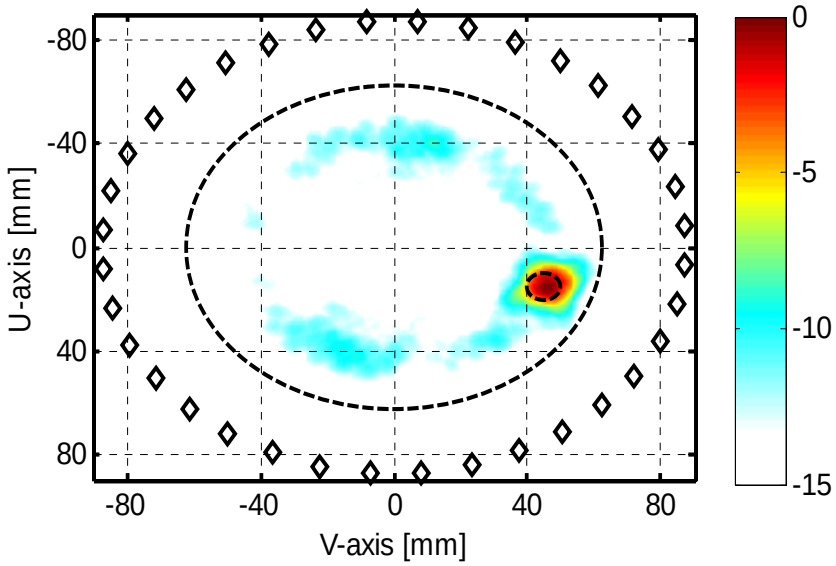

(b)

Figure 7.38: Scenario – H radar images for GFMCW cases with sequence (a) SQ wave, (b) 3-bit m-sequence

Scenario – I: Target Water Filled Plastic Tube – II

In this scenario the water filled plastic tube target was placed on the second quadrant of the cylindrical phantom. Antenna crosstalk reflection, as expected, overshadows the desired target return signal as seen in the radar image presented in Figure 7.39.

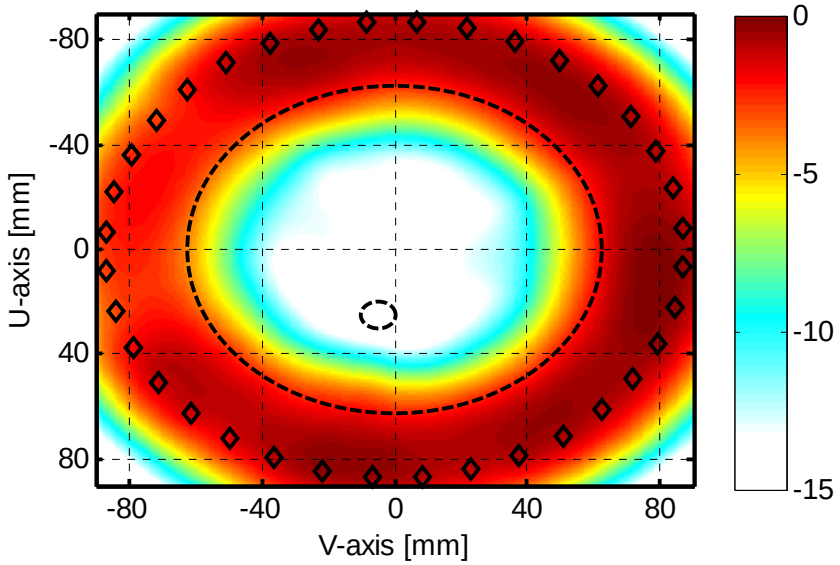

Figure 7.39: Scenario – I radar image for FMCW (*No Gating*) case

By suppressing the antenna crosstalk signals through the GFMCW technique the target return can be enhanced. Figures 7.40 (a)-(b) show the radar image for the

GFMCW cases with similar gating sequence parameters as in the previous scenario. Although the target energy can be clearly seen, in both images, spurious components are also present which can be mistaken as targets. One way to remove these components from the area of interest could be to further apply a post-processing clutter removal technique to the received GFMCW signals.

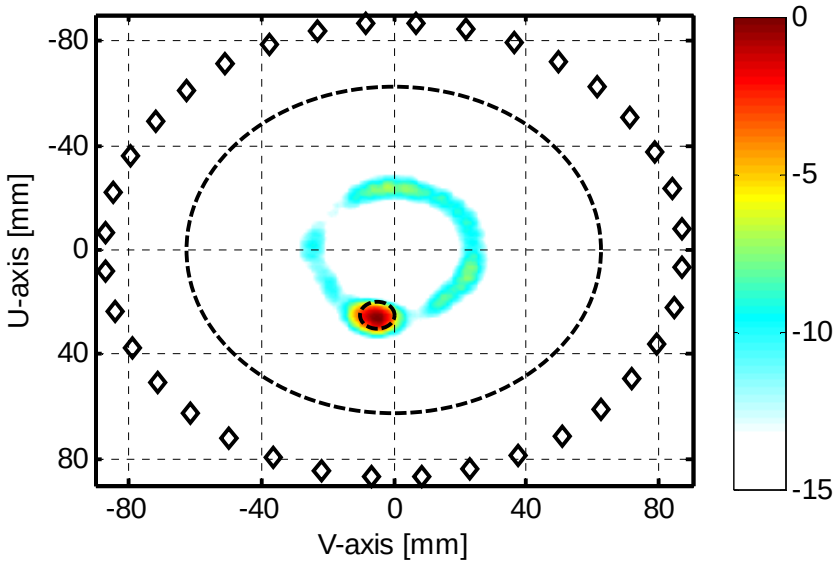

(a)

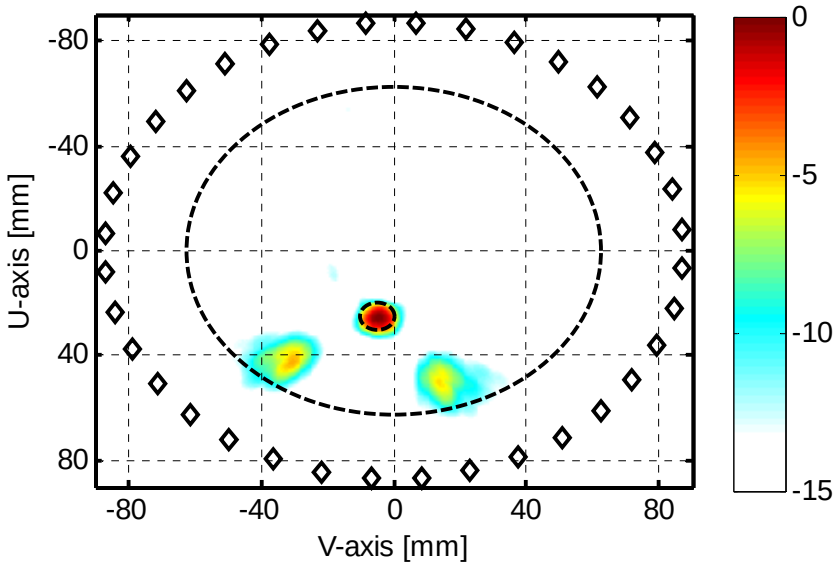

(b)

Figure 7. 40: Scenario – I radar images for GFMCW cases with sequence (a) SQ wave, (b) 3-bit m-sequence

7.4 Summary

In this chapter, the experimental validation of the proposed GFMCW technique in scenarios involving TTWRI, GPR and MIR has been presented. The effectiveness of the technique was shown through radar images of the scenarios under-test when a normal FMCW or GFMCW waveform with a propriety gating sequence is used. The presented radar images were obtained through the post-processing of the received signal using the delay-and-sum algorithm discussed in Chapter 2.

Two radar systems have been used in the measurements. These are, namely: "*GFMCW radar system based on AWG*" – which was used in through-the-wall imaging radar with targets such as metallic plate, human beings, and water filled plastic bucket being placed in office like environment behind realistic walls. Also this system was used in the ground penetration radar experiments which involved detecting metallic objects buried under different depths on a layer of builder soil with a 7.5% gravimetric water content. The "*GFMCW radar system based on VNA*" – which achieves a wider bandwidth (in excess of 6.5 GHz) was used in medical imaging experiments for the detection of breast cancer tumour. Preliminary breast phantoms with the fat tissue represented by sunflower oil, the skin by body cream and the tumour by water or metallic object were built for the experiments.

The scenarios images showed that the strong unwanted (i.e. crosstalk plus the wall, air-ground, or skin) reflections obscure the desired target in the images when the FMCW waveform is used. On the other hand when the GFMCW waveform with an appropriate gating sequence is used those unwanted reflections are suppressed which allow the target energy to be clearly visible in the image.

7.5 References

[1] F. Fioranelli, S. Salous, I. Ndip, and X. Raimundo, "Through the wall detection with gated FMCW signals using optimized patch-like and vivaldi antennas," *IEEE Transactions on Antennas and Propagation,*vol. 63, pp. 1106-1117, 2015.

[2] A. Thajudeen, F. Ahmad, and T. Dogaru, "Measured complex permittivity of walls with different hydration levels and the effect on power estimation of twri target returns," *Progress In Electromagnetics Research B,* vol. 30, pp. 177-199, 2011.

[3] A. Muqaibel, A. Safaai-Jazi, A. Bayram, A. Attiya, and S. Riad, "Ultrawideband through-the-wall propagation," *IEE Proceedings Microwaves, Antennas and Propagation,*vol. 152, pp. 581-588, 2005.

[4] P. Meaney, M. Fanning, T. Raynolds, C. Fox, Q. Fang, C. Kogel, *et al.*, "Initial clinical experience with microwave breast imaging in women with normal mammography," *Acad Radiol.,* vol. 14 . pp. 207-218, 2007.

[5] M. Klemm, I. Craddock, J. Leendertz, A. Preece, and R. Benjamin, "Experimental and clinical results of breast cancer detection using UWB microwave radar," *IEEE Antennas and Propagation Society International Symposium,* pp. 1-4, 2008.

[6] T. Henriksson, M. Klemm, D. Gibbins, J. Leendertz, T. Horseman, A. Preece, *et al.*, "Clinical trials of a multistatic UWB radar for breast imaging," in *Loughborough Antennas and Propagation Conference (LAPC),* pp. 1-4, 2011.

[7] S. Hagness, A. Taflove, and J. Bridges, "Two-dimensional FDTD analysis of a pulsed microwave confocal system for breast cancer detection: Fixed-focus and antenna-array sensors," *IEEE Transactions on Biomedical Engineering,* vol. 45, pp. 1470-1479, 1998.

[8] K. Paulsen and P. Meaney, "Nonactive antenna compensation for fixed-array microwave imaging. I. Model development," *IEEE Transactions on Medical Imaging,* vol. 18, pp. 496-507, 1999.

[9] R. Conceicao, M. O'Halloran, M. Glavin, and E. Jones, "Comparison of planar and circular antenna configurations for breast cancer detection using

microwave imaging," *Progress In Electromagnetics Research,* vol. 99, pp. 1-20, 2009.

[10] M. Bialkowski, Y. Wang, A. Bakar, and W. Khor, "Microwave imaging using ultra wideband frequency-domain data," *Microwave and Optical Technology Letters,* vol. 54, pp. 13-18, 2012.

[11] Z. Haoyu, T. Arslan, and B. Flynn, "Microwave imaging of a realistic cancerous phantom using an ultra-wideband antenna transceiver system," in *Loughborough Antennas and Propagation Conference (LAPC),* pp. 112-116, 2013.

[12] S. Salvador and G. Vecchi, "Experimental Tests of Microwave Breast Cancer Detection on Phantoms," *IEEE Transactions on Antennas and Propagation,* vol. 57, pp. 1705-1712, 2009.

[13] I. Unal, B. Turetken, K. Surmeli, and C. Canbay, "An experimental microwave imaging system for breast tumor detection on layered phantom model," *XXXth URSI General Assembly and Scientific Symposium,* pp. 1-4, 2011.

[14] M. Helbig, J. Sachs, F. Tansi, and I. Hilger, "Experimental feasibility study of contrast agent enhanced UWB breast imaging by means of M-sequence sensor systems," *8th European Conference on Antennas and Propagation (EuCAP),* , pp. 311-315, 2014.

[15] X. Li, S. Davis, S. Hagness, D. Van der Weide, and B. Van Veen, “Microwave imaging via space-time beamforming: experimental investigation of tumor detection in multilayer breast phantoms,” *IEEE Transactions on Microwave Theory and Techniques,* vol. 52, no. 8, pp. 1856-1865, 2004.

[16] J. Sill and E. Fear, "Tissue sensing adaptive radar for breast cancer detection - experimental investigation of simple tumor models," *IEEE Transactions on Microwave Theory and Techniques,*vol. 53, pp. 3312-3319, 2005.

[17] N. Ghavami, G. Tiberi, D. Edwards, and A. Monorchio, "UWB microwave imaging of objects with canonical shape," *IEEE Transactions on Antennas and Propagation* vol. 60, pp. 231-239, 2012.

CHAPTER 8

Conclusions and Further Work

8.1 Conclusions

In microwave radar imaging the scenario under test is illuminated with an electromagnetic wave, from different locations. The collected backscattered signals are then processed in order to create an image map of the scenario and target detection. Three microwave radar imaging applications have been considered in this work namely: through-the-wall radar, ground penetrating radar, and medical imaging radar. Through-the-wall radar aims at detection of targets (e.g. human beings) located behind wall structures or buried under rubble. Whereas, ground penetrating radar (GPR) aims at detecting objects (e.g. land mine, archaeological artefacts) buried below the surface of the Earth. Microwave medical imaging radar has been considered for detection of breast cancer.

A common problem in the aforementioned microwave radar imaging applications is the need to effectively suppress the undesired scatter reflections from the received signal before target detection or formation of the radar image. Undesired signals such as: antenna crosstalk, wall reflections (in TTWR), ground surface reflection (in GPR), and skin reflection (in MIR) are stronger in magnitude than that of the actual target reflection. Consequently, if not suppressed, these strong

reflections may overshadow the target signature, especially those with low radar cross section, therefore making detection a difficult task. Furthermore, these strong unwanted reflections may limit the receiver's instantaneous dynamic range and in the worst case cause it to saturate, therefore making weak signals appear as noise.

In this thesis, the effectiveness of a proposed clutter suppression technique in the aforementioned radar applications have been successfully validated through numerical simulations and experimental campaigns. The proposed technique, known as gated frequency modulated continuous waveform, has being used in the past in applications such as ionospheric channel sounding and sea-surface remote sensing to provide isolation between transmission and reception, as the use of single antenna (i.e. monostatic radar operation) was desirable back then. The use of GFMCW in TTWR, GPR, and MIR applications as unwanted signal suppression technique is a novelty. In GFMCW, the transmitter and receiver are switched "on" and "off" in complementary function, resulting on the radar system to be range sensitive. Consequently, signals from certain ranges, depending on parameters of the gating sequence, are blocked or at least attenuated while others are received unaltered.

In Chapter 3, a non-exhaustive review of other techniques reported in the literature for the removal of undesired signals in TTWR, GRP and MIR applications was given. Chapter 4 gave a detailed mathematical analysis of the proposed GFMCW technique with a focus on gating sequences used in the experiments and numerical simulations, their corresponding range sensitivity profiles, in the form of MRS and MRP, and the influence of sequence parameters (sequence length, bit duration, and receiver's sequence duty cycle variation) on the sensitivity and overall system performance.

Numerical radar simulations, presented in Chapter 6, have been performed to evaluate the performance of GFMCW approach using commercially available 3D electromagnetic solver software (namely: CST Microwave Studio). To avoid potential instability in the CST software that gives rise to large ripples appearing in the recorded waveform, due to sharp transitions in the user chosen or defined excitation waveform, a methodology involving windowing and gating through post processing have been adopted throughout the simulation. Thus, in the simulations,

the excitation signal was defined as a Hamming windowed FMCW waveform. Once a simulation was completed the computed received raw data was loaded into Matlab and corresponding user specified gating sequence was applied to it before further processing. The adopted methodology brought both flexibility and time saving benefits as for the same simulation the computed raw data can be tested with a number of user specified gating sequences without the need of re-running the simulation every time. In the simulated scenarios for the respective TTWR, GPR, and MIR radars the dielectric properties of the included materials (walls, soils, breast tissues) were chosen appropriately.

Two radar systems, one based on AWG and the other on VNA, both capable of generating FMCW and GFMCW waveforms have been built and used on the TTWR, GPR, and MIR experimental campaigns. The block architecture of both systems was described in detail in Chapter 5. The AWG based radar system is able to generate a waveform with maximum frequency of 3.5 GHz and of duration of 0.9 ms. This system was primarily used in TTWR and GPR measurements as the available bandwidth is sufficient for these applications. It essential to point out that with this system GFMCW are created without the need of extra circuitry, e.g. gating sequence generator together switches or multiplier, but rather the desired waveform (FMCW or GFMCW) is realised in software (Matlab) and loaded into the respective AWGs memory for generation. The VNA based radar system on the other hand has a waveform frequency limit up to 8.5 GHz, and this system was used mainly in MIR experiments due to higher achievable range resolution compared to the former. On the system extra hardware (fast switches, switch drive, and gating sequence generator) were employed to create the GFMCW waveform.

In order to ensure the different devices or hardware on the radar systems were synchronised, and thus avoid jittering and possible unwanted artefacts on the profile, all the necessary clock signals were locked onto a single stable rubidium clock source. Two distinct Vivaldi antennas models have been specifically designed and manufactured to operate with the radar systems. Moreover, an X-Y positioner system has also been assembled to automatically move the antennas into pre-defined positions. The experimental campaigns, described in Chapter 7, were performed within the facilities of the School of Engineering and Computing Sciences at

Durham University. For the TTWR radar the scenarios involves office-like room made of concrete or plastered wall and the target, within it, being a human, a plastic bucket filled with water, or a metallic object. Whereas, for the GPR radar experiment, builders sand with gravimetric water content of 7.5% was used, with metallic target (mimicking land mine, or pipe) buried on it at different depths. Meanwhile, in MIR the breast tissue phantoms were represented by oil (fat), body lotion (skin), and water or metallic object (target).

In both numerical simulation and experimental campaign scenarios, the normal FMCW and the GFMCW waveforms were used. Comparisons of the resultant radar images clearly show the potential of the GFMCW waveform, opposite to the normal FMCW, in successfully suppressing or at least attenuating the undesired strong signals (from antenna crosstalk and wall, ground surface, or skin reflections) and thus enhancing the detection of the target. In comparison with post-processing based clutter suppression techniques, GFMCW offers the potential of mitigating unwanted clutter on the hardware, that is before the digitization of the signal, thus avoiding the reduction of the system's dynamic range and the risk of blocking the receiver. Moreover, GFMCW neither needs prior information about the about the clutter type, shape, or electrical properties nor is susceptible to modelling error, unlike some post-processing based approach.

It worth mentioning, that although the proposed approach "GFMCW" can suppress the strong early unwanted reflections, clutter within the latter part of the signal may still overshadow the target signature and making a much harder task for detection. The latter clutter signal could be originated from a scatter within the scenario or even ringing on the waveform caused by certain type of material (e.g. wall with internal cavity, skin). Furthermore, the gating sequence parameter needs to be carefully chosen to ensure that while the blind range covers the unwanted reflections, it does not extend into time delays (range) related to possible target, especially if shallow target is involved. In any case, GFMCW waveform can be used in combination with existing post-process based method, such as those described in Chapter 3, for an overall clutter suppression performance.

8.2 Further Work

From the experience gained in the radar imaging work discussed in this thesis the following improvements can be suggested for future work:

Regarding the hardware:

- The radars currently operate in a bistatic mode and the system / antennas had to be physically moved into different predefined measurement locations (creating a SAR) with the assumption that the targets are stationary. It would be more beneficial replacing both antennas with a physical antenna array to reduce the measurement processing time and also to give the ability of forming a MIMO radar system. Due to the limited number of transmitters and receivers in the system having a physical array would also require implementing a switching network together with control and synchronisation circuitry to select the distinct pairs of transmitting and receiving antennas during the measurement.
- The small memory of the Euvis limits the duration of the waveform or group of waveforms that can be loaded onto it. It would be beneficial having it increased or making Euvis access an external memory (of larger capacity) in which waveforms of different gating sequences can be stored and accessed without the need for having to re-load the waveforms.
- In the VNA based radar, the isolation of the switches limits the level of attenuation caused by a gating sequence therefore hindering the system performance. An alternative can be using mixers instead.
- In the VNA based radar the expensive AWG units that generate the gating sequences (for the transmitter and receiver respectively) could be replaced by lower cost FPGA devices.
- The receiver of the AWG based radar has a fixed gain baseband amplifier. This unit can be replaced by an “automatic gain and control unit”, such as those in-house developed units used in the receiver of the multiband channel sounder. These units offer variable gain / attenuation which are adjusted based on the incoming signal level so that it is within the ADC requirements when digitised.

- In both radar systems, the computer radar images are the result of off-line processing of the received waveform through Matlab. So instead of off-line processing and data having to be transferred into Matlab, it would be beneficial to use "specifically programmed or designed FPGA and display units" to deliver real-time processing and graphical interface of the scenario under test.

Regarding the measurement scenarios:

- The MIR experiments were conducted with simple homogeneous layered phantoms. Assessment of GFMCW technique on a more heterogeneous phantom composed of material that better mimic the dielectric properties of the breast tissues would be beneficial.
- GFMCW can be extended for detection of non-metallic targets in GPR.

Regarding the signal processing:

- The square complementary gating sequences employed in this work have a slow rising slope, of one bit duration, on its MRP. Targets close to the undesired scatter may also be attenuated / affected by the slope. Further investigation could be made on the effects of pulse shaping of the sequence MRP.
- Although the early undesired reflections were successfully mitigated with GFMCW approach, late undesired reflections which also influence the target signature are not suppressed. Further work can be made to combine the GFMCW approach with a post-processing technique described in Chapter 3 with a view of improving the overall system's performance.

Appendix

Appendix A: Radar Matlab Codes

A.1 Extracting the Radar Range Profile

The Matlab script below "*MySignatecReader_GPR.m*" reads the raw data recorded by the ADC used in the "*GFMCW Radar System Based on AWG*" and convert it into range profiles / channel impulse response. On each measurement the sweeps were saved in a single file as a long stream. The program reads the data from this file and breaks the data into sweeps / segments and the range profile / channel response for each segment is extracted via FFT (see extracting the range profile on Chapter 4). After the channel responses have been obtained the mean response for that measurement is saved to be used in further processing.

MySignatecReader_GPR.m

```
clear all
clc
 Tch= 400e-6; %Chirp Duration
BW= 2.1e9; %Chirp Bandwidth
Fsam=20e6; %Sampling frequency of ADC
LastSampFirstSeg = 13034; % Last sample number of the First sweep
FirstSampSecSegment = 15034; % First sample of the second sweep
EndSize=2000-1; %
FirstData = 5034; % First sample number of the First sweep
numPos=1;
```

```
for posindex=1:1:numPos
  filename=horzcat('C:\Users\xavier\Desktop\GPR\Dec 12\Gated\testg');
  filename = [filename '.rd16'];
  fid=fopen(filename); % Open the file
  rawdata = fread(fid,'uint16'); % Reads the file containing the raw data
  fclose(fid);
  ch1data= rawdata(1:length(rawdata));
      % Convert data values in Volts
  R=2.2; %This is the pk-pk range in the ADC
  if ch1data>=32768;
     ch1data = (R/2) + ((ch1data/65532)*R);
     else ch1data = (-R/2) + ((ch1data/65532)*R);
  end;
  SegSize=Fsam*500e-6; % Number of sample per sweep or segment size
  BeginSize=1;
  aax = [ posindex ]
  EndSize = LastSampFirstSeg - FirstSampSecSegment -1;
  ch2data = ch1data(FirstData+1:end); % swapeed channels in Xavi's measurements
  for k=1:floor(length(ch2data)/SegSize)-1
     ch2dataTime(:,k)=ch2data(BeginSize+SegSize*(k-1):SegSize*(k)-EndSize);
  end   %ch2dataTime is a matrix with column representing sweep number
       %ch2dataFreq is a matrix with the FFT of each sweep for each column
  NFFT = 2^(nextpow2(size(ch2dataTime,1))+1);
  win = repmat(hamming(size(ch2dataTime,1)),1,size(ch2dataTime,2));%Hamming
  ch2dataFreq= fft(ch2dataTime.*win,NFFT);
     %Cut the image frequency (MATLAB artefact) and plot the AVG of the FFT
  ch2dataFreq=ch2dataFreq(1:round(size(ch2dataFreq,1)/2-1),:);
  freqaxis=linspace(0,Fsam/2,size(ch2dataFreq,1)); %up to half the sampling freq
  time = freqaxis * Tch/BW ;
  figure % Plot the mean impulse response
  plot(time*1e9,20*log10(mean(abs(ch2dataFreq'))),'k');
  axis([5 70 -20 40])
  xlabel('Time [ns]', 'FontSize', 16)
  title('Average Range Profile [dB] - Hamming win', 'FontSize', 16)
```

```
  grid on
  ch2dataFreqAvg(:,posindex)=mean(ch2dataFreq');
end
Test_gated = ch2dataFreqAvg;
save ('C:\Test_gated', 'Test_gated','freqaxis','BW','Tch','Fsam','-v7.3');
```

A.2 Delay-and-Sum Image Algorithm

The Code below is an example of the implemented delay-and-sum image algorithm (discussed in Chapter 2) used to create an image map of the radar scenario under test when FMCW or GFMCW waveform is used.

```
%% On this code quasi-monostatic so Tx-Rx is collocated is considered
clear all; close all; clc
Ant_InterSpace = 55; % Space between antennas
skin_thickness = 0;  % The Thickness of the skin
dgap  = 100;  % Space between antenna tip and the Phamton
tau_ant = [33.5]*1e-9;    % Relative Zero delay
Per = 2.5^2; % Medium Permitivity
Per_Ski = [30]; % Skin Permitivity
C = 3e8;  %Speed of light on free space in [m/s]
C = C*1e3;  % Speed of light on free space in [mm/s]

    %% Load the Range Profiles Data
file_locat = 'C:\Disk Metal\Profiles\MSeq3bit_Disk_Metal_I';
fileToRead  = horzcat(file_locat,'.mat');
rawData2 = load(fileToRead);  % Load the processed measurement data

S21_time = rawData2.Disk_Metal_I; %Extract the profile data
time =  (rawData2.freqaxis * rawData2.Tch)./rawData2.BW;  % Time axis
    %% Creating the Pixel Grid
 beggrid  = -20;
 xp1 = beggrid:2:dgap;  % Grid beginning to the soil surface
```

```
xp2 = dgap+2:2:450; % Soil surface to the end
yp = [-170:2:170]; % Pixel grid on Y - direction
Xp = horzcat(xp1,xp2); % Pixel X – direction

  %% Transmitter and Receiver Position
yr = (-130:10:130)+(-Ant_InterSpace/2);
yt = (-130:10:130)+(Ant_InterSpace/2);
xt = 0; xr = 0;
id = length(yt); % Number of transmitter

 %% Reshaping geometrical data for efficient MATRICIAL approach
XP1 = repmat(xp1,[length(yp) 1  length(yr)]);
XP2 = repmat(xp2,[length(yp) 1  length(yr)]);
YP1 = repmat(yp',[1 length(xp1)  length(yr)]);
YP2 = repmat(yp',[1 length(xp2)  length(yr)]);
yr_aux = reshape(yr,1,1,length(yr));
yt_aux = reshape(yt,1,1,length(yt));
YR1 = repmat(yr_aux,[length(yp) length(xp1) 1]);
YR2 = repmat(yr_aux,[length(yp) length(xp2) 1]);
YT1 = repmat(yt_aux,[length(yp) length(xp1) 1]);
YT2 = repmat(yt_aux,[length(yp) length(xp2) 1]);
 for ixb = 1:length(tau_ant)

   % Compute the delay from Tx - Pixel and Pixel - Receiver
   TOAtx1 = (sqrt((XP1-xt).^2)+sqrt((YP1-YT1).^2))./C;
   TOArx1 = (sqrt((YP1-YR1).^2+(XP1-xr).^2))./C;
   dair1 = dgap./(cos(atan((sqrt((YT2-YP2).^2))./(sqrt((XP2-xt).^2))))); %in [mm]
   dair2 = dgap./(cos(atan((sqrt((YR2-YP2).^2))./(sqrt((XP2-xr).^2))))); %in [mm]
   TOAtx2 = (sqrt((YP2-YT2).^2+(XP2-xt).^2)*sqrt(Per) - dair1.*(sqrt(Per)-1))./C -
skin_thickness.*(sqrt(Per_Ski)-1)./C;
   TOArx2 = (sqrt((YP2-YR2).^2+(XP2-xr).^2)*sqrt(Per) - dair2.*(sqrt(Per)-1))./C -
skin_thickness.*(sqrt(Per_Ski)-1)./C;
  delay = horzcat(TOAtx1+TOArx1,TOAtx2+TOArx2)+tau_ant(ixb); % Delay
```

```
   Antmatrix = abs((S21_time));
  for i=1:id  % For each Measurement Position
      aaa = Antmatrix(:,i);
      imag_matrix(:,:,i) = interp1(time,aaa,delay(:,:,i),'cubic'); % Image matrix
   end

   imag_matrix = sum((imag_matrix),3);  % Sum pixels
   imag_matrix_log = 20.*log10(abs(imag_matrix)); % Energy in log scale
   imag_matrix_log = imag_matrix_log - max(max(imag_matrix_log)); %Normalize
   im_dynamic_range = 15;  % Assign a dynamic range for the image
   ampl_clim = [max(max(imag_matrix_log))-im_dynamic_range
max(max(imag_matrix_log))];

   figure
   imagesc(Xp/10,Yp/10,imag_matrix_log,ampl_clim) % image in logscale
   xlabel('Down Range [Cm]');    ylabel('Cross Range [Cm]');
   title('Image of Pixel Logscale')
   grid;
   hold on;
   rectangle('Position',[22,-6.5,0.5,13],'Curvature',[0,0],...
          'LineWidth',2,'LineStyle','--')
 end
```

Appendix B: X-Y Positioner and Code

In Chapter 5 the hardware of the X-Y positioner systems and the control mechanism were introduced. The commands controlling the motion of the positioner axis are so called G-code and the control of the input or output systems are through the so called M-code (written in the VBA language). Both codes are loaded and run on the commercially available machine control software known as Mach-3, Figure B.1 shows the Mach-3 software environment.

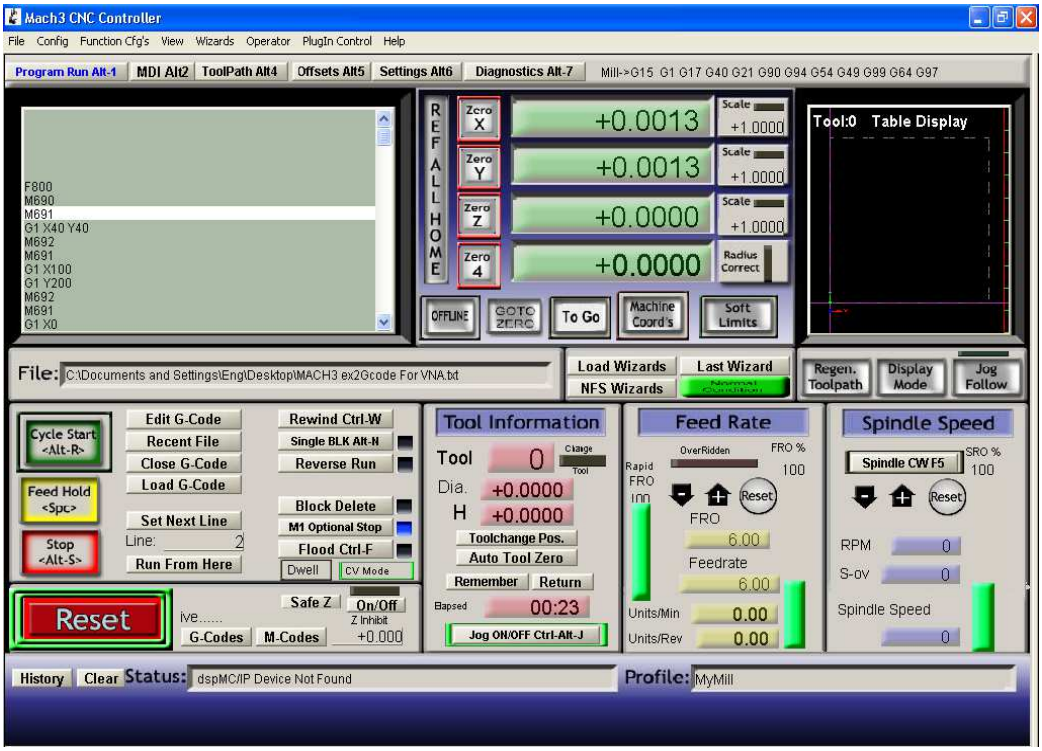

Figure B.1: Mach – 3 software

The basic synchronisation protocol between Mach-3 and radar system based on VNA have also been described in Chapter 5. Figure B.2 shows the graphical interface of the written visual basic program controlling the VNA. This program sets the VNA into trigger waiting mode. Once the VNA completes the measurement the program requests the measured data and saves it in a user's specified location in the PC in sequence. Furthermore, the VB program communicates with Mach-3 through some of the VNA input and output ports which are connected with the X-Y positioner I/O ports, respectively. Therefore, while the positioner is moving no

measurement takes place and vice versa. The input and output signals on Mach-3 are generated or read through the M-code.

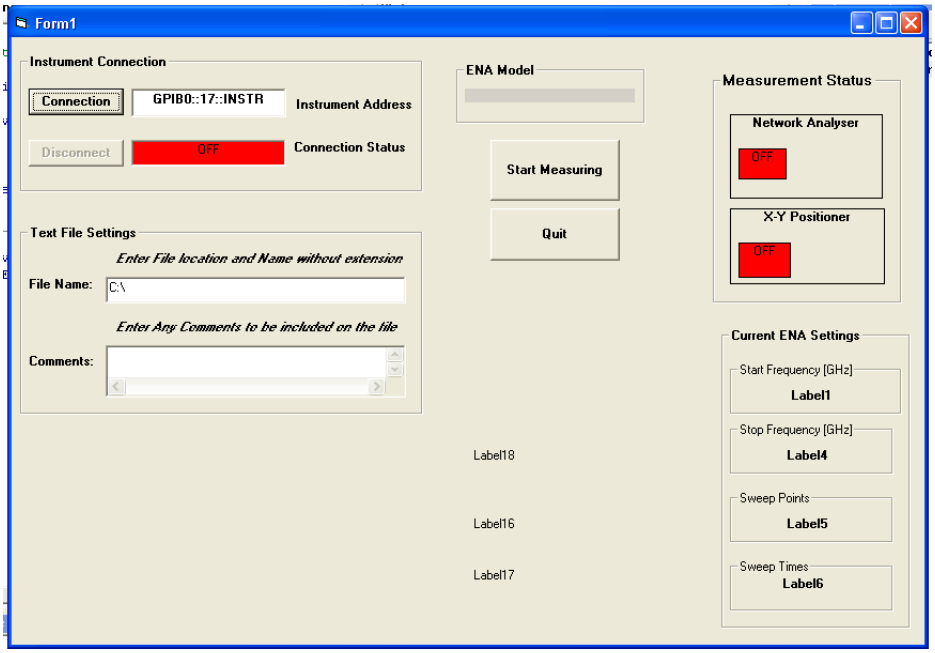

Figure B.2: Graphic interface of the VB script controlling the VNA

B.1 Example-1 of the Mach-3 G-code and M-code

In the example below the X-Y positioner is to move into coordinates (in mm) (0, 0); (40, 40); (100, 40); (100, 80); in sequence and radar based on VNA measurement is performed at each location.

F800 *' Sets the motor Speed*

G1 X0 Y0 *' Move to point P(0, 0)*

M692 *' Tells VNA that X-Y Move Completed*

M691 *' Check VNA Finished Measurement*

G1 X40 Y40 *' Move to point P(40, 40)*

M692 *' Tells VNA that X-Y Move Completed*

M691 *' Check VNA Finished Measurement*

G1 X100 *' Move to point P(100,40)*

M692 *' Tells VNA that X-Y Move Completed*

M691 *' Check VNA Finished Measurement*

G1 Y80 *' Move to point P(100, 80)*

M692 *' Tells VNA that X-Y Move Completed*

B.2 The M-code Script for M692

```
Option Explicit
Dim In1, In2 As Boolean ' Variable definition
Dim Res, LCK_vna, ACK_vna As Integer ' Variable definition

LCK_vna =0 ' Variable assignment to test the input of MACH3
ACK_vna = 1 ' Variable assignment to test the input of MACH3

Call SendFinish   ' MACH3 tells VNA that it finished moving
sleep(500)        ' Stays dormant for 0.5 s
Call getIn   'Scans the Input ports
While Res <> ACK_vna ' Checks for the VNA acknowledgement
        sleep(500)     ' Stays dormant for 0.5 s
        Call getIn  ' Scans the input signal
Wend    ' Repeat the while loop until test is true
Call SendUnLCK      'Mach3 sends the Unlock command (VNA free to measure)
sleep(500)        ' Stays dormant for .5 s
Call getIn       'Scans the Input ports
While Res <> LCK_vna     ' Check if the VNA as LCK (VNA in Measurement)
        sleep(500)  ' Stays dormant for 0.5 s
        Call getIn  ' Scan the input signal
Wend   ' Repeat the while loop until test is true

Sub getIn()  ' Scans the inputs Subroutine
        In1 = IsActive(Input1)  ' Get Input – 1 state
        In2 = IsActive(Input2) ' Get Input – 2 state
        If In1 = False And In2 = False Then Res  = 0
        If In1 = False And In2 = True Then  Res  = 1
        If In1 = True And In2 = False Then  Res  = 2
        If In1 = True And In2 = True Then   Res  = 3
End Sub ' End of the Subroutine

Sub SendFinish()  ' Mach-3 finished moving Subroutine
```

```
    deactivateSignal(OUTPUT1) ' Deactivate Output – 1
    activateSignal(OUTPUT2)   ' Activate Output – 2
    activateSignal(OUTPUT3)   ' Activate Output – 3
End Sub    ' End of the Subroutine

Sub SendUnLCK()    ' Mach-3 Tells VNA can Measure Subroutine
    deactivateSignal(OUTPUT1)     ' Deactivate Output – 1
    deactivateSignal(OUTPUT2)     ' Deactivate Output – 2
    activateSignal(OUTPUT3)       ' Activate Output – 3
End Sub    ' End of the Subroutine
```

B.3 The M-code Script for M691

```
' This Macro Is for the Mach-3 start of Movement, the following is done:
 ' 1 - Checks for the Move command  from the VNA and ACK once it is received
 ' 2 - Checks for the Unlock command from the VNA once received Sends a Lock

Option Explicit
Dim In1, In2 As Boolean ' Variable definition
Dim Res, Move_vna, UnLCK_vna As Integer  ' Variable definition

Move_vna = 2  ' Variable assignment to test the input of MACH3
UnLCK_vna = 3   ' Variable assignment to test the input of MACH3

Call getIn   ' Scans the input signals
While Res <> Move_vna ' Check if the VNA as sent a Move command
        sleep(1000)  ' Stays dormant for 1s
        Call getIn  ' Scans the input signal
Wend   ' Repeat the while loop until test is true

Call SendACK    ' Send an Acknowlodgement
sleep(500)  ' sleep for 500ms
Call getIn  ' Scans the input Signals
While Res <> UnLCK_vna ' Check if the VNA as sent the UnLCK command
```

```
        sleep(1000)  ' Stays dormant for 1s
        Call getIn 'Scans the input Signal
Wend   ' Repeat the while loop until test is true
Call SendLCK   'Lock or go into Busy state to start the Moving Command
sleep(500)  ' Stays dormant for 0.5s
Call getIn  ' Scans the input Signals
While Res <> Move_vna ' Check if the VNA as sent the UnLCK command
        sleep(1000)  ' Stays dormant for 1s
        Call getIn 'Scans the input Signals
Wend ' Repeat the while loop until test is true

Sub getIn()    ' Scans the inputs Subroutine
        In1 = IsActive(Input1)  ' Get Input – 1 state
        In2 = IsActive(Input2)  ' Get Input – 2 state
        If In1 = False And In2 = False Then Res  = 0
        If In1 = False And In2 = True Then  Res  = 1
        If In1 = True And In2 = False Then  Res  = 2
        If In1 = True And In2 = True Then   Res  = 3
End Sub

Sub SendAck()  ' Send Acknowledgement Subroutine
    activateSignal(OUTPUT3)                ‘Activate   Output   –   3
    activateSignal(OUTPUT1)    ' Activate Output – 1
    deactivateSignal(OUTPUT2) ' Deactivate Output – 2
End Sub     ' End of the Subroutine

Sub SendLCK()  ' Mach-3 Ready to Start moving Command Subroutine
    activateSignal(OUTPUT3)  ' Activate Output – 3
    activateSignal(OUTPUT1)    ' Activate Output – 1
    activateSignal(OUTPUT2)    ' Activate Output – 2
End Sub     ' End of the Subroutine
```

B.4 Example-2 of the Mach-3 G-code and M-code

The following is the example code to move the X-Y positioner into coordinates {in mm} (0, 10); (30, 10); (60, 20) in sequence with the positioner controlled by the user action (button pressed) to move onto next location. This was used for measurement experiments that do not involve the VNA, such as the on GPR scenarios where the X-Y positioner and radar based on AWG were used.

```
F800        ' Sets the motor Speed
G1 X0 Y10   ' Move to point P(0, 10)
M650        ' Check User actions
G1 X30      ' Move to point P(30, 10)
M650        ' 'Check User actions
G1 X60 Y20  ' Move to point P(60, 20)
```

B.5 The M-code Script for M650

```
Option Explicit
Dim In3 As Boolean ' Variable definition
Dim Res, MoveXY As Integer  ' Variable definition
MoveXY = 1  ' Variable assignment to test the input of MACH3
sleep(500)  ' sleep for 500ms
Call getIn  ' Scan the input Signal
While Res <> MoveXY ' Check button has been pressed
    sleep(500)  ' sleep for 500ms
    Call getIn 'Scan the input Signal
Wend ' Repeat the while loop until button is pressed true
MsgBox("Ready to Move") 'Pop-up box and program waits until ok is pressed
Sub getIn()  ' Scans the inputs Subroutine
    In3 = IsActive(Input3)        ' Get Input – 3 state
    If In3 = False Then Res  = 0
    If In3 = True Then  Res  = 1
End Sub   ' End of the Subroutine
```

Appendix C: Channel Characterization and Performance Prediction

As the need for higher data rate and the number of wireless technologies increases it is foreseen that future wireless systems and networks will rely on some or a combination of techniques, such as: ultra-wideband, multiple antennas techniques (MIMO, SIMO, MISO), and multiband spectrum usage, to mitigate impairments and to cater for the high speed demand. This chapter starts by presenting the results of MIMO measurement campaign performed within a reference environment, namely "Reverberation Chamber" to assess the channel capacity and diversity gain of UWB Discone antennas with variable inter-element spacing. Furthermore, results of the channel measurement campaigns in both indoor and outdoor environments using a newly designed and developed multiband channel sounder will also be presented. The bit error rate performance comparison of the in-house developed measurement based channel simulator with the widely used Matlab multipath channel simulator will be given. At the end of the appendix, numerical simulation results of the designed UWB Discone antenna will be detailed.

C.1 Reverberation Chamber MIMO Channel Characterization

A reverberation chamber is a room designed to create a diffused or random incidence electromagnetic wave. Unlike the anechoic chamber, in which the walls are made of absorbing structure or material, the reverberation chamber is normally an enclosed room of highly reflective material in which the inside is equipped with paddles of asymmetric shapes fixed on one or more turntables. Due to the large echoes produced in the chamber any movement or rotation of the turntable causes the behaviour of the electromagnetic field strength within the chamber to change. In fact, the field strength may change, at any point within the chamber, from a maximum to a minimum (or vice versa) as the movement of the stirrers change the boundary conditions [1, 2]. Reverberation chambers offer the advantage of providing a reference and controlled environment in which repeatable Rayleigh fading statistics can be created easily. As previously reported in the literature the electromagnetic

fields inside the reverberation chamber have characteristics similar to that of a multipath fading environment associated with mobile communication in indoor and urban scenarios [1-3].

It is well known that the radio propagation channel, especially where multipath exists, negatively affects the performance of the mobile communication system. It is envisaged that future wireless systems will rely on multiple antenna techniques (such as MIMO) in order to mitigate the impairments caused by multipath propagation [4, 5]. Therefore, there is still a need to fully understand and characterize the figure of merit of the implementation of MIMO in a multipath environment such as that provided by the reverberation chamber. In this section a 2x2 MIMO figure of merit, such as diversity and capacity, for UWB (ultra-wideband) antennas with different inter-element spacing are analysed. Related work on MIMO figures of merit in a reverberation chamber have been reported in [3, 6, 7], but unlike the work reported here, those measurements involved narrowband antennas.

Selection combining diversity, which involves monitoring all the Tx-Rx antenna links and selecting the link exhibiting the highest signal-to-noise ratio at its output, was adopted in this section to evaluate the multi-antenna element diversity gain. The choice of using selection combining technique is merely due to its simplicity and also as a proof of concept. The diversity gain in this case relates to the enhancement / increase in the SNR due to the combination of the received signals.

The UWB MIMO capacity was estimated as the average of the narrowband capacity using equation (C.1):

$$C_{UWB} = \frac{1}{N_f}\sum_{i=1}^{N_f} log_2\left[det\left(I_{n_R} + \frac{\rho}{n_T} H_i {H_i}^H\right)\right] \qquad \text{(C.1)}$$

where: ρ is the signal-to-noise ratio (SNR), N_f number of sub channels, n_R and n_T number of antennas at the receiver and transmitter respectively, *det(.)* matrix determinant, H_i is the n_R x n_T matrix containing the sampled channel transfer function for each sub-channel *i,* and $(.)^H$ is the complex transpose of the matrix. The MIMO channel matrix used in (C.1) was normalised with the Frobenious normalization, described in [8], to provide an average gain of unity.

C.1.1 Measurement Methodology

Measurements were performed within the National Physical Laboratory's (NPL) reverberation chamber using a four-port vector network analyser (VNA). Figure C.1 shows the MIMO LOS measurement set-up inside the chamber. The dimensions of the chamber are equal to 6.55 m x 5.85 m x 3.5 m and the operating frequency range is between 0.17 GHz up to 18 GHz. Four UWB discone antennas connected to individual ports of the VNA through long SMA cables were used throughout the measurements. The VNA was set to operate in the frequency range of 2-6 GHz with 25 MHz steps resulting in a total of 161 frequency points across the band. Moreover, the transmit power was configured to 0 dBm. Before the desired measurements were carried out the VNA was calibrated to compensate for the cable and connector losses. The transmitting and receiving antennas were set in the LOS and Non-LOS configuration with a distance between the masts shown in the diagram in Figure C.2. The heights of the masts were 135 cm for A and 150 cm for B, respectively.

A number of LOS and NLOS 2x2 MIMO measurement scenarios were created by changing the inter-element spacing between antennas on the same mast. The possible inter-element antennas spacing were 5.5 cm, 11 cm, and 16.5 cm designated as small, medium and large respectively. In each scenario, measurements were performed for each of the 200 chamber's stirrer position which allows adequate statistics to emulate a Rayleigh fading process.

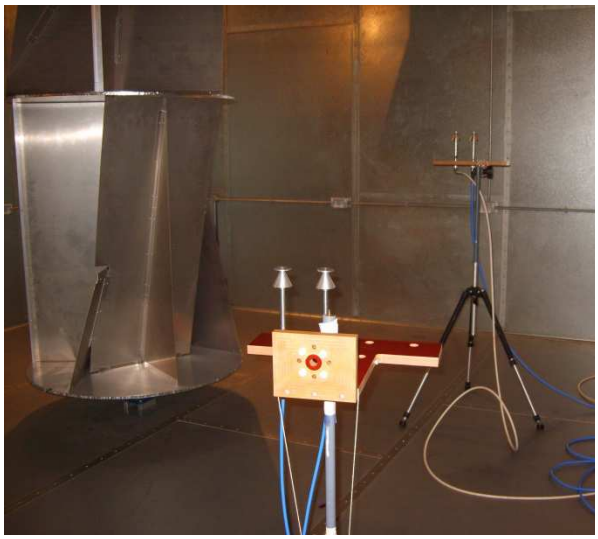

Figure C.1: Line of sight 2x2 MIMO configuration in the reverberation chamber

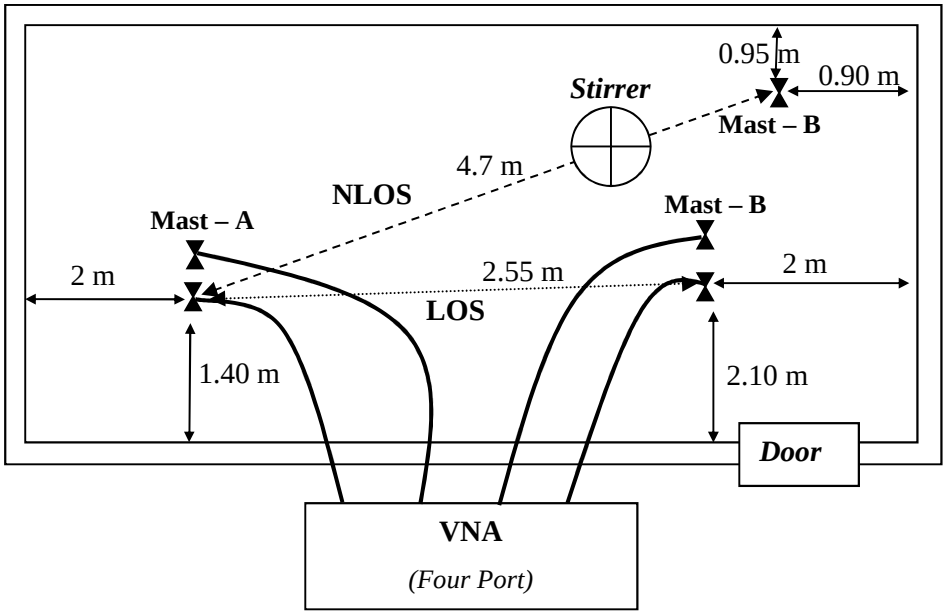

Figure C.2: Antenna mast distances and measurement topology in the chamber

C.1.2 Results and Analyses

For statistical fitting purposes the four individual single input single output (SISO) channels of the 2x2 MIMO matrix were merged into a single data pool and the goodness of fit to a Rayleigh distribution were tested using the Kolmogorov-Smirnov (K-S test) function available in Matlab. The results and the test give a good fit to the Rayleigh distribution in both LOS and NLOS scenarios as presented in Figure C.3 (a)-(b) for the Small – Small antenna separation at frequencies 2 GHz, 4 GHz and 6 GHz respectively.

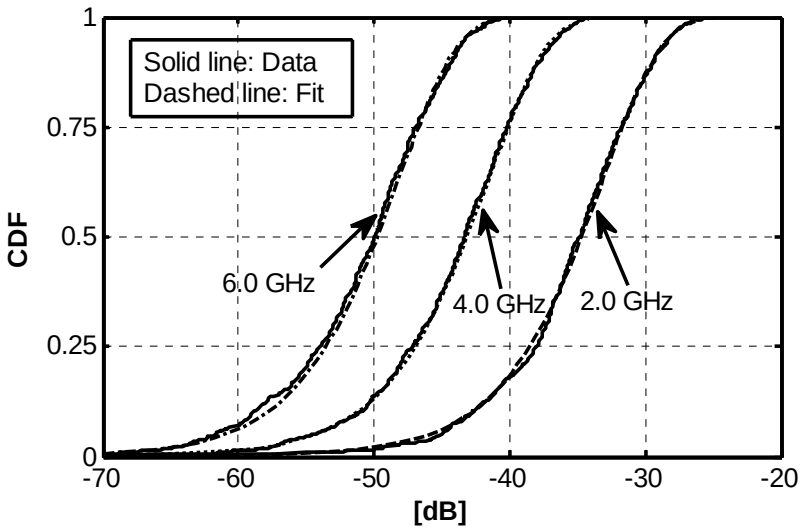

(a)

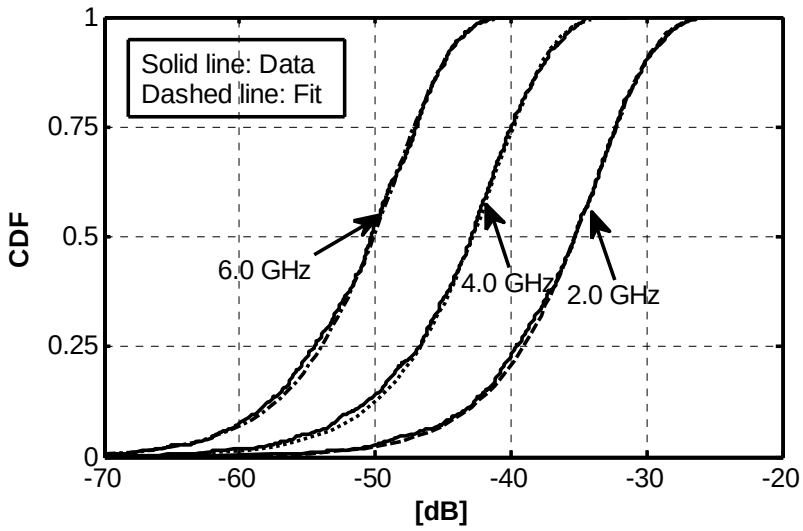

(b)

Figure C.3: CDF of the Small – Small measurement channels and its Rayleigh fitting in (a) LOS case, and (b) NLOS case

The 2x2 MIMO channels were arranged to create SIMO (1x 2) and MISO (2x1) channel configurations. The apparent antenna diversity gain was computed for both channel configurations for LOS and NLOS scenarios using the selection combining technique. Figure C.4 (a)-(b) gives the CDF of the received signal strength for the 2x1 channel configurations, in which the diversity branch is created by selecting the strongest signal between the two antenna links, in both LOS and NLOs scenarios for large – large (LL) inter-element antenna separation at 2 GHz.

The diversity gain is estimated as the difference between the diversity branch and the strongest link taken at 50 % of the CDF value.

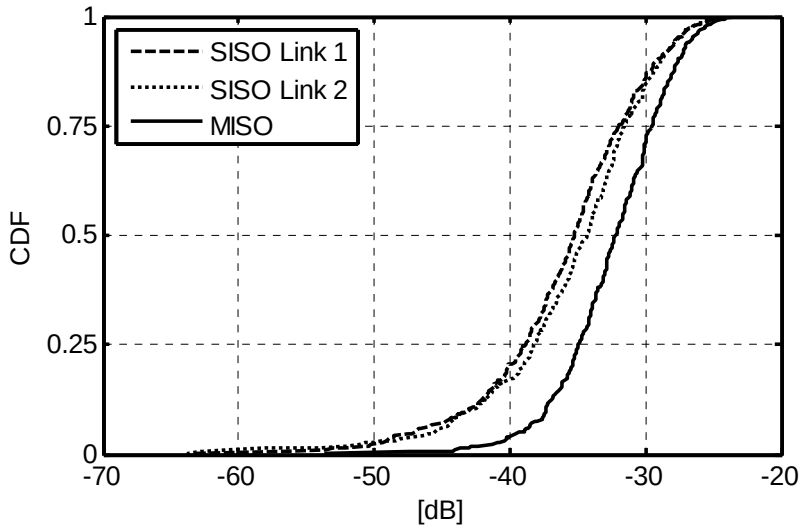

(a)

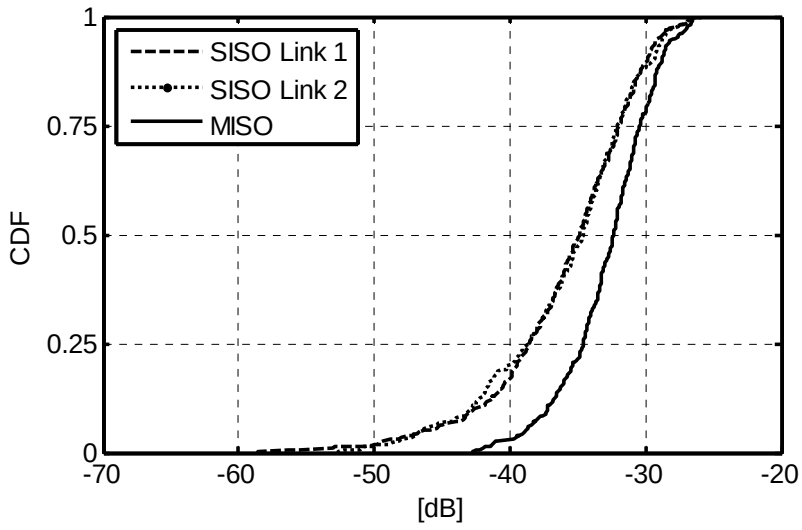

(b)

Figure C.4: CDF of MISO channels for LL antenna spacing at 2 GHz (a) LOS and (b) NLOS

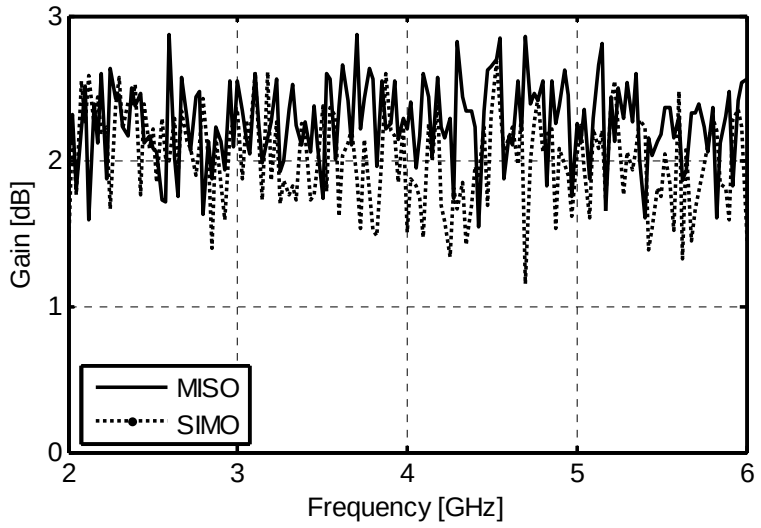

(a)

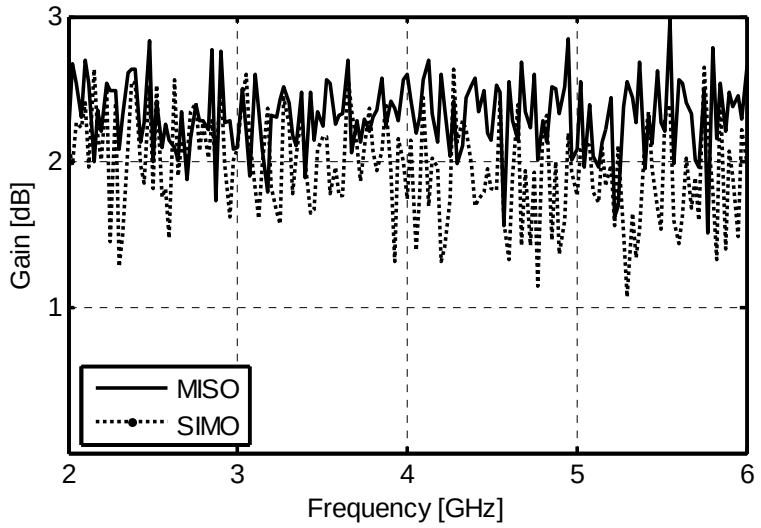

(b)

Figure C.5: Diversity gain for LL antenna spacing in (a) LOS and (b) NLOS

Table C.1 gives the overall summary of the MISO and SIMO median diversity gain for the different antenna configuration cases at frequencies 2, 4 and 6 GHz as well as the average value across the frequency band. It can be seen from the table that the apparent diversity gain using selection combining technique is between 1.4-2.7 dB.

Figure C.6 (a)-(b) display the normalised 2x2 MIMO channel capacity for 30 dB SNR for the LOS and NLOS cases in the reverberation chamber. Table C.2 gives a summary of the capacity values at 90% CDF for the different antenna spacing at both the transmitter and receiver. The values are seen to be similar as both LOS and NLOS sets of data in the reverberation chamber exhibited Rayleigh fading.

Table C.1: Diversity gain for different inter-element antenna spacing

	Diversity Gain [dB] at CDF = 50%							
	2 GHz		***4 GHz***		***6 GHz***		***Mean***	
Case	***LOS***	***NLOS***	***LOS***	***NLOS***	***LOS***	***NLOS***	***LOS***	***NLOS***
MISO (L,L)	2.04	2.24	2.22	2.60	2.56	2.66	2.27	2.32
SIMO (L,L)	1.48	2.10	1.51	1.75	1.45	1.99	2.02	1.96
MISO (L,M)	1.91	1.71	2.39	2.15	2.10	2.63	2.3	2.30
SIMO (L,M)	2.32	2.43	1.51	2.36	1.92	2.36	1.97	2.00
MISO (L,S)	2.26	2.25	2.40	1.85	2.44	2.53	2.28	2.29
SIMO (L,S)	2.12	2.42	1.76	1.86	1.81	1.94	1.95	1.99
MISO (M,M)	2.38	2.28	2.63	2.30	2.79	1.44	2.27	2.29
SIMO (M,M)	2.09	2.28	2.35	1.69	1.26	1.62	1.97	2.00
MISO (M,S)	2.13	2.58	2.08	2.37	1.64	2.62	2.26	2.28
SIMO (M,S)	1.90	1.64	2.68	2.16	2.07	1.73	1.92	1.92
MISO (S,L)	2.56	2.43	2.32	2.22	2.38	2.55	2.27	2.32
SIMO (S,L)	1.85	1.68	2.04	1.67	1.74	1.56	1.89	1.94
MISO (S,S)	2.43	2.43	2.63	2.25	2.19	2.66	2.27	2.30
SIMO (S,S)	2.38	2.13	2.24	1.80	2.12	2.56	1.99	1.93

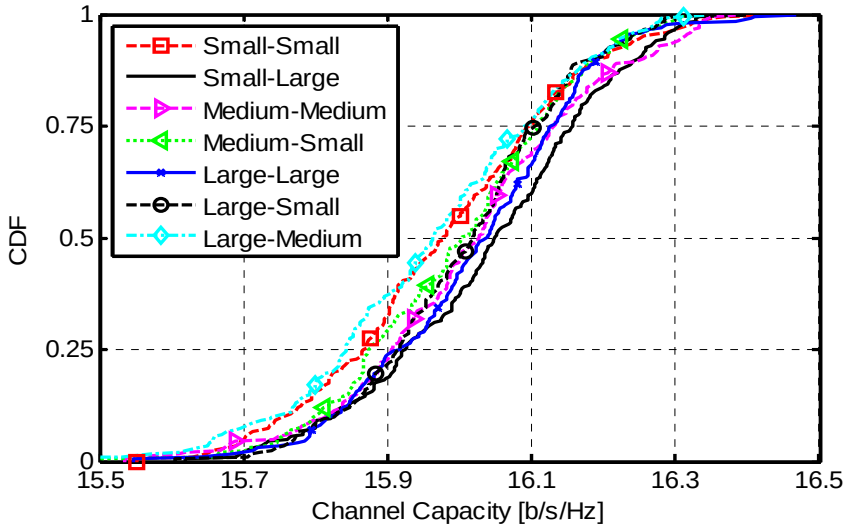

(a)

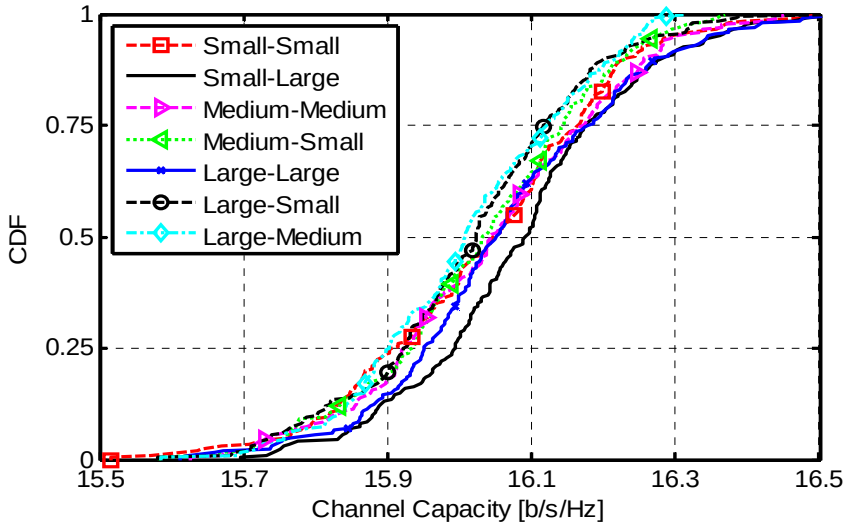

(b)

Figure C.6: 2x2 MIMO channel capacity for different antenna separation in (a) LOS and (b) NLOS

Table C.2: 2x2 MIMO capacity [B/s/Hz] at CDF = 90%

	SS	**SM**	**MM**	**SL**	**LS**	**LM**	**LL**
LOS	16.20	16.19	16.26	16.24	16.19	16.18	16.20
NLOS	16.23	16.23	16.26	16.28	16.20	16.22	16.27

C.2 Multiband Channel Characterization

This subsection presents the channel characterization results in terms of delay spread and path loss parameters obtained through indoor and outdoor channel measurements in the 2 GHz and 60 GHz bands using a newly in-house developed multiband chirp based channel sounder.

C.2.1 Multiband Chirp Sounder

Figure C.7 shows the basic block diagram of the multiband channel sounder.

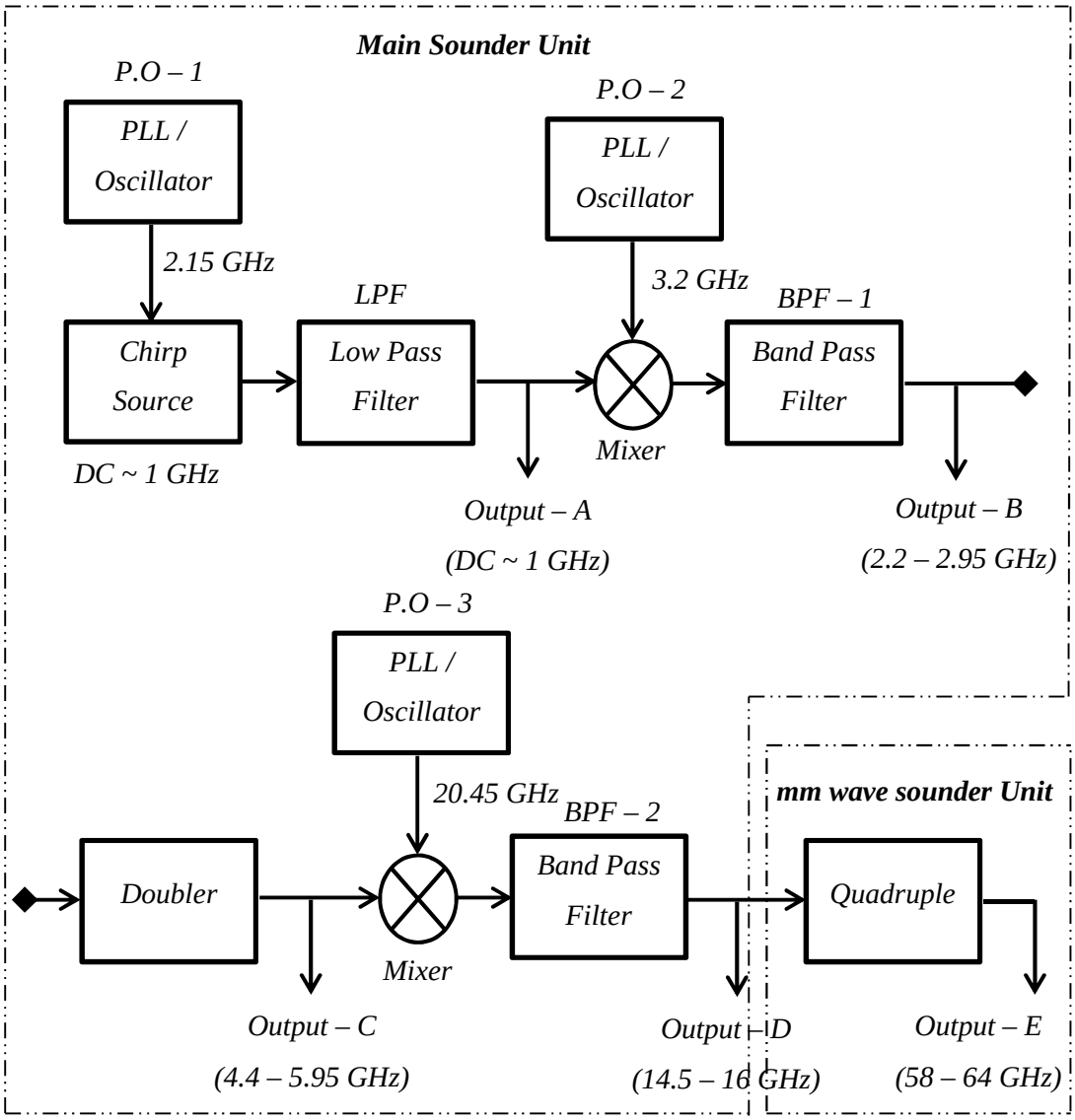

Figure C.7: Basic block diagram of the in-house built Multiband Chirp Sounder

The developed multiband channel sounder is based on FMCW or chirp signal technique (see: *Chapter 4* for theoretical discussion on FMCW signal). At the transmitter side the chirp parameters (duration and frequency range) are user-defined

and programed into the direct digital synthesiser (*chirp source*) which is clocked at 2.15 GHz generated by PLL / oscillator (*P.O – 1*) source. The synthesiser generates baseband signals up-to a frequency of ~ 1 GHz. Its output is first low pass filtered in order to remove the high frequency components which the synthesiser generates by default. The filtered signal is used as output (*output – A*) for channel measurements in the lower frequency band up to 1 GHz. The same signal is up-converted into 2.2-2.95 GHz by mixing it with a 3.2 GHz clock generated by the PLL / local oscillator (*P.O – 2*) and band pass filtering (*BPF – 1*) the resultant product with a filter of 750 MHz bandwidth. The up-converted signal is also used as output (*output – B*) for channel measurements. For higher frequency measurements the up – converted signal is further multiplied by two to generate a signal with a maximum bandwidth of 1.5 GHz in the 4.4-5.95 GHz band (*used as output - C*) and furthermore this is up – converted to 14.5-16 GHz band (*used as output - D*) using the PLL / oscillator (*P.O – 3*) of 20.45 GHz clock source and a band pass filter (*BPF – 2*). The main sounder unit and its synchronisation unit are shown in Figure C.8.

The 14.5-16 GHz signal output also serves as input into the mm wave unit in which the signal is quadrupled to generate an output (*output – E*) signal of 6 GHz maximum bandwidth in the 60 GHz band. Figure C.9 shows a picture of the "*mm wave sounder unit*" with horn antennas connected to its output.

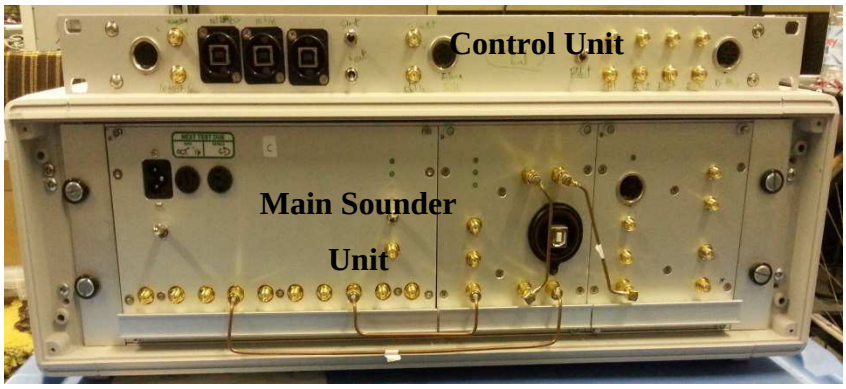

Figure C.8: Transmitter part of the Main Sounder Unit together with its Control Unit

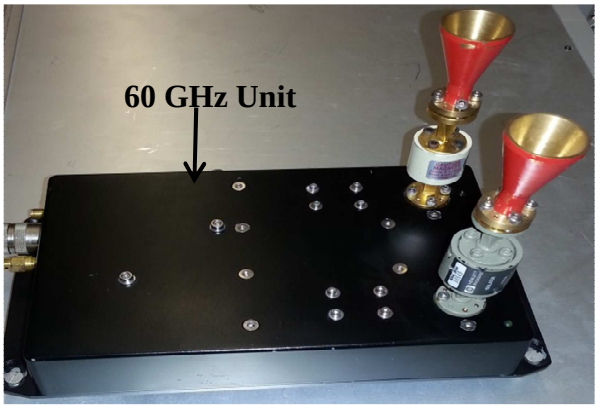

Figure C.9: The transmitter part of the 60 GHz unit

The receiver has similar architecture with the additional heterodyne mixer and low pass filter to generate the beat-note. The beat-note signals are digitised for off-line processing. The frequency bands up to 14.5-16 GHz are currently based on single input single output architecture with the possible use of a fast RF switch for multiple antenna applications. On the other hand the 60 GHz band has two parallel transmitters which are switched on and off sequentially every sweep and two parallel receivers for simultaneous acquisition. The minimum chirp or sweep duration in the sounder is 204.8 µs. The computation of the RMS delay spread and the path loss exponent were performed using equations 3.74 and 5.43 presented in reference [9].

C.2.2 Measurement and Results in the 2 GHz band

Radio channel propagation measurements at 2 GHz band were performed under the Open Call – 1 of the Cognitive Radio Experimental World (CREW) project in three test beds, namely: office environment at the Technical University of Berlin (TUB), air cabin in EADS, and semi – shielded industrial environment in iMinds. SISO channel measurements were conducted with the sounder set to a centre frequency of 2.475 GHz, a bandwidth of 0.55 GHz and chirp repetition rate of ~1.1 kHz. The sounder's transmit power was set to 26 dBm. The antennas were placed (were possible) in close proximity to the node(s) in the test beds. In the case of TUB the transmitting / receiving antennas were placed either at the ceiling level (2.6 m) or at 1.5 m with the measurements performed in the office and corridor environments. In iMinds both antennas were mounted at similar height to the nodes at about 1.5 m, whereas, for the air cabin in EADS the antennas were mounted at a different height to replicate the scenario such as access point to access point, ceiling

to laptop, and ceiling to trolley. Measurements were taken at various positions of Tx / Rx distances within the scenario under consideration. At each position, measurements were recorded for one second duration. Figure C.10 shows example of the normalised 1s average power delay profile (PDP) in the semi-shielded environment in iMinds. Table C.3 provides a summary of the RMS delay spread presented in Figure C.11.

Comparing the results of the office environment at 2.6 m and 1.5 m, the RMS delay spread for the lower antenna height is generally higher when the antenna is placed at 1.5 m. This is due to the higher attenuation experienced at the ceiling level due to the construction of the building which had beams below the ceiling. Overall, the semi-shielded environment at iMinds presents the highest RMS delay spread. This is mainly due to the large number of metallic structures such as pipes therefore leading to a large number of reflections.

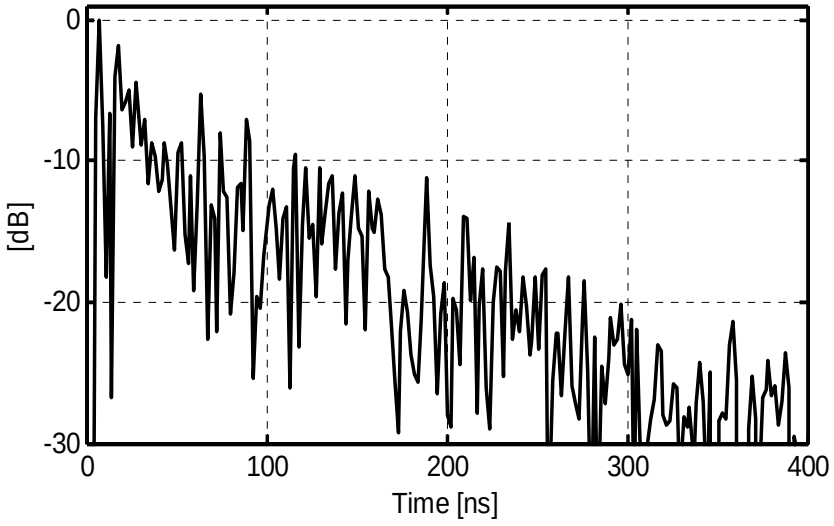

Figure C.10: Channel PDP in iMinds semi-shielded environment

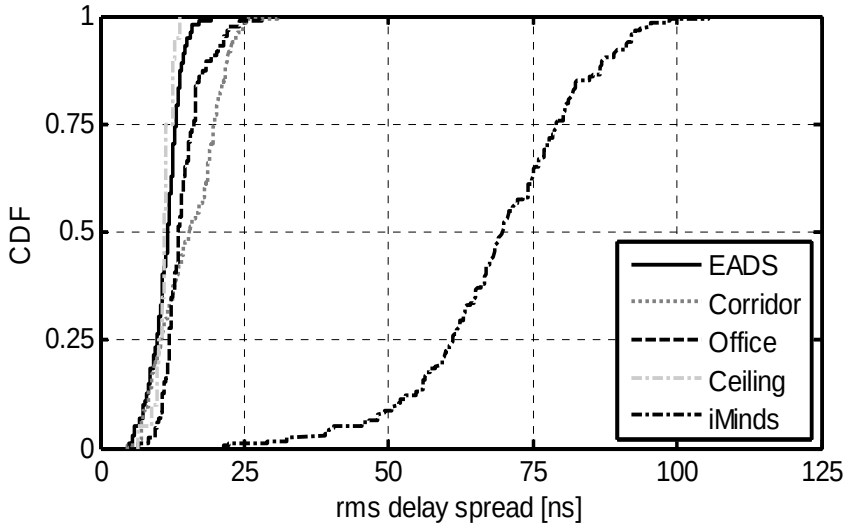

Figure C.11: The CDF of the RMS delay spread in different scenarios

Table C.3: Obtained RMS delay spread for different values of CDF

	Technical University of Berlin			**iMinds**	**EADS**
CDF level	*Office Tx/Rx @ 2.6 m*	*Office Tx/Rx @ 1.5 m*	*Corridor Tx/Rx @ 1.5m*	*Semi shield*	*Air Cabin*
10 %	8 ns	10.74 ns	8.49 ns	51.5 ns	7.98 ns
50 %	11 ns	13.74 ns	18.53 ns	69.2 ns	11.89 ns
90 %	12.5 ns	20.15 ns	25.16 ns	87.2 ns	14.47 ns

In addition to the RMS delay spread the path loss for the TUB measurement with both transmit and receive antennas at ceiling height (2.6 m) and for the iMinds environment were computed as shown in Figure C.12 (a)-(b). The path loss coefficient factor 'n' which is a measure of the loss rate of change as a function of distance was estimated by the gradient of the empirical loss polynomial fit line. The estimated path loss coefficients for these two environments were found to be n = 4.4 for the office environment when the antennas are placed close to the ceiling and n = 3.3 in the semi-shielded environment where a large number of reflectors are present due to the metallic structures.

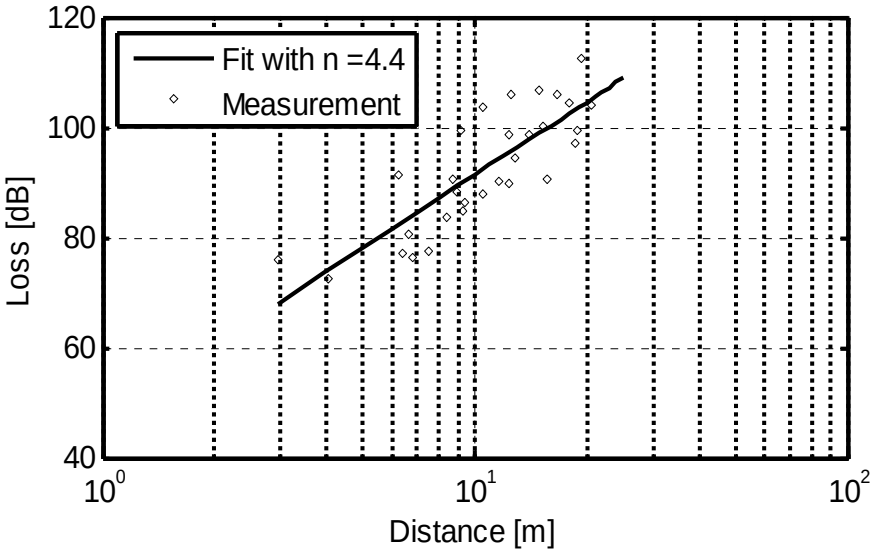

(a)

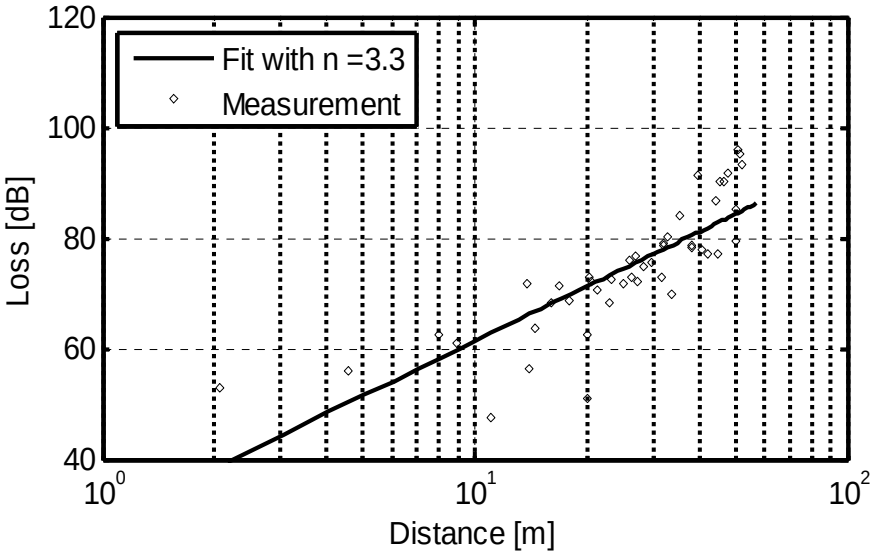

(b)

Figure C.12: Estimated path loss coefficient in (a) TUB and (b) iMinds

C.2.3 Measurement in the 60 GHz Band

Currently, there is a great deal of interest within the research community in using the mm wave band e.g. the 60 GHz band to provide short range high speed communication in both indoor and outdoor environments [10-12]. This interest is mainly fuelled by the limited bandwidth and spectrum overcrowding in the lower frequency bands. Consequently, the millimetre wave band is viewed as a solution for higher data rates in future short range wireless communication systems, such as: wireless LAN, on-body communication, back-haul and outdoor lamp-post to user content delivery. In this sub-section results of the RMS delay spread and path loss of the measured channel using the in-house built multiband channel sounder in the 60 GHz band in both indoor and outdoor scenarios are presented. The sounder was configured for a bandwidth of 4.4 GHz, a transmit power of 7 dBm and chirp duration of 0.82 ms. To enable the 2x2 MIMO measurements two-way switching at the transmitter was used while receiving in parallel. Directional horn antennas were used in both the transmitter and receiver. Measurement data were recorded using a 14 bit ADC for one second at each location while the receiver was stationary.

Indoor Scenario and Results

In this scenario, the receiver was held in a fixed location with the 60 GHz unit mounted close to the ceiling at 2.35 m whereas the transmitter was moved at pre-defined positions with its antenna height of 1.46 m, as shown Figure C.13.

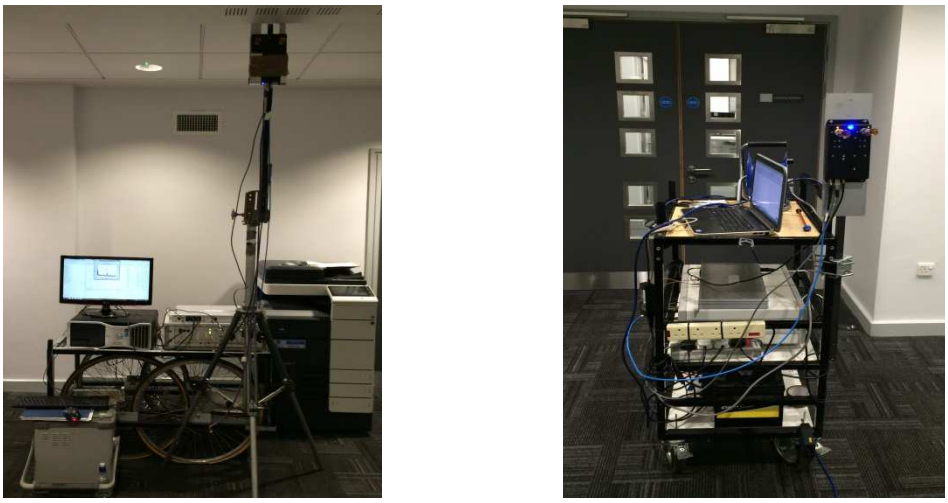

Figure C.13 Indoor scenario (left) receiver unit set-up, (right) transmitter unit set-up

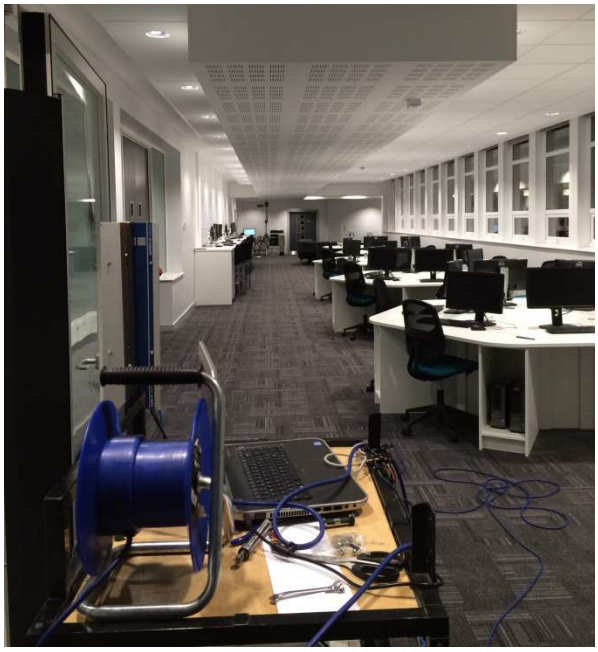

Figure C.14: Indoor measurement scenario

The measured environment is shown in Figure (C.14) where it can be seen to consist of workstations with computers, a light well on the right hand side and offices on the opposite side. The measurements were taken along a path starting from a distance of ~9.4 m to a distance of 35 m. Recorded measurement data were analysed to estimate the RMS delay spread for different threshold values and the path loss exponent. Figure C.15 displays the power delay profile of one of the Tx – Rx links in the last measurement position.

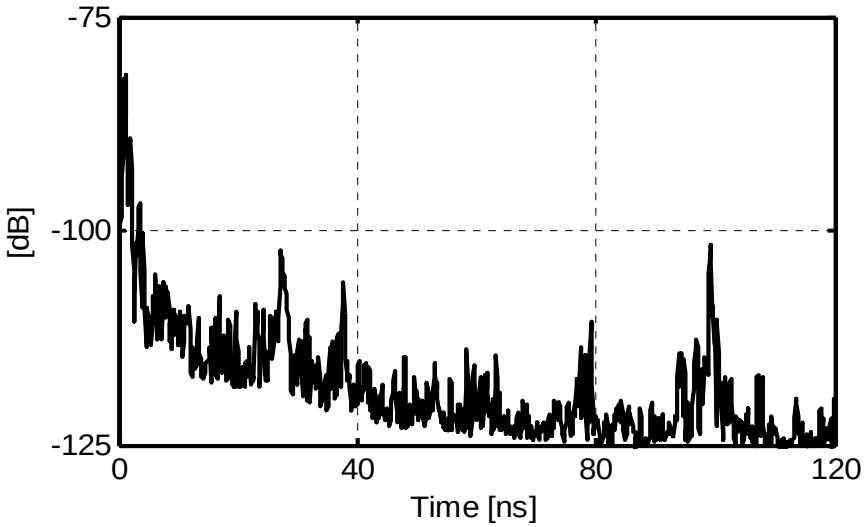

Figure C.15: PDP for the antenna Tx2 – Rx2 link

As the SNR in all the measurement positions is at least 40 dB the RMS delay spread was computed for different threshold levels namely 20 dB, 30 dB, and 40 dB.

The resulting RMS delay spread for the four channels combined at different threshold levels is shown in Figure C.16. Taking the median values (50 % CDF) gives an RMS delay spread of 0.42, 5.13, and 8.46 ns for the 20, 30, and 40 dB thresholds respectively and corresponding 90% values equal to 1.33, 10.74 and 14.46 ns.

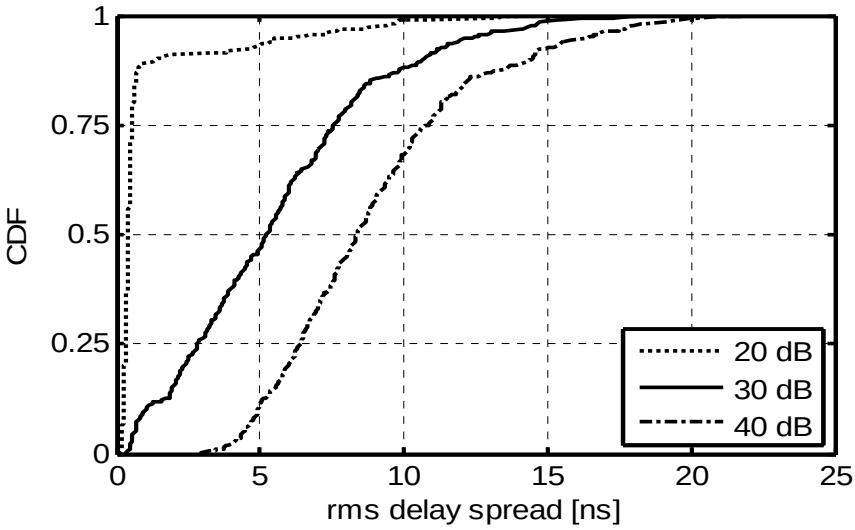

Figure C.16: CDF for the combined links RMS delay spread

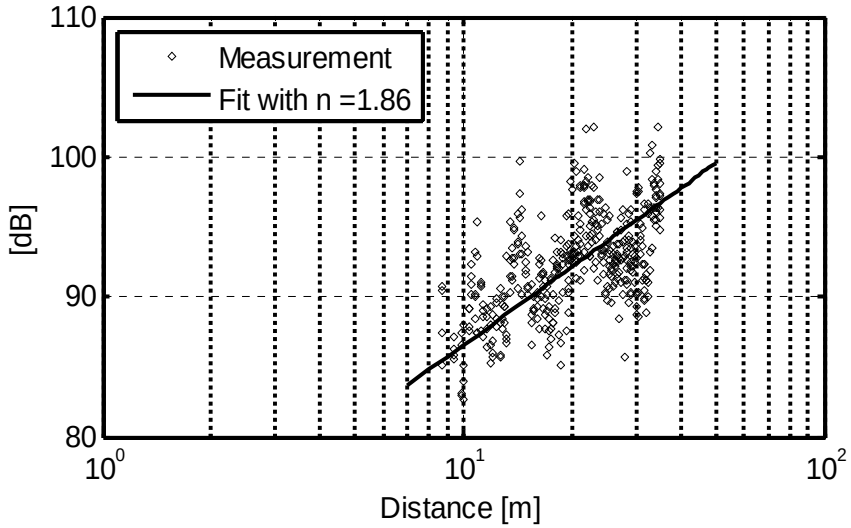

Figure C.17: Estimated channel path loss coefficient for the combined links

The RMS delay spread is smaller at 20 dB threshold due to the fact that at this level the PDP mainly captures the dominant components whereas for the lower thresholds the farther away components are included. The extent of the RMS delay spread in the measured environment could be due to the glass windows surrounding

the space and the glass door which led to a highly reflective surface. Figure C.17 shows the channel path loss for the four MIMO channel links combined. The value of 1.86 was estimated as path loss coefficient from the polynomial fitting line. A lower coefficient than that of free space path loss (n = 2) was expected as the scenario resembles a wide corridor.

Outdoor Scenario and Results

Like the previous scenario the receiver was fixed while the transmitter mounted on a trolley was moved in predefined positions. The heights of the antennas were 1.50 m and 2.35 m for the transmitter and the receiver respectively. Measurements were performed over a distance from 28 m up to 178.42 m in almost a straight line. The data were calibrated and analysed for RMS delay spread and path loss. Figure C.18 shows a view of the scenario in question with the stationary receiver system with a computer positioned close to the car barriers outside the building, housing the Engineering and Computing Sciences Department, and the mobile transmitter system just away from it. Figure C.19 provides a representation of the trajectory of the transmitter unit (represented with black triangle) on the university campus map, while the receiver unit (represented in black circle) remained fixed.

Figure C.18: Outdoor measurement scenario

Figure C.19: Representation of the Transmitter trajectory on campus map

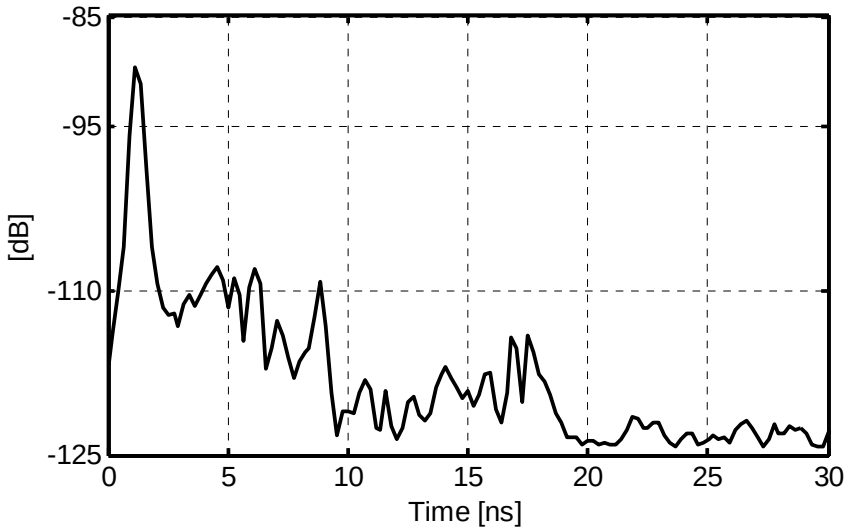

Figure C.20: PDP for the Tx2 – Rx2

Figure C.20 displays an example of a SISO link measured power delay profile at a particular location. The dynamic range for most of the measured profiles exceeded 25 dB hence the RMS delay spread channel parameters were estimated for two threshold levels: 20 dB and 25 dB down from the peak. The data from the four channels were processed to estimate the RMS delay spread and the path loss from the area under the power delay profile. Figures C.21 and C.22 show the RMS delay spread and path loss of the combined SISO links. The results of the RMS delay spread for 20 dB and 25 dB threshold are summarised in Table C.4 for 50 % and 90% value as obtained from the CDF curves. The path loss coefficient (n) was estimated as 1.93 a value which is much closer to the free space path loss.

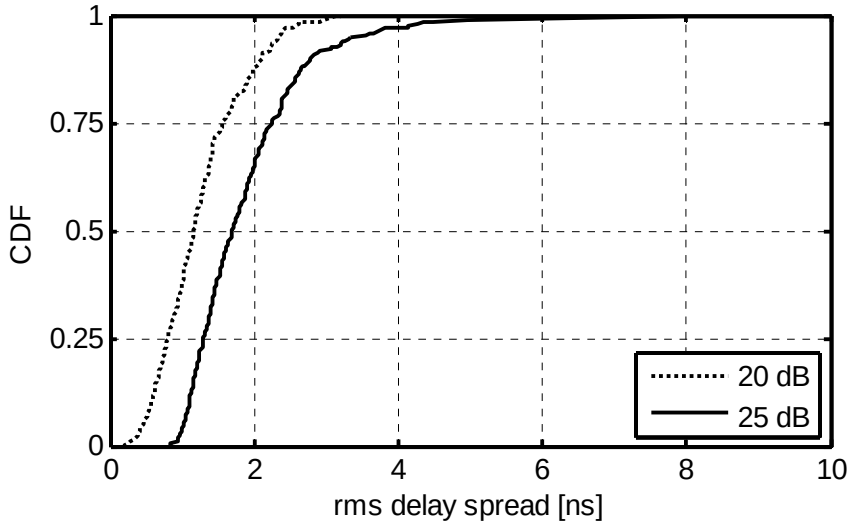

Figure C.21: CDF for the combined links RMS delay spread

Table C.4: Summay of the RMS delay spread for 20 and 25 dB threshold

	Individuals Tx – Rx channels		**Combined Tx – Rx channels**	
	SNR = 20 dB	*SNR = 25 dB*	*SNR = 20 dB*	*SNR = 25 dB*
50 % CDF	1.00 – 1.28 ns	1.42 – 1.96 ns	1.67 ns	1.70 ns
90 % CDF	1.91 – 2.29 ns	2.42 – 3.32 ns	2.12 ns	2.79 ns

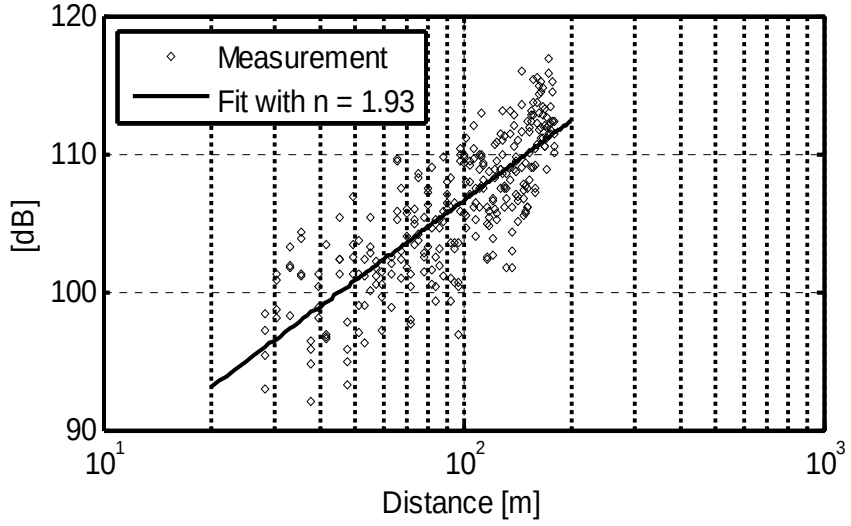

Figure C.22: Estimated channel path loss coefficient for the combined links

C.3 Radio Channel Performance Prediction

There are many ways in which to predict the performance of the radio system, these could be: analytically through theoretical models, or by the use of a software simulator or hardware emulator. Alternatively, one can also predict the system performance by re-creating the channel from the parameters estimated from the measurements or by using the actual channel measurements data of a typical environment [9].

Radio channel simulators are used to emulate the effects of the propagation channel under diverse repeatable testing conditions in order to aid in the estimation and assessment of the performance of communication systems. The simulators can be constructed either in the time domain using the finite impulse response transversal filter, commonly referred as the tapped delay line, or in the frequency domain using the channel time variant frequency function T(*f,t*) [13, 14]. The output signal of a tapped delay line model is a linear convolution of the channel delay spread function and the input signal in time, whereas for the frequency domain simulator the convolution is performed in frequency through point wise multiplication of the input signal spectrum and the channel frequency response.

In this chapter, the performance, in terms of bit error rate (BER) comparison, of the 'playback' based channel simulator designed in [13, 15], which uses the actual channel measurements in the form of time variant frequency function, with the standard tapped delay line multipath fading channel simulator built-in in MATLAB SIMULINK [16], which recreates the channel responses based on the user's specified parameters, have been validated. In this case the user's specified parameters were estimated from the same measurement data used in the playback simulator.

Both simulators were used in conjunction with the IEEE 802.16 physical layer model designed in [15]. The performance of the channel simulators were computed with the physical layer model configured with 256 OFDM carriers, a modulation order of 16 QAM and with ¾ rate channel coding. In the simulations the transmitted OFDM signal is fed into the channel followed by an addition of a complex Gaussian noise and the resultant signal is fed into the receiver for demodulation, detection and BER estimation.

The used channel measurement data were obtained from the channel sounding in rural / semi-rural environment around the city of Ipswich (U.K) in both 3.5 GHz and 5.8 GHz frequency bands. The method of moment and the complex based estimator were used to extract the necessary parameters needed to configure the Matlab multipath channel simulator.

C.3.1 Channel simulators

Multipath fading Channel Simulator

This subsection gives a brief overview of the simulator and a more in-depth explanation can be found in reference [16]. The multipath fading channel simulator is based on the tapped delay line model and it is able to simulate both the channel time selectivity due to Doppler spreading and frequency selectivity due to time spreading. The simulator requires user specified channel parameters such as: the relative time delay and amplitude of the multipath component(s), as well as the maximum Doppler frequency and the Doppler spectrum type. For a Rician channel the multipath component(s) K-factor (*K*), line of sight (*LOS*) Doppler shift and initial phase are also needed.

The effect of time selectivity of the propagation channel is created by generating (independently) an interpolated complex Gaussian fading process with the desired spectral properties and average power for each user defined multipath. The desired spectral property (*Doppler spectrum shape*) of the i^{th} multipath component is achieved by filtering the zero-mean and unit variance complex Gaussian noise process with the component's pre-selected Doppler filter. Interpolation of the fading process is performed to match the higher sampling rate of the input signal. After interpolation the samples are scaled accordingly to obtain the specified component average power gain. The complex discrete path gain "*h[n]*" for the i^{th} multipath component is obtained using equation (C.2),

$$h[n] = \sqrt{\frac{K\Omega}{K+1}} e^{j(2\pi f_0 nT + \phi_0)} + \sqrt{\frac{\Omega}{K+1}} x[n] \qquad \text{(C.2)}$$

where: K is the Rician K-factor defined as the ratio of the power between the LOS and the scattered component; Ω is the averaged path power gain $\Omega = E[|h[n]|^2]$; f_0 is

the Doppler frequency of the LOS component, ϕ_o is the initial phase of the LOS component, *x[n]* is the interpolated Doppler filtered complex Gaussian random process representing the diffuse scattering component; and *T* is the input signal sampling rate.

In general the envelope of h[n] has a Rician probability density function (pdf) but for a particular case of K = 0 it exhibits a Rayleigh pdf. For computational speed and efficiency of the simulator the time spreading effect of the channel is replicated by transforming the channel impulse response (tapped delay line with variable differential delays) into a band-limited impulse response (tapped delay line with equally spaced symbol delay) before convolution with the input signal.

Measurement Based "Playback" Channel Simulator

Different from the multipath fading channel simulator the "*playback*" channel simulator does not recreate the channel from user defined parameters, but rather it imports the channel frequency response directly from the Matlab workspace. Consequently, real channel time variant frequency functions can be used. The operation of the simulator is illustrated in Figure C.23. The simulator was implemented in MATLAB SIMULINK using digital signal processing (DSP) techniques [15].

The simulator operation is as follows: During the set-up phase the measured channel impulse responses are pre-processed to a minimum SNR of 20 dB and time-aligned to start at zero time delay. The responses are bandlimited (using equation (18) in [16]) to match the simulator input signal sample rate. Subsequently, the responses are zero padded (up-to the length of 512 samples) and then the FFT is applied to obtain the bandlimited time variant frequency response of the channel $H(f,t_n)$ which is stored in the Matlab workspace.

Throughout the simulation phase, the channel frequency responses are individually imported into the simulator and held constant for a period equivalent to the measurement acquisition rate. This is enabled by the use of the "First Order Hold" and the "Re-sample" blocks in the simulator. The convolution with the input signal is performed by point wise frequency multiplication of the channel response with the zero padded (up-to 512 samples in length) input signal frequency response.

The product of the multiplication is converted back into the time domain (*through the use of IFFT*) and the excess samples are removed to produce the output signal.

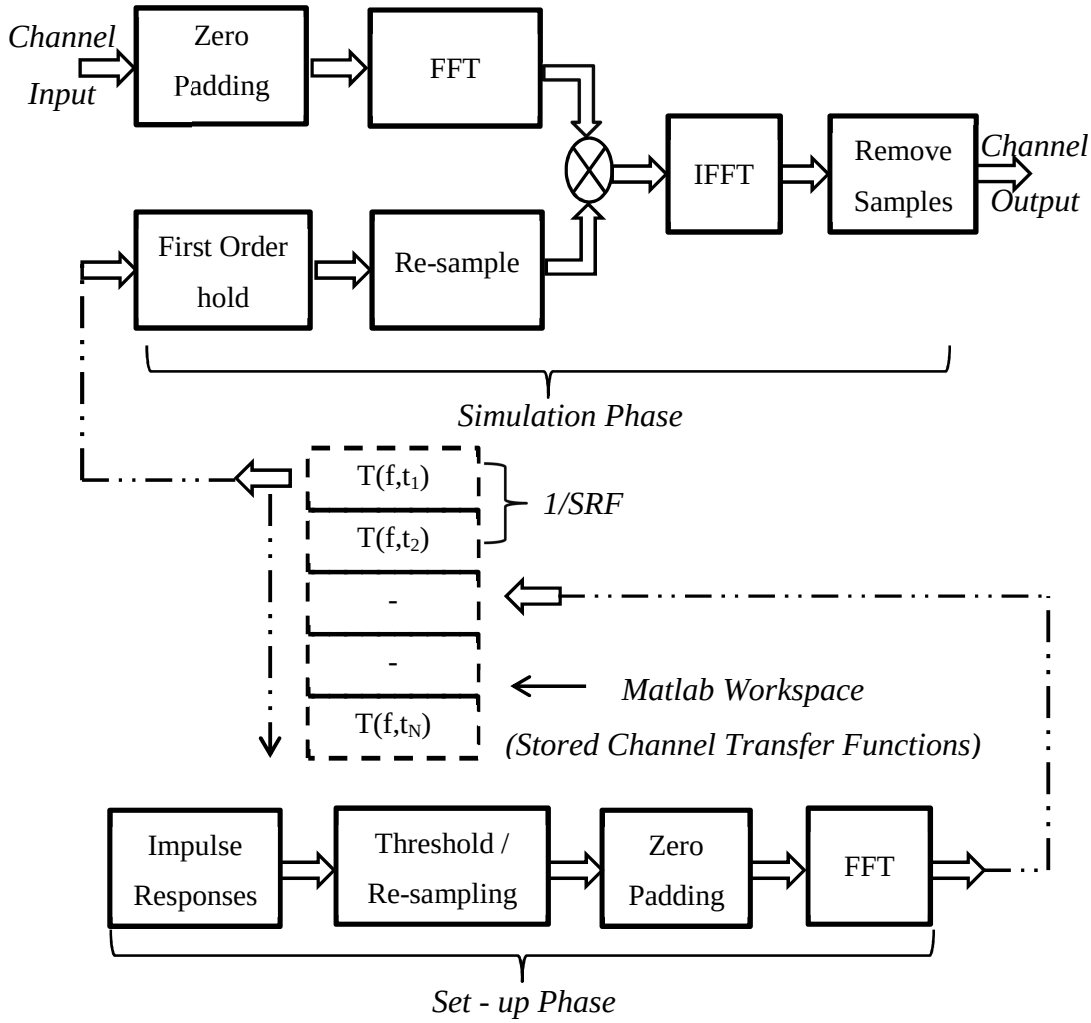

Figure C.23: Playback or measurement based channel simulator

C.3.2 Channel Measurement and Statistic Estimators

The channel measurements were performed in a rural/semi-rural area of Ipswich with a multiband chirp sounder which is able to operate simultaneously on centre frequencies 2.5 GHz, 3.5 GHz and 5.8 GHz with a bandwidth of 10 MHz. The data were collected for the duration of one second and with a sweep repetition rate of 250 Hz. The transmitter and receiver antennas were kept stationary during the measurement. Consequently, any measured Doppler shift must have been due to the changes in the environment caused from cars driving by, people walking, and moving trees. Figures C.24 (a)-(c) and C.25 (a)-(c) show the results of the one second average power delay profile, the time variant frequency response and delay Doppler function for the 3.5 GHz and 5.8 GHz bands respectively.

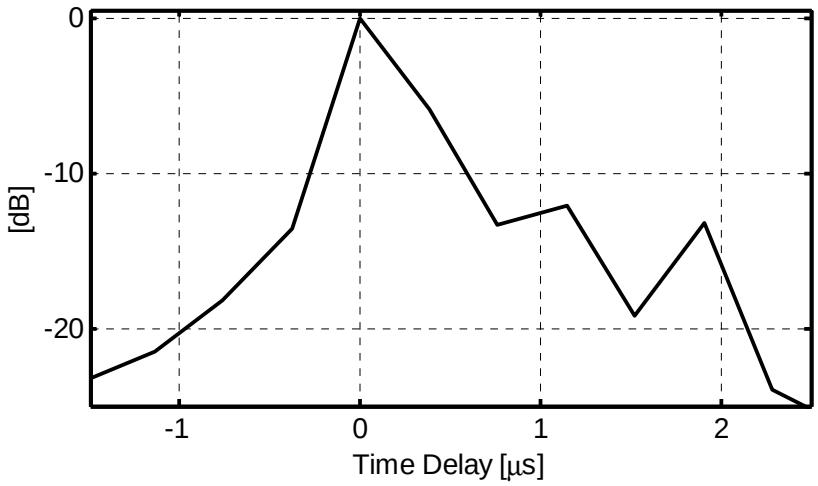

(a)

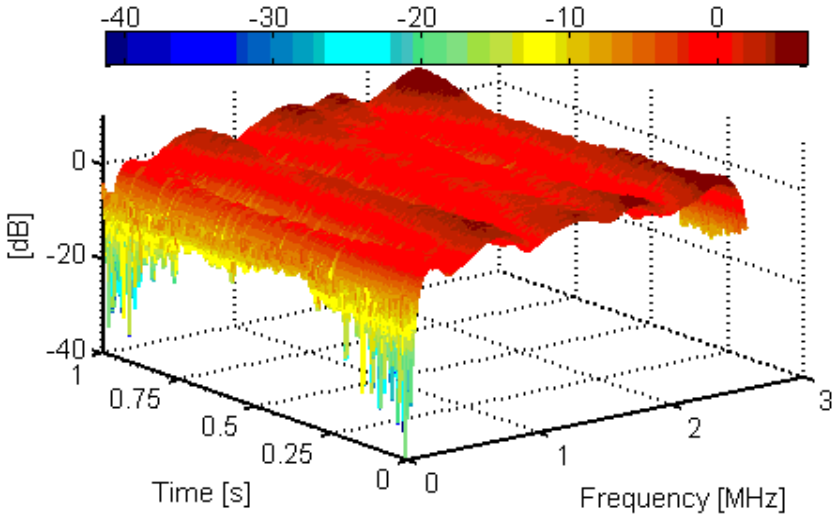

(b)

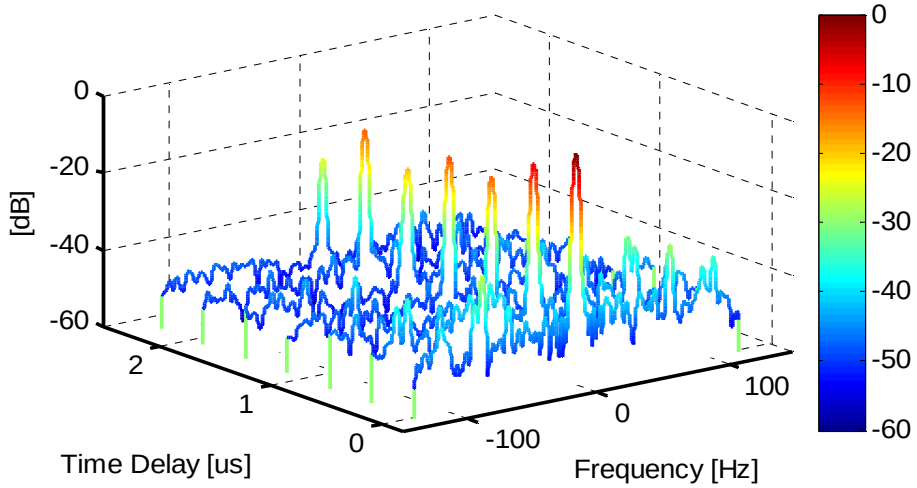

(c)

Figure C.24: 3.5 GHz measurement data (a) Normalised PDP; (b) Time variant frequency response; and (c) Normalised Delay – Doppler function

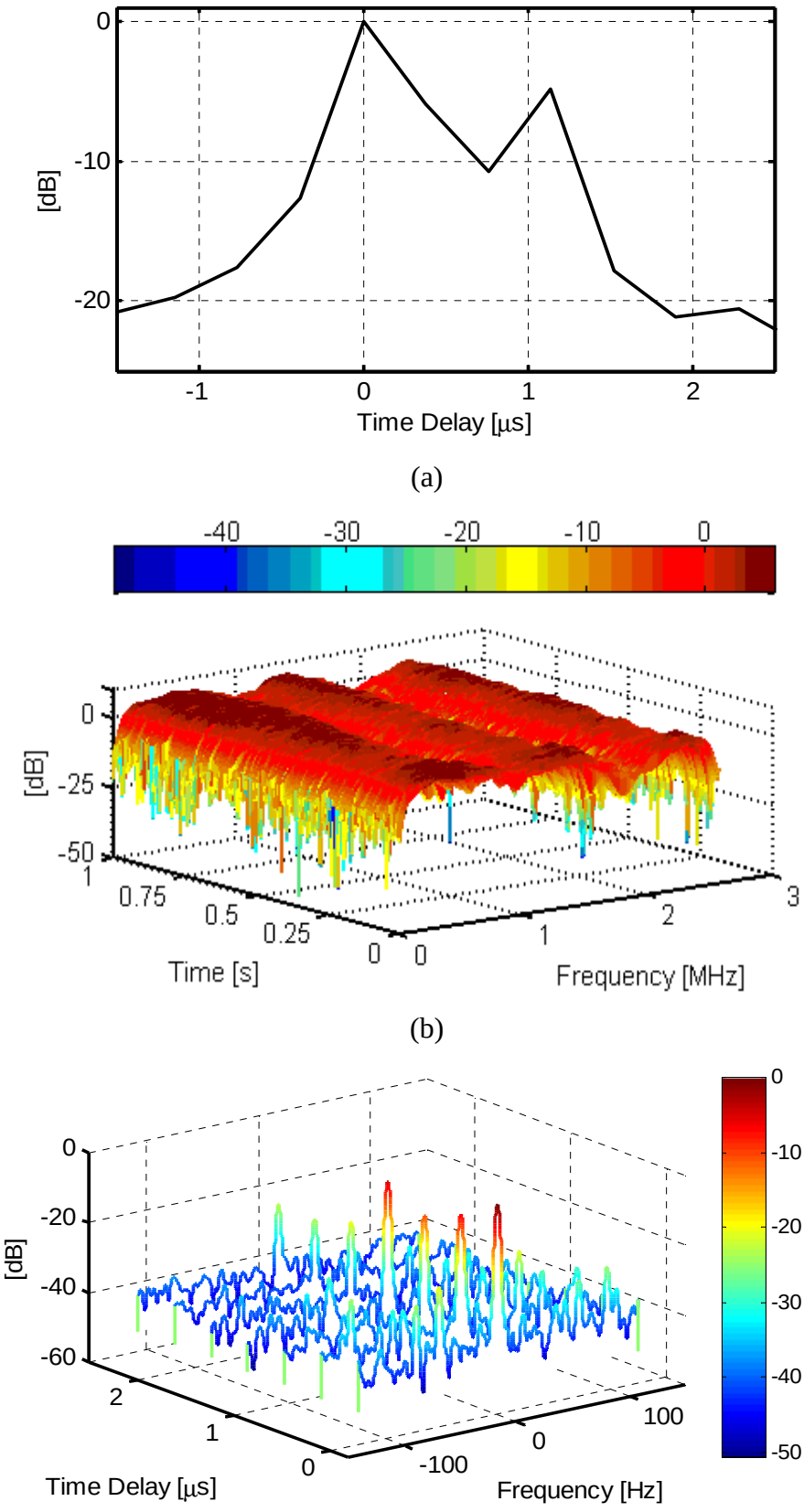

Figure C.25: 5.8 GHz measurement data (a) Normalised PDP; (b) Time variant frequency response; and (c) Normalised Delay – Doppler function

A detailed explanation of the architecture of the channel sounder used in these measurements as well as further measurement results can be found in references [13, 17].

The multipath fading channel simulator regenerates the channel based on user specified parameters of the corresponding multipath components. In both measurements the number of multipath components was obtained from the delay Doppler function and the power delay profile by assuming a threshold of -20 dB. Taking the peak at 0 µs delay as the reference (first) multipath component any relative path delay(s) with an average gain and a peak Doppler spectrum within the threshold were considered in the simulation. Consequently, 6 and 4 discrete multipath components at delay times [0 1 2 3 4 5]*381 ns and [0 1 2 3]*381 ns for the 3.5 GHz and 5.8 GHz measurements respectively were estimated. In this simulator the rounded Doppler spectrum type was chosen with a maximum Doppler shift set to 2.5 Hz as it provided a better approximation to the measured components Doppler spectrum. Figure C.26 (a)-(b) shows the normalised PSD of both the Doppler and rounded Doppler fitting for the 3.5 GHz and 5.8 GHz bands respectively. The rounded Doppler spectrum is also recommended in the IEEE802.16 standard [18] as a better approximation to the scattered component's Doppler power spectrum density (PSD) for fixed wireless channels [16]. The next sub-sections provide a description of the statistical estimators used to estimate the parameters, for the individual multipath components, needed to configure the multipath fading channel simulator.

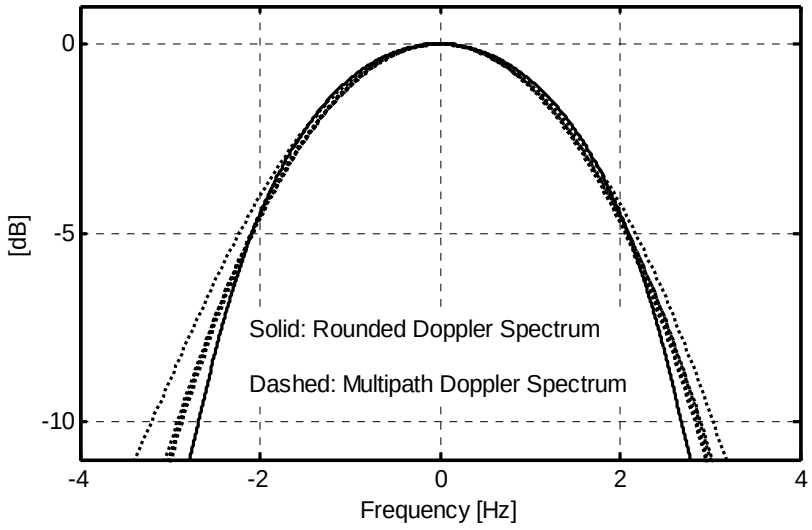

(a)

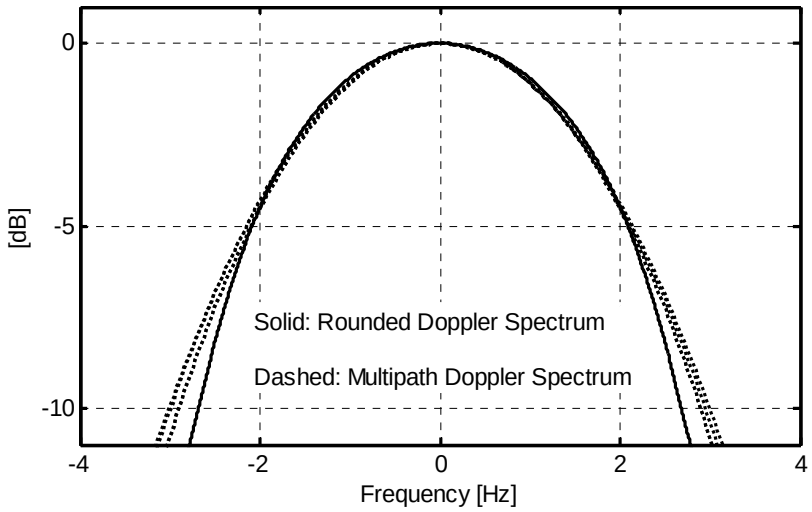

(b)

Figure C.26: Normalised Doppler spectrum and Rounded Doppler fit for

(a) 3.5 GHz band and (b) 5.8 GHz band

Method of Moment Statistic Estimator

Various methods of moment (MoM) estimators, also referred to as envelope based estimators, for the evaluation of the fading statistics (mainly K-factor) have been reported in the literature. In this work, the method of moment estimator proposed in [19] was used. The parameters estimation was performed on each discrete multipath component time-bin independently. The estimator uses the first and second moment's statistic of the component power samples to estimate both the K–factor (K) and the averaged power (Ω). Assuming the magnitude and the phase of the i^{th} discrete multipath component at time "n" to be given as in equations (C.3) and (C.4) respectively, then the first moment (μ_1) of the received power time-series can be computed as in equation (C.5).

$$r_n = \sqrt{\left(h_{real,n}\right)^2 + \left(h_{imag,n}\right)^2} \tag{C.3}$$

$$\theta_n = arctan\left(\frac{h_{imag,n}}{h_{real,n}}\right) \tag{C.4}$$

$$\mu_1 = E\{r^2\} = \frac{1}{N}\sum_{n=0}^{N-1} {r_n}^2 \tag{C.5}$$

The second moment (μ_2) of interest relates to the variance of power samples around its mean μ_1 and is given by:

$$\mu_2 = \left\{E\{(r^2 - \mu_1)^2\}\right\}^{1/2} = \left\{\frac{1}{N}\sum_{n=0}^{N-1}({r_n}^2 - \mu_1)^2\right\}^{1/2} \tag{C.6}$$

Using equations (C.5) and (C.6) the mean power of the deterministic LOS component ($|A|^2$) and of the scattered component ($2\sigma^2$) are given by equations (C.7) and (C.8) respectively:

$$|A|^2 = [{\mu_1}^2 - {\mu_2}^2]^{1/2} \tag{C.7}$$

$$\sigma^2 = \frac{1}{2}\left\{\mu_1 - ({\mu_1}^2 - {\mu_2}^2)^{1/2}\right\} \tag{C.8}$$

Finally, the K–factor using the method of moment is estimated as follows:

$$K = \frac{|A|^2}{2\sigma^2} \tag{C.9}$$

The technique described above relies solely on the samples envelope to estimate the component K–factor and does not utilize the additional phase information provided by the samples. Tables C.5 and C.6 give the estimated results of the K-factor and averaged power for the discrete multipath components of the 3.5 GHz and 5.8 GHz bands respectively.

Table C.5: MoM estimated statistic for the 3.5 GHz band

Path	*Path 1*	*Path 2*	*Path 3*	*Path 4*	*Path 5*	*Path 6*
K	46.09	3.24	6.05	10.42	5.23	30.97
Ω [dB]	0.00	-5.49	-13.08	-11.98	-18.89	-13.23

Table C.6: MoM estimated statistic for the 5.8 GHz band

Path	*Path 1*	*Path 2*	*Path 3*	*Path 4*
K	27.15	3.04	5.11	42.77
Ω *[dB]*	0.00	-6.58	-11.08	-4.85

Note that the parameters "f_o" and "ϕ_o" of equation (C.2) cannot be estimated with the method of moment, as the estimator only uses the envelope of the signal to compute the fading parameters. Consequently, unless stated for the simulations configured with the parameters estimated from the MoM the multipath components parameters "f_o" and "φ_o" were set to zero.

Complex Based Estimator

Unlike the MoM, the complex based estimator, also known as I/Q estimator, estimates parameters related to equation (C.2), based on the envelope and phase provided by the complex samples of the multipath components**.** In this study the complex based estimator algorithm detailed in [20] was used. A brief theoretical analysis of it is provided in this subsection. It has been shown in [18, 20] that the I/Q estimator outperforms the method of moment estimator as it uses additional information provided by the phase of signal samples. The CBE performance relies on the accurate estimation of the line of sight Doppler frequency component "f_o". This is obtained by locating the peak value in the Doppler spectrum as shown in (C.10).

$$f_o = \ argmax_f \left| \frac{1}{N} \sum_{n=0}^{N-1} h_n e^{-j2\pi fTn} \right| \tag{C.10}$$

For a practical sample size, the N-point FFT may not provide enough resolution to reliably estimate the specular frequency and this can lead to significant errors in the estimation of the *K–factor*. One improvement could be to zero pad, by appending M-N zeros (with M=16N) the complex vector "*h*" prior to computing the Fast Fourier transform (FFT) and finding the peak, may result in a high computational complexity. Consequently, the peak search frequency estimator

developed in [21] was used to locate the LOS Doppler frequency. This algorithm has an advantage compared to the previous method as it only requires N-point FFT.

Using equations (C.3) and (C.4) and the estimated "f_o" the average powers of the LOS ($|A|^2$), the scatter components (σ^2) and the initial phase (φ_0) of the LOS can be estimated as:

$$|A|^2 = \left| \frac{1}{N} \sum_{n=0}^{N-1} r_n e^{j(\theta_n - 2\pi f_0 T n)} \right|^2 \tag{C.11}$$

$$2\sigma^2 = \left| \frac{1}{N} \sum_{n=0}^{N-1} {r_n}^2 - |A|^2 \right| \tag{C.12}$$

$$\phi_o = arctan \left| \frac{\sum_{n=0}^{N-1} r_n \, sin(\theta_n - 2\pi f_0 T n)}{\sum_{n=0}^{N-1} r_n \, cos(\theta_n - 2\pi f_0 T n)} \right| \tag{C.13}$$

The Rician *K–factor* and the total average power taking into account the finite number of samples is given by equations (C.14) and (C.15), respectively.

$$K = \frac{1}{N} \left[(N-2) \frac{|A|^2}{2\sigma^2} - 1 \right] \tag{C.14}$$

$$\Omega = \frac{|A|^2 (K+1)}{K} = \quad 2\sigma^2 \, (K+1) \tag{C.15}$$

Table C.7: CBE estimated statistic for the 3.5 GHz band

Path	*Path 1*	*Path 2*	*Path 3*	*Path 4*	*Path 5*	*Path 6*
K	46.78	8.14	11.12	16.67	2.70	34.15
Ω [dB]	0.00	-5.90	-13.37	-12.14	-20.16	-13.27
f_0 [Hz]	-0.38	-0.41	-0.39	-0.34	-0.27	-0.38
Φ_0 [rad]	0.32	0.08	-0.27	-1.07	0.75	0.51

Table C.8: CBE estimated statistic for the 5.8 GHz band

Path	*Path 1*	*Path 2*	*Path 3*	*Path 4*
K	19.46	4.15	6.32	22.74
Ω [dB]	0.00	-6.20	-10.88	-4.88
f_0 [Hz]	-0.56	-0.58	-0.52	-0.60
Φ_0 [rad]	1.15	-1.50	0.61	0.82

Table C.7 and C.8 present a summary of the estimated parameters using the complex based estimator for the 3.5 GHz and 5.8 GHz measurement bands respectively.

C.3.3 BER performance comparison

In this sub-section the bit error rate results of the IEEE 802.16 physical layer model using the *Playback* channel simulator and the multipath fading channel simulator are presented and compared. In oder to match the input signal sampling rate in the *Playback* channel simulator, as described in sub-section *Measurement Based "Playback" Channel Simulator*, the measured channel impulse responses were bandlimited to 3.56 MHz bandwidth prior to the simulator set-up phase.

The BER results of the simulators in the 3.5 GHz and 5.8 GHz band are presented in Figures C.27 (a) and (b), respectively. In these figures the "*Playback*" curve marked as a solid line with rectangle represents the results from the measurement based channel simulator; the "*MoM*" curve marked as dashed line with a solid triangle represents the results from the multipath channel simulator when configured with channel parameters estimated from the method of moment estimator; the "*CBE*" curve marked as dashed line with rectangle represents the results from the multipath channel simulator when configured with channel parameters estimated from the complex based estimator.

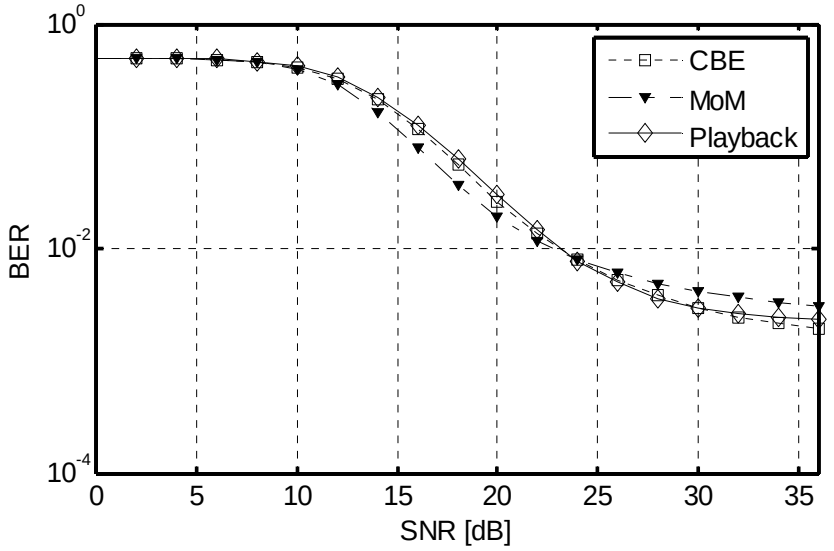

(a)

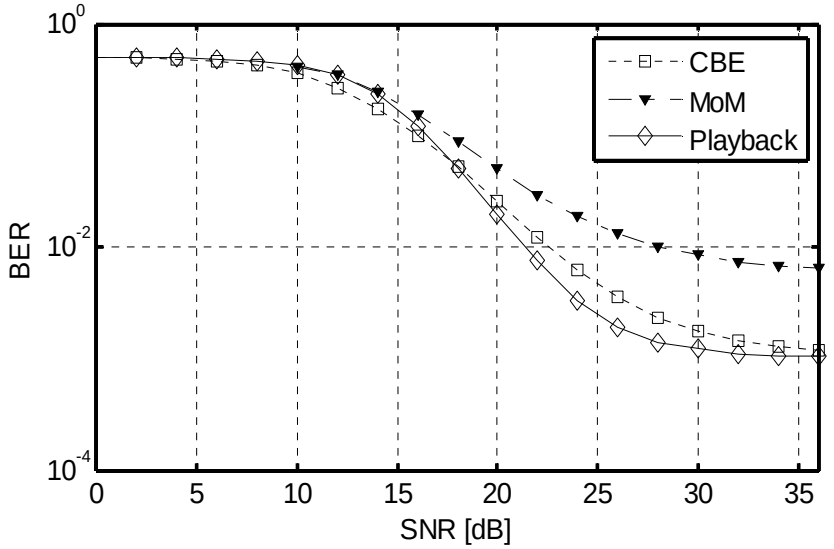

(b)

Figure C.27: BER performance for the (a) 3.5 GHz band and (b) 5.8 GHz band

The results in the figures show good agreement between the measurement based channel simulator and the multipath simulator configured with parameters estimated from the complex based estimator. This closer approximation was expected, since the complex based estimator provides an estimation of all the necessary parameters in equation (C.2). Consequently, the multipath fading simulator is able to recreate a channel with much closer approximation of the real measured channel [16, 18, 20]. On the other hand, Figure C.27 (a) shows comparable agreement between the "*Playback*" curve and the MoM curve. However, large BER

differences between the "*Playback*" curve and the multipath simulator, with parameters estimated from the MoM can be noticed in Figure C.27 (b). This difference could be attributed to the fact that although the MoM estimates the K-factor and the average power from the measured channel path(s), it fails to provide an estimation of the path(s) LOS component intial phase and Doppler frequency. Consequently the multipath fading simulator may not, in this case, regenerate the channel responses with characteristics similar to those of a non-zero "f_0" and "Φ_0" measurement channel.

In order to understand the effect of the LOS Doppler and initial phase on the BER curves, simulations in the Matlab multipath simulator for the cases of the measurement parameters (K-factor and average power) estimated from CBE but with the LOS Doppler and intial phase set to zero and the case of the parameters (K-factor and average power) estimated from the MoM and "f_0" and "Φ_0" estimated from CBE were performed.

In Figure C.28 (a)-(b) the CBE_N curve marked as a dashed line with a circle represents the result from the multipath channel simulator for the case in which the K-factor and average power are estimated from the CBE estimator but the LOS Doppler (f_0) and intial phase (Φ_0) are set to zero; MoM_w curve marked as dashed line with cross represents the case where the channel parameters (K-factor and average power) are estimated from the MoM estimator and the LOS Doppler (f_0) and intial phase (Φ_0) are estimated from the CBE estimator.

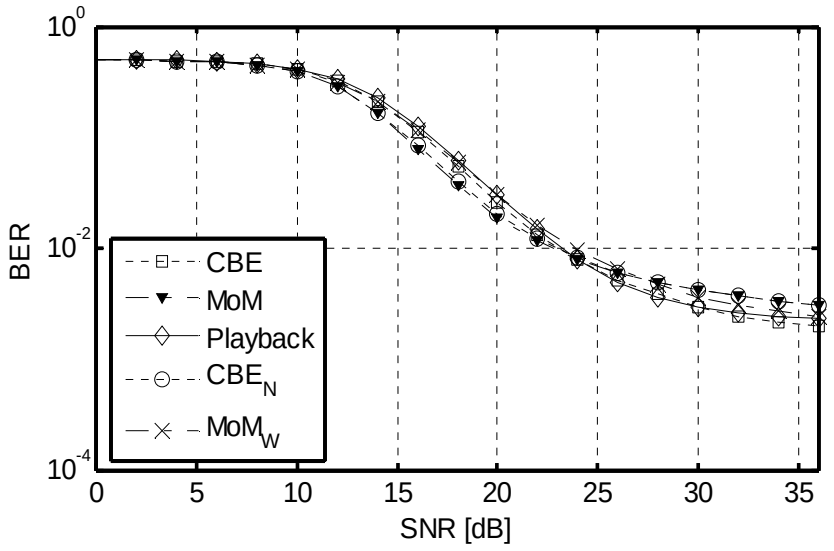

(a)

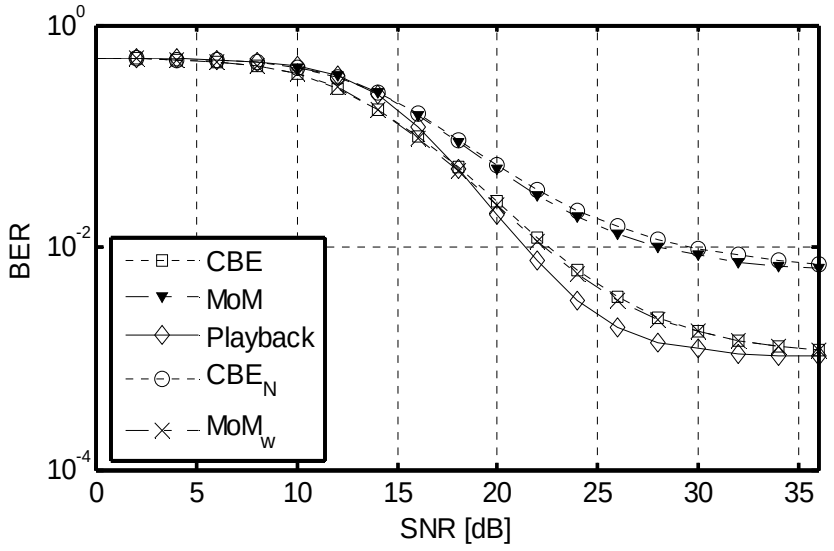

(b)

Figure C.28: BER performance effect of the LOS initial phase and Doppler frequency for (a) 3.2 GHz and (b) 5.8 GHz

The results in Figure C.28 (b) show that the BER perfomance of the complex based estimator (CBE_N curve) is similar to that of the method of moment estimator (*MoM* curve) as in this case both estimators intial phase (Φ_0) and LOS Doppler (f_o) information were set to zero. Furthermore, with the channel parameters (K-factor and average power) estimated from the method of moment and the intial phase (Φ_0) and LOS Doppler (f_o) estimated from the complex based estimator the BER result (MoM_w curve) is very close to that of the CBE curve. This behaviour is also observed for the 3.5 GHz measurement in Figure C.28 (a).

C.4 Discone Antenna

Discone antennas have been designed and manufactured for the channel sounding measurements in the 2-8 GHz frequency band detailed on previous subsection. This type of antenna has been widely used in UWB applications due to its wide impedance bandwidth and an omnidirectional radiation pattern (uniform on azimuth-plane) across the frequency band.

Figure C.29 shows the geometry of the proposed antenna. The antenna consists of three main parts: the top shaped disc acting as a radiator with its centre connected to the feed line of a coax; the cone which is connected to the ground; and the insulator which ensures that the disk and cone are not in short circuit.

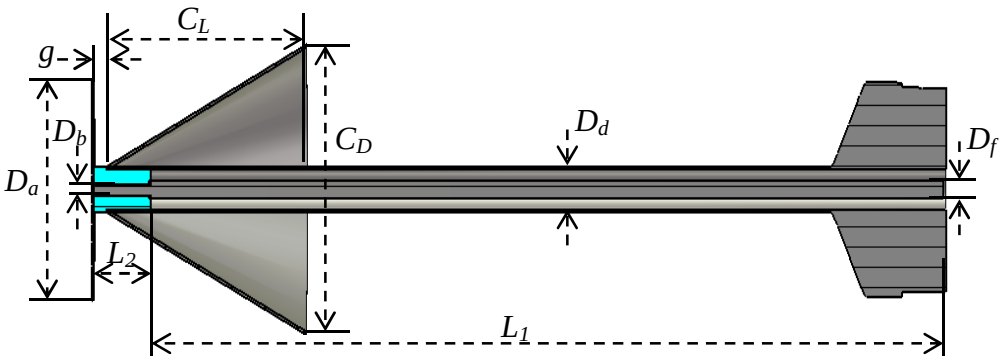

Figure C.29: Geometry of the proposed Discone antenna

Table C.9: Proposed Discone antenna parameters dimension

Parameter	L_1	D_a	C_L	C_D	D_b	D_d	D_f	L_2	g
Dimension	179	39	50	50	2	7	3.18	13	3

The antenna was designed and optimised in CST software to operate over a frequency range from 2-8.5 GHz. Table C.9 provides the final dimension of the proposed antenna. The antenna shows a return loss better than -10 dB across the desired frequency band, as displayed in Figure C.30. As expected, the antenna exhibits a uniform omnidirectional pattern in the H-plane across the frequency range, as shown in Figure C.31.

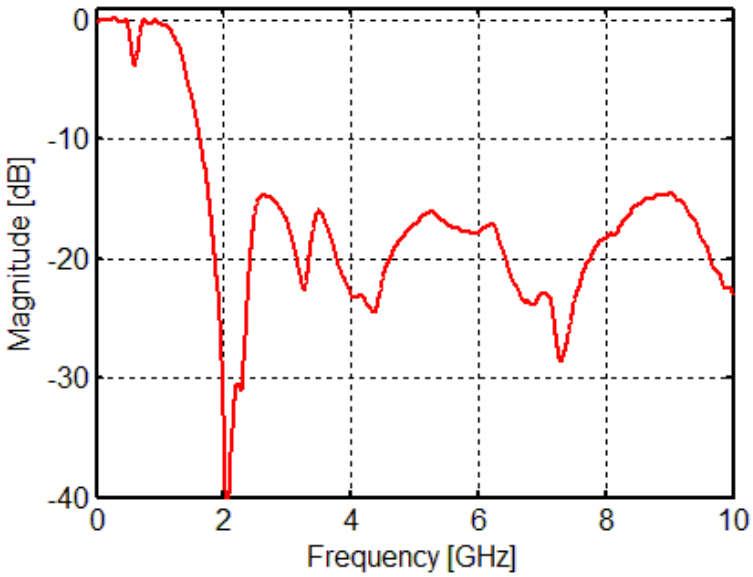

Figure C.30: Simulated return loss of the proposed Discone antenna

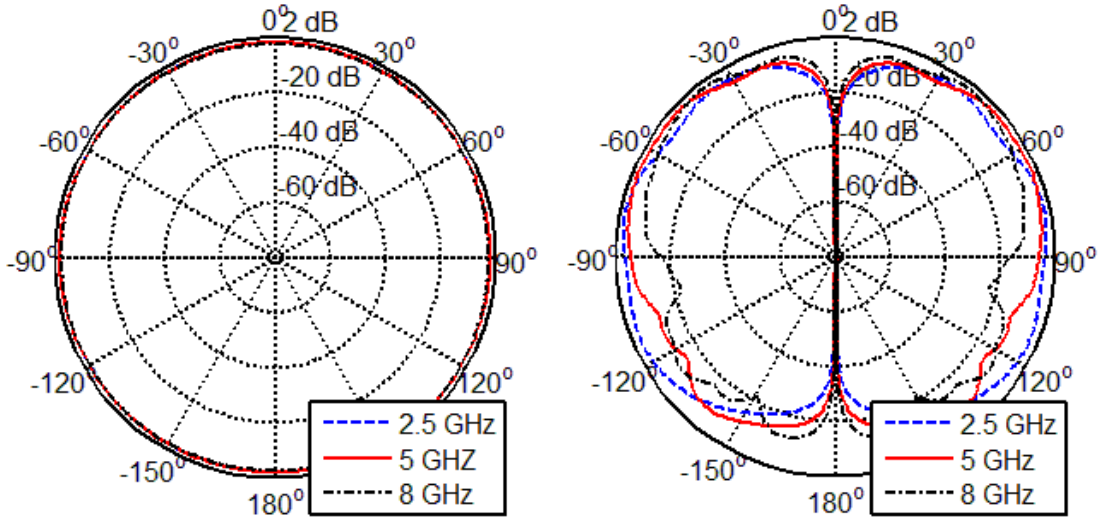

(a) H-plane (b) E-plane

Figure C.31: Normalised simulated radiation pattern of the discone antenna

C.5 Summary

The characterization of the electromagnetic signal propagation through the environment is essential for the understanding of the effects of the environment on the wireless systems performance. This appendix presented the results of channel measurement campaigns conducted at different frequency bands and in different environments: namely: reverberation chamber, indoor (offices and corridor like scenarios), and outdoor. Also, BER performance validation of the "Playback" channel simulator was presented for an outdoor measurement scenario around Ipswich City in the 3.5 GHz and 5.8 GHz frequency bands.

Measurements in a reverberation chamber were performed using a VNA with ultra-wideband Discone antennas connected to its ports. Measurements in this environment were performed to obtain reference figures of merit for the assessment of the diversity gain and MIMO capacity with different antenna separations. The computed apparent diversity gains across the band in this environment for 1x2 and 2x1 antenna configurations were on the order of 1.5-2.5 dB and the achievable normalised channel capacity for both LOS and NLOS cases were in the region of 16.18-16.27 b/s/Hz.

A brief overview of the architecture of the newly developed multiband channel sounder, at the Centre of Communication Systems at Durham University (U.K), has been presented. Results of the delay spread and path loss exponent in the 2.475 GHz and 60 GHz frequency bands for both indoor and outdoor environments using the newly built sounder have been presented.

Bit error rate performance comparisons of the measurement based channel simulator against the theoretical Matlab built-in multipath fading channel simulator have been performed, for the IEEE 802.16 physical layer model. The measurement based simulator imports the real channel measurement directly from the Matlab workspace; whereas the multipath fading simulator regenerates a theoretical channel response based on the user's specified channel parameters. In the study, real channel measurements obtained from channel sounding in a rural / semirural environment in the 3.5 GHz and 5.8 GHz frequency bands were used. The parameters for the multipath fading simulator have been extracted from the measurement channel data using two different estimators namely the method of moment and the complex based estimator.

With parameters estimated from the method of moment, the BER performance of the multipath fading simulator were found to be much different from that of the measurement based simulator. A reason for these differences could be down to the fact that the measurement profiles contain non-zero LOS Doppler frequencies and initial phases and the method of moment estimator only provides the estimations of the K-factors and average powers. Consequently, with an assumption of zero LOS initial phases and zero Doppler frequencies, the channel responses regenerated by the multipath fading simulator might not fully represent the measurement channel. This is reflected in the BER performance curves. Differently, the complex based estimator not only estimates the K-factor and average power from the measurement channel but also estimates the initial phase and Doppler frequency of the LOS component. Consequently, the multipath fading simulator configured with parameters from this estimator offers a BER performance which fits best to that of the measurement based simulator.

C.6 References

[1] M. A. Garcia-Fernandez, J. Sanchez-Heredia, A. Martinez-Gonzalez, D. Sanchez-Hernandez, and J. Valenzuela-Valdes, "Advances in mode-stirred reverberation chambers for wireless communication performance evaluation," *Communications Magazine, IEEE,* vol. 49, pp. 140-147, 2011.

[2] K. Rosengren and P. Kildal, "Study of distributions of modes and plane waves in reverberation chambers for the characterization of antennas in a multipath environment," *Microwave and Optical Technology Letters,* vol. 30, pp. 386-391, 2001.

[3] P. Kildal, K. Rosengren, J. Byun, and J. Lee, "Definition of effective diversity gain and how to measure it in a reverberation chamber," *Microwave and Optical Technology Letters,* vol. 34, pp. 56-59, 2002.

[4] J. Parsons, D. Demery, and A. Turkmani, "Sounding techniques for wideband mobile radio channels: a review," *IEE Proceedings in Communications, Speech and Vision,* vol. 138, pp. 437-446, 1991.

[5] G. Kadel and R. Lorenz, "Impact of the radio channel on the performance of digital mobile communication systems," *6th IEEE International Symposium*

on Personal, Indoor and Mobile Radio Communications, vol. 2, pp. 419-423, 1995.

[6] H. Song, A. Bekaryan, J. Schaffner, A. Hussain, and P. Kildal, "Effects of mutual coupling on lte mimo capacity for monopole array: comparing reverberation chamber tests and drive tests," *IEEE Antennas and Wireless Propagation Letters* , vol. 14, pp. 454-457, 2014.

[7] P. Kildal and K. Rosengren, "Correlation and capacity of MIMO systems and mutual coupling, radiation efficiency, and diversity gain of their antennas: simulations and measurements in a reverberation chamber," *IEEE Communications Magazine,* vol. 42, pp. 104-112, 2004.

[8] J. Wallace, M. Jensen, A. Swindlehurst, and B. Jeffs, "Experimental characterization of the MIMO wireless channel: data acquisition and analysis," *IEEE Transactions on Wireless Communications,*vol. 2, pp. 335-343, 2003.

[9] S. Salous, *Radio Propagation Measurement and Channel Modelling*. Chichester, UK.: John Wiley & Sons, 2013.

[10] X. Wu, Y. Nechayev, C. Constantinou, P. Hall, A. Brizzi, A. Pellegrini, *et al.*, "Preliminary estimates for observability of 60 GHz wireless body area networks," *IEEE Asia-Pacific Conference on Antennas and Propagation (APCAP)*, pp. 110-111, 2012.

[11] A. Maltsev, R. Maslennikov, A. Sevastyanov, A. Lomayev, A. Khoryaev, A. Davydov, *et al.*, "Characteristics of indoor millimeter-wave channel at 60 GHz in applications to perspective WLAN systems," *4th European Conference on Antennas and Propagation (EuCAP)*, pp. 1-5, 2010.

[12] R. Daniels and R. Heath, "60 GHz wireless communications: emerging requirements and design recommendations," *IEEE Vehicular Technology Magazine,* vol. 2, pp. 41-50, 2007.

[13] K. Khokhar and S. Salous, "Frequency domain simulator for mobile radio channels and for IEEE 802.16-2004 standard using measured channels," *IET Communications,* vol. 2, pp. 869-877, 2008.

[14] P. Bello, "Characterization of randomly time-variant linear channels," *IEEE Transactions on Communications Systems,* vol. 11, pp. 360-393, 1963.

[15] K. Khokhar, "Design and development of mobile channel simulators using digital signal processing techniques," PhD, Engineering and Computer Sciences, Durham University, Durham, 2006.

[16] C. Iskander, "A Matlab-based object-oriented approach to multipath fading channel simulation," Hi-Tek Multisystems, 2008.

[17] S. Salous, S. Feeney, K. Khokhar, and R. Lewenz, "Measurements of radio channels and bit error rate estimation of IEEE802.16 standard in semi-rural environment at three frequencies in the 2-6 GHz frequency band," *IET Communications,*vol. 2, pp. 878-885, 2008.

[18] K. Baddour and T. Willink, "Improved estimation of the ricean K factor from I/Q samples," *IEEE 66th Vehicular Technology Conference, 2007*, pp. 1228-1232, 2007.

[19] L. Greenstein, D. Michelson, and V. Erceg, "Moment-method estimation of the Ricean K-factor," *IEEE Communications Letters,* vol. 3, pp. 175-176, 1999.

[20] K. Baddour and T. Willink, "Improved estimation of the Ricean K-factor from I/Q fading channel samples," *IEEE Transactions on Wireless Communications,*vol. 7, pp. 5051-5057, 2008.

[21] E. Aboutanios, "A modified dichotomous search frequency estimator," *IEEE Signal Processing Letters,*vol. 11, pp. 186-188, 2004.

Appendix D: List of Publications

D.1 Journal Papers

1. X. Raimundo, S. Salous, and F. Fioranelli, "Interrupted FMCW waveforms for suppression of interface reflections in through-the-wall, Ground Penetrating and Medical Radio Imaging Radar," IET Radar, Sonar & Navigation. [Submitted].

2. F. Fioranelli, S. Salous, I. Ndip, and X. Raimundo, "Through the wall detection with gated FMCW signals using optimized patch-like and vivaldi antennas," *IEEE Transactions on Antennas and Propagation*, vol. 63 pp. 1106-1117, 2015.

3. F. Fioranelli, S. Salous, X. Raimundo, "Frequency-modulated interrupted continuous wave as wall removal technique in through-the-wall imaging," *IEEE Transactions on Geoscience and Remote Sensing*, vol.52, no.10, pp.6272-6283, 2014.

D.2 International Conferences

1. S. Salous, A. Cheema, and X. Raimundo, "Radio channel propagation measurements using a multiband agile chirp sounder," *XXXIth URSI General Assembly and Scientific Symposium (URSI GASS)*, pp.1-4, 2014.

2. X. Raimundo, S. Salous, and F. Fioranelli, "Frequency modulated interrupted continuous wave signals in different radar imaging applications," *XXXIth URSI General Assembly and Scientific Symposium (URSI GASS)*, pp.1-4, 2014.

3. X. Raimundo and S. Salous, "Bit error rate comparison of MATLAB multipath fading channel simulator and measurement based channel simulator using real measurement data," *International Symposium on Signals, Systems, and Electronics (ISSSE)*, pp. 1-6, 2012.

4. X. Raimundo, S. Salous, and K. Nasr, "UWB MIMO measurements in reverberation chamber and indoor environment," *International Symposium on Signals, Systems, and Electronics (ISSSE)*, pp.1-5, 2012.

D.3 COST (IC1004) Meetings

1. S. Salous, X. Raimundo, and A. Cheema “Small cell wideband measurements in the 60 GHz band,” COST IC1004 TD(14) 11024, Krakow, Poland, 2014.

2. S. Salous, X. Raimundo, and A. Cheema, “Wideband measurements in the 60 GHz band,” COST IC1004 TD(14)10066, Aalborg, Denmark , 2014.

3. S. Salous, A. Cheema, and X. Raimundo, “Radio channel propagation measurements and spectrum sensing using an agile chirp sounder,” COST IC1004 TD(14) 09032, Ferrara, Italy, 2014.

4. X. Raimundo and S. Salous, “Bit error rate comparison of the tapped delay line stochastic channel model with the ‘Playback’ channel from measured data in a WiMAX IEEE802.16-d simulator,” COST IC1004 TD(12)05082, Bristol, UK, 2012.

5. K. Nasr, S. Salous, and X. Raimundo, “Measurements of the diversity gain of UWB arrays in reverberation and indoor environments,” COST 2100 TD(10) 12051, 2010.

D.4 External Presentations

1. X. Raimundo, S. Salous, and F. Fioranelli, “Frequency modulated interrupted contimous wave for ground penetrating radar,” presented on IET/EuroGPR Colloquium on RF design for Ground Penetrating Radar, University College of London, UK, 2014.

2. F. Fioranelli, X. Raimundo, and S. Salous, “A novel approach to wall reflection suppression in through-wall radar,” presented at the UK URSI Festival of Radio Science, University of Birmingham, UK, 2013.

3. F. Fioranelli, S. Salous, and X. Raimundo, “Through-the wall radar imaging using UWB signals,” poster presented at the 2nd IET Technical Enterprise Workshop on “Today’s RF Tommorrow’s Medicine”, Queen Mary University, UK, 2013.

4. X. Raimundo and S. Salous, “Performance comparison of frequency domain and Matlab time-domain channel simulator with use of measured channel data,” presented at UK URSI Festival of Radio Science, Durham University, UK, 2012.

5. X. Raimundo and S. Salous, “Diversity gain of ultra-wideband antenna array in reverberation chamber and indoor measurement,” presented at UK URSI Festival of Radio Science, University of Leicester, UK, 2011.

6. [Presenter] Z. Wang and S. Salous, “Directional spectrum occupancy,” poster presented at the IET Cognitive Radio Communications Seminar, IET London: Savoy Place, UK, 2010.

7. X. Raimundo and S. Salous, “Antennas and algorithms for ultra wideband radar based microwave imaging,” presented at UK URSI Festival of Radio Science, University of Birmingham, UK, 2009.

D.5 Internal Presentations

1. X. Raimundo, “Skin and clutter suppression on uwb microwave imaging for breast cancer detection,” presented at Durham University Research Day, School of Engineering and Computing Sciences, UK, 2010.

2. X. Raimundo, “Radar based microwave imaging for breast cancer detection,” poster presented at Durham University Research’s Poster Competition, Durham Town Hall, UK, 2010.

3. X. Raimundo, “Microwave imaging for early breast cancer detection,” poster presented at Durham University Research Day, School of Engineering and Computing Sciences, UK, 2011.

4. X. Raimundo, “Breast cancer detection using microwave”, poster presented at Durham University Research Day, School of Engineering and Computing Sciences, UK, 2011.